Universitat Autònoma de Barcelona

New Fluorescent Nanovesicles, by Self-assembly of Organic Fluorophores, Sterols and Surfactants, as Probes for Bioimaging

Antonio Ardizzone

Universitat Autònoma de Barcelona

New Fluorescent Nanovesicles, by Self-assembly of Organic Fluorophores, Sterols and Surfactants, as Probes for Bioimaging

Antonio Ardizzone

Tesis Doctoral

Programa de Doctorado de Ciencia de Materiales

Directores

Prof. Jaume Veciana Miró

Dr. Nora Ventosa Rull

Tutor

Dr. Roser Pleixats Rovira

Departamento de Química
Facultad de Ciencias

2017

La present memòria es presenta per aspirar al Grau de Doctor per:

Antonio Ardizzone,

Vist i plau:

Prof. Jaume Veciana Miró

Dr. Nora Ventosa Rull

Dr. Roser Pleixats Rovira

Bellaterra, 10 de Març de 2017

JAUME VECIANA MIRÓ, Research Professor, and **NORA VENTOSA RULL**, Scientific Researcher, of the Spanish Council of Research at the Materials Science Institute of Barcelona (ICMAB-CSIC)

CERTIFY

That **Antonio Ardizzone**, Master in Chemical Engineering, has performed, under their management, the research work entitled **"New Fluorescent Nanovesicles, by Self-assembly of Organic Fluorophores, Sterols and Surfactants, as Probes for Bioimaging"**. This work has been performed under the mark of the Materials Science Ph.D. program of the Chemistry Department of the Autonomous University of Barcelona.

And in witness whereof this is signed by

Directors

Prof. Jaume Veciana Miró

Dr. Nora Ventosa Rull

March 10, 2017

Contents

1

Introduction and Objectives

1.1 Introduction

1.1.1 An overview of the common fluorescent probes used in bioimaging

For centuries the fundamental tool for biological imaging has been the optical microscopy. The opportunity to understand complex biological systems relies on our ability to visualize and quantify events and processes with high spatial and temporal resolution. Despite the many efforts, application of optical microscopy has been limited for a long period to visualization at less than 10 μm of depth, due to the light scattering of biological tissues avoiding the acquisition of information from elements beyond that distance from the surface [1, 2]. In the last decades new technological innovation on fluorescence microscopy, such as the development of confocal and multiphoton microscopes setups, allowed to image far below that limit, going deep to the millimeters scale in living tissues [3][4][5]. This was a total revolution for biologists, allowing the noninvasive study of processes in living organisms at high penetration depths and making possible their 3D reconstructions. Despite the huge innovation on imaging depth and 3D imaging brought by confocal and multiphoton microscopes, no strong improvement in resolution was made until the last 10 years. Optical microscopes have in fact an intrinsic limitation in spatial resolution, due to the wave nature of light (known as Abbe's diffraction limit). With the best optics, the resolution of fluorescence microscopy is limited to ~ 200 nm on the focal plane and ~ 500 nm on the optic axis, not permitting therefore the visualization of many cellular structures and events occurring at a lower scale [6]. Only in 2006 this limitation was circumvented with the first successful experimental setups on stimulated emission depletion (STED) microscopy and several other techniques which allowed to high-precisely localize single fluorophores, such as Stochastic Optical Reconstruction Microscopy (STORM) and Photo-activated localization microscopy (PALM) [7]. Eric Betzig, Stefan W. Hell and William E. Moerner

were awarded in 2014 with the Nobel Prize in Chemistry for their invention in super-resolution microscopy.

However, the possibility of surmounting the technological limits that lead to these new innovations has been intrinsically linked to the development of new fluorescent probes, with adequate physicochemical properties [8][9]. In order to take advantage of the full potential of the today's fluorescence imaging and detection setups with respect to speed, resolution and sensitivity, probes that first of all guarantee extremely high brightness and photostability are required.

Ideal fluorescent probes for bioimaging must fulfill several requirements [2, 10] (a brief description of the electronic transitions and related optical properties of fluorescent probes is given in Appendix 1):

- High brightness, i.e. the combination of large molar absorption coefficient (ε) at the excitation wavelength and a high fluorescence quantum yield (φ). The brightness of a probe is in fact defined as φ times ε and it gives a measure of the intensity of fluorescence signal obtained upon excitation at a specific wavelength. Bright fluorophores allow to reduce the laser power and exposition time under the microscope, with high signal-to-noise ratios and generally higher quality images.

- Excitation and emission wavelengths in a window where no attenuation effects, due to both scattering and absorption of the biological matter, occur. Especially concerning the *in vivo* applications, in fact, excitation and emission wavelengths must be centered in the biological transparency windows, located in the near infrared (NIR) region [11]Figure 1.1: first window (NIR-I) spans from 700 nm to 950 nm, while second window (NIR-II) from 1000 nm to 1350 nm, each one characterized for high transparency toward biological matter.

- High Stokes shift, which is the energy difference between the maximum absorption and emission. Probes with low Stokes shift generally experience re-absorption phenomena, which limit the quantitative analysis, and complicate the experimental setup.

- Low cytotoxicity, in the case of live cells imaging or *in vivo* applications.

- Adequate physicochemical properties as, for example, solubility or dispersability in relevant buffers, cell cultures media or body fluids, depending on the application. Moreover chemical stability and low tendency to aggregation are crucial for longer time imaging.

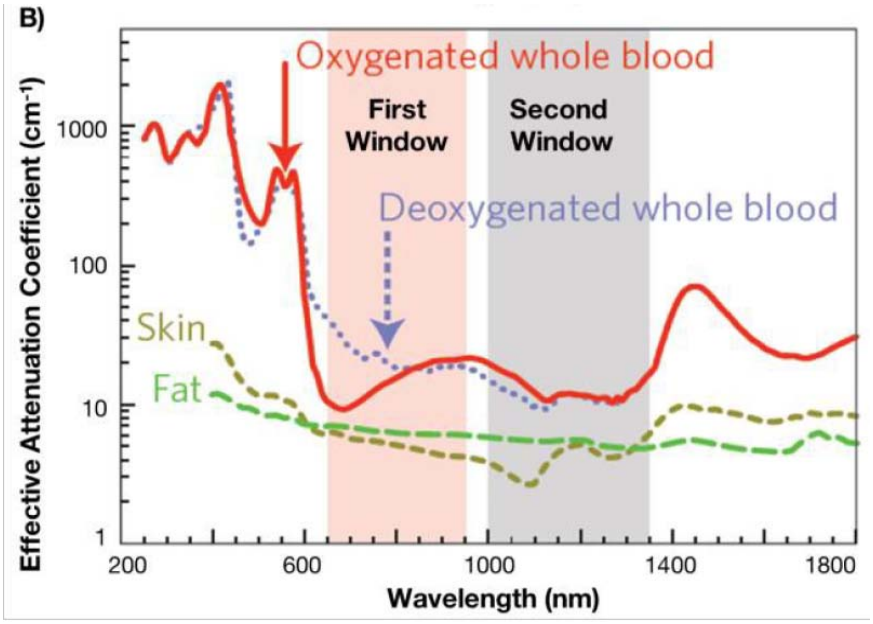

Figure 1.1: Attenuation coefficient versus wavelength of different body substances: oxygenated (red) and deoxygenated (purple) blood, skin (yellow) and fat (green) aiming for sub-skin imaging. Adapted from Ref. [11]

- Presence of functional groups for site-specific targeting, required for the precise imaging of an organ or cell compartment.

- Opportune size, which has a strong impact on the biodistribution of the probes in imaging of living organism. Small molecules, for example, can be useful for specific applications as vascular imaging, while for tumors imaging fluorescent nanoparticles are more efficient, being preferentially accumulated in tumors than in healthy tissues.

- High two-photon cross-section (σ_{2p}), which is necessary for deep imaging with two-photon microscopes. It is a measure of the probability of a fluorophore to be excited by the simultaneous absorption of two photons at a certain wavelength.

Matching all these parameters constitute a tough challenge and for this reason many classes of fluorescent probes exist in literature that are currently used in fluorescence microscopy. In Figure 1.2 the commonly used fluorescent probes, including organic dye molecules, fluorescent proteins, inorganic and organic nanoparticles, are schematized. Each family of probes has its own advantages/disadvantages and main applications, which will be hereafter discussed.

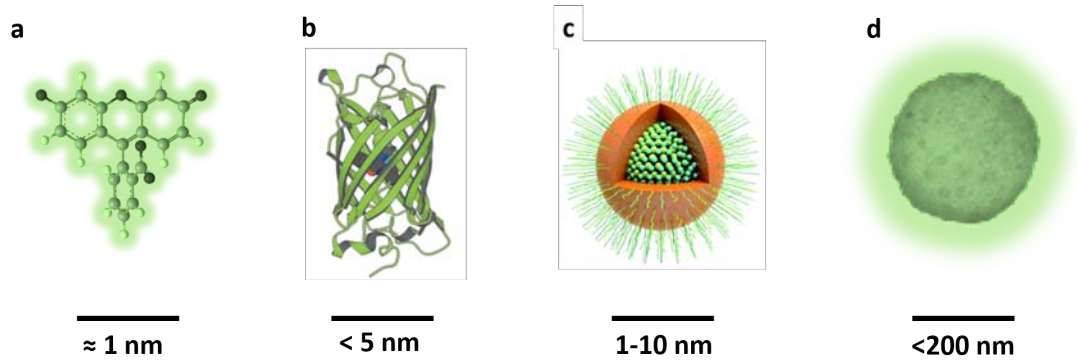

Figure 1.2: Schematization of the labels commonly used in fluorescence microscopy and corresponding sizes. a) molecular organic fluorophore (e.g. fluorescein); b) fluorescent proteins (e.g. green fluorescent protein, GFP); c) fluorescent inorganic nanoparticles (e.g. PEGylated Quantum Dot, QD. Image from [12]); d) fluorescent organic nanoparticle (e.g. polymer nanoparticle).

Organic dyes, with small size (~ 1 nm), have optical properties which can be finely tuned, being the structure-property relationship known for many classes of fluorophores. Fluorescent compounds are generally aromatic structures and the emission properties depend on the electronic transitions involved, which can be either delocalized over the whole chromophore structure or due to intramolecular charge transfer. The most common organic fluorophore families include fluoresceins, rhodamine, BODIPY, cyanines, coumarins, but this list is far to be exhaustive [13]. Absorption coefficients of molecular dyes can reach values as high as ~10^5 $M^{-1}cm^{-1}$ (as in the case of resonant dyes, such as the cyanines) and fluorescence quantum yield can be close to 1 (in the visible region), but it is generally low for dyes emitting in the transparency windows (red/infrared dyes) [10]. The large π-conjugated systems of the red-shifted dyes, which have higher degrees of vibration, lead in fact to an increased number of non-radiative decay pathways and thus lower efficiency.

The combination of low quantum yield, small Stokes shift and, in many cases, limited photo- and chemical stability hampers the application of organic fluorophores especially in *in vivo* applications. Despite these limitations molecular dyes are diffusely used, thanks to low cost and huge commercial availability. Water-soluble red- and NIR-emitting cyanines (as Cy5, Cy7 or IndoCyanine Green, ICG) are, for example, commonly employed labels. However, despite the numerous developments of new cyanine dyes, the only FDA (US Food and Drug Administration) approved NIR probe for *in vivo* use in medical applications is ICG which finds strongly limited applications, due to its low Stokes shift and very poor chemical stability [2, 14].

Another major drawback of organic fluorescent dyes, particularly related to *in vivo*

microscopy purposes [15], where dyes emitting in the biological transparency windows are required, concerns their solubility in aqueous media. Red and NIR emitting dyes have in fact extended π-conjugated aromatic structures, which make them strongly hydrophobic and poorly bioavalaible. Several chemical modifications to increase the hydrophilicity of these dyes have been proposed, mainly based on the addition of polar groups, as for instance sulfonate [16] and saccharide [17] functions or polyethylene glycol (PEG) chains. For example, Antaris et al. synthesized a NIR-II window ($\lambda_{emission}$>1000 nm) emitter which was modified with a 44-units PEG chain, significantly improving its water solubility. This molecule showed superior quality for mouse blood and lymphatic vasculatures imaging. [14]. In alternative to the chemical modification, non-water soluble dyes can be dispersed in water, taking advantage of their hydrophobicity, by processing them as nanoparticles, as discussed afterwards.

The small size of molecular dyes make them suitable especially for cells biology application. In living organism imaging in fact, the fast body clearance of molecular probes (*via* kidneys and urine, in the case of highly hydrophilic dyes, or *via* liver and bile excretion in the case of more lipophilic ones, as ICG), on one side limits the dye toxicity while on the other hand limits the temporal window in which imaging can be performed and, without any targeting agent, the biodistribution of the fluorophore over the body.

The discovery of Green Fluorescent Protein (GFP) in 1962 was a revolution, especially concerning the study of cancers, helping revealing mechanisms of growth and metastatic behaviors [18]. For this reason, O. Shimomura, M. Chalfie and R.Y. Tsien were awarded with the Nobel prize in Chemistry in 2008. Typically fluorescent proteins (FPs) have a structure similar to the one indicated in Figure 1.2b, with polypeptide chains folded in a barrel shape with a central helix, which holds the chromophore. Oppositely to the wide tuneability of organic dyes, the can-like structure of the FPs (with a diamter of 3-4 nm) partially limits the possibility of tailoring the emission color of the chromophore held within, especially concerning red- and infrared-emitting dyes which have large planar π-conjugated structures [19]. However, a large variety of fluorescent proteins has been engineered, spanning the entire visible spectra. Molar absorption coefficients of fluorescent proteins are in the order of 10^4 $M^{-1}cm^{-1}$ and generally brightness is lower compared to organic dyes. Very few bright fluorescent proteins are reported emitting in the red-edge region of the visible spectrum [20]. A major issue concerning FPs is also related to their low photostability, which limits the applications of such structures with techniques requiring strongly intense laser powers (multiphoton microscopy, for example). Despite some limitations related to the spectral properties, FPs are extensively

used, particularly as intracellular labels, thanks to their exceptional biocompatibility and reduced toxicity. Among the generally used fluorescent proteins, the modified Enhanced GFP (mEGFP) remains one of the best and more versatile, thanks to the low tendency to form oligomers, modest brightness in the green and photostability. Orange/red emitting FPs in fact generally show higher tendency to form oligomer and typically undergo accelerated photobleaching. [21]. Despite more than 20 years of research have been dedicated to the study of fluorescent proteins, these structures are still intensively investigated and novel applications are discovered, such as the possibility of use them for thermal sensing in living organisms [22]. However, the issues concerning the large-scale productions and the structural stability of proteins, which may undergo aggregation towards the formation of oligomers or even denaturation, are critical in the full development and commercialization of such structures for imaging and, more in general nanomedicine purposes [23].

The need of efficient probes able to overcome the common problems of fluorescent molecules and fluorescent proteins, including limited photostability and brightness in the red-infrared region, necessary for applications such as deep *in vivo* imaging, boosted the research on fluorescent nanoparticles (FNPs), schematized in Figure 1.2 c-d, as new probes for fluorescence microscopy.

Engineering of FNPs can benefit in several ways to the design of probes. Whereas small organic dyes are quickly cleared during the imaging of living organisms, the nano-sized distribution of FNPs is an advantage itself, favoring, for example, the passive accumulation in tumors, the so-called enhanced permeability and retention (EPR) effect, generally occurring for nanoparticles in the range 15-200 nm. This process, based on the enhanced permeability of the blood vessels in tumors, is not efficient for low molecular weight dyes (<5 nm), which diffuse aspecifically without being accumulated in the tumors [15]. Moreover, if on one hand the FNPs are generally big enough to avoid the fast clearance through kidneys (in contrast to small molecules), on the other hand they are small enough to prevent the uptake by the phagocytic system, showing therefore longer circulation lifetimes within body with higher chances to reach the targeted cells, a crucial factor for the imaging of living organism.

The targeting capability of FNPs can be more specifically designed, by decorating the surface with particular units (such as ligands, antibodies etc.) promoting cells recognition, especially when aiming to diagnostic applications. Targeting with FNPs is efficient thanks to the high surface to volume ratio offered by the nanoparticles, which in few words means that most of the atoms composing the nanoparticles stays in contact

with the environment. Moreover, it allows the surface functionalization with agents able to prevent unspecific interactions [24, 25]. The generally high colloidal and chemical stability of fluorescent nanoparticles in biological media, associated to the low renal clearance, allows the long-term imaging required in the case of long timescale processes, *in vivo* imaging or other emerging applications like the fluorescence guided surgery [26].

For *in vitro* applications, the brightness and contrast of an image are determined by the amount of probe incorporated inside the cells. In the case of FNPs, the effectiveness of incorporation depends on several factors, such as size, shape and surface properties, which, nowadays can be properly tailored [27]. Chithrani et al. for example found that the number of gold nanoparticles incorporated in living cells is a function of their size and an optimum is reached at 50 nm [28].

The possibility of tailoring the nanoparticles chemical composition, size, shape and surface properties opens to the design of multifunctional systems, as schematically represented in Figure 1.3.

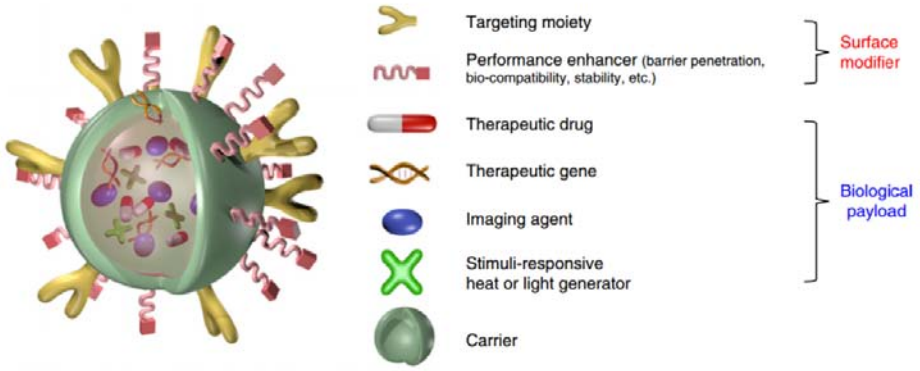

Figure 1.3: Schematic representation of a multifuncitonal nanoparticle with a biomedical payload, consisting of imaging and therapeutic agents, and surface modifier, such as targeting agent and performance enhancer. Adapted from Ref. [29]

The design of smart FNPs is critical in the progress of emerging personalized medicine strategies, such as theranostics, which is based on the design of nanostructures combining diagnostic (such as imaging agents) and therapeutic (for example a drug) functions. These systems have several advantages, such as the precise spatio-temporal control of the dosage while monitoring the treatment therapeutic efficiency [29, 30]. The full development up to the clinical validation of smart nanoprobes for emerging applications, including theranostic or fluorescence guided surgery, relies on the fulfillment of essential quality criteria, in terms of physicochemical properties, purity and detailed information on the interaction with the biological environment, for

example. The combination of all these elements, along with the robustness of the production processes in Good Manufacturing Practice (GMP) conditions, will facilitate the commercialization of new specific nanoprobes and their translation to clinics [15, 31].

FNPs can be divided in two main groups, depending on the nature of their constituents: fluorescent inorganic nanoparticles and fluorescent organic nanoparticles.

Among the fluorescent inorganic nanoparticles, quantum dots (QDs) have emerged in the last 20 years as an excellent alternative for fluorescence imaging, especially thanks to their superior photophysical properties. Excitation of QDs, which are semiconductors nanocrystals, involves the promotion of an electron from the valence band across the energy gap, making it a conduction electron and leaving a hole. The electron-hole pair (i.e. exciton) is confined in the small size of the nanocyrstals and when it recombines a photon is emitted at a given wavelength. The size of the confining nanocrystals determines the energy of the emitted photon, i.e. the emission wavelength of the QDs is ruled by the size of the formed nanocrystals. Sizes of QDs are generally in the interval 1-10 nm and they are made of combination of elements (e.g. CdSe, CdTe and ZnS among the most used in life science applications).

QDs have generally attractive properties, such as broad absorption and sharp emission bands (tuneable by the size of the nanocrystals), huge extinction coefficients (in the order of 10^5-10^6 $M^{-1}cm^{-1}$), high fluorescence efficiency (even for NIR-emitting QDs), tipically large two-photon cross sections and high photostability, generally orders of magnitude higher than molecular probes [10, 27, 32].

The major issue of QDs concerns their toxicity. Most of these nanoparticles contain indeed toxic elements (Cd, Pb, Se, Te, etc.) whose release and accumulation in organisms/cells is a relevant problem not fully assessed yet [33]. In addition to that, often surface treatment (polymer coating, small molecules functionalization among the others) is required in order to improve their generally poor water-solubility and bioavailability as well as reducing their cytotoxicity [34][35], making more complex the preparation route and the control of their structural properties. It has been shown that QDs, with a proper surface treatment, can be retained in the body for at least 2 years and remain fluorescent. The presence of heavy metals makes the regulatory approval of these particles and their translation to patient care unlikely and still very few works exist on the full clinical evaluation of QDs [36, 37].

Dye-loaded silica nanoparticles (SiNPs) constitute another interesting system for bioimaging, and have been adopted as a nontoxic alternative to QDs, thanks as well to

their versatile surface chemistry. Fluorophores can be encapsulated inside the pores of a silica matrix, preserving their optical properties and obtaining a non toxic system. It has been demonstrated that a wide series of organic fluorophroes can be encapsulated in SiNPs, with different chemical and physical properties [38, 39].

When a fluorescent material is exposed to light at a certain wavelength, it generally emits photons of lower energy than the excitation light. A new class of inorganic nanoparticles, named upconversion nanoparticles (UCNPs) has been developed in the recent years [32]. The phenomenon of upconversion is described as a non linear process in which two or more photons at a certain wavelength are absorbed and a photon at shorter wavelength is emitted. However, in contrast to two-photon absorption, upconversion agents are excited at lower laser power than two-photon excitation processes (~1000 times lower). UCNPs have some advantages, coming from the excitation in the red or NIR such as the minimization of damages to tissues, high penetration and low interference of the background radiation. These nanoparticles generally are constituted by rare earth-doped inorganic matrices, with some intrinsic drawbacks, as the low extinction coefficients and fluorescence quantum yields.

1.1.2 Fluorescent organic nanoparticles (FONs)

The necessity of finding nanoprobes which combine superior optical properties, in comparison to molecular fluorophores, with simple preparation routes, preventing at the same time the issues related to toxicity and stability in aqueous environment, strongly encouraged the research on new fluorescent organic nanoparticles. Among all the FONs, the four families which are mostly studied are schematically represented in Figure 1.4.

In the last years, carbon-based FONs have emerged as strongly attractive fluorescent structures with different forms (fullerenes, nanotubes, nanoparticles and so on) and as alternative to the semiconductors nanoparticles, due to the low intrinsic toxicity of their constituent [27]. In particular, the so called carbon-dots nanoparticles have aroused great interest, after showing high brightness and photostability, size-dependant tunable color and extremely high two photon cross sections [40].

Unimolecular fluorescent nanostructures, i.e. dendrimers or hyperbranched molecules (sizes in the range 1-20 nm), present interesting features in terms of tuneability of the physicochemical, thanks to the superficial functional groups, and excellent optical properties, given by the fluorophore conjugated to the structure, and they have been proposed as “all-organic” alternative to QDs [32]. Although their use in

bioimaging has not been widely explored yet, such structures offer interesting optical properties. Mongin et al. [41] for example built up a dendrimeric structure with a high number of two-photon chromophores (up to 96), confined in a structure of around 4 nm, which showed extremely high two-photon brilliance, comparable to that of highly performant QDs. Although interesting strategies towards the preparation of multifunctional dendrimers have been designed, these structures present some drawbacks related to the uncertainty about structural information and polidispersity, along with poor control over the distribution of the different functional groups [42].

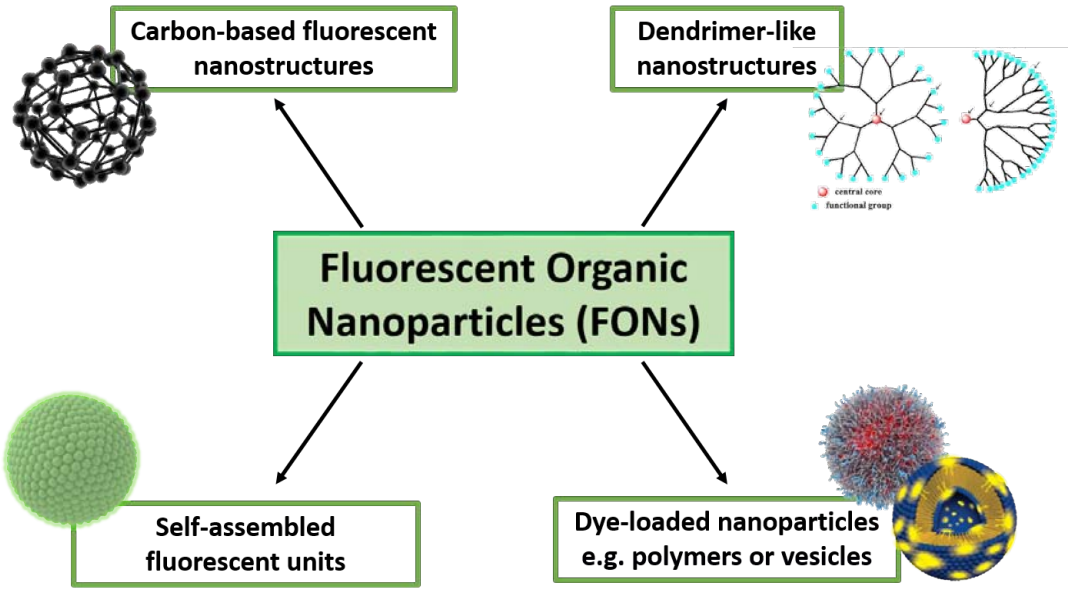

Figure 1.4: Schematic classification of the mostly studied fluorescent organic nanoparticles (FONs) depending on their different structural composition.

A completely different approach is based on taking benefits of the luminescence of a molecular fluorophore by re-arranging it as a nanostructure. These types of FONs can be divided in two main categories: dye-loaded nanoparticles, i.e. nanoparticle in which the photoluminescence is given by a fluorophore loaded into a non-luminescent matrix, and FONs based on the self-assembly of π-conjugated luminescent units. Thanks to these strategy, some of the major limits attributed to molecular fluorophores, such as water solubility, brightness and photostability, can be overcome by organizing them as nanoparticles.

As previously mentioned, poor water solubility is a strong challenge of conventional organic red and NIR dyes, due to their mostly hydrophobic character. Nevertheless, taking advantage of the non-covalent interactions between hydrophobic molecules is desirable, aiming to design self-assembled fluorescent nanoparticles. Martinic et al. reviewed several strategies for water dispersion of commercial and novel deep red/NIR

emitters, including cyanines, squarains and BODIPYs dyes.[2]. In many of the works listed, in order to transfer the good emission properties of the dyes in aqueous media, encapsulation in polymer nanoparticles was found to be a successful strategy [11, 43, 44]. Following another lead, Reddy et al. synthesized a bright cytosine-based red emitting fluorophore which maintained its fluorescence efficiency upon precipitation as π-conjugated nanoparticles, being moreover non toxic and useful for cytoplasm staining of cancer cells [45].

The adequate design of FONs allows to obtain probes with superior luminescence efficiency, in comparison with single molecular fluorophores. The huge gain in brightness is extremely important especially in view of applications "under the microscope". There is in fact a link between the spatio-temporal resolution and sensitivity, which both improve with the brightness of the probe used [46, 47]. The principle for achieving high brightness in FONs relies on the confinement of a high number of fluorophores (typically hundreds or thousands) in a nanosized structure. In such a way the brightness of the particle is much higher compared to that of the single fluorophore, thanks to the much larger absorption coefficient of the particle ε_p ($\varepsilon_p = n\varepsilon_f$, where ε_f is the absorption coefficient of the single fluorophore and n is the number of fluorophores in the nanoparticle). For example, for one FON loading 100 dye molecules with $\varepsilon_f \sim 10^4$ $M^{-1}cm^{-1}$, then the $\varepsilon_p \sim 10^6$ $M^{-1}cm^{-1}$. In this regard, the development of a proper manufacturing method which allows to precisely control the number of fluorophores per nanoparticles, i.e. finely tuning the brightness of the FONs is fundamental. In Figure 1.5 a hypothetical situation in which a molecular fluorophore and a fluorescent nanoparticle, in which the photoluminescence is given by n molecular fluorophores organized as a nanostructure, are used to label the same structure, e.g. a portion of a cell membrane, is schematized. Under the same illumination intensity in fact, the response of the FON will be n times higher than that of the single fluorophore. A higher photon emission rate from the molecular fluorophores could be reached by increasing the laser intensity, but photostability of the dyes and the phototoxicity experienced by biological samples under illumination limit the light power and the observation time window [48].

As effect of the re-organization as a nanoparticle, the photostability of a dye can be influenced by several factors. The photodegradation rate of a fluorophore, when incorporated in a nanoparticle, is in fact generally significantly enhanced, thanks to the protection from oxygen and other reactive species that take part in photodegradation processes. This is for example the case of ICG which, upon confinement in NPs, experiences a strong enhancement of chemical and photo-stability [49, 50]. However,

when processed as nanoparticles, molecular probes can form aggregates which may undergo different photo-degradation paths and provoke a loss in stability upon irradiation [51].

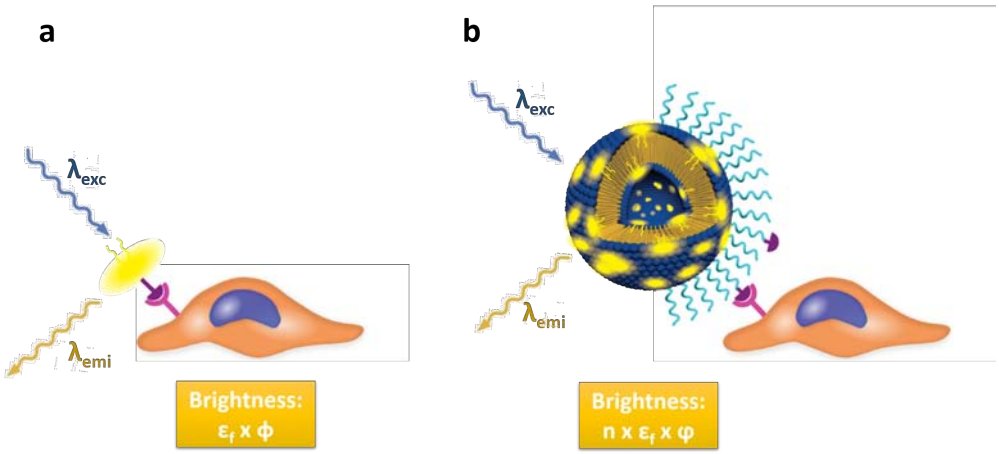

Figure 1.5: Schematic representation of the selective labeling of a cell membrane by using a) single dye molecule and b) a fluorescent nanoparticle. The brightness of the nanoparticles is proportional to the number of fluorophores incorporated, their extinction coefficient (ε_f) and quantum yield (φ). Adapted from Ref. [47]

Concerning the self-assembly of π-conjugated molecules, the proper processing of aromatic molecules can lead to the formation of (most of the times) amorphous aggregates in water, generally driven by the self-assembly *via* the π-π stacking and, depending on the substituents in the aromatic structures, other non-covalent interactions such as hydrogen bonding, electrostatic interactions and Van der Waals forces can take place [52, 53]. This strategy is especially used for the dispersion in water of strongly hydrophobic compounds and it is generally based on easy, economic and highly reproducible reparation routes, like solvent displacement methods, as precipitation. This single step method consists on the addition of an organic solution of the fluorophore into a stirring non-solvent phase, typically water with eventual addition of surfactants as stabilizing agents. The instantaneous diffusion of the organic solvent into the aqueous phase causes the immediate precipitation of the nanoparticles in the sub-micron size range [54, 55].

However, upon aggregation in a confined space, fluorophores can show unaltered, reduced or improved efficiency, i.e. fluorescence quantum yield, when compared to their solution. The so-called aggregation-caused quenching (ACQ) is, unfortunately, a really common phenomenon of aggregating fluorophores. The aromatic structures of the dyes, responsible of their luminescent properties, experience intense intermolecular π-π stacking interactions and, as consequence, non-radiative channels of decay from the

excited to the ground state are favored, resulting in the quenching of the emission of the fluorophore [56]. For example, triphenylamine-based dyes showed this behavior, showing an abrupt decrease of quantum yield from 40% (in several organic solvent) down to 7% in FONs in water [57]. In another case, an oligotiophene fluorophore with D-pi-A structure and strong intramolecular charge transfer character showed poor quantum yield (around 2%) when processed as FONs, while in apolar solvent (toluene) the efficiency was up to 50% [58]. More or less 15 years ago, a new phenomenon called aggregation-induced emission (AIE) was discovered [59]. In the AIE process, a non-emissive fluorophore in solution is induced to emit upon formation of aggregates. Molecules which undergo strong intramolecular rotations or molecules with flexible structures, able to bend or vibrate in solution, have favored relaxation channels from the excited to the ground state and therefore their emission is strongly quenched. However, upon aggregation, the restriction of intramolecular motion or intramolecular vibration can activate the radiative decay pathways and strongly enhance the emission [60]. An exhaustive description of the AIE-based fluorophores for imaging and opto-electronic applications can be found in this review of Mei et al. [56].

Smart synthetic routes have been developed to solve the ACQ issue and maintain, or even improve, the optical properties of a fluorophore when moved from solution to a nanoparticle. For example, short polyethylene glycol (PEG) chains have been used to tailor the self-assembly of perylene bisimide dyes which, depending on the hydrophobic/hydrophilic balance between the different moieties, can form micelles or vesicles, with enhanced emission in the red-infrared [61]. The π-conjugated planar structures of red/NIR emitters is generally responsible for the strong tendency to the assembly in weakly emissive aggregates [62] and this is a major obstacle in the design of bright FONs emitting in the transparency window of biological tissues. Recently, Jiang et al. [63] modified a diketopyrrolopyrrole (DPP) chromophore, a red brilliant and extremely stable molecule, with tetraphenylethene groups in order to prevent the π-π accumulation upon aggregation and induce the AIE effect. A similar strategy was followed by Gao et al. [64], who modified a DPP core with triphenylamine side groups achieving a quantum yield of 11% ca. in solid state, obtaining moreover the extension of the π-conjugated structure with a strong enhancement in two-photon brightness upon aggregation. In some cases, modification with simple alkyl chains, which can intercalate in the aggregate states between layers of conjugated molecules, has been proved to enhance the fluorescence quantum yield once assembled as nanoparticle [65].

Most of the strategies discussed so far are based on the chemical modification of the fluorophores structure, with the addition of moieties capable to limit or, in some cases,

reverse the ACQ effect. An alternative approach consists in dispersing the fluorophores in an organic non-fluorescent nanostructures, aiming to obtain a water-soluble FON with limited ACQ. The incorporation of the fluorophore in the nanostructure can occur either by physical entrapment, exploiting the molecular affinity between the dye and the matrix, or by covalent conjugation to the material constituting the nanostructure [15]. In this regard, a large variety of materials of different nature with well-studied physicochemical properties have been used: polymeric nanospheres[47], micelles [66], dendrimers [67, 68], vesicles[69] and solid lipid nanoparticles[70].

The insertion of a molecular emitter in a nano-sized matrix is strongly promising, taking benefits first of all from the large knowledge of nanomaterials and preparation methodologies from the field of drug delivery, in which biocompatible and non toxic matrices are generally used [47, 71]. By this strategy, fluorophores with different physico-chemical properties, including those non-water soluble, have been structured in water. The further addition of therapeutic and targeting agents leads to the formation of nanostructures with multifunctional activity with promising future application in personalized medicines [72, 73, 74, 75].

The encapsulation of the water-soluble Indocyanine Green in nanoparticles, such as micelles [76] and polymeric nanostructures [77] was shown to improve the dye optical properties and its chemical stability. Commercial cyanines (DiI, DiD and DiR) have been dispersed by using either lipids (mainly made by soybean oil) [70] and polymers (PLGA-PEG copolymer) [78]. In all the cases results were positive and ACQ effect was limited until reaching a certain amount of loading fluorophores per nanoparticle (generally <1 wt%).

A conceptual difference between the dye- and drug-loaded nanoparticles in imaging and drug release applications, respectively, is that while in the last case the encapsulated drug is meant to be released in the surrounding medium (e.g. tumor cells or some specific organelle), in the case of dye-loaded FONs the release of the fluorophore is unwanted. Fluorophore leaching causes in fact both the decrease of brightness of the nanoparticle while increasing the background signal [47]. Dye leaching is an issue especially concerning the formulations in which a dye is physically entrapped in a matrix. For example Chen et al. encapsulated two different lipophilic cyanines in block copolymer micelles for multicolor imaging, observing that, upon exposition to cells, the dyes were released and incorporated in cells membrane [79]. Inspired by these results, McDonald et al. incorporated the same dyes in PVA-based nanoparticles, which maintained their integrity even after incubation in cells for long times (25 hours) [80].

The stability of FONs in water and biological fluids is an extremely important aspect, especially in the case of *in vivo* imaging, for example in imaging blood vessels and

circulation [5, 81] or to obtain a suitable accumulation of the probes in tumors. The colloidal stability of the FONs is ensured by the composition of their surfaces, i.e. the moieties exposed to the aqueous external environment. Thus, self-assembled FONs from the direct precipitation of strongly hydrophobic chromophores present a hydrophobic surface which causes low colloidal stability and it is generally not easy to functionalize [47]. PEGylation of the NPs surface is a widely used strategy to increase circulation lifetime and stability of the FONs. In a recent study, polymeric micelles of peptide-PEG block copolymer incorporating different cyanines for multicolor imaging showed high stability up to 96 hours [82]. Delmas et al. developed a new class of dye-lipid nanoparticles, named "Lipidots^{TM}", based in the incorporation of lipophilic fluorophores in oil-in-water nanoemulsion. The main inconvenient of such nanoemulsion is the intrinsic poor colloidal stability, which has been overcome by using mixture of surfactants (phospholipids and PEG-sterate)[83, 84].

1.1.3 Vesicles: characteristics and advantages as structures for nanomedicine

Vesicles, e.g. liposomes, are among the most promising carriers in nanomedicine, being intensively studied in the pharmaceutical field thanks to the great versatility with respect to size, composition, surface properties, biocompatibility, biodegradability, possibility of surface functionalization and capacity to integrate various hydrophilic and/or hydrophobic compounds [85]. Vesicles are spherical objects, with diameter varying from few nm up to several microns, consisting of a bilayer (unilamellar) or several layers (multilamellar) of amphiphilic molecules which separate a liquid compartment (lumen) from the outer surrounding medium [86].

Depending on the number of the bi-layers constituting the vesicles (i.e. lamellarity) and their size, vesicles can be classified, as schematized in Figure 1.6, as small unilamellar vesicles (SUVs, size <200 nm and single bilayer), large unilamellar vesicles (LUVs, size ranging from 200 - 1000 nm and single bilayer), giant unilamellar vesicles (GUVs, size > 1000 nm and single bilayer), multilamellar vesicles (MLVs, consisting of several concentric bilayers) and multivesicular vesicles (MVVs, composed by several small vesicles entrapped into larger ones). Size and lamellarity are important factors which determine the performance as drug carriers of the vesicles [87, 88, 89, 90].

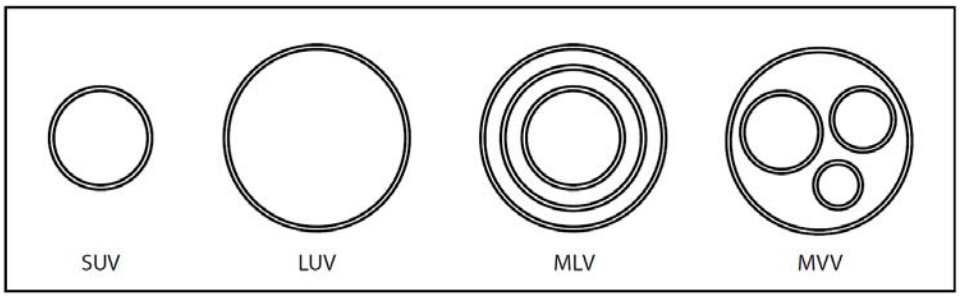

Figure 1.6: Types of vesicles classified based on their size and lamellarity. SUV: small unilamellar vesicle; LUV: large unilamellar vesicle; MLV: multilamellar vesicle; MVV: multivesicular vesicle. From [91]

Liposomes are vesicles made of phospholipids and in the last 50 years they have been intensively investigated for applications in several fields, including pharmaceuticals [92, 93], cosmetics [94] and food industry [95]. Liposomes are used in these fields because they allow protecting, transporting and specific delivering of active compounds [96, 97]. Liposomes properties can be specifically adapted for different applications, by tailoring their chemical composition, structure and size. For example, their membrane can be precisely functionalized to promote accumulation of a drug in a targeted tissue or cell. In Figure 1.7, the different types of liposomal drug delivery systems are schematized, representing different strategies of surface modification.

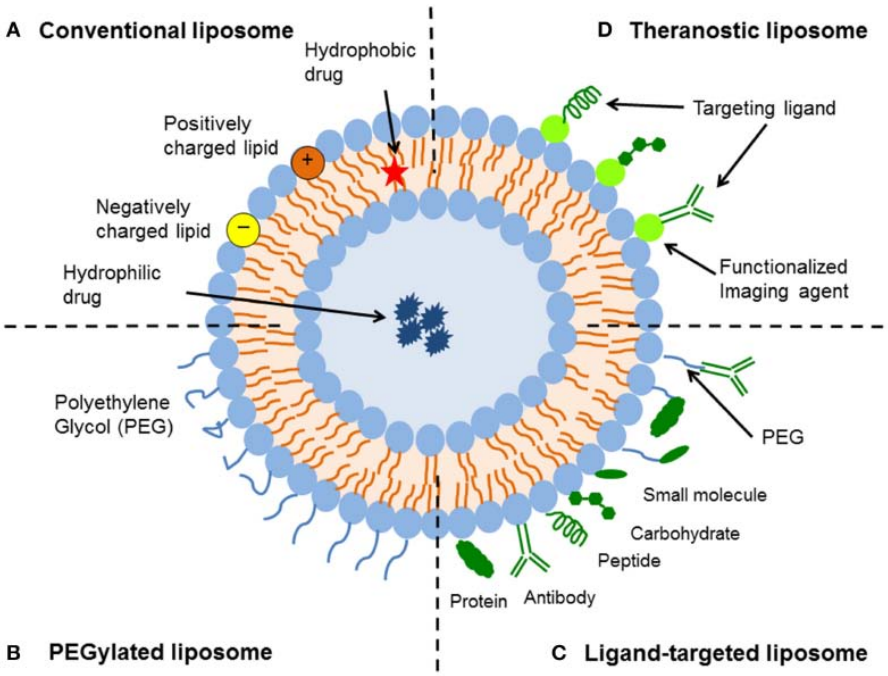

Figure 1.7: Schematic representation of the different types of liposomal drug delivery systems. From Ref. [97]

Despite their versatility in terms of compositions, structure and applications, in order to achieve self-assembled vesicles with superior performance, a high structural homogeneity is required. The stability, rigidity and permeability, functionalization and response to external stimuli of a vesicle are ruled by their membrane. Therefore, the behavior of vesicles is tightly linked to their vesicle-to-vesicle homogeneity, in size and morphology, but also in composition and supramolecular organization [98]. The importance of the vesicle-to-vesicle structural homogeneity and composition homogeneity is schematized in Figure 1.8, although this scheme can be extended to other classes of dye- or drug-loaded nanoparticles.

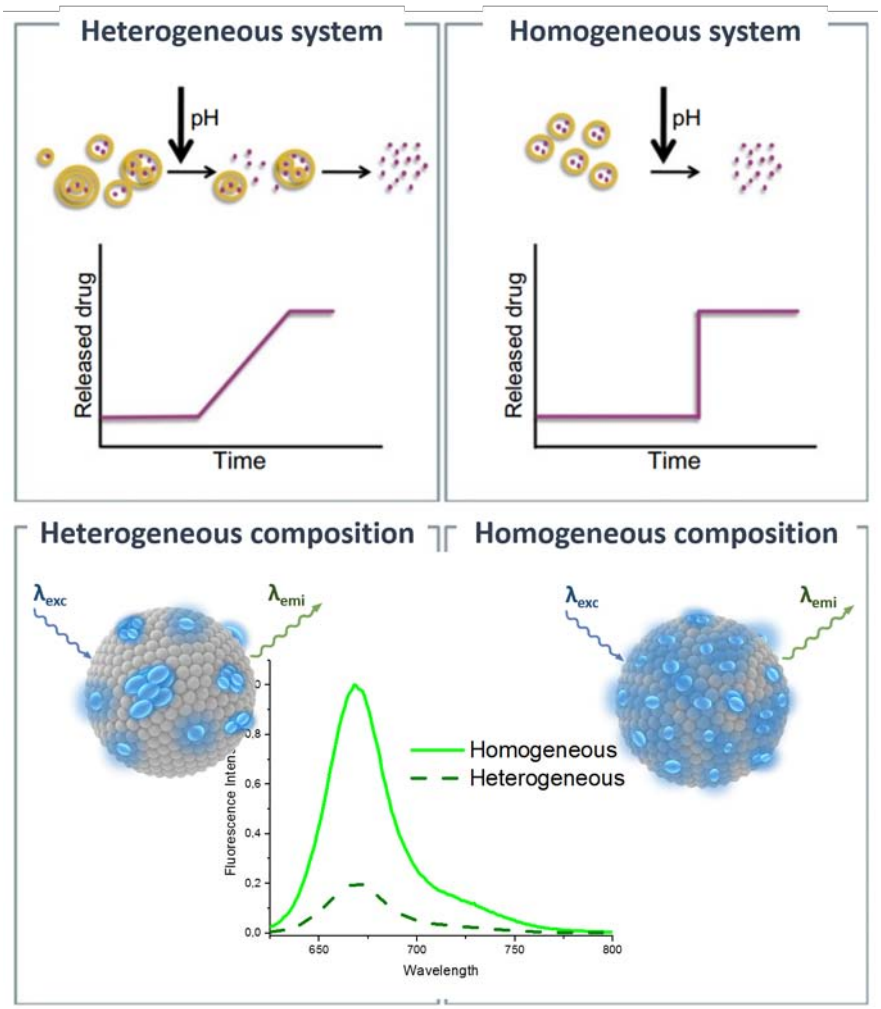

Figure 1.8: Top) Schematic illustration of the response to an external stimulus, like a pH change, presented by a vesicular drug delivery system with homogeneous (right) and heterogeneous (left) vesicle-to-vesicle structural characteristics in terms of size and lamellarity. Bottom) Schematic representation of the impact of the homogeneous composition on the brightness of a vesicle loaded with a fluorophore which undergo aggregation-caused quenching

For instance, in the case of vesicles used as drug delivery systems, the structural

homogeneity with respect to size and lamellarity plays a crucial role in order to have a sharp response to an external stimulus, which allows the homogeneous release of a drug in the targeted site. In fluorescence imaging applications, a vesicles loaded with a fluorophore susceptible of aggregation-caused quenching would give a much lower fluorescent signal if the dye molecules are not evenly distributed over the membrane. Oppositely, homogeneously distributed fluorophores will make the vesicle much brighter.

In some cases, liposomal-based formulations met the pharmaceutical quality criteria concerning the physico-chemical properties, reproducibility, shelf stability and clinical requirements, and have been therefore approved by regulatory agencies and are now commercialized [99]. Despite the advances made in the development of liposomal formulations for nanomedicine, these structures suffer severe drawbacks concerning their colloidal stability. Liposomes in fact, correspond to metastable kinetically trapped states, formed by an energetic external input (e.g. by sonication) over a planar lamellar stable phase. The kinetically driven stability of such architectures is therefore limited by the water non-solubiliy of their building blocks, the phospholipids. In a thermodynamic-wise view, the equilibrium state is not the round-shaped vesicle, but the planar lamellar bi-layer [100, 101]. In addition to that, the phospholipids are not long-term chemically stable, undergoing hydrolysis, oxidation or peroxidation, which are generally limited by the addition of antioxidant and low-temperature storage. Physical instability of liposomes leads, for example, to issues related to the permeability of their membrane which induces undesired fast leakage of the loads. To overcome this issue, cholesterol is usually incorporated in the liposomes, enhancing the rigidity and stability of the membrane and reducing their permeability[102, 103, 104].

1.1.4 Routes for the preparation of vesicles

The performance of a functional materials like a vesicle as drug carrier or imaging nanoprobe is strictly bounded to the possibility of finely control the structural characteristics of the self-assembled structures. In a vesicle, the supramolecular organization of the bilayer is strongly influenced by the path that leads to the self-assembly of the monomeric units. Current methodologies for the formation of vesicles, such as lipid thin-film hydration (TFH) [105, 106] or reverse-phase evaporation (RPE) [107] generally provide systems with poor structural homogeneity, i.e. non-uniform vesicle-to-vesicle lamellarity and structures with very different sizes. In those cases, post-production modification steps, such as sonication [108], extrusion

[109, 110], freeze thawing [111] are required in order to obtained the desired properties, as schematized in Figure 1.9. Beside that, some of the common routes for vesicles preparation, such as TFH, involve a solvent-free step (as described in detail in Section 3.1.2 of Chapter 3), which may favor the de-mixing of the membrane components and provoke the formation of a non-uniform composition of the bilayer. Another drawback of these conventional routes is related to the large amounts of toxic organic solvents required and their generally incomplete removal which constitute a problem both at lab- and large-scale production [112]. Additionally, bio-active and other sensitive molecules for the production of multifunctional vesicles may be damaged during these multi-steps and time consuming procedures. Thus, developing mild processes aiming to control the structure at the nanoscale and suitable to be scaled at large production is crucial [113].

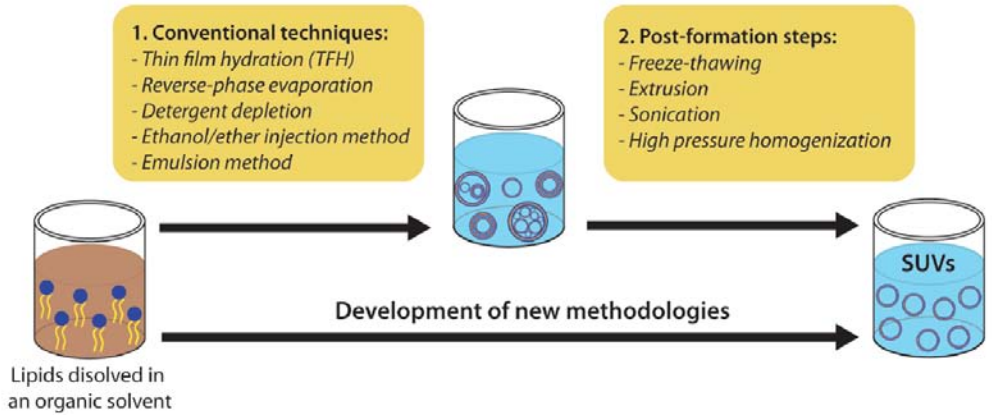

Figure 1.9: Conventional methodologies for the preparation of vesicles and the most common post-formation steps for their homogenization.

1.1.4.1 DELOS-SUSP method using compressed CO_2

In the last 25 years, several compressed fluid (CF) based methodologies for the preparation of nanostructured materials have been developed [114, 115, 116]. CFs exist as gas at normal conditions of pressure (P) and temperature (T), but can be converted into liquids or supercritical fluids increasing P. The supercritical region is reached above the critical temperature (Tc) and pressure (Pc) and, in this state, the fluids have viscosity and diffusivity comparable to those of a gas, while the density is close to that of a liquid. The possibility of obtaining such special behavior at conditions below or near the critical point (subcritical region), allows working at mild conditions of T and P, reducing the cost related to the use of elevated pressures and decreasing the risk of damaging the structure and properties of fragile molecules to be processed.

Concerning the production of nanomaterials, the solvation capacity of a CF (both in

the liquid or supercritical phase) is one of the most important parameters. It can indeed be tuned by pressure changes, which propagate more quickly than temperature and composition variations. In this way, a fine control over the morphology of materials at the microscopic scale can be achieved, opposite to most of conventional processing techniques [117, 118]. CO_2 is the most used compressed fluid in this sense, thanks to its low critical pressure (Pc=74 bar) and temperature (Tc=31°C), which allows working at mild conditions, with low production cost and reduced damage to the processed molecules. In addition to that, it is non-flammable, non-toxic, inexpensive and non-polluting, all properties that have made it is a green-substitute to conventional organic solvents for the preparation of nanomaterials.

On these principles, the procedure named Depressurization of an Expaned Organic Solution (DELOS), based on compressed CO_2, for the production of micron- and submicron-sized crystalline materials with high polymorphic purity has been developed in the Nanomol group [119, 120], where the entire work of this Thesis has been carried out. As novelty, the process uses the CO_2 as co-solvent, being completely miscible at a given pressure and temperature with an organic solution containing the solute to be crystallized [121, 122]. Thanks to the mild conditions used (T<35 °, P<10 MPa) DELOS method allows the processing of heat labile compounds, moreover reducing the investment cost for the scale-up of the plant. The DELOS process has been slightly modified, for the production of cholesterol-rich nanovesicles, e.g liposomes and Quatsomes [123]. The new method, named Depressurization of an Expanded Organic Solution-Suspension (DELOS-SUSP), allows the one-step preparation of multifunctional cholesterol-rich nanovesicles, including nanovesicles-bioactive hybrids [124, 125]. For example, α-Galactosidase-A (GLA)-nanovesicle and epidermal growth factor (EGF)-nanovesicles hybrids were prepared recently by DELOS-SUSP and they were found highly efficient (compared to the free proteins) in both pre-clinical *in vitro* and *in vivo* assays and in compassionate treatments with patients, respectively [125, 126].

Full details on the DELOS-SUSP for the preparation of SUVs are discussed in Section 3.1.2 of Chapter 3 and in Section 7.2.1 of the Experimental Part.

1.1.5 Quatsomes: an innovative family of cholesterol-rich nanovesicles

Due to the inconveniences previously evidenced in liposomal formulations and to the high price of phospholipids, there is a great interest in finding non-phospholipid building blocks which can self-assemble into stable vesicles. Among the others,

surfactants have been used as cheaper and more stable molecules than phospholipids in pharmaceutical and cosmetic applications. Vesicles originating from the combinations of cationic and anionic surfactants or vesicles made by non ionic surfactants, named *catananionic* vesicles and *niosomes [127, 128, 129]*, respectively, are two examples of vesicles with well-defined structural properties and high stability.

In the very last years, the NANOMOL group, where this Thesis has been done, has developed a new class of nanoscopic unilamellar vesicles, composed by sterols and quaternary ammonium surfactants, named Quatsomes. Dr. Lidia Ferrer-Tasies, during her PhD Thesis, discovered that a stable suspension of Quatsomes can be formed by cholesterol and hexadecyltrimethylammoniumbromide (CTAB). As schematically shown in Figure 1.10a, CTAB and cholesterol, when placed in water, form micelles and crystals, respectively. However when opportunely processed (by DELOS-SUSP or by sonication, for example) they self-organize into exceptionally homogeneous bilayer vesicles with average diameter smaller than 100 nm, as shown by Dynamic light scattering (DLS) size distribution and cryogenic transmission electron microscopy (cryo-TEM) images (Figure 1.10b).

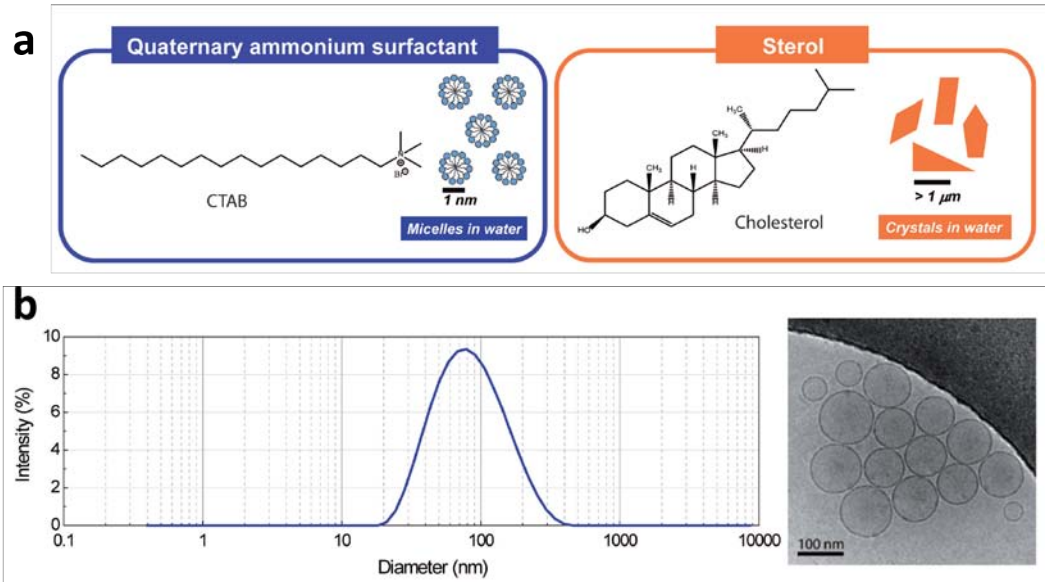

Figure 1.10: a) Molecular structure of CTAB and cholesterol along with a schematic representation of the structures formed in water b) Particle size distribution (left) by DLS and cryo-TEM image (right) corresponding to a vesicular system composed of cholesterol and CTAB in water. Adapted from [130]

The preparation by DELOS-SUSP lead to the formation of vesicles with higher homogeneous composition, compared to other conventional preparation routes, like the hydration method [131]. Quatsomes are stable for periods as long as several years and

their morphology does not change upon rising temperature or dilution. The phase behavior analysis of these two compounds showed that a vesicular system, characterized by a remarkable vesicle-to-vesicle homogeneity regarding size and morphology, is formed when cholesterol and CTAB are processed in an equimolar ratio of both components. Several experiments, including tests on the structural homogeneity by small angle x-ray scattering (SAXS), supported the thermodynamic analysis of this vesicular composition which revealed that Quatsomes are elastically stabilized vesicles, i.e. vesicles that are in an equilibrium state, having a spontaneous curvature and a large bending rigidity (kc) [132, 133]. Although some thermodynamically stable vesicles are formed by simply mixing the membrane components [128], the supply of energy for the formation of cholesterol/CTAB Quatsomes is necessary. This energy (provided by sonication, for example) is in fact required to reduce the size of the initial hydrophobic cholesterol crystals in water.

Molecular Dynamic (MD) simulations (Figure 1.11) revealed that cholesterol and CTAB self-assemble in a unique bi-moleular synthon that works as a single entity. The synthon, formed by the union of a conical molecule (the CTAB) and an inverted conical molecule (the cholesterol) has a cylindrical-like shape, which is required for the formation of the spherical bilayer. Thus, the cholesterol molecules are fully incorporated within the hydrophobic compartment of the membrane, while the quaternary ammonium groups of the CTAB are located at the interface with water. The cationic "heads" of the surfactant confers to Quatsomes strong positively charged inner and outer surfaces, which are responsible of the durable stability of these vesicles because of the mutual electrostatic repulsion in their suspension.

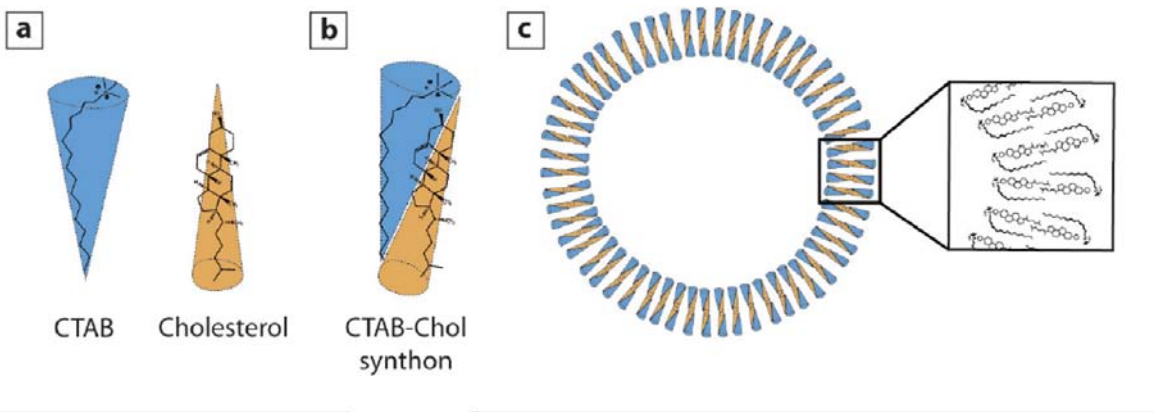

Figure 1.11: Schematic illustration of (a) the shape of CTAB and cholesterol molecules, (b) the formation of a Chol-CTAB bimolecular synthon and (c) their self-assembed disposition into bilayer vesicles. Adapted from Ref. [134]

According to their peculiar structures, Quatsomes are good candidates as platform for the incorporation of both lipophilic actives, which can be stored within the core of the bilayer, and hydrophilic ones, which can be encapsulated in the inner aqueous lumen or, if negatively charged, can either interact with the surface of the vesicles.

The present Thesis is devoted to the study of the Quatsomes as a versatile scaffold for the nano-structuration in aqueous media of fluorescent dyes with different chemicophysical behavior, including those non-water soluble, and optical properties.

1.2 Objectives

Finding new fluorescent organic nanoparticles (FONs) with the potential to overcome the limits of common fluorescent probes as molecular fluorophores, fluorescent proteins and inorganic nanoparticles is a subject of strong interest for materials scientists developing new probes for fluorescence microscopy and theranostics. In the recent years, Nanomol group has developed innovative non-liposomal nanovesicles using quaternary ammonium surfactants and sterols, named Quatsomes, which have showed exceptional stability and high structural homogeneity, being promising candidates for applications as multifunctional drug carriers. The self-assembly of the sterols and surfactants into Quatsomes can be achieved by using compressed fluids (CFs)-based technologies, such as the DELOS-SUSP method.

Within this scenario, the main objective of this Thesis is to explore the possibility of using Quatsomes as a vehicle for nanostructuring in aqueous media several dye molecules, irrespective of their physicochemical and optical properties, in order to obtain new fluorescent organic nanoparticles (FONs) with superior colloidal stability and enhanced fluorescent features, especially with high brightness, in relation to single fluorophore molecules in solution.

Thus, the aim of Chapter 2 is to study how the nanostructuration over Quatsomes affects the optical properties of a water-soluble dye, like fluorescein, used as a model dye. The possibility of using Quatsomes as vehicles to disperse in water a family of commercial non-water soluble fluorophores with lipophilic properties, like the carbocyanines, has been explored in Chapter 3, investigating whether the DELOS-SUSP method can be adequate for the preparation of these FONs and studying in depth the properties of the resulting fluorescent nanovesicles. The applicability of these FONs in cutting-edge super-resolution techniques, such as STORM microscopy, and the possibility of engineering more complex structures with multicolor capability has been also explored. Encouraged by the necessity of developing red-shifted emitting FONs, the Chapter 4 of this Thesis was devoted to disperse in water, by mean of Quatsomes, a novel-synthesized hydrophobic fluorophore belonging to the family of diketopyrrolopyrroles (DPPs) and probe it for the imaging of cells. Finally, the aim of Chapter 5 was to develop a new nano-probe, based on Quatsomes incorporating a hydrophobic fluorene derivative, for the targeting and tracking of lysosomes, organelles whose activity is linked to several pathologies.

2

Quatsomes: a scaffold for nanostructuring dyes in aqueous media

2.1 Quatsomes-based FONs with water soluble fluorescein

As mentioned in the Introduction, Quatsomes are small unilamellar vesicles composed of cholesterol and a quaternary ammonium surfactant, like the CTAB. The supramolecular organization of these compounds offers different strategies for the nanostructuration of dyes over the membrane of the vesicles. On one hand, the hydrophobic compartment within the bi-layer can be used to "store a load", i.e. a dye which is non-water soluble, as discussed in the next Chapters of this Thesis. On the other hand, the positively charged membrane of these vesicles can be decorated with water-soluble anionic fluorophores, in order to form a new class of FONs . Therefore, in order to explore the possibility of structuring a water-soluble dye over the Quatsomes and monitor how the optical properties of the dye are affected by the re-organization over a nano-sized architecture, fluorescein has been used as model anionic dye, as schematized in Figure 2.1.

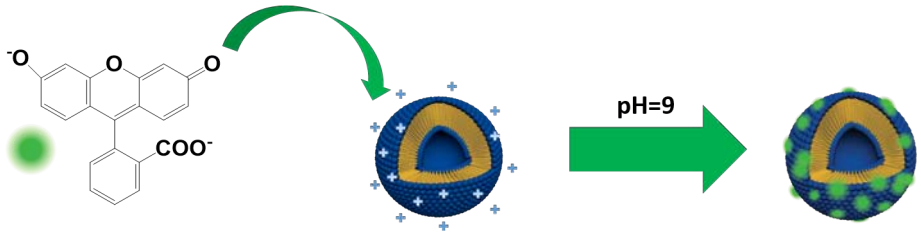

Figure 2.1: Scheme of interaction between fluorescein, which is a di-anion at basic pH, and Quatsomes, which have a positively charged surface

Fluorescein (Fl) is among the most investigated and used fluorescent probes due to the modest brightness, large absorption in the visible range and easy chemical

modification for labeling to biomolecules. The photophysical properties of fluorescein strictly depend on its environment and many works exist in literature regarding, for example, the study of the spectral properties of fluorescein under interaction with BSA [135], silica [136], micelles of several surfactants (SDS, CTAB and TX-100) [137] and in liposomes [138] among others.

In this Thesis, fluorescein sodium salt has been used as a model water-soluble probe to compare its photophysical properties in water solution and nanostructured in an aqueous phase, through the decoration of Quatsomes membrane, and to check whether the colloidal properties of the vesicles are affected by the presence of the dye. By taking advantage of the strong positive charge of Quatsome surfaces, conferred by the cationic head of CTAB molecules constituting the membrane, it is possible to nanostructure fluorescein in a basic water medium simply by addition to a suspension of pre-formed Quatsomes.

2.1.1 Preparation of Fluorescein-decorated Quatsomes

The compressed CO_2 methodology, DELOS-SUSP, has been used for the preparation of plain Quatsomes. A detailed description of the process is given in Section 3.1.2 of Chapter 3 and in the Experimental Section 7.2.1.

Fluorescein in aqueous solution can be found in different states, from cationic to di-anionic forms, going from acidic to basic pH, making its absorption and emission properties strongly pH dependent [139]. In the present work, water solutions were kept at pH=9 (by addition of NaOH) in order to ensure that the fluorescein is present in the di-anionic state.

In order to evaluate whether the amount of dye per vesicle affects the photophysical properties of the Fl-decorated Quatsomes, samples at different loading, [L], of Fl have been prepared, where [L] is defined as the molar ratio: $\text{moles}_{\text{Fl}}/(\text{moles}_{\text{chol}}+\text{moles}_{\text{CTAB}})$.

The preparation of the Fl-decorated Quatsomes was made as follow: 0.1 mL of a 0.1 mM solution of Fl in MilliQ water was added to different vials containing 9.9 mL of a plain Quatsomes suspension in pure MilliQ water, in which the pH was modified by addition of few drops of a 0.01M NaOH solution until reaching pH=9. The concentration of Quatsomes was different in each vial, in order to obtain samples with the same concentration of Fl but different number of Quatsomes, as schematized in Figure 2.2. Samples were incubated at room temperature, under gentle stirring, for 30 minutes before measurements. The samples prepared are listed in Table 2.1. The amounts of cholesterol and CTAB used for the calculation of [L] are the nominal ones, i.e. the

quantities weighted at the beginning of the DELOS-SUSP protocol.

The code used to name the samples in the entire Thesis is made of three parts: the first one refers to the dye used (Fl, in this case), the second one refers to the type of nanoparticle used (QS, i.e. Quatsomes) and finally, the last one, is a number associated to the dye loading, as in this case from 1 to 7 at increasing loading.

For each sample, three batches were prepared in order to check the reproducibility of the results. Minor differences have been detected in all the cases.

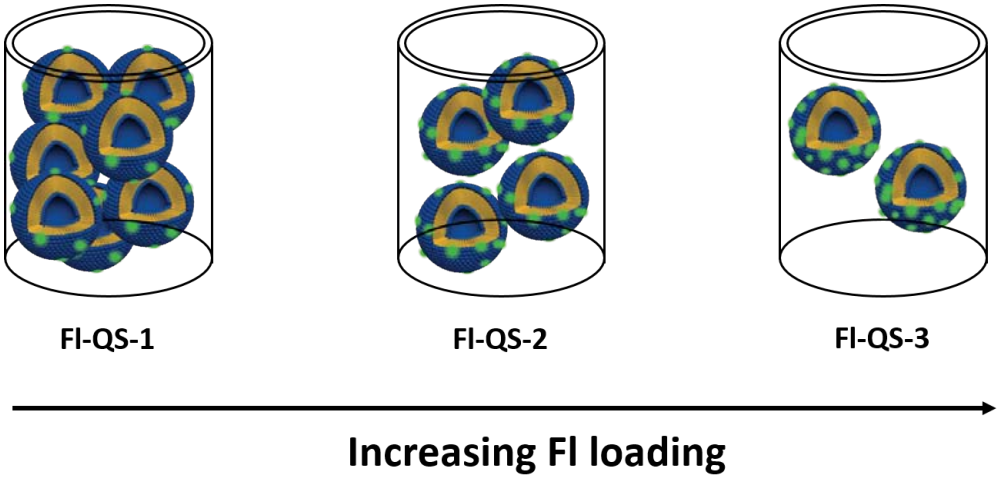

Figure 2.2: Scheme of the prepared Fl-decorated Quatsomes at different loading of fluorescein.

Taking into account the electrostatic interaction between the di-anionic form of Fl (Fl^{2-}) and the quaternary ammonium of CTAB and due the strong hydrophobic nature of the inner part of the bi-layer, the crossing of Fl^{2-} from the outside to the inner aqueous lumen of Quatsomes can be safely excluded. For this reason, it can be assumed that only half of the CTAB molecules present in the system, i.e. those that are facing outwards, towards the surrounding medium of Quatsomes, are actually available to interact with Fl^{2-}. This ratio, expressed as $moles_{Fl}/(0.5moles_{CTAB})$, is listed in the second column of Table 2.1, and it gives a more representative snapshot of the interactions between the different species in the samples.

All the prepared samples were not purified after the addition of Fl, because release of Fl molecules was noticed during the purification by diafiltration (see Experimental Section 7.2.2), even at low loadings. This is most probably due to the equilibrium between fluorescein molecules bound to Quatsomes surface and those that are un-bounded and free to diffuse in the medium. This equilibrium can be shifted towards the unbound fluorescein during the diafiltration, because the free molecules are continuously removed from the sample during this process, which works as a series of

washing cycles with fresh MilliQ water. Thus, no separation is possible, without completely removing all the fluorescein molecules decorating Quatsomes surface. Thus, the weak electrostatic interaction between the anionic dye and the positive surface of Quatsomes does not ensure a stable binding of the fluorophores to the vesicles, compromising the integrity of the FONs upon large dilutions, for example. This is a major issue in the design of FONs suitable for imaging purposes, in which the fluorescent probes are, for example, highly diluted in cells growth media. Fluorophores leaching would give, in fact, serious problems such as the loss of brightness of the FONs, high background signal and unwanted staining of objects during the images acquisition.

Table 2.1: Fl-loaded Quatsomes samples prepared together with their composition

Sample[a]	**[L]**[b] $\times$ **10**$^{-3}$	**Fl/CTAB molar ratio**[c] $\times$ **10**$^{-3}$
Fl	-	-
Fl-QS-1	0.1	0.4
Fl-QS-2	0.5	2
Fl-QS-3	1	4
Fl-QS-4	5	20
Fl-QS-5	10	40
Fl-QS-6	50	200
Fl-QS-7	170	670

[a] Each sample contains a Fl concentration of 1 μM. pH=9 was maintained in all samples to ensure the di-anionic form of Fl

[b] [L] = $\text{moles}_{\text{Fl}}/(\text{moles}_{\text{chol}}+\text{moles}_{\text{CTAB}})$

[c] Molar ratio between Fl and CTAB molecules available to interact with Fl

The presence of unbounded dye in Fl-QS samples was monitored by using centrifugal filters (Centricon, Merck Millipore) with 100kDa cut off. Presence of non-attached Fl molecules was verified for the samples Fl-QS-5, -6 and -7, i.e. samples with loading equal or higher than $10\text{x}10^{-3}$. This means that for samples having lower loadings, even if fluorescein molecules are present in the medium surrounding Quatsomes, their presence was not detectable by mean of the UV-vis and fluorescence spectroscopy or the signal was negligible compared to the correspondent Fl-QS sample.

2.1.2 Colloidal and optical properties of Fluorescein-decorated Quatsomes

In order to check whether the nanostructuration of the anionic dyes over the positively charged surface of Quatsomes affects their colloidal stability, size distributions of Fl-decorated Quatsomes have been monitored by Dynamic Light Scattering (DLS), one week and two months after the preparation (Figure 2.3). The DLS is equipped with an appropriate laser (633 nm) for the light scattering analysis of Fl-decorated Quatsomes. At this wavelength, in fact, Fl is transparent and light is only scattered by the samples (no absorption/emission phenomena occurring). Detailed information about light scattering analysis of fluorescent Quatsomes is given in the Experimental Section 7.4.

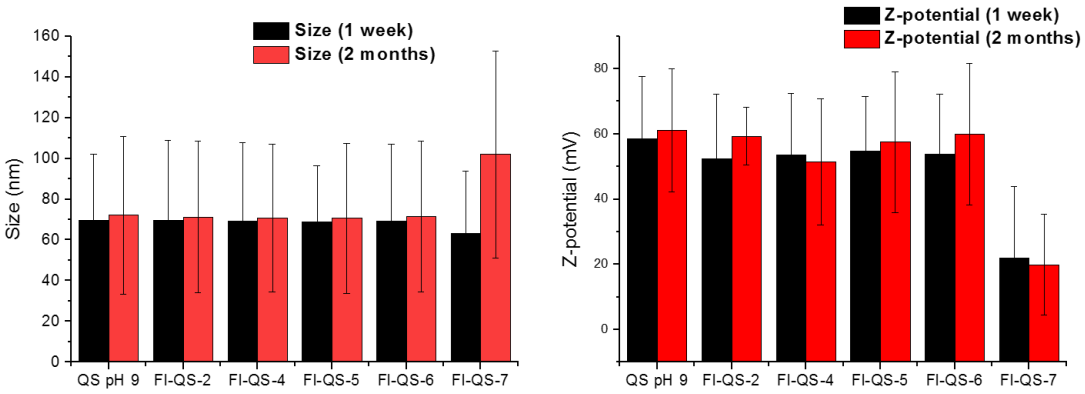

Figure 2.3: Size and Z-potential (monitored by DLS) of Fl-decorated Quatsomes at different loading, one week (black) and 2 months (red) after the preparation.

No relevant variations of QS average sizes have been noticed by the addition of Fluorescein. For all samples, except the one with the highest amount of Fl, the mean size measured by DLS is around 70 nm and it is maintained over the two months. The colloidal stability of the samples is further proofed by the high Z-potential, above +50 mV for all the samples tested except the last one, which is 60% ca. lower than plain Quatsomes, probably due to the shielding effect of Fl over the positive charge of CTAB. Likely for the same reason, the size of the sample with the highest loading of Fl increased over two months, suggesting the ongoing aggregation of the vesicles. All the other tested samples were found stable along time.

An insight on the actual morphology of the single Fl-decorated Quatsomes was obtained by cryo-transmission electron microscopy (cryoTEM), which allows the direct observation of nanoscale size objects, both synthetic or biological, which have not been fixed or stained, therefore showing them in their natural environment. CryoTEM images

reveal therefore details on the supramolecular structures and aggregation at the nanometer resolution. More information about cryoTEM microscopy and the procedure to acquire the images is given in the Experimental Section 7.4.3.

The cryoTEM micrographs (one week after the preparation) of Fl-decorated Quatsomes at different loading (Fl-QS-2, -4, -5, -6 and -7) are shown in Figure 2.4.

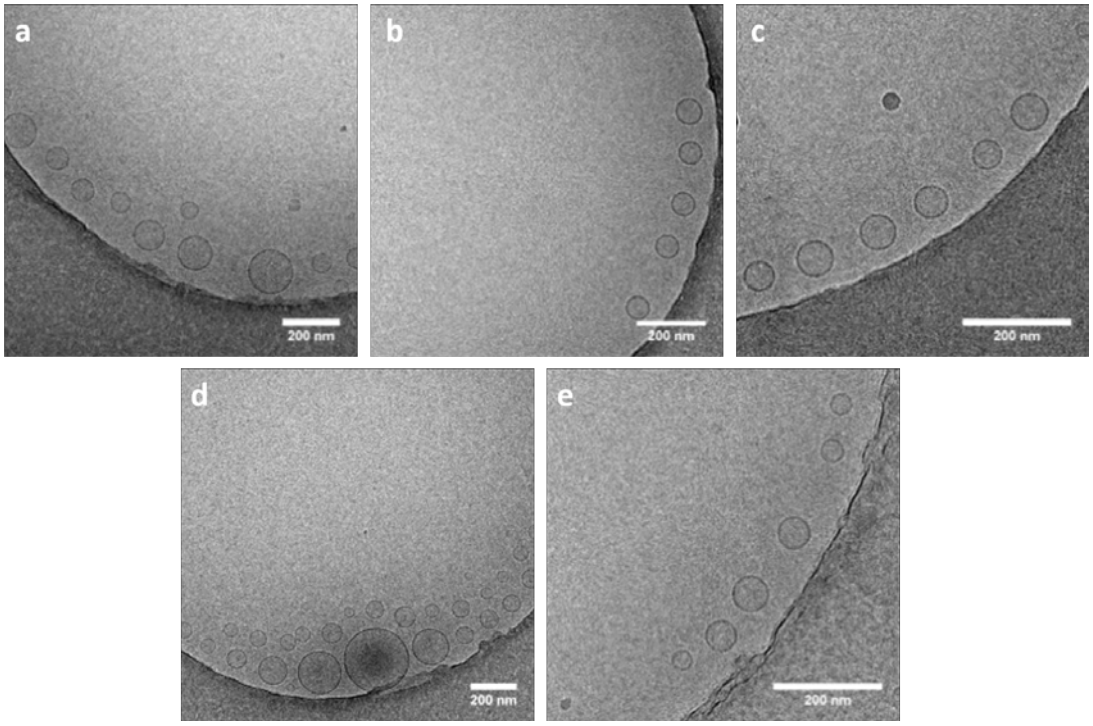

Figure 2.4: CryoTEM micrographs of Fl-decorated Quatsomes at different loading: a) Fl-QS-2; b) Fl-QS-4; c) Fl-QS-5; d) Fl-QS-6; e) Fl-QS-7.

The CryoTEM images show that the five samples monitored constitute of a distribution of small unilamellar vesicles, even at the highest loading tested, indicating that the presence of Fl does not affect the morphology of the vesicles.

The effect of the structuration over Quatsomes on the photophysical properties of the dye as been evaluated by comparing the photophysical properties of Fl-decorated Quatsomes and Fl in a water solution. The UV-vis absorption and emission of Fl-decorated Quatsomes are shown in Figure 2.5, whereas photophysical properties are listed in Table 2.2. Fluorescence quantum yield φ of the samples has been estimated by a comparative method, as explained in Experimental Section 7.5.

The results shown are coherent with other works reported in literature about the interaction of fluorescein with CTAB micelles [137, 140]. Both absorption and emission (normalized by absorbance at λ_{exc}) of Fl-decorated Quatsomes are red-shifted, probably due to a stabilization of the excited state of the probe when interacting with CTAB. As a

consequence of the increased loading of fluorophores, self-quenching of the emission is noticed, as shown by the decrease of emission intensity (Figure 2.5, right) and φ in Table 2.2. The dashed spectra refer to Fl-QS samples in which unbound fluorescein has been detected, as explained in Section2.1.1. We speculate that at higher loading, the contribution of free Fl becomes more relevant than that of Fl molecules interacting with Quatsomes membrane, as evidenced by the increase in φ coupled with an increase in the Stoke's shift.

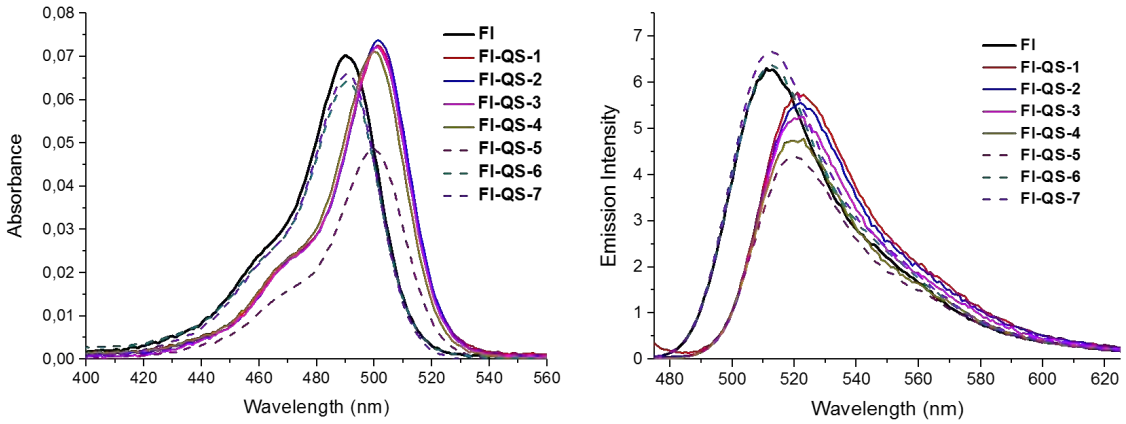

Figure 2.5: UV-vis absorption (left) and emission normalized by absorbance at λ_{exc} (right) of Fl and Fl-decorated Quatsomes at different loading.

Table 2.2: Photophysical properties of Fl and Fl-decorated Quatsomes at different loading

Sample	$\lambda_{\textbf{Max abs}}$ **nm**	$\lambda_{\textbf{Max emi}}$ **nm**	**Stoke's Shift** **cm** $^{-1}$	**Fluorescence** ϕ %
Fl	490	512	877	95
Fl-QS-1	501	521	767	93
Fl-QS-2	501	521	767	89
Fl-QS-3	501	521	767	78
Fl-QS-4	500	520	769	73
Fl-QS-5	500	520	769	67
Fl-QS-6	490	512	877	99
Fl-QS-7	490	512	877	1

[a] FLuorescence quantum yield ±10%. Fluorescein (0.1M NaOH) has been used as standard

As mentioned in the Introduction, the re-organization over a nanoparticle can have a positive effect on the photostability of a dye. It has been reported that water soluble fluorophores which undergo photobleaching upon a photoxydation mechanism (as in

the case of Indocyanine Green, ICG) experience a strong enhancement in photostability when encapsulated, for example, in polymeric nanostructures [49, 50].

Photodegradation of fluorescein occurs via an interaction of the fluorophore in the ground state with oxygen in the singlet state [141]. For this reason, the photostability of Fl in water has been compared to that of Fl-decorated Quatsomes, to check whether the nanostructuration over the vesicles has an ameliorative effect.

Two types of photostability measurements are usually reported in literature: (a) direct observation of the nanoparticles under microscopes illumination or (b) irradiation via a lamp or a laser of a sample in a cuvette [47]. Due to the differences in excitation power (under a microscope excitation power can be up to 1000 times higher than in cuvette), results may differ, depending on the method used. A spectroscopic method, developed by Profs. K. Belfield and M. Bondar [142, 143], was used to determine the efficiency of photodegradation of the probes. The measurements were performed in collaboration with Siarhei Kurhuzenkau, in the group of Prof. A. Painelli, during a short stay at the University of Parma.

Photostability under continuous-wave excitation was determined by measuring the photodegradation quantum yield (PQY):

$$PQY = N_{mol}/N_{phot}$$

where N_{mol} is the number of bleached molecules and N_{phot} is the number of absorbed photons. The number of bleached molecules was determined by the kinetic decrease of fluorescence intensity, under the assumption that the fluroescence of the photoproducts is negligible in the spectral region of the dye main fluorescence band. Samples were placed in a cuvette and irradiated with a diode laser (λ_{exc}=476 nm; I=10 mW/cm^2) in such a way that the whole sample is simultaneously illuminated in order to exclude the influence of diffusion on photochemical process. Samples have not been de-gased before running the measurements. See Section 7.5.5 in the Experimental Part for further details.

The evolution of the measured fluorescence is shown in Figure 2.6, while the photodecomposition quantum yield (PQY) of the samples is shown in the Table 2.3. Only the samples with lower Fl contents were monitored in order to exclude any possible contribution of free Fl in water to the observed emission.

Emission of free Fl decreases more than 60% after 40 minutes of irradiation, while it decreases less than 15% when it is decorating the QS surfaces, showing how the surrounding of the dye molecule affects its rate of degradation, as previously shown in the case of fluorescein-like fluorophores entrapped in PVA matrices [144]. We speculate

that, when interacting with QSs, fluorescein is protected from getting in contact with oxygen, limiting the photodegradation of the dye and making therefore fluorescein more photostable when attached to QSs [47, 145].

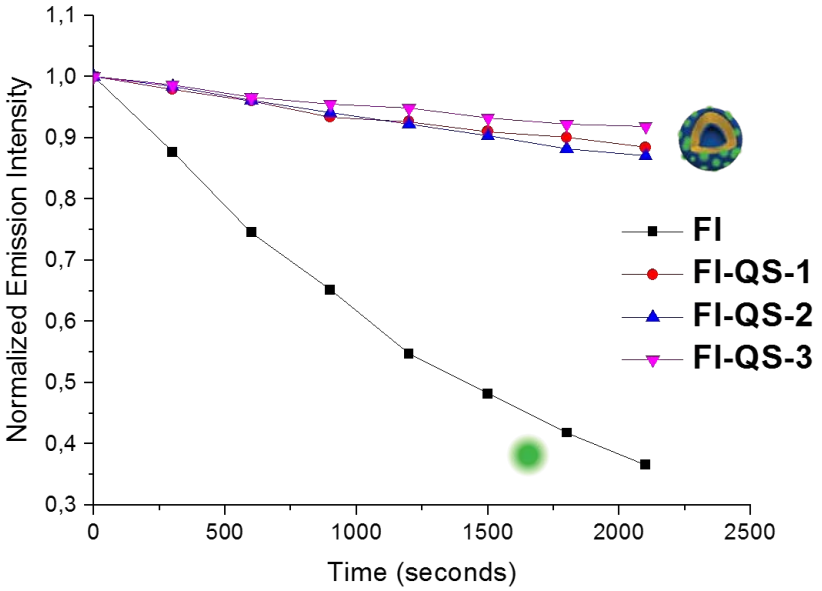

Figure 2.6: Variation of measured fluorescence of fee Fl (black) and Fl-QS at different irradiation times. The fluorescence intensity has been normalized by the value before starting the irradiation.

Table 2.3: Photodegradation Quantum Yield (PQY) of Fl in water and Fl-QS at different loading

Sample	**Photodegradation Quantum Yield PQY** $\times 10^{-5}$
Fl	8±2
Fl-QS-1	1.3±0.5
Fl-QS-2	3±1
Fl-QS-3	2.2±0.6

[a] Photodegradation quantum yield, calculated as explained in Section 7.5.5 of the Experimental Part. (λ_{exc}=476 nm, I=10mW/cm^2

2.1.3 Molecular Dynamics (MD) simulations of FI-QS

Molecular Dynamics simulations performed by Dr. Jordi Faraudo (ICMAB, CSIC) and summarized by Dr. Lidia Ferrer in her PhD Thesis [130, 134], permitted to assess the interaction between cholesterol and CTAB that lead to the formation of Quatsomes double-layer membrane.

In that case, it was shown that one molecule of CTAB and one of Cholesterol, depicted as a conical and an inverted conical molecules, respectively, form a supramolecular synthon, with a cylindrical-like shape, which is the repetitive unit of the bi-layer (Figure 2.7a). The atomistic distribution of the membrane revealed that a homogeneous double layer is obtained (as shown in Figure 2.7b), with cholesterol molecules fully incorporated in the hydrophobic region of the membrane and the quaternary ammonium of CTAB at the interface with water, as shown in the density distribution of the atoms of the molecules forming Quatsomes in function of the distance from the center of the bi-layer (Figure 2.7 c).

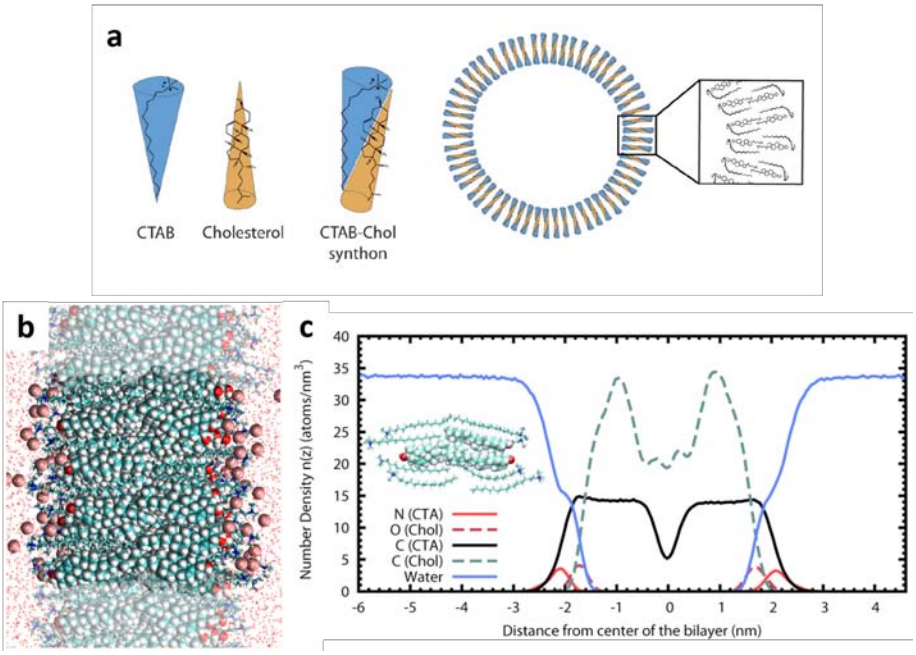

Figure 2.7: Resume of the Molecular Dynamics simulation previously studied, showing the interaction of CTAB and cholesterol that lead to the formation of Quatsomes. a) Schematic illustration of cholesterol and CTAB forming the bi-layer vesicles b) Snapshot corresponding to the simulation of Quatsomes membrane. For sake of clarity, only cholesterol molecules and Br^- counterions of CTAB are shown. c) Average density profile of atoms of CTAB and cholesterol as a function of z coordinate (perpendicular to the membrane). Solid red line: nitrogen atoms of CTAB; dashed red line: oxygen atom of cholesterol; black solid line: carbon atom from CTAB; black dashed line: carbon atoms from cholesterol; blue line: water density. Adapted from [130].

As shown in the previous Section, the photophysical properties of fluorescein

significantly change when Fl-decorated Quatsomes are formed. A deeper comprehension of the interaction between Fl molecules and Quatsomes membrane by mean of Molecular Dynamics (MD) simulations could help in the interpretation of the results previously discussed. The simulations were conducted by Silvia Illa, at Jawaharlal Nehru Centre for Advanced Scientific Research (JNCASR, India) and Dr. Jordi Faraudo, at the Institut de Ciència de Materials de Barcelona (ICMAB-CSIC).

First of all, a model of fluorescein di-anion (Fl^{2-}) has been developed by using CGenFF parameters and validated with QM and MM calculations. Thus, a single molecule of Fl^{2-} was added in a simulation box containing a portion of a Quatsome membrane in water. In order to have a realistic comparison with the experiments, four different simulations (S1, S2, S3 and S4) representing four different loadings of Fl have been carried out. Details on the four simulations are indicated in Table 2.4 and in Appendix 2. All the simulations have been built up starting from the system of Quatsomes in water described in Ref. [134] and, as starting point, the Fl^{2-} molecules have been added at the top of the simulation box, in such a way that the Fl^{2-} is quite far from the bi-layer. Water molecules were added using the VMD plug-in in order to solvate only the added Fl molecules and to obtain the experimental density of the solvent. As consequence, the cubic box size increases in z direction. Once the system is solvated, the two negative charges of Fl^{2-} have been balanced (total charge of the system must be zero) and for this reason sodium ions were added to the system.

Table 2.4: Details on MD simulations of fluorescein interacting with Quatsomes. Each simulation corresponds to a certain loading of Fl, analogously to the experimental study.

	Atoms (total)	**Number of molecules Fl/water/CTAB**	**Fl/CTAB[a] $\times 10^{-3}$**	**Simulation time /ns**
S0	23727	0/5443/54	0	90
S1	25708	1/6091/54	18	110
S2	27037	4/6497/54	74	120
S3	26794	10/6342/54	185	110
S4	30268	28/7278/54	520	90

[a] Molar ratio between Fl and CTAB molecules available to interact with Fl

As example, the S2 simulation build-up is shown in the snapshot in Figure 2.8. On the left the molecules are shown surrounded by water, while, on the right, the counter-ions (Br^- and Na^+) are represented and water molecules have been removed for sake of clarity (but included in the simulation). QS bi-layer is located in the center of the box and four fluorescein molecules are added on the top, solvated by water.

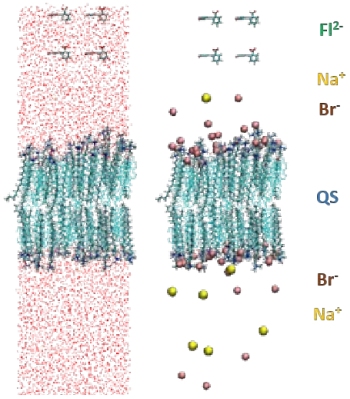

Figure 2.8: Scheme of S2 simulation build-up. On the left, water molecules are represented; on the right, water molecules are omitted and counter-ions (Br^- and Na^+) are shown.

The first simulation, S1, corresponds to the experimental sample Fl-QS-4 with [L]=$5*10^{-3}$, i.e. the experiment realized with highest loading without detecting the presence of unbound Fl molecules. In S1 simulation, only 1.5 ns were required for the adsorption of a Fl^{2-} molecule to QS surface. In this case, the attractive interaction between the vesicle and the di-anion is strong enough to hold the Fl^{2-} tightly close to the surface of QS during the whole calculation time (110 ns). Diffusive motion of the Fl^{2-} over the membrane of the vesicles has been noticed over the entire simulation.

The radial distribution function g(r) describes the probability of finding a pair of atoms at a certain distance, r. By analyzing g(r) between the two negative oxygens of Fl^{2-} and the N^+ atom of the CTAB, information on the orientation of fluorescein on Quatsomes surface can be extracted. As shown in Figure 2.9, Fl^{2-} can stay in two possible orientations. The first with the hydroxyl group in contact with the cationic head of CTAB which is more likely (66%) than the second, where the the carboxylate takes part to the interaction (34%).

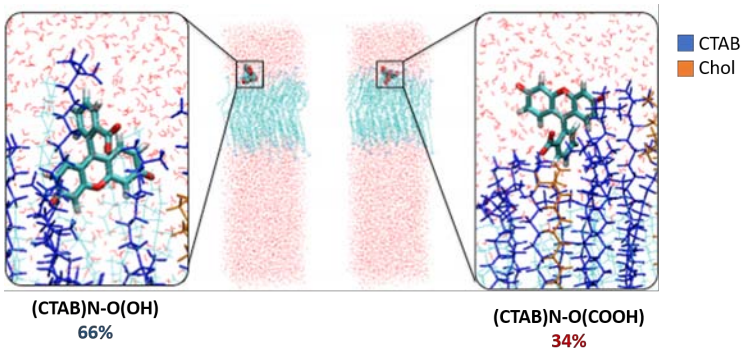

Figure 2.9: Snapshots of the S1 large simulation box with emphasis on a single Fl molecule orientation adsorbed over QS surface. Water is shown in red and QS in light blue. Two orientations can occur, where hydroxyl and carboxyl anions of Fl^{2-} are close to nitrogen atoms of CTAB.

Other three simulations (S2, S3 and S4) were run, corresponding to experiments with

higher Fl^{2-} loadings on Quatsomes in which the presence of unbound fluorescein has been detected. In particular, S2 corresponds to a hypothetical sample intermediate between Fl-QS-5 and Fl-QS-6 (Fl loading between $10*10^{-3}$ and $50*10^{-3}$); S3 corresponds to the Fl-QS-6 sample and S4 corresponds to Fl-QS-7, the sample with the highest ratio of Fl/CTAB experimentally tested. Since the beginning, it was noticed that the higher the number of Fl molecules in the system, the longer time is required for them to get close to QS surface. Nevertheless, the interaction between Fl^{2-} and QS surface occurs within few ns. The representative snapshots of S2, S3 and S4 simulations at a random instant are shown in Figure 2.10 and the main results are listed below.

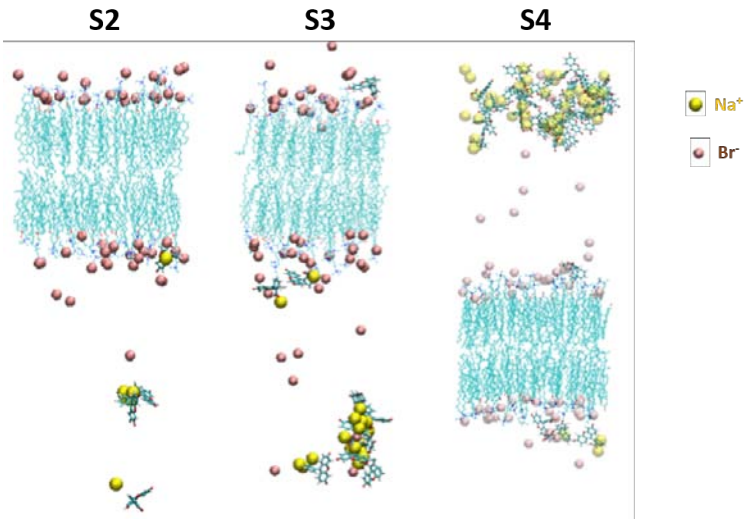

Figure 2.10: Snapshot of S2, S3 and S4 simulations at a random instant of the simulation. The three simulations correspond to the experimental samples at hither loading of dye, i.e. the samples in which unbounded fluorescein has been detected (samples Fl-QS-4, -5 and -6, respectively).

• When there are two or more Fl^{2-} attached to the surface of the vesicle, they can independently interact with QS or either adsorb one on each other on QS surface. In any case, a strong fluctuations of the molecules is observed throughout all the simulation time, molecules get close to the surface, deposit on them and then fly away and other molecules can do the same cycle. However, at every time, at least one Fl^{2-} is attached on QS surface.

• Molecules that are not interacting with the surface, form aggregates in water and the size of the aggregates get bigger at higher FL/CTAB ratio, as shown in S3 and S4 simulations of Figure 2.10;

• In S2 simulation, only one molecule is attached on QS surface during all the simulation time, since the other three fluctuate in water without forming aggregates;

• In S3 and S4 simulations, at least one molecule is attached on the QS surface during

all the simulation time (at the instant at which the snapshot was acquired there are three bound on the QS surface), and the others form aggregates.

2.1.4 Summary and Perspectives

In this Chapter it has been shown that Quatsomes, thanks to their positively charged surface, can be successfully used to nanostructure anionic water soluble dyes in an aqueous environment. Fluorescein (Fl), in the di-anionic form, has been used as model dye to check how the optical properties of the fluorophore change upon structuration over Quatsomes compared to the dye in solution and whether the stability of the vesicles is affected by the interaction with the dye. Different samples have been studied, varying the loading, i.e. the amount of dye per vesicles. Summarizing, the main results are as follow:

- It was not possible to isolate Fluorescein-decorated Quatsomes from free unbounded molecules in solution, likely due to the equilibrium between molecules of Fl adsorbed over the surface of the vesicles and those freely diffusing in solution.

- The physicochemical properties of Quatsomes, in terms of size distribution, colloidal stability and morphology, are, in large extent, not affected by the presence of fluorescein. Only in one case, upon addition of a very high amount of dye, the colloidal stability of the vesicles is compromised. The emission properties of Fl change upon nanostructuration over Quatsomes. Interestingly, fluorescein-decorated Quatsomes were found more photostable than the dye in solution.

- Molecular Dynamics simulation revealed the nature of the interaction between Fl molecules and the membrane of the vesicles, indicating a preferential orientation of the Fl molecules and their strong fluctuations (molecules moving close and away from the membrane) throughout the simulation time.

Despite these results are encouraging, aiming to enhance the optical properties of molecular dyes by nanostructuring them over Quatsomes, the strategy used in this Chapter is not adequate for the preparation of FONs for imaging purposes. The labile interaction (of electrostatic nature) between the dye and the vesicles raises problems related, for example, to the stability to dilutions of these FONs. This is a major drawback "under the microscope" because fluorophores leaching would likely cause a loss of the

FONs brightness, a strong background signal and the undesirable stain of unnecessary bodies/objects during the imaging process.

3

Quatsomes-based FONs with non-water soluble cyanines

In the previous Chapter, it was shown that Quatsomes can be used as scaffolds for the nanostructuration of water-soluble anionic fluorophores, using fluorescein as a model. Despite the positive results concerning the enhancement of some optical properties, such as the photostability of the dye, which resulted higher in the case of fluorescein-decorated Quatsomes in comparison with the free dye in solution, the strategy pursued showed severe drawbacks related to the dye leaching from the Quatsomes to the surrounding water. When dealing with FONs, the leakage of fluorophores may cause major drawbacks "under the microscope", including reduced brightness of the nanoparticles and higher background signal.

In this Chapter, a new class of Quatsomes-based FONs have been designed, aiming to disperse non-water soluble dyes in aqueous media. A group of commercially available dyes, known as carbocyanines (DiI, DiD and DiR), have been selected for such a purpose. Thus, the properties of these new FONs will be thoroughly examined, with particular attention to the impact of the preparation method on the optical properties along with a deep study of their colloidal and optical stability. Moreover, the possibility of preparing Quatsomes-based multicolor nanoparticles, incorporating simultaneously more than one dye, will be evaluated. In the last Section, the resulting carbocyanine-loaded Quatsomes will be used as probes for super-resolution microscopy (STORM) in order to find out whether single Quatsomes can be visualized by this technique and used as probes for bioimaging.

3.1 Introduction

Cyanines were originally studied, back to the 19^{th} century, as light sensitizers in photography. Since then, they have found many applications in several industrial fields including photography, semiconducting materials, optical devices, industrial paintings

and as probes for biological systems in fluorescence microscopy.[146]

The general cyanine structure consists of two nitrogen atoms (one of which is positively charged) linked by a conjugated chain of carbons (Figure 3.1). This class of dyes, referred as well as polymethine dyes, generally have high extinction coefficients and absorption/emission bands that can be shifted from visible to infrared simply by increasing the lenght of the polymethine chain.[147]

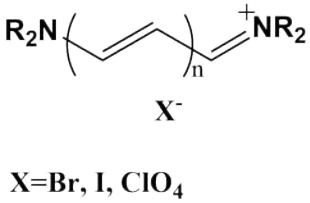

Figure 3.1: Generic structure of cyanine dyes

Carbocyanines are a subclass of cyanines, in which the *R* substituents are two long aliphatic chains (C_{18}), which are non soluble in aqueous solutions, like DiI, DiD and DiR (commercialized by ThermoFisher, see structures in Figure 3.2). These three carbocyanines are widely used as biological membrane probes, especially for labeling neurons [148, 149].

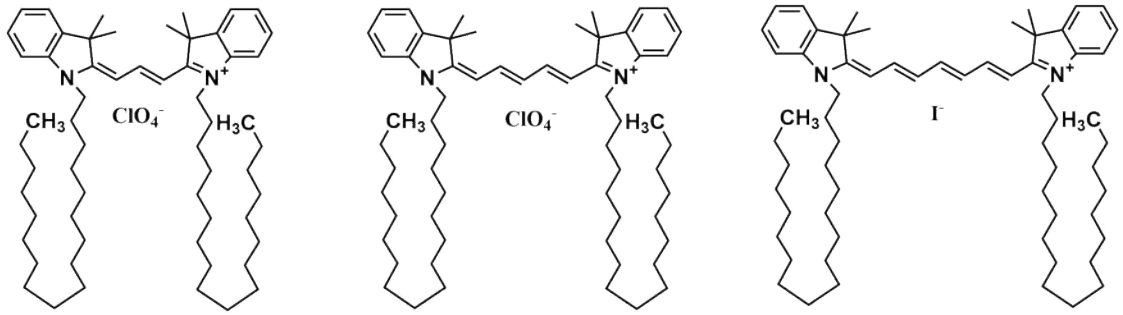

Figure 3.2: Molecular structures of commercially available carbocyanines studied in this work: DiI (left), DiD (center) and DiR (right)

Normalized UV-vis absorption and emission in EtOH of the three dyes are shown in Figure 3.3. The three dyes have a different number of methyne units (n) in the conjugated chains. DiI (n=3) emits in the orange-red region of the visible spectrum, DiD (n=5) is a red emitter and DiR (n=7) emits in the near-infrared (NIR). Although these dyes are weakly or not fluorescent when dispersed in water as aggregates, they are bright and photostable when inserted in cell membranes.

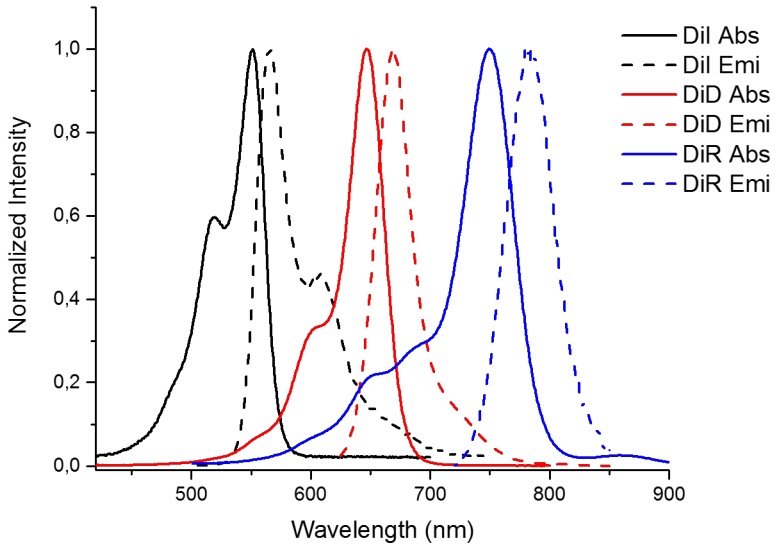

Figure 3.3: Normalized UV-vis absorption and emission of DiI (black), DiD (red) and DiR (blue)

Cyanines are dyes with a well known tendency to self-aggregation and the relation between their aggregate structures and spectral properties has been deeply studied [146]. The self-association of dyes molecules in solution or at solid-liquid interface, due to strong inter-molecular van der Waals attractive forces, is a frequent phenomenon in dye chemistry. These aggregates in solution exhibit net changes in absorption bands compared to the monomeric state. Dye aggregates with an absorption band which is bathochromically shifted (to longer wavelength) with respect to the monomer band are called J-aggregates. On the other hand, aggregates with absorption band hypsochromically shifted (to shorter wavelengths) with respect to the monomer band are called H-aggregates and, in most of the cases, these aggregates are not fluorescent. Such kind of aggregates were indeed observed, almost 80 years ago by Scheibe and Jelley [150][151], who where studying the aggregation in solution of a cyanine dye (the pseudoisocyanine chloride, generally referred as PIC).

The shifts in the absorption bands of H- and J-aggregates have been explained in terms of the molecular exciton coupling theory, based on the coupling of the transition moments of the dye molecules. It is well established that H- and J-aggregates are given by molecules stacked parallel plane-to-plane and end-to-end respectively. Defining the angle of slippage (α) as the angle between the line of the centers of a pillar of molecules and the long axis of any of the parallel molecules, then larger slippages, with a small angle α, result in bathochromic shift (J-aggregates) while small slippages, with α close to 90°, give hypsochromic shits (H-aggregates). In accordance with the exciton coupling

theory, the molecule can be considered as a point dipole and the excitonic state of the aggregates, due to the interaction of transition dipoles, splits into two levels, with higher and lower energy than the monomer excitonic band, as shown in Figure 3.4. If the molecules are plane-to-plane parallel stacked, H-aggregates are formed, generally with broad bands and very low fluorescence quantum yields. When the molecules are preferentially disposed in a head-to-tail parallel arrangement, J-aggregates are formed, with low Stokes shifts and high quantum yields.

Whereas the aggregation of the cyanines in solution strictly depends on the concentration [152], the formation of dimers, H- and J-aggregates can be modulated by the presence of other compounds even at low concentrations. Gadde et al. [153], for example, showed that with opportune polyelectrolites it is possible to modulate in water the forms and extent of aggregates of two water-soluble cyanines (including one similar to DiI). Micelles can strongly alter the aggregation state and the optical properties of this class of dyes in solution. It has been shown [154] that a cyanine which forms mainly dimers in aqueous solution (with a blue-shifted absorption band and lower intensity compared to the monomer), can be de-aggregated and dispersed as monomers in presence of CTAB micelles, thanks to the hydrophobic interaction between the dye molecules and the surfactant.

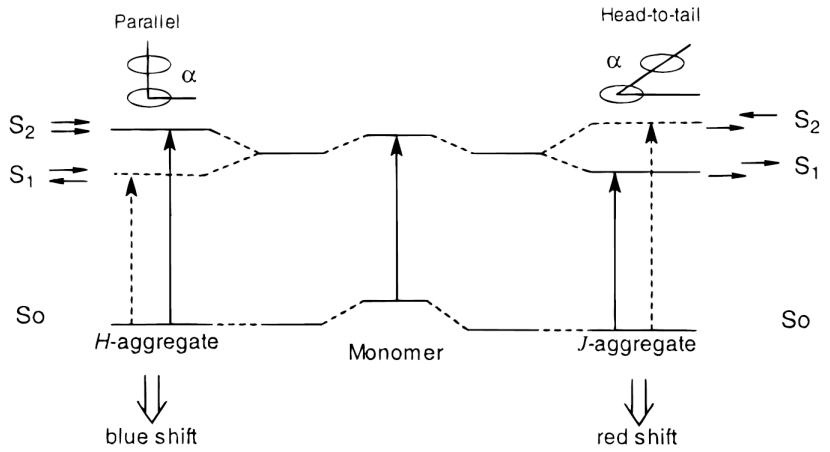

Figure 3.4: Schematic representation of the exciton coupling theory and relationship between the chromophore arrangement and spectral variations (From Ref. [146])

Similar studies are reported in the literature on the effect of other nanostructures, including TiO_2 nanoparticles[155] and lipid vesicles [156], over the aggregation state of cyanines.

In this Chapter, a new strategy has been pursued in order to disperse in aqueous media the three non-water soluble carbocyanines, DiI, DiD and DiR. This strategy

consists in the formation of a new class of FONs, based on the incorporation of the three dyes in Quatsomes. A comprehensive study on the influence of the dye nanostructuration in Quatsomes over the physicochemical and optical properties of these new FONs has been conducted, including the impact of the preparation route, loading and a comparison with other cyanines-based nanostructures.

3.1.1 Dispersion in water of DiI, DiD and DiR using Quatsomes

3.1.1.1 Preparation of cyanines-loaded Quatsomes

As described in the Introduction, the DELOS-SUSP methodology is a robust method for the production of multifunctional nanovesicles, including Quatsomes bearing water non-soluble compounds [117, 124, 131]. Therefore, DELOS-SUSP has been studied as well in this Thesis, for the preparation of Quatsomes loaded with water non-soluble DiI, DiD and DiR dyes, following the method described in Section3.1.2 and in the Experimental Section 7.2.1, where details on the preparation of fluorescent Quatsomes are given.

Cholesterol was dissolved in a 0.1 mM solution of the probe (DiI, DiD and DiR) in EtOH and added to the reactor. Afterwards, the standard procedure for the preparation of dye-loaded Quatsomes was followed. Samples were purified by diafiltration (see Experimental Section 7.2.2) and stored at 4°C for one week before analysis. The samples studied in this Section are listed in Table 3.1.

In order to provide an information about the amount of fluorophore present in each sample, the loading, [L], is expressed as the molar ratio: $moles_{probe}/(moles_{chol}+moles_{CTAB})$. The amount of dye in each sample has been evaluated by UV-vis spectroscopy while the amounts of cholesterol and surfactant used for the calculation of [L] are the nominal ones; i.e. the quantities weighted at the beginning of the DELOS-SUSP protocol. Please, find information about the calculation of dye loading in each sample in the Experimental Section 7.5.2. The code used to name the samples in the entire Thesis is made of three parts: the first part refers to the dye used, the second one refers to the type of nanoparticle and finally, the last one, is a number associated to a certain loading. For instance, in the sample I-QS-1, the letter "I" refers to the DiI (the letters "D" and "R" are used for DiD and DiR, respectively), "QS" means that the dye is loaded in Quatsomes, and finally "1" refers to the lowest loading tested.

For each sample two batches have been prepared (three in the case of D-QS-1) to check reproducibility of the results and only minor differences have been detected in all the studied cases.

Table 3.1: List of cyanine-loaded Quatsomes studied in this Section

Sample	Dye	[L][a] $\times 10^{-3}$
I-QS-1	DiI	0.6
D-QS-1	DiD	0.6
R-QS-1	DiR	0.5

[a] For the calculation of dye loading see Experimental Section 7.5.2

3.1.1.2 Physicochemical and optical characterization of I-QS-1, D-QS-1 and R-QS-1

In order to check whether the incorporation of the cyanines affects the colloidal stability of Quatsomes, size distributions and mean sizes of I-QS-1, D-QS-1 and R-QS-1 have been evaluated after one week and two months of storage at 4°C.

The determination of size distribution of fluorescent nanoparticles by light scattering methods is not a trivial issues and it requires a critical analysis. Two different techniques, both based on light scattering, have been used for the determination of size distributions of cyanines-loaded Quatsomes: Dynamic Light Scattering (DLS) and Nanoparticle Tracking Analysis (NTA).

In the case of I-QS-1, a DLS equipped with a 633 nm laser has been used for the determination of particles size distribution and Z-potential. DiI is transparent at 633 nm, so light is only scattered by I-QS-1, which does not absorb neither emit when excited at this wavelength. As explained by Geissler *et al.* [157], DLS measurements of strongly bright nanoparticles (e.g. quantum dots or polymeric nanoparticles loaded with probes with high extinction coefficient and good fluorescent efficiency) can be severely affected by both absorbed and emitted light, eventually leading to misinterpretation of the results. For this reason, in the case of D-QS-1 and R-QS-1, the size distribution and colloidal stability were monitored by Nanoparticle Tracking Analysis (NTA). This technique allows the visualization of the single nanoparticles, giving as result the mean size and the particles size distribution. The instrument is equipped with a laser at 488 nm, at which both DiD and DiR are transparent and light is only scattered by the particles. Indeed it was not possible to study the size distribution of QSs loaded with DiD and DiR by the DLS due to the relevant absorbance (extinction coefficients are in the order of 10^5 $M^{-1}cm^{-1}$) and the fluorescence of the dyes in the red region of the visible

spectrum. More information about DLS and NTA, including principles of operation and a comparison between the two techniques, is given in details in Experimental Section 7.4.

An inspection on the morphology of the individual Quatsomes loaded with the dyes in the three samples was obtained by cryo-transmission electron microscopy (cryo-TEM) (see Section 7.4.3 of the Experimental Part for further details), a powerful tool that allows the direct observation of nanoscale size objects, both synthetic or biological, which have not been fixed or stained, therefore showing them in their natural environment. CryoTEM images reveal details on the supramolecular structures and aggregation at nanometer resolution.

The size distributions and cryoTEM images of I-QS-1, D-QS-1 and R-QS-1 suspensions one week after their preparation are shown in Figure 3.5, while the average hydrodynamic diameters one week and two months after the preparation are shown in Table 3.2, along with the Z-potential of I-QS-1.

In accordance to cryoTEM images, the three samples show a homogeneous distribution of exclusively small unilamellar vesicles, with diameters in most of the cases smaller than 100 nm, meaning that the presence of the dye has no effect on the morphology of the self-assembled vesicles. The diameters of the vesicles observed in the cryoTEM micrographs are smaller than those measured by the light scattering methods (see Table 3.2), as expected considering that both DLS and NTA provide the hydrodynamic diameter (i.e. diameter of a solvation sphere that has the same translational diffusion coefficient as the particle) and not the real size of the particles under measurement, as previously shown for Quatsomes in Dr. Ferrer-Tasies's Doctoral Thesis [130].

As explained in Experimental Section 7.4, where the comparison between DLS and NTA results on the same samples of plain Quatsomes is shown, the minimum size of organic nanoparticles detectable by NTA is around 40-45 nm. For this reason, the average diameters of D-QS-1 and R-QS-1 listed in Table 3.2 are likely overestimated. However, these two samples were found highly stable, showing the same size over the entire examination period (two months). The colloidal stability of I-QS-1 is further supported by the high Z-potential value (around 82 mV).

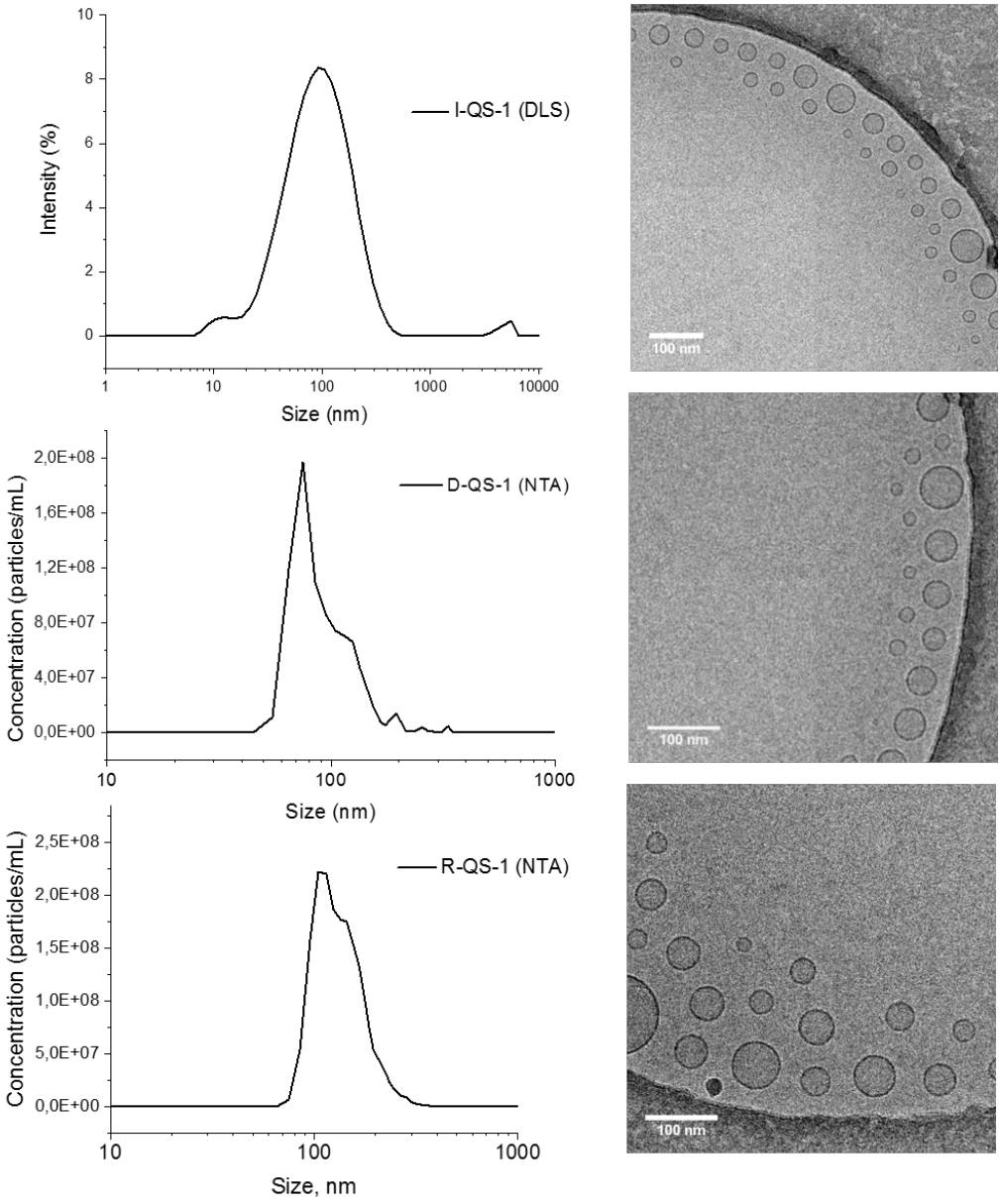

Figure 3.5: CryoTEM images (right) and size distributions (left) one week after the preparation of: top) I-QS-1, measured by DLS; middle) D-QS-1, measured by NTA; bottom) and R-QS-1, measured by NTA.

Table 3.2: Physicochemical properties of I-QS-1 (DLS), D-QS-1 and R-QS-1 (NTA) one week and two months after their preparation.

Sample	Size distr.(one week)[c] nm	Size distr.(two months)[c] nm	Z-potential mV
I-QS-1[a]	72±43	69±52	82±18
D-QS-1[b]	96±40	114±33	-
R-QS-1[b]	126±47	121±51	-

[a] Measured by DLS. See Experimental Section 7.4.1
[b] Measured by NTA. See Experimental Section 7.4.2
[a] Size distribution is shown as the mean average hydrodynamic diameter ± mean PdI

As already mentioned in the previous Section, the aggregation of the cyanines plays an essential role in the optical properties of this class of fluorophores. In solution, at low concentrations, cyanines are mainly monomers but, if loaded into a matrix for the dispersion in aqueous media or even in solution at high concentrations, these dyes undergo self-aggregation in form of dimers, either H and/or J-aggregates. Therefore, in the case of cyanines-based FONs, controlling the self-aggregation of the fluorophores is critical in order to tune the optical properties of the obtained dye-loaded nanoparticles.

As dimers and aggregates of cyanines are generally associated to peculiar changes in the absorption/emission bandshapes compared to the monomeric state, the normalized absorption, excitation and emission spectra of water suspensions of I-QS-1, D-QS-1 and R-QS-1 have been compared to solutions of DiI, DiD and DiR in EtOH, respectively, as shown in Figure 3.6, in order to find out whether these fluorophores are dispersed as monomers over the membrane of Quatsomes or either they tend to form aggregates inside the membranes.

The photophysical properties of I-QS-1, D-QS-1 and R-QS-1 suspensions in comparison with those of the dyes in EtOH are resumed in Table 3.3. Molar extinction coefficients at the maximum absorption wavelenght, ε ($M^{-1}cm^{-1}$), and fluorescence quantum yields, φ (%), were estimated as explained in Section 1.4 of the Experimental part. φ has been calculated from the fluorescence collected exciting the samples at the wavelength in correspondence of the maximum in the excitation spectra.

The absorption spectra of DiI, DiD and DiR in EtOH are centered at 550 nm, 647 nm and 749 nm, respectively. In cyanines with higher number of polymethine conjugated units (DiR>DiD>DiI) absorption bandshapes appear broader, with minor absorption bands in the blue edge of the main peak, as effect of the symmetry breaking in long polymethine chains [158].

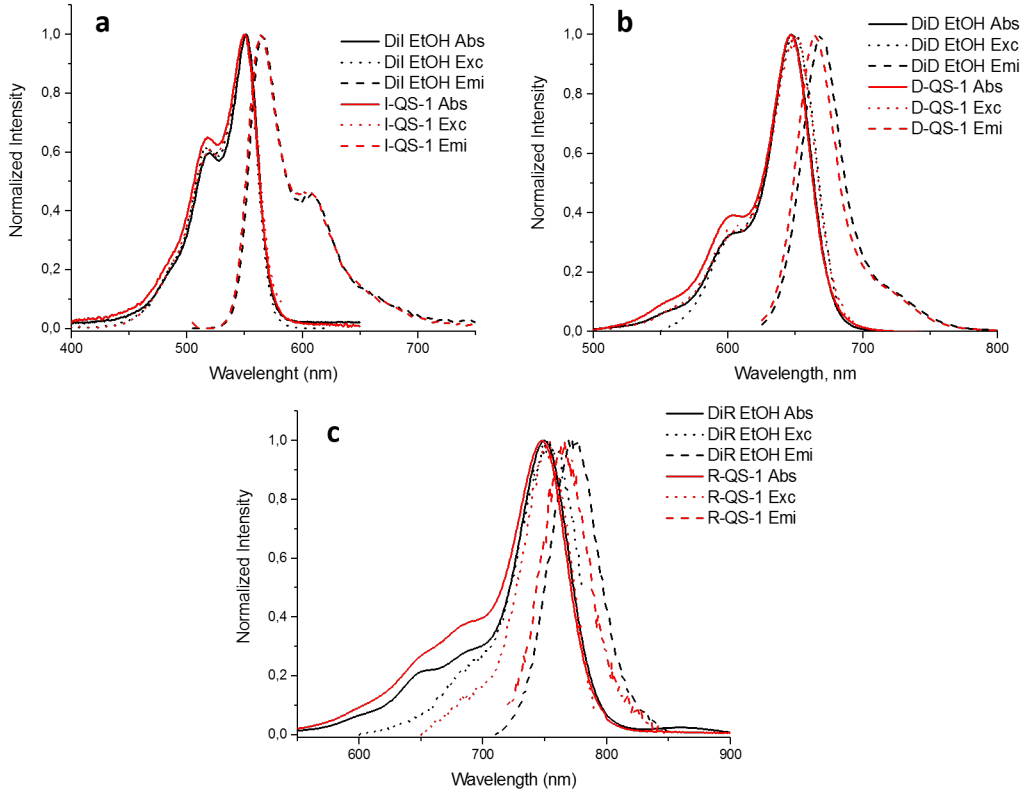

Figure 3.6: Normalized absorption, excitation and emission spectra of a) I-QS-1 and DiI in EtOH; b) D-QS-1 and DiD in EtOH; c) R-QS-1 and DiR in EtOH.

Absorption and emission main peaks of I-QS-1 are 1 nm blue-shifted compared to the monomer in EtOH. The slight increase of the absorbance at 518 nm in I-QS-1 sample can be probably ascribed to environmental effects and not to aggregation of DiI in Quatsomes membrane. In the case of D-QS-1, the main absorption and emission peaks are 1 nm and 4 nm blue-shifted, respectively, compared to EtOH. While the absorption of R-QS-1 is 1-2 nm blue-shifted than the DiR in EtOH, the emission spectrum of DiR loaded into QS is 9 nm blue-shifted than in EtOH. The solvatochromism in emission, stronger for DiR and DiD, is due to the higher intramolecular charge transfer occurring in these two probes which results in a large dipole moment in the excited state and, subsequently, stronger solvent effects.

Absorption spectra of D-QS-1 and R-QS-1 show minor differences compared to the respective monomers in EtOH, especially at 603 nm and shorter wavelengths (in the case of D-QS-1), and in the region between 600 nm and 700 nm (in the case of R-QS-1). These variations may be ascribed to the presence of dimers/aggregates, as shown in other works with DiD and DiR loaded nanoparticles [78][70] , or either variations of local environment.

Table 3.3: Photophysical properties of DiI, DID and DiR in EtOH and suspensions of I-QS-1, D-QS-1 and R-QS-1 in water

Sample	$\lambda_{\textbf{Max abs}}$ **nm**	$\lambda_{\textbf{Max emi}}$ **nm**	**Stokes shift cm^{-1}**	ϕ[a] %	ϵ[b] M^{-1} cm^{-1}	**Brightness**[c] M^{-1} cm^{-1}
DiI EtOH	551	566	481	11	140,000	15,400
I-QS-1	550	565	483	20	115,000	23,000
DiD EtOH	647	669	508	30	246,000	73,800
D-QS-1	647	664	396	23	247,000	56,800
DiR EtOH	749	774	431	10	270,000	27,000
R-QS-1	748	765	297	3	201,000	6,000

[a] FLuorescence quantum yield ±10%. Fluorescein (0.1M NaOH) has been used as standard for DiI and I-QS-1. Cresyl Violet (MeOH) has been used as standard for DiD, DiR, D-QS-1 and R-QS-1
[b] Molar extinction coefficients at the maximum absorption wavelength
[c] Brightness calculate as $\epsilon \times \phi$

The ε and φ of DiI, DiD and DiR in EtOH are coherent with those found in literature for the same (or similar) dyes in organic solvents [70, 159, 160]. In the case of I-QS-1 and D-QS-1 the extinction coefficients and fluorescence efficiency values are comparable to those of the fluorophores in EtOH, especially in the case of DiI, which is even brighter when inserted in the membrane of Quatsomes than when dissolved in EtOH. The brightness of the DiR dramatically decreases when the fluorophore is inserted in the membrane of Quatsomes. This is likely due to the presence of aggregates of DiR (as visible in the absorption spectra of Figure 3.6), whose extinction coefficients and quantum yield are lower than those of the monomers [152]. A key role in the different emission behavior of the three dyes could be played either by the nature of the counterion or by the different length of the conjugated chains. Indeed, Iodine (I^-), counterions of DiR, is a well-known effective fluorescence quencher, accelerating the rate of intersystem crossing and hence promoting non-radiative decays by colliding with the luminescent molecules. While the quenching due to I^- is "disabled" in EtOH, being the two ions solvent separated, it is determining in the condensed phase, as demonstrated by Zhao et al. [161], and it could be efficient in Quatsomes membrane reducing drastically the quantum yield. On the other hand, the DiR has a larger aromatic structure, which could determine the increased number of non-radiative decay pathways in a polar environment or either the higher tendency to form non-fluorescent aggregates within the vesicles.

These important results show that thanks to the incorporation in Quatsomes membrane, water non-soluble dyes, such as the carbocyanines, can be successfully

dispersed in water, obtaining new FONs with good optical properties. A comparison can be made with the work of Wagh et al. [78], who incorporated DiD in PLGA-PEG-maleimide polymer nanoparticles (with size of 60 nm ca.), obtaining φ around 26% and ε around $1.8x10^5 M^{-1}$ cm^{-1} with a loading of 0.25 % w/w, really close to the values of D-QS-1 (whose loading in mass is 0.2 % w/w).

The photophysical properties of the cyanine-loaded Quatsomes can be compared with those of Cy3, Cy5 and Cy7 fluorophores [162, 163], which have the same chromophoric structures as DiI, DiD and DiR, respectively, but modified with sulfonate groups to achieve a higher water solubility (shown in Figure 3.7).

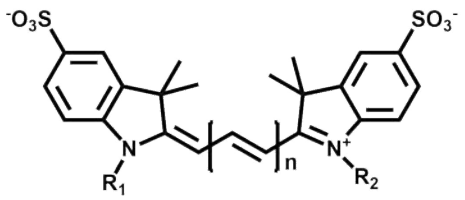

Cy3: n=1
Cy5: n=2
Cy7: n=3

Figure 3.7: Structures of Cy3, Cy5 and Cy7, water soluble analogues of the carbocyanines DiI, DiD and DiR, respectively

It must be remarked that, despite the similar chemical structures of the fluorophores, we are comparing photophysical properties of two physically different states. Thus, the data of Cy3,Cy5 and Cy7 refer to molecules dissolved in water, whereas, in the case of I-QS-1, D-QS-1, R-QS-1, the fluorophores are assembled with other compounds (i.e. cholesterol and CTAB) as FONs. As a matter of fact, the principle for achieving high brightness in dye-loaded FONs relies on confining a large number of dyes in a small space, thus strongly increasing their absorption coefficient, without drastically decreasing the fluorescence efficiency as effect of the aggregation-caused quenching [47]. By knowing the real number of fluorophore per nanoparticle, i.e. number of cyanines loaded in each Quatsomes, the extinction coefficient per particle ($\varepsilon_p = n \times \varepsilon$) can be calculated. Although measuring the real number of dyes per Quatsomes is not trivial, an estimation can be done and rough numbers can be calculated in order to make a comparison with some other FONs studied in literature and with quantum dots (QDs). Assuming that all the fluorophores in the system are distributed in a homogeneous manner over the entire population of Quatsomes (i.e. under the hypothesis that the distribution of dyes has not preferential pathways and all the nanoparticles have in average the same density of fluorophores in their membrane independently of their

size), the number n of fluorophores per particles can be calculated as $n = \frac{C_{cyanine,bulk,}}{C_{Quatsomes}}$, where $C_{cyanine,\ bulk}$ is the bulk concentration of the cyanine in each sample (measured as explained in Experimental Section 7.5) and $C_{Quatsomes}$ is the concentration of Quatsomes as measured by the Nanoparticle Tracking Analysis (NTA). As previously mentioned, the minimum size of organic nanoparticles detectable by NTA is around 40-45 nm, meaning that a relevant portion of Quatsomes population is not observed during NTA measurements. As consequence, the concentration of Quatsomes measured (generally between 10^{12} and 10^{13} particles/mL) is abundantly underestimated. Aware of this error, the estimated n for I-QS-1, D-QS-1 and R-QS-1 is around 10^2 fluorophores/Quatsomes. Thus, in Table 3.4, the extinction coefficients (ε) and brightness of the fluorophores, in the case of the Cy3, Cy5 and Cy7 in water solution, whereas in the case of DiI, DiD and DiR incorporated in Quatsomes, are compared. Moreover the absorption coefficients ($\varepsilon_p = n \times \varepsilon_f$) and the brightness ($\varepsilon_p \times \varphi$) of single cyanine-loaded Quatsomes are also estimated, as they give a more representative idea of the improvement in brightness of the cyanine-loaded Quatsomes compared to the cyanines molecules dissolved in water.

Table 3.4: Comparison of the photphysical properties of cyanine-loaded Quatsomes with those of Cy3, Cy5 and Cy7, water-soluble analogues of DiI, DiD and DiR

Sample	ϕ [a] %	ϵ [b] ($\times 10^5$) $M^{-1}\ cm^{-1}$	**Brightness** [c] ($\times 10^5$) $M^{-1}\ cm^{-1}$	ϵ_p [d] ($\times 10^5$) $M^{-1}\ cm^{-1}$	**Brightness** [e] $_p$ ($\times 10^5$) $M^{-1}\ cm^{-1}$
Cy3[f]	15	1.5	0.22	-	-
I-QS-1	20	1.15	0.23	115	23
Cy5[f]	28	2.5	0.7	-	-
D-QS-1	23	2.47	0.57	247	57
Cy7[f]	28	2	0.56	-	-
R-QS-1	3	2	0.06	200	6

[a] FLuorescence quantum yield ±10%. Measured as shown in Table 1.3
[b] Molar extinction coefficient at the maximum absorption wavelength of the fluorophore
[c] Brightness of the fluorophore calculate as $\epsilon \times \phi$
[d] Molar extinction coefficient at the maximum absorption wavelength of a single Quatsome, calculated as $n \times \epsilon$, where n is the estimated number of fluorophores per vesicle (details in the text)
[e] Brightness of a single fluorescent Quatsome calculate as $\epsilon_p \times \phi$
[f] Values of ϵ and ϕ extracted from the references shown in the text

Therefore, the values of ε_p (calculated as nxε) jump to values in the order of $10^7 M^{-1}$ cm^{-1}, similar to those of the most common quantum dots [2] and dye-loaded polymeric nanoparticles [47], which show values in the range 10^6-$10^8 M^{-1}$ cm^{-1}.

Generally cyanine dyes, especially NIR absorbing cyanines, fast undergo photodegradation. Photostability of fluorophores is therefore a fundamental parameter that determines the applicability of fluorescent dyes in laser technologies and imaging. Many studies exist in literature, for example, on the influence of substituents in the polymethine chains [164] as well as counter ions [165] and the effects on photodegradation mechanisms. In the present work, the photostability of DiD in EtOH and D-QS-1 were measured and compared to that of Cy5 in water, studied in literature [166].

We used a spectroscopic method, developed by Belfield and Bondar [142, 143], to determine the efficiency of photodegradation of the probes. Thus, photostability under continuous-wave excitation was in fact determined by measuring the photodegradation quantum yield PQY,

$$PQY = N_{mol}/N_{phot}$$

where N_{mol} is the number of bleached molecules and N_{phot} is the number of absorbed photons. The number of bleached molecules was determined by the kinetic decrease of the absorbance, under the assumption that the absorbance of photoproducts are negligible in the spectral region of the dye main absorption band [167]. Samples were placed in a cuvette and irradiated with a diode laser (λ_{exc}=660 nm; I=22 mW/cm^2) in such a way that the whole sample is simultaneously illuminated in order to exclude the influence of diffusion on photochemical process. Samples have not been de-gased before running the measurements. See Section 7.5.5 in the Experimental Part for further details.

In Figure 3.8 the absorbance variation of DiD in EtOH and D-QS-1 is shown in function of the irradiation time (absorbance has been normalized with respect to the initial absorbance value), while the value of the PQY are shown in Table 3.5. It is well established that cyanines undergo photodegradation by an oxidative mechanism, mainly via the formation of oxygen superoxide anion[168][167]. Although the solubility of oxygen in EtOH is higher than that in water, DiD is much more photostable when dissolved in EtOH than when incorporated inside QSs membrane. The PQY of D-QS-1 is in the same order of magnitude of the one reported for Cy5 [166].

However, the direct comparison between the photobleaching properties obtained is not straghtforward, being photostability very solvent dependent. We must be careful when comparing the photobleaching of a dye in an organic solvents with that in water, where generally rate of intersystem crossing to the triplet state (among the principal causes of dyes photobleaching) is higher [166]. In several cases, differences of order of

magnitude have been found in photostability of dyes in ethanol and water, as in the case of some rhodamines [169].

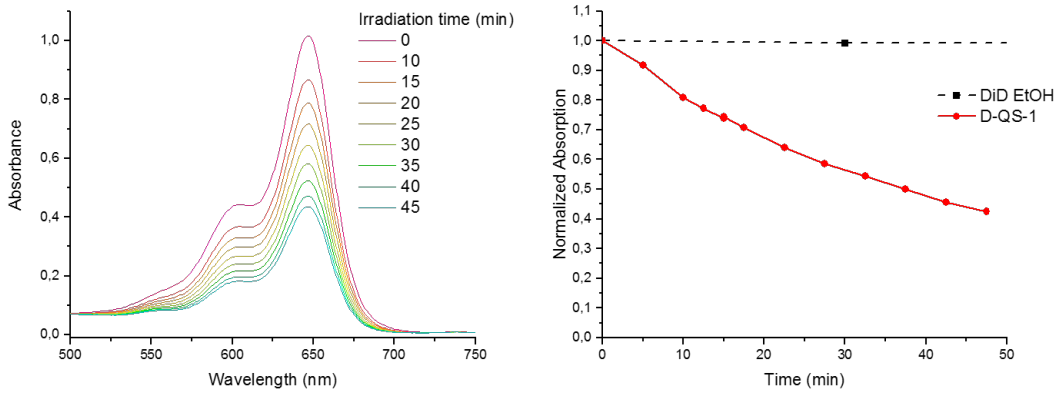

Figure 3.8: Left) Variation of D-QS-1 absorption upon laser irradiation (λ_{exc}= 660 nm, I=22 mW/cm^2). Right) Variation of the maximum absorbance with time of DiD in EtOH and of D-QS-1 in water

Table 3.5: Photodegradation Quantum Yield (PQY) of DiD in EtOH, D-QS-1 and Cy5 (from [166])

Sample	**Solvent**	**PQY[a]** $\times$ **10**$^{-5}$**
DiD	EtOH	<0.008
D-QS-1	Water	1.3±0.4
Cy5	Water	0.5[b]

[a] Photobleaching quantum yield, calculated as explained in Section 7.5.5. (λ_{exc}=660 nm, I=22mW/cm^2

[b] From ref 166

3.1.2 Influence of the preparation route on the optical properties of cyanines-loaded Quatsomes

In the previous Section of this Chapter the effect of the self-aggregation of cyanines (i.e. formation of dimers, H- and J-aggregates) on their optical properties has been discussed. Concerning the preparation of cyanines-based materials, controlling the self-aggregation of the dyes may have a dramatic effect on the optical properties of the obtained FONs.

Elizondo et al. [131] showed that the preparation method has a strong influence on the degree of components homogeneity of the membrane in self-assembled lipid

vesicles, both in liposomes and in cholesterol-CTAB Quatsomes. Analogously, in this Section, a sample of DiD-loaded Quatsomes (D-QS-2) has been prepared by different routes, in order to study whether the preparation method has an impact on the physicochemical and photophysical properties of the obtained FONs. There are different routes described in literature for the preparation of vesicles loaded with active compounds, referring especially to the preparation of liposomes. Among them, Thin Film Hydration (TFH), Sonication (SON) and Incubation (IC) are some of the most common [106].

As previously described, the DELOS-SUSP is a robust method for the production of multifunctional nanovesicles [117, 124, 131]. So, in this Chapter, the preparation of DiD-loaded QS by DELOS-SUSP, TFH, SON and IC methods is studied, making a comparison of the optical and morphological properties of the obtained samples. The different preparation routes are schematized in Figure 3.9 and described in details below.

The samples studied in this Section are listed in Table 3.6. The loading is expressed as the molar ratio: $moles_{DiD}/(moles_{chol}+moles_{CTAB})$. All the preparations have the same concentrations of CTAB and Cholesterol and similar loadings [L].

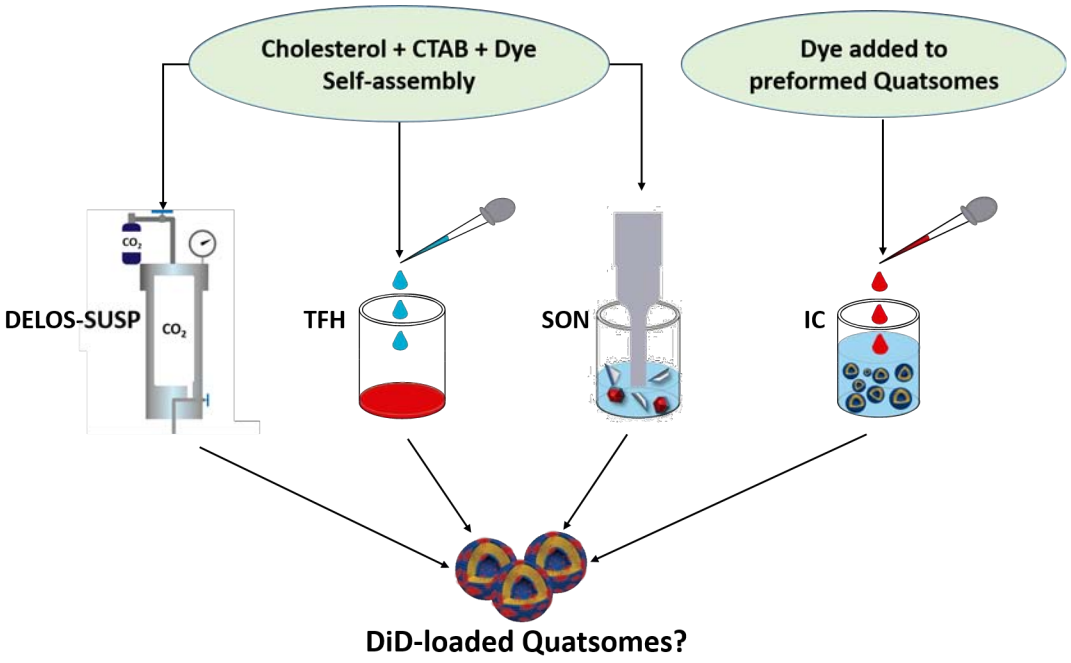

Figure 3.9: Schematic representation of the different preparation methods explored to optimize the dispersion of a dye (DiD) in Quatsomes membrane. From left to right: DELOS-SUSP, Thin Film Hydration (TFH), Sonication (SON) and Incubation (IC)

Table 3.6: List of D-QS-2 samples prepared by different method and corresponding compositions.

Sample	Preparation method	Components concentration mM	[L][a] $\times 10^{-3}$
D-QS-2	DELOS-SUSP	Chol: 7; CTAB: 7; DiD: 0.018	1.3
D-QS-2-TFH	Thin Film Hydration	Chol: 7; CTAB: 7; DiD: 0.02	1.4
D-QS-2-SON	Sonication	Chol: 7; CTAB: 7; DiD: 0.02	1.4
D-QS-2-IC	Incubation	Chol: 7; CTAB: 7; DiD: 0.02	1.4

[a] $[L]=moles_{DiD}/(moles_{chol}+moles_{CTAB}$. See Experimental Section 7.5.2 for details on determination of [L]

DELOS-SUSP method The DELOS-SUSP is a compressed fluid (CFs)-based procedure for the production of multifunctional small unilamellar vesicles (SUVs). In the last 25 years, several CFs-based methodologies for the preparation of nanostructured materials have been developed [114][115][116]. CFs exist as gas at normal conditions of pressure (P) and temperature (T), but can be converted into liquids or supercritical fluids increasing P. Concerning the production of nanomaterials, the solvation capacity of a CF (both in the liquid or supercritical phase) is one of the most important parameters. It can indeed be tuned by pressure changes, which propagate more quickly than temperature and composition variations. In this way, a fine control over the morphology of materials at the microscopic scale can be achieved, opposite to most of conventional processing techniques [117][118]. CO_2 is the most used compressed fluid in this sense, thanks to its low critical pressure (P_c=74 bar) and temperature (T_c=31°C), which allow working at mild conditions, with low production cost and reduced damage to the processed molecules. In addition to that, it is non-flammable, non-toxic, inexpensive and non-polluting, all properties that have made it as a green-substitute to conventional organic solvents for the preparation of nanomaterials.

On these principles, the procedure named Depressurization of an Expaned Organic Solution (DELOS), based on compressed CO_2, for the production of micron- and submicron-sized crystalline materials with high polymorphic purity has been developed [119, 120], where the entire work of this Thesis has been carried out. In that case, the driving force of the crystallization is the abrupt and extremely homogeneous temperature decrease produced by the evaporation (induced by a instantaneous depressurization) of CO_2, which was previously dissolved at a given working pressure (P_w) and temperature (T_w) in an organic liquid solution containing the compound to be crystallized. The rapid homogeneous temperature decrease produces a uniform supersaturation in the whole volume of the solution, promoting the nucleation process

in comparison with the competitive crystal growth process, thus favoring the formation of micro- and sub-micron sized particles with a narrow size distribution and superior structural homogeneity.

The DELOS process has been slightly modified, for the production of water dispersed systems, such as small unilamellar vesicles, e.g Liposomes and Quatsomes. The new method, named Depressurization of an Expanded Organic Solution-Suspension (DELOS-SUSP), allows the one-step preparation of multifunctional cholesterol-rich nanovesicles, including nanovesicles-bioactive hybrids [124, 125, 126]. A scheme of the DELOS-SUSP process for the formation of multifunctional nanovesicles is shown in Figure 3.10. In few words, a solution of the membrane lipid components and the non-water soluble compounds (e.g. cholesterol and non water soluble dyes) in an organic solvent (in this case ethanol) is loaded into a high-pressure autoclave, at the working temperature (Figure 3.10a). The reactor is then pressurized by addition of compressed CO_2 until reaching the working pressure (10 MPa), in order to obtain a CO_2-expanded solution of the compounds (Figure 3.10b). Finally, in the last stage, the vesicular structures are formed by depressurizing the CO_2-expaned solution over an aqueous phase, which contain the surfactant (e.g. CTAB) and any other water-soluble compound to be encapsulated (Figure 3.10c). In the final step, N_2 at the working pressure is added to the reactor to keep constant the pressure inside the autoclave during the depressurization. As effect of the depressurization, the CO_2-expanded solution experiences an abrupt and homogeneous temperature decrease (induced by the evaporation of CO_2) which likely is the cause of the high structural homogeneity in terms of composition, size and morphology of the obtained vesicles. Thanks to this, no further post-processing steps, generally required with the conventional methods of vesicles production, are necessary in order to reduce and homogenize the size of the formed vesicles.

It is important to highlight that during DELOS-SUSP the lipids that form the membrane and the actives to be incorporated are processed in solution in each stage of the preparation, in contrast to other conventional methods, such as Thin Film Hydration (see next paragraph). In the latter case, a solvent-free stage is involved [170], which can cause the de-mixing of membrane components responsible of the heterogeneity in the composition of the membrane. For instance, during the preparation of cholesterol-rich SUVs by TFH, domains of cholesterol can be formed, leading for example to an instability of the self-assembled structures [131, 170].

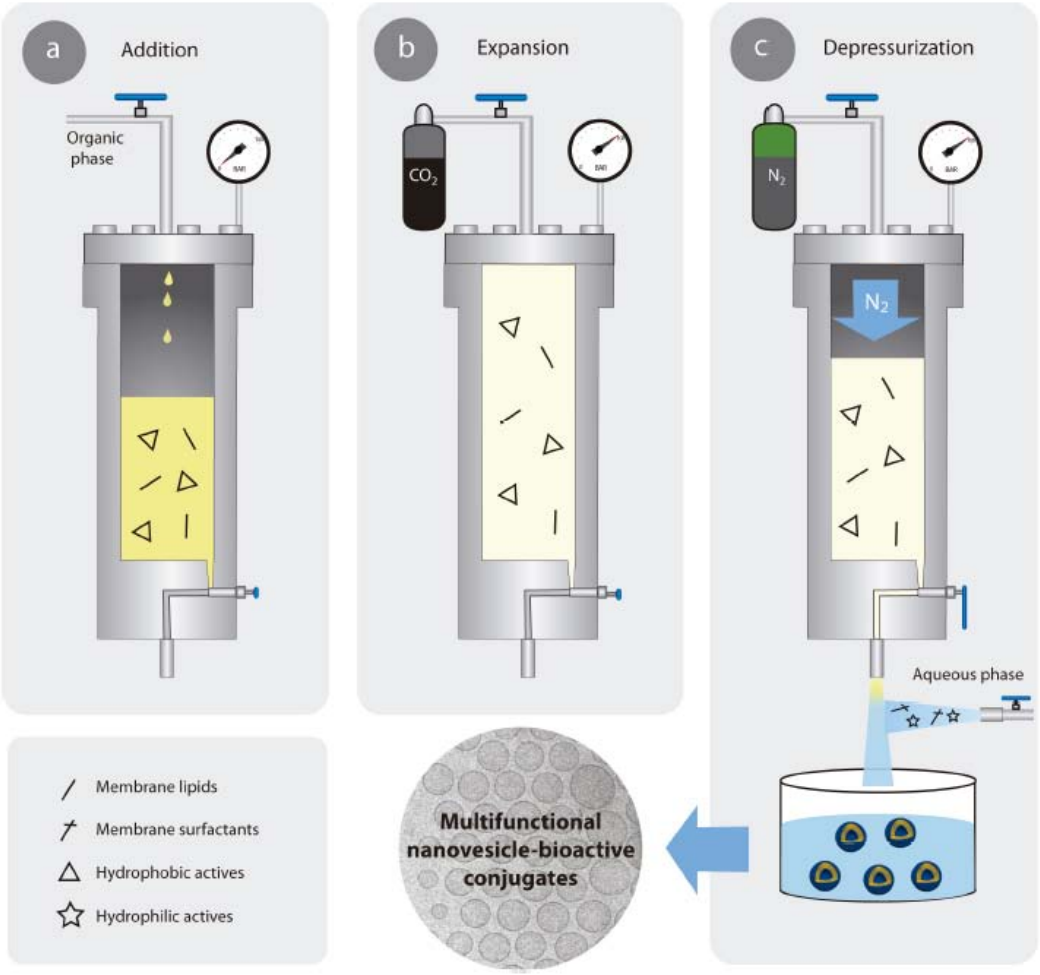

Figure 3.10: Schematic representation of the DELOS-SUSP process for the preparation of multifunctional nanovesicle-bioactive conjugates. The three stages of the process are described in the text.

For the preparation of D-QS-2 by DELOS-SUSP the configuration and procedure described in the Experimental Section 7.2.1 has been used. In few words, 111 mgr of Cholesterol were dissolved in 4.2 mL of a 0.2 mM solution of DiD in EtOH. The solution was then added to a high pressure vessel at atmospheric pressure and at T_w of 308 K. After 20 minutes the vessel was pressurized with CO_2 at the working pressure P_w of 10MPa. The reactor was kept at the working condition for one hour, in order to homogenize the system. The organic solution was then depressurized over 35 mL of Milli-Q water, where 100 mg of CTAB had been previously dissolved. During the depressurization, N_2 at P_w was used to keep constant the pressure inside the reactor.

Thin Film Hidration (TFH) TFH is a widely diffused method for the preparation of vesicles [106][85][171]. By TFH generally heterogeneous systems, concerning size and

lamellarity, are obtained and for this reason, post-processing steps, such as freeze-thawing [172][111], sonication[108] and extrusion [109] [110] are required in order to guarantee the reduction of vesicle size and the homogenization of the system. Apart of being time-consuming, these steps may affect the functionality of labile active molecules, e.g. labile drugs, loaded in the vesicles. This process has other several major drawbacks, including the involvement of the solvent-free state previously mentioned. Moreover, the large amount of organic solvents required is an issue, especially if the target is large scale productions.

For the preparation of D-QS-2 by TFH method, 28.3 mg of cholesterol, 25.5 mg of CTAB and 0.2 mL of a 1mM DiD solution in EtOH were mixed and dissolved in chloroform. Afterwards, the solvent was gently evaporated in order to form a thin film on the bottom of the flask and then placed under vacuum for 4 hours. Once dried, the film was hydrated at room temperature overnight using 10 mL Milli-Q water + 10 of EtOH (vol. %). In the conventional TFH method, ethanol (or any other organic solvents) is no added to the hydration step. However, for comparison to the DELOS-SUSP, the same amount of alcohol was added to the hydration medium. As the final step, the obtained DiD-loaded QS were downsized by sonication for 5 minutes. Detailed information about the TFH method are discussed in Section 7.2 of the Experimental Part.

Sonication (SON) Dr. Lidia Ferrer-Tasies showed in her Doctoral Thesis [130] that a homogeneous population of Quatsomes (Chol-CTAB 1:1 molar ratio) can be also obtained by a simple sonication step. For this reason, the same method has been used in this Thesis for the preparation of D-QS-2-SON. So, 28.3 mg of cholesterol and 25.5 mg of CTAB were weighted in a vial. 9 mL of MilliQ water and 1 mL of a solution 0.2 mM of DiD in EtOH were then added to the mixed solids. The resulting dispersion was then sonicated (at 20kHz) at room temperature using a titanium probe for 8 minutes. No further steps were required. Details on SON are given in Section 1.2.2.2 of the Experimental Part.

Incubation (IC) This method is the one proposed by Thermofisher for labeling the membrane of cells with the carbocyanines. The manufacturer suggests to prepare a solution of the probe (in DMF, DMSO or EtOH) and then to add to the cell culture. In our case 0.2 mL of a 1 mM solution of DiD in EtOH were added to a suspension of 9.8 mL of preformed QSs, in Milli-Q + 10 of EtOH (vol. %) and then incubated for 24 hours under gentle agitation. During the incubation time the UV-vis absorption spectra of the sample was monitored and some precipitation of DiD was observed. The UV-vis absorption spectrum and the cryoTEM images shown in this work have been acquired after two

hours of incubation.

All the samples, except the one prepared by IC, were purified by Diafiltration, as explained in Experimental Part 1.2.3.

3.1.2.1 Influence of the preparation route on the optical and morphological properties of DiD-loaded Quatsomes

As showh in Figure 3.11, the bandshape of the normalized UV-vis absorption spectra of D-QS-2 changes drastically depending on the preparation route. Thus, DiD in EtOH solution (dashed grey line) is characterized by a narrow peak (centered at 647 nm) and a shoulder at 605 nm, with some minor absorption bands which appear in the blue edge of the peak (around 550 nm). The UV-vis absorption spectra of D-QS-2, prepared by the DELOS-SUSP method, and D-QS-2-TFH (both almost overlapped) are very similar to the bandshape of the probe dissolved in EtOH, excluding almost completely the presence of any aggregates of the probe in the membrane. The marginal variations, at 603 nm and shorter wavelenghts, can be ascribed both to the minor presence of aggregates/dimers or to variations of the local environment. On the other hand, D-QS-2-SON and D-QS-2-IC show relevant increments in the bands at 550 nm and 600 nm, attributed to the presence of H-aggregates and dimers of DiD respectively [70, 153], and a general broadening of the whole absorption spectrum. According to this result, the formation of self-aggregated structures of DiD is almost completely avoided by DELOS-SUSP and TFH methods, both based on the simultaneous self-assembly of the three compounds leading to the dispersion of isolated monomers of DID into a double layer membrane.

In accordance to CryoTEM images of D-QS-2 prepared by the four different routes (shown in Figure 3.12), all the samples show a homogeneous distribution of unilamellar vesicles except for D-QS-2-TFH (Figure 3.12,c) which, in absence of freeze-thaw and extrusion post-preparation steps, evidences the presence of multilamellar structures along with some distorted vesicles and crystals, likely of precipitated cholesterol.

In conclusion, the DELOS-SUSP method was found to be the best route to get a dispersion of isolated DiD molecules inside QSs bilayer in a one-step preparation route. The same result can be obtained by the commonly used TFH, although cryoTEM images evidence that without further post-processing steps, the suspension obtained by DELOS-SUSP is much more homogeneous in terms of size and lamellarity of the vesicles.

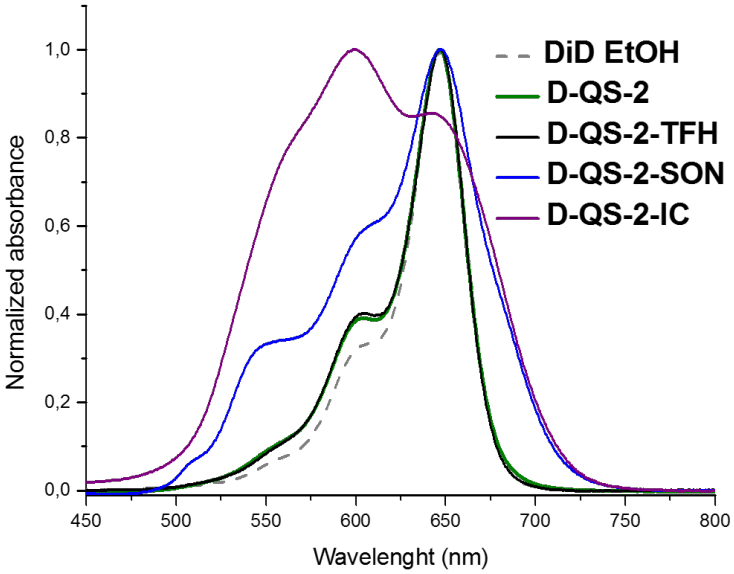

Figure 3.11: Normalized UV-vis absorption spectra of D-QS-2 prepared by different routes: DELOS-SUSP (green line), Thin Film Hydration (black line), Sonication (blu line), Incubation (purple line). The absorption spectrum of DiD in EtOH (grey dashed line) is plotted for comparison.

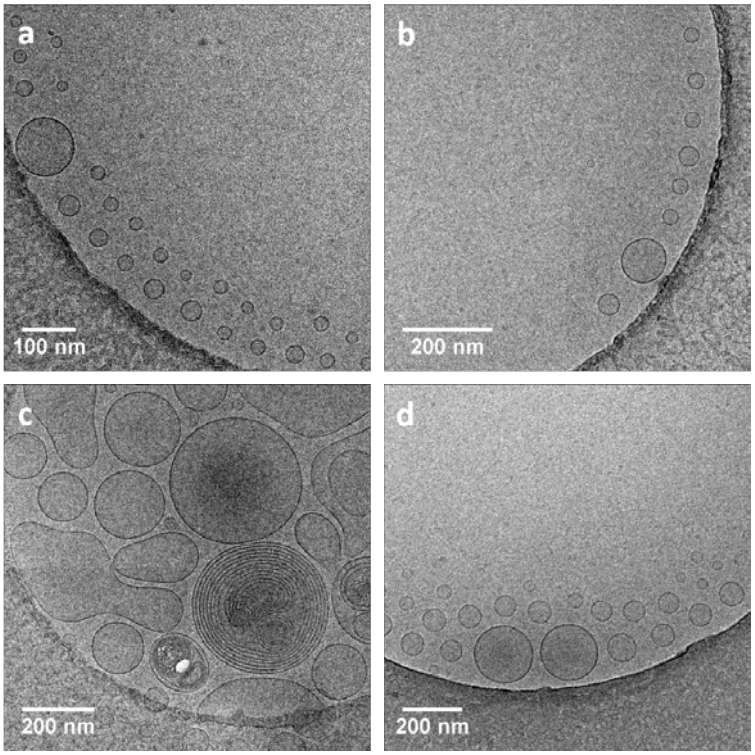

Figure 3.12: CryoTEM images of DiD-loaded QSs prepared by different methods: a) D-QS-2, b) D-QS-2-SON, c) D-QS-2-TFH, d) D-QS-2-IC

3.1.3 Molecular Dynamic (MD) simulations of cyanines-loaded Quatsomes

In the previous Sections, it has been shown that a family of non-water soluble fluorophores, the carbocyanines (DiI, DiD and DiR) can be stabilized in aqueous media by mean of their incorporation inside Quatsomes, obtaining a new class of FONs with excellent optical and colloidal properties. Moreover, a critical evaluation of the preparation methodology showed that a homogeneous dispersion of monomers of the probe inside the bi-layer is obtained only by the simultaneous self-assembly of the three compounds (cholesterol-CTAB-cyanine), *via* DELOS-SUSP.

In order to determine the correlation between the optical properties of cyanines-loaded Quatsomes and the interaction between the fluorophores and the bi-layer of the vesicles, Molecular Dynamics (MD) simulations have been run on Quatsomes loaded with DiI and Quatsomes loaded with DiD. All simulations were conducted by Silvia Illa, at Jawaharlal Nehru Centre for Advanced Scientific Research (JNCASR, India) and Dr. Jordi Faraudo, at the Institut de Ciència de Materials de Barcelona (ICMAB-CSIC).

In the case of DiI-loaded Quatsomes, two different simulations, S5 and S6, have been performed, as schematized in Figure 3.13, with details listed in Table 3.7. Both simulations try to mimic the experimental procedures used for the incorporation of DiI into the membrane. Simulation S5 imitates the process occurring in the preparation method of IC, while the simulation S6 that of the DELOS-SUSP. In the case of DiD-loaded Quatsomes, only one simulation (S7), analogue to the S6 simulation, has been performed, in order to explore whether the length of the conjugated chain of the dye has an impact on the dye disposition within the bilayer. Further information on MD simulations, such as protocols and parameters, can be found in Appendix 2.

S5 takes into account the DiI molecule outside the membrane, so it corresponds to an experimental setup in which I-QS is prepared by adding the dye to preformed Quatsomes, equivalent to the preparation of cyanine-loaded Quatsomes by incubation (IC). In order to do that, the molecule is added on the top of the simulation box and then solvated by water. On the other hand, in the S6 simulation, the DiI is inserted into the bi-layer and this configuration is the starting point of the simulation. So, S6 corresponds to an experimental setup in which I-QS exists with the dye already inserted in the membrane, i.e. the DiI is incorporated in Quatsomes during the formation of the membrane, corresponding to the preparation by DELOS-SUSP.

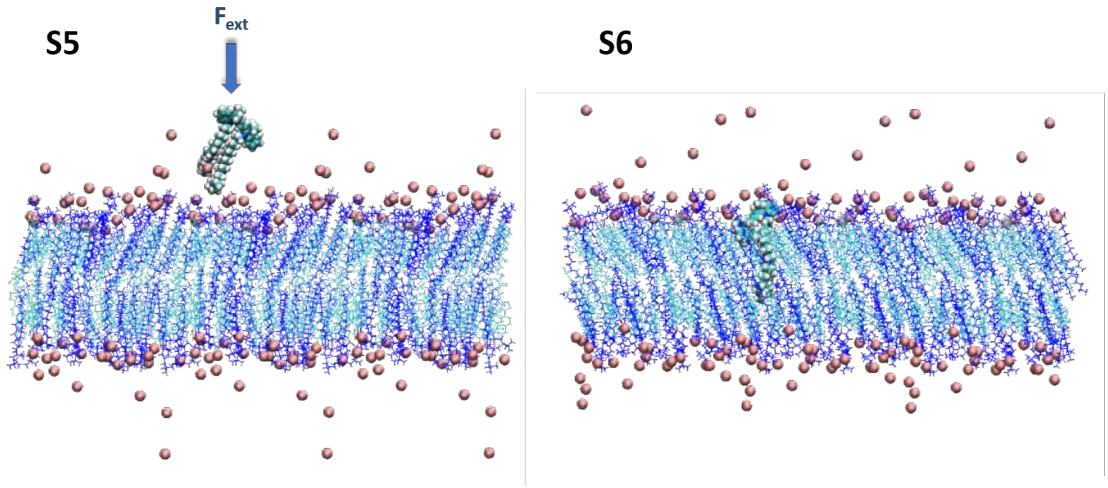

Figure 3.13: Scheme of the MD simulations mimicking the experimental procedures for the incorporation of DiI into the membrane of Quatsomes. Left) Snapshot of the starting point of S5 simulation. DiI is added to a pre-formed membrane of Quatsomes (analogously to the preparation by IC) and forced, by applying F_{ext}, to move towards the surface of the membrane. Right) Snapshot of the starting point of S6 simulations. A DiI molecule is inserted in the membrane at the moment of formation of the bilayer, analogue to the self-assembly occurring during the preparation by DELOS-SUSP. Dark blue: CTAB; light blue: cholesterol.

Table 3.7: Computational details for the simulations (S5 and S6) run on DiI-loaded QS and S7, run on DiD-loaded QS.

Simulation	Atoms (total)	Number of molecules DiI/water/CTAB	Simulation time /ns
S5	26946	1/6463/54	12
S6	26946	1/6463/54	90
S7	26848	1/6429/54	90

In the case of S5 simulation, the DiI molecule is surrounded by water on the top of the simulation box and it is free to move. Despite its hydrophobic character, the molecule is not attracted at all by the bi-layer of Quatsomes. In order to "push" the DiI molecule inside the membrane, a 1 ns SMD simulation was run, which allowed the application of an external force to the system. A force equal to 1573.77 pN was then applied to the center of mass of the DiI, forcing its movement toward QS surface (only in z direction), as schematized in Figure 3.13, S5. Afterwards, a 1 ns NPT simulation with superficial tension equal to 0 was applied, expecting the diffusion of DiI inside the membrane. Curiously, we found out that the molecule straightly bounced from the surface of the vesicle to the top of the simulation box. Accordingly to these results, it is not possible to insert the DiI to

Quatsomes just by addition of the molecule to a pre-formed vesicle, as experimentally observed in Section Section3.1.2.

On the other hand, DiI is stably anchored to the membrane in S6 simulation during the entire simulation time (90 ns). As mentioned in the introduction to this Chapter, the carbocyanines are widely used as cell membrane labels, thanks to the penetration of the two aliphatic chains into the membrane and thus stably anchoring the probe, as described in the manufacturer (ThermoFisher) webpage. The simulation S6 confirms that, when self-assembled with cholesterol and CTAB, the carbocyanines (DiI in this case) are anchored by the same mechanism to the membrane of Quatsomes, as schematized in Figure 3.14 .

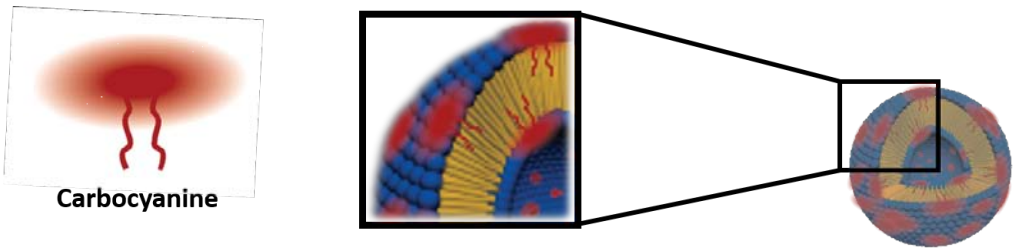

Figure 3.14: Schematic representation of the interdigitation of alkyl tails of the carbocyanines into the membrane of Quatsomes.

The C_{18} alkyl tails of the fluorophore are inserted (as a "hairpin") inside the bi-layer while the polar chromophore of the dye stays partially in contact with water. To support this result, the density profile of the main atoms in the system in function of the distance from the center of the bi-layer (z direction, perpendicular to the membrane) was simulated and the obtained results are shown in Figure 3.15

The nitrogen atom of DiI (blue solid line in Figure 3.15), located in the chromophore of the dye stays partially in contact with water (cyan solid line) and it is positioned really close to the nitrogen of the surfactant (solid red line), where it stays for the whole duration of the simulation. The density distribution of the carbon atoms of the alkyl chains of DiI (green dotted line) show that these tails are located inside the bi-layer, similarly to the carbons of the CTAB.

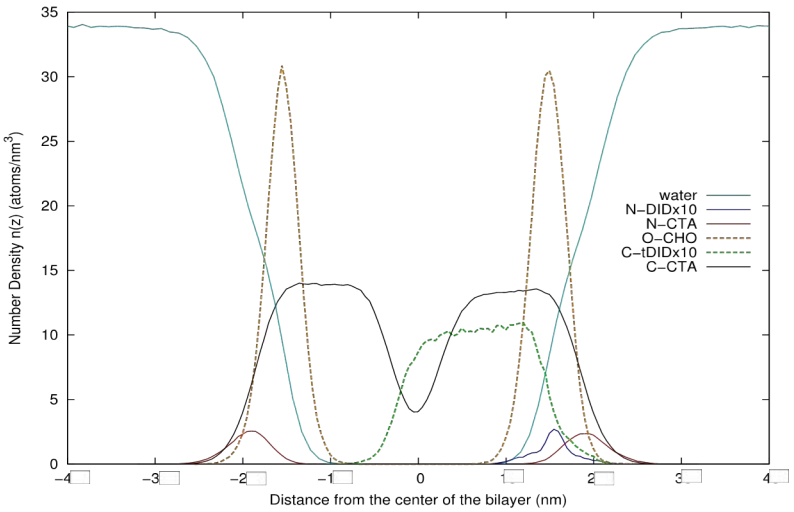

Figure 3.15: Average density profile of atoms of DiI-QS as a function of z coordinate (perpendicular to the membrane). Solid cyan line: water density; solid blue line: nitrogen atoms of DiI; solid red line: nitrogen of CTAB; orange dashed line: oxygen atoms from cholesterol; green dashed line: carbon atoms from DiI; black solid line: carbon atoms of CTAB.

MD simulations have been also employed to study how the molecules move around in Quatsomes membrane, i.e. to study their diffusion movements and calculate the diffusion coefficients. Diffusion of DiI within the membrane was observed during the S6 simulation. Therefore, it was considered interesting to study how the DiI diffuses inside QSs membrane and compare its diffusion coefficient (D) with that of CTAB . In order to calculate D, an atom of interest must be selected and, by calculating the mean square displacement (MSD), the diffusion coefficient for that particular atom can be calculated. In the case of DiI, the atom corresponding to the center of mass of the chromophore (a carbon atom) has been selected. Temperature (298 K) and pressure (1 atm) has been maintained fixed during the simulation.

Mean square displacement (in $Å^2$) in function of time (ps) is shown in Figure 3.16 along x (left) and y (right) directions respectively . The diffusivity coefficients, along the two directions, can be calculated as the mean slope of the graphs. The diffusivity is only measured along x and y because the molecules constituting the vesicles can not diffuse in Z direction (perpendicular to the membrane) otherwise they would cause the rupture of the vesicle.

In Table 3.8 the diffusivity values of the DiI, CTAB and water molecules are expressed in cm^2/s. The atoms selected to calculate diffusion coefficients are the hydrogen of the methyl group located at the end of the C_{18} tail, for CTAB, and, for water, the oxygen atom of a random selected molecule. For comparison, diffusivity of phospholipids from Ref. [173] are also listed in the Table 3.8. The diffusion coefficients of CTAB in absence of DiI

is also reported to check if the incorporation of the dye has any effect on the diffusion.

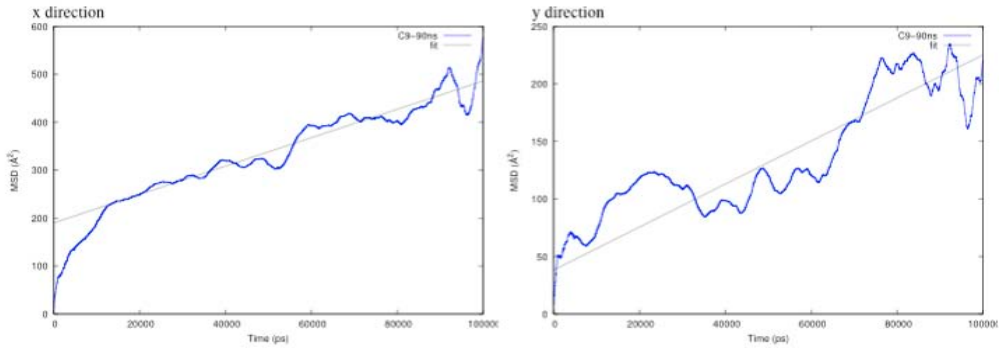

Figure 3.16: Mean square displacement (MSD) in function of time of the carbon atom in the center of mass of DiI chromophore

Table 3.8: Diffusion coefficient of DiI, CTAB, CTAB in Quatsomes in absence of DiI, water and phospholipids [173]

Molecule	**Diffusion coefficient** $(cm^2/2) \times 10^{-7}$
DiI_x	2.9
DiI_y	1.8
$CTAB_x$	4.6
$CTAB_y$	5.2
$CTAB_x^a$	4.08
$CTAB_y^a$	4.23
Water	500
Phospholipids[b]	1

[a] Diffusion coefficient of CTAB in absence of DiI
[b] See reference in the text

The DiI diffuses in both directions in a similar way to CTAB, with diffusion coefficients of 10^{-7} cm^2/s in both cases. The values in the Table 3.8 show as well that the diffusivity of CTAB in absence of DiI does not vary much with the values in presence of the dye. On the contrary, the diffusivity of water is much higher than that of molecules in Quatsomes, which is reasonable considering that the molecules forming the bilayer are tightly laterally packed in the membrane. Finally, the diffusion coefficients of Quatsomes components are of the same magnitude of the one of phospholipids present in living cells, which are known to be fluid bi-layers. This suggest that the bi-layer of Quatsomes behaves as a fluid membrane, which is in line with results found by Dr. Lidia Ferrer-Tasies in her PhD

dissertation, where she investigated the liquid-ordered phase behaviour of cholesterol-CTAB Quatsomes membrane.

The results from the MD simulation run in the case of DiD-loaded Quatsomes are not shown, since only negligible differences are present in the disposition of DiD within the membrane, in comparison with DiI. Also in this case, the aliphatic chains of the DiD are immersed inside the hydrophobic core of QSs, with the chromophoric portion of the molecule which stays almost parallel to the interface with water. The diffusion coefficients of DiD, when inserted in the bilayer, are similar to those of the DiI.

3.1.4 Comparison of DiD-loaded Quatsomes (D-QS) with other DiD-based FONs: DiD Nanoparticles (D-NP) and DiD-loaded CTAB micelles (D-MIC)

As extensively explained in the Introduction, several strategies exist in order to disperse non water-soluble fluorophores in aqueous media. The formation of nanoparticles (NPs) based on self-assembly of π-conjugated systems is a widely used method [52][58], especially for systems presenting aggregation induced emission (AIE) [60], which allows high concentration of fluorophores without encountering the usual quenching effects. Among others, incorporation in micelles is another commonly used strategy in order to overcome solubility issue of chromophores and increase their practical application in microscopy [66, 174, 175].

Hence, in this Section these strategies have been explored, preparing CTAB micelles loaded with DiD (D-MIC) along with DiD nanoparticles (D-NP), made only of pure DiD suspended in water. Thus, the optical and colloidal properties of DiD-loaded Quatsomes (D-QS-2) will be compared to D-NP and D-MIC. The three different studied structures are schematized in Figure 3.17.

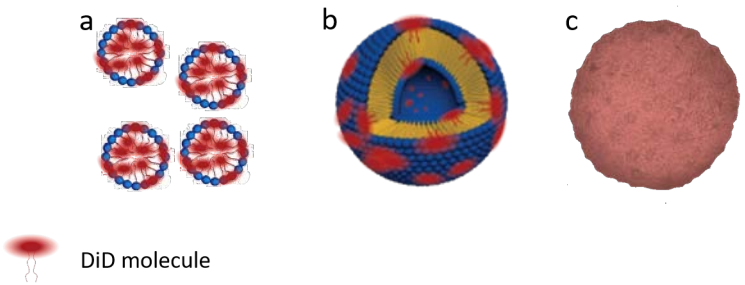

Figure 3.17: Schematic representation of the different DiD-based FONs studied in this section: a) DiD-loaded CTAB micelles (D-MIC); b) DiD-loaded Quatsomes (D-QS-2); c) DiD nanoparticles (D-NP)

3.1.4.1 Preparation of the different DiD-based FONs

D-QS-2 was prepared by DELOS-SUSP, as explained in Section3.1.2.

D-MIC was prepared using as well the DELOS-SUSP configuration, shown in Experimental Section 7.2.1. Thus, for the preparation of D-MIC, 4.2 mL of a 0.2 mM DiD solution in EtOH were added to the high pressure vessel at atmospheric pressure and T_w (T_w=308 K). Afterwards the vessel was pressurized with CO_2 until reaching the working pressure P_w of 10MPa. After one hour, the CO_2-expandend solution of DiD was depressurized over 35 mL of Milli-Q water, in which 100 mg of CTAB were previously dissolved.

D-NP was prepared by two different methods, by DELOS-SUSP (D-NP_{DS}) and by the common reprecipitation method (D-NP_R). In the case of D-NP_{DS}, 4.2 mL of a 0.5 mM DiD solution in EtOH were loaded into the reactor at T_w and then CO_2 was added until reaching P_w. After one hour, the depressurization was performed over 95.8 mL of Milli-Q water. To prepare D-NP_R, a 1 mM solution of DiD in EtOH was filtered using a Teflon filter with pores size of 220 nm. 100 μL of the filtered solution were then dropped in 9.9 mL of Milli-Q water at room temperature under vigorous stirring for 1 hour.

The composition of the samples studied in this Section are listed in Table 3.9. In order to properly compare D-QS-2 and D-MIC, the two samples have been prepared maintaining the same molar ratio between the dye and the CTAB.

Table 3.9: List of the different DiD-based FONs studied in this section

Sample	Preparation method	Molar ratio DiD/CTAB $\times 10^{-3}$
D-QS-2	DELOS-SUSP	2.6
D-MIC	DELOS-SUSP	2.8
D-NP_{DS}	DELOS-SUSP	-
D-NP_R	Reprecipitation	-

3.1.4.2 Comparison of the optical and colloidal properties of the different DiD-based FONs

The morphology of D-QS-2 and D-NP_{DS} one day and one week after their preparation is shown in cryoTEM images of Figure 3.18. In the case of D-NP_{DS} TEM microscopy was employed, in contrast with D-QS-2 micrographs, acquired by cryoTEM microscopy, due to the low concentration of nanoparticles. Further details on the acquisition of TEM and cryoTEM images are given in Experimental Section 7.4.3.

The size distributions and colloidal stability of D-QS-2 and D-NP_{DS}were monitored by Nanoparticle Tracking Analysis (NTA) over two months (for D-QS-2) and three weeks (for D-NP_{DS}) and the resulting values are listed in Table 3.10.

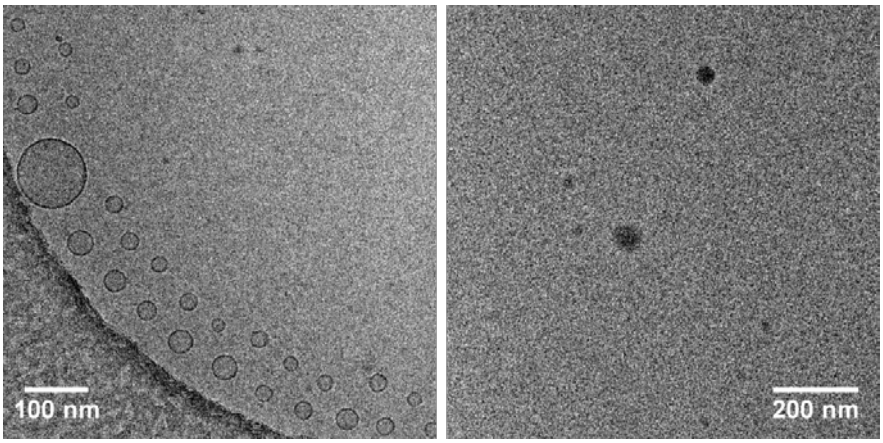

Figure 3.18: Left) cryoTEM image of D-QS-2 one week after the preparation. Right) TEM image of D-NP_{DS} one day after the preparation. Uranyl acetate was used as contrast agent for the acquisition of the images of D-NP_{DS}.

Table 3.10: Physicochemical properties of D-QS-2 and D-NP_{DS}, measured by NTA, over the examination period (two months for D-QS-2 and three weeks for D-NP_{DS}).

Sample	**Initial Size[a] nm**	**Final Size[b] nm**
D-QS-2	105±34	101±51
D-NP_{DS}	78±36	112±52

[a] Size measured by NTA at the beginning of the examination period corresponding to one week and one day after preparation for D-QS-2 and D-NP_{DS}, respectively

[b] Size measured by NTA at the end of the examination period corresponding to 2 months and three weeks after preparation for D-QS-2 and D-NP_{DS}, respectively

As previously commented in Section3.1.2.1, D-QS-2 constitutes of a population of SUVs which maintains their size over two months, confirming the colloidal stability of DiD-loaded Quatsomes. TEM images of D-NP_{DS} (Figure 3.18, right) one day after preparation show that this sample contains round-shaped particles with size of less than 100 nm, in agreement with the values given by NTA (mean size around 80 nm). However,

while no variation in size has been detected in D-QS-2 over two months, mean size of D-NP_{DS} grows of 43% ca. over three weeks, likely as effect of aggregation of the nanoparticles. Moreover solid precipitated on the wall and bottom of the vial containing D-NP_{DS} was observed at the end of the examination period, evidencing that D-$NP_{DS}$is an unstable colloidal phase.

As explained in the Introduction of this Chapter, the spectral characteristics of cyanines change drastically depending on their supramolecular organization, i.e. their aggregation state. For this reason we compared the absorption, excitation and emission spectra of D-NP_{DS} and D-QS-2 with those of DiD dissolved in EtOH (Figure 3.19).

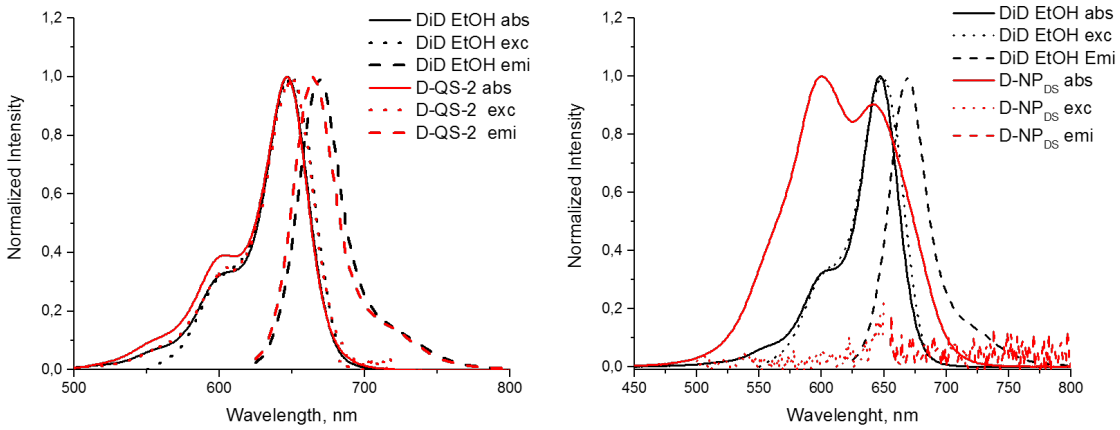

Figure 3.19: Left) Normalizd UV-vis absorption, excitation and emission of D-QS-2 and DiD in EtOH. Right) Normalized UV-vis Absorption, excitation and emission of D-NP_{DS} and DiD in EtOH

The presence of dimers and aggregates of DiD in D-QS-2 can be safely excluded, as shown by the overlap of the absorption bands of the DiD in EtOH and D-QS-2 (explained in Section3.1.2.1). On the other hand, the absorption spectrum of D-NP_{DS} (Figure 3.19, right), indicates a strong contribution of species like dimers (peak at 600 nm) and H-aggregates (peak at 550 nm) [70, 153]. As previously mentioned, these aggregates are not luminescent and in fact no peaks at all are detected in the excitation nor in the emission spectra, suggesting that the fluorescence of DiD in D-NP_{DS} is totally quenched. The comparison between the emission properties of these two supramolecular organizations of DiD, D-QS2 and D-NP_{DS}, highlights the importance of the supramolecular structure on the optical properties of fluorescent probes. Summarizing, in the case of carbocyanines, like the DiD, the self-aggregation induced by DELOS-SUSP in order to obtain D-NP_{DS} lead to the formation of structures mainly constituted of non fluorescent aggregates of the dye (dimers and H-aggregates). So, in order to obtain a photoluminescent dispersion of DiD in water, it is necessary to disperse the fluorophores

as monomers in a matrix, like in the case of Quatsomes membrane.

The optical stability of D-QS-2 has been monitored by acquiring absorption and emission spectra over two months, Figure 3.20 (left). In a similar manner, the optical stability of D-NP_{DS} has been monitored by acquiring the absorption spectra over two weeks (Figure 3.20, right).

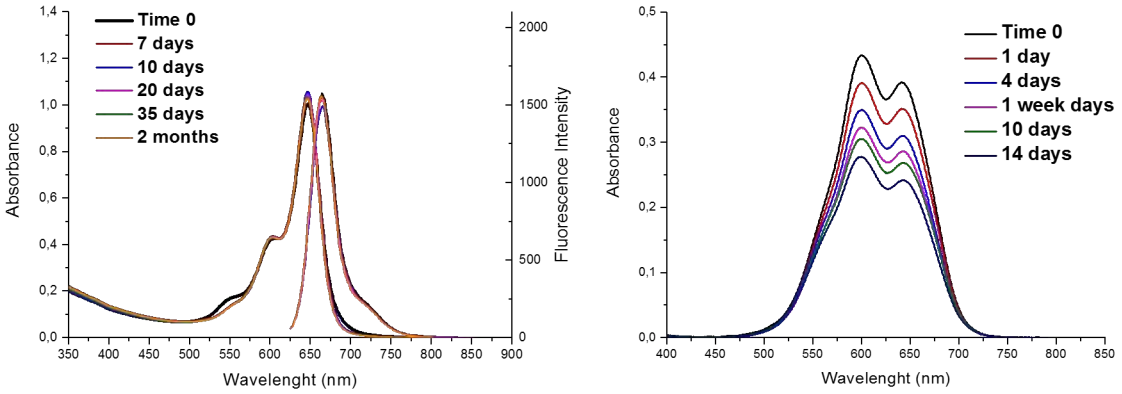

Figure 3.20: Left) Optical stability of D-QS-2 over two months evaluated by UV-vis and emission spectroscopy. Right) Stability of D-NP_{DS}over two weeks, monitored by UV-vis spectroscopy.

After an initial reorganization of the dye, where some aggregates seem to disappear (band at 550 nm in the absorption black curve), the absorption and emission of D-QS-2 are maintained over time. This proves the chemical stability of the dye once inserted in QSs membrane. Moreover it shows that there is no release of the DiD to the surrounding media over time and hence the fluorophore stays stably anchored to the membrane of the vesicles. On the other hand, although D-NP_{DS} absorption spectra maintain the same shape over two weeks, the continuous decrease of the intensity reflects the aggregation and finally precipitation of the nanoparticles, as already confirmed by NTA.

Even if only D-NP_{DS} has been described in this Section, results of D-NP prepared by reprecipitation (D-NP_R) were very similar, suggesting that colloidal and optical properties of aggregates of DiD in water are independent of the preparation method.

In diagnostics and theranostics applications, where FONs are generally employed, dilutions of the nanoparticles in large volumes of cell cultures or body fluids generally occur. For this reason, the stability of the FONs to dilution is a critical parameter in order to validate their possible *in vivo* and *in vitro* applications.

The colloidal properties of Quatsomes have been deeply studied during the PhD Thesis of Dr. Lidia Ferrer Tasies [130] where she found that these structures are

thermodynamically stable. In addition, it has been observed that QSs are much more stable to dilution than the correspondent micelles made by the CTAB, as occurred for example in the case of water dispersions of silicon nanocrystals (SiNCs). CTAB is a quaternary ammonium surfactant, which self-assembly into spherical micelles with a diameter of 2-3 nm at concentration higher than the critical micellar concentration (CMC, 1 mM ca.)[176][177]. They are generally formed by 60-70 molecules of CTAB (in de-ionized water at concentration slightly higher than CMC) [178] and undergo rupture if diluted below the CMC. When SiNCs were dispersed using Quatsomes, dilution occurring during dialysis, necessary for the purification of the samples, did not affect the structure of Quatsomes. Oppositely, when SiNCs were dispersed by CTAB micelles, multiple dilution lead to the rupture of these structures and instability of the SiNCs water dispersion.

Hence, the stability upon dilution of D-QS-2 and D-MIC (see Table 3.9) were compared by monitoring their absorption and emission at concentrations higher and lower than the CMC of CTAB. So, absorption and emission were monitored by diluting with Milli-Q water both samples at concentrations above (1.58xCMC) and below (0.3xCMC and 0.1xCMC) the CMC of CTAB in water (CMC=1 mM). Emission spectra were divided by the absorbance at the excitation wavelength (λ_{exc}= 610 nm), in order to have an estimation of the real brightness of the samples at the different dilutions.

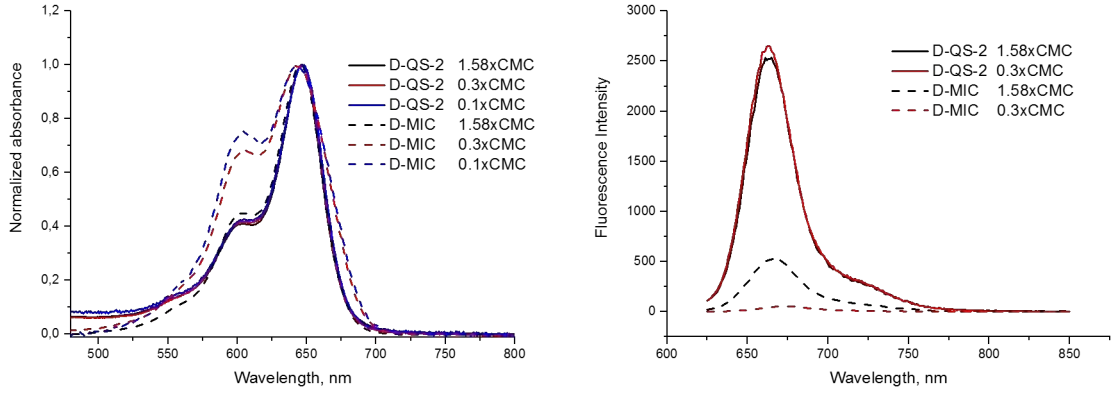

Figure 3.21: Left) Stability upon dilution of D-QS-2 and D-MIC, measured by absorption. Right) emission divided by the absorption at the excitation wavelenght(λ_{exc}= 610 nm)

At concentrations higher than CMC (1.58xCMC), it is possible to notice that, although no H-aggregates neither dimers of DiD are detected in the D-MIC sample (the absorption spectrum closely resemble the one of the DiD in EtOH solution). Moreover, D-QS-2 is much brighter than micelles containing DiD (5 times brighter ca., as shown by

the values of the emission intensities normalized by the absorption at the excitation wavelength). The surprising difference in brightness, due to the sensible quenching of DiD when incorporated in CTAB micelles, could be caused by π-π interactions as effect of the close proximity between the chromophores inside the small micelles (which have diameters of 2-3 nm, so much smaller than QSs).

The stability of Quatsomes upon dilution is verified as well in this case, since no changes in absorption are in fact detected and the sample maintains its brightness even at concentrations of CTAB lower CMC (emission spectrum of DiD-QS 1.58xCMC is exactly overlapped to the one at 0.3xCMC). On the other hand, emission of D-MIC diluted to concentrations below the CMC (up to 0,3xCMC) is completely quenched (almost no signal from the emission spectrum). This is likely due to the partial rupture of the micelles and the consequent release to the DiD to the aqueous environment, where the fluorophore starts to aggregates, as shown by the absorption spectra of DiD-CTAB 0,3xCMC and 0,1xCMC, with the appearance of a relevant band at 600 nm.

3.1.5 Effect of the cyanines-loading on optical and colloidal properties of Quatsomes-based FONs

One of the advantages of the dye-doped organic nanoparticles is that each nanoparticle can incorporate many fluorophore molecules, providing a much amplified optical signal than the single fluorophore [32]. Unfortunately, as already explained in the Introduction, fluorophores molecules that are trapped in a matrix, if sufficiently close, experience strong π-π interactions, that can lead to a severe quenching of the fluorescence, a phenomenon known as aggregation-caused quenching (ACQ). In the case of carbocyanines, it has already been shown in literature [78] that emission of DiD and DiR, when encapsulated in polymeric nanoparticles at high loading, is strongly quenched.

In order to study how the fluorophore loading, [L], affects the properties of cyanines-loaded Quatsomes, different samples of DiD-, DiI- and DiR-loaded Quatsomes have been prepared, each one with a different loading, defined (see Experimental Section 7.5.2) as the molar ratio between the probe and QSs membrane component ([L]= $moles_{probe}/(moles_{chol}+moles_{CTAB})$. In this way, the same number of vesicles in every batch is likely obtained, but each one contains a different number of fluorophores per vesicle.

A schematization of cyanines-loaded Quatsomes with different loading is represented in Figure 3.22

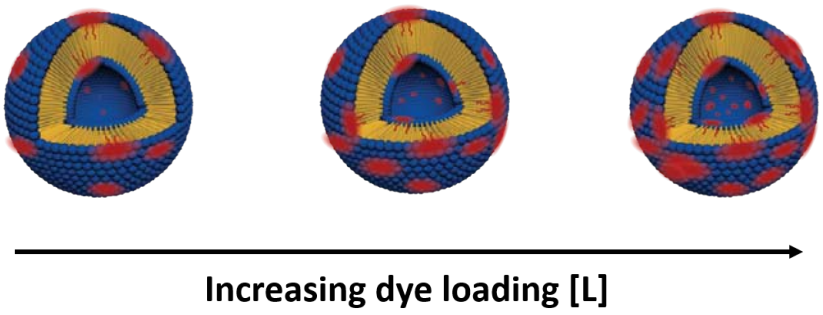

Figure 3.22: Schematic representation of cyanines-loaded Quatsomes at increasing loading

3.1.5.1 Effect of fluorophore loading on colloidal and optical properties of DiD-loaded Quatsomes (D-QS)

Five different samples of DiD-loaded Quatsomes with different loadings have been prepared by DELOS-SUSP (see Experimental Section 7.2.1). The samples are listed in Table 3.11, along with the mean size one week and two months after their preparation, measured by NTA (see Experimental Section 7.4.2).

For each sample two or three batches have been prepared, to check the reproducibility of results. Only minor differences have been detected in all the cases. Samples have been stored for one week (4°C) before analysis. NTA data show that all the samples are composed of a dispersion of nanovesicles, with hydrodynamic diameter of 100 nm ca. irrespective of the loading of DiD, which maintain their mean sizes over two months.

Table 3.11: List of DiD-loaded Quatsomes studied and their corresponding mean sizes one week and two months after their preparation

Sample	**[L]**[a] **$\times 10^{-3}$**	**Size(one week)** [b] **nm**	**Size (two months)** [b] **nm**
D-QS-1	0.57	96±40	114±33
D-QS-2	1.3	105±34	101±51
D-QS-3	3	85±39	9±36
D-QS-4	4.2	89±38	97±36
D-QS-5	6.6	106±38	109±43

[a] [L]=$moles_{DiD}/(moles_{chol}+moles_{CTAB}$. See Experimental Section 7.5.2 for details on determination of [L]

[b] Size distribution, measured by NTA (Experimental Section 7.4.2), is shown as the mean hydrodynamic diameter ± mean PdI.

CryoTEM images (Figure 3.23) of the samples one week after the preparation indicate

the formation of unilamellar vesicles for all analyzed samples. Only the sample at higher loading shows the presence of few different supramolecular structures (indicated with a red arrow in Figure 3.23, e), which maybe due to a different self-assembly of the fluorophore with cholesterol and CTAB.

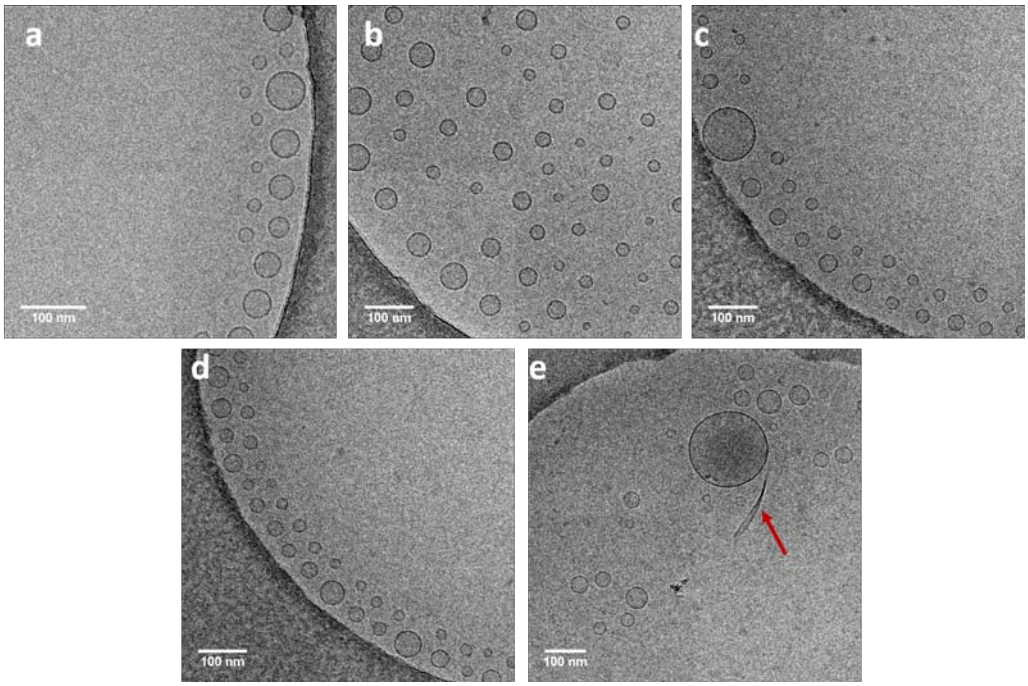

Figure 3.23: CryoTEM images of DiD-QS at different loading: a) D-QS-1, b)D-QS-2, c)D-QS-3, d)D-QS-4, e)D-QS-5

The normalized UV-vis absorption, excitation and emission of the samples are shown in Figure 3.24, in comparison with the spectra of DiD in EtOH, and the photophysical properties are resumed in Table 3.12. The UV-vis absorption spectra (Figure 3.24,a) suggest that as more fluorophore is loaded in QSs bi-layer more aggregates are formed, as indicated by the increase of the bands at 550 nm and 600 nm, attributed to H-aggregates and dimers, respectively. The excitation profiles of DiD-loaded QS (Figure 3.24, b) show that the H-aggregates and dimers formed are not emitting since the excitation spectra of all the five tested samples are perfectly overlapped to the excitation of the DiD in EtOH. This confirms that the only fluorescent species is the monomer of DiD, as supported as well by the exact overlap between the emission spectra of all samples (Figure 3.24, c).

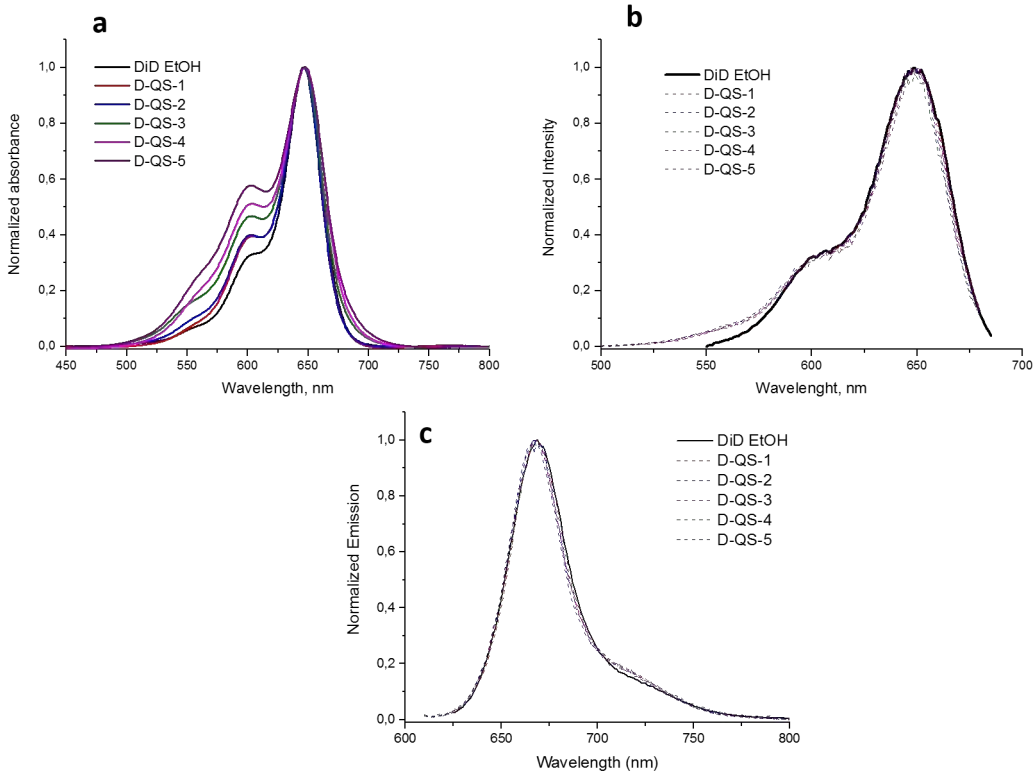

Figure 3.24: Normalized UV-vis absorption (a), excitation (b) and emission (c) spectra of DiD in EtOH and DiD-loaded QS at different loadings.

Table 3.12: Photophysical properties of DiD-loaded Quatsomes at different loading

Sample	$\lambda_{\textbf{Max abs}}$ **nm**	$\lambda_{\textbf{Max emi}}$ **nm**	ϕ^{a} %	ϵ^{b} $\mathbf{M}^{-1}$ cm^{-1}	**Brightness**[c] $\mathbf{M}^{-1}$ cm^{-1}
DiD EtOH	647	669	30	246,000	73,800
D-QS-1	647	664	23	247,000	56,800
D-QS-2	647	664	19	200,000	38,000
D-QS-3	647	664	11	170,000	18,700
D-QS-4	647	664	10	161,000	16,100
D-QS-5	647	664	7	140,000	9,800

[a] FLuorescence quantum yield ±10%. Cresyl Violet (MeOH) has been used as standard
[b] Molar extinction coefficients at the maximum absorption wavelength
[c] Brightness calculated as $\epsilon \times \phi$

The comparison of the photophysical properties of D-QS-1 and DiD in EtOH has already been discussed in Section3.1.1.2. As shown in the Table 3.12, φ and ε of DiD progressively decrease at higher loading. This result is reasonable, considering that ε and

φ of monomers of cyanines are higher than those of H-aggregates and dimers of DiD, which are indeed not luminescent at all, as shown in Figure 3.19.

Some studies in literature report an effect of the dye aggregation on the photostability of the nanoparticles [47], as in the case of some perylene derivatives in PLGA matrix [51], in which aggregation of the dyes induced a decrease in the photostability of the corresponding FONs. For this reason, it was considered interesting to study whether the presence of H-aggregates and dimers affect the photostability of DiD when incorporated into Quatsomes.

The comparison between photostability of D-QS-1 and DiD in EtOH has been discussed in Section3.1.1.2. The effect of the loading of DiD has been studied by monitoring the variation of maximum absorbance in function of the irradiation time (Figure 3.25). The calculated photodegradation quantum yield (PQY) values are listed in Table 3.13. Details on photobleaching studies can be found in Section 7.5.5 of the Experimental Part.

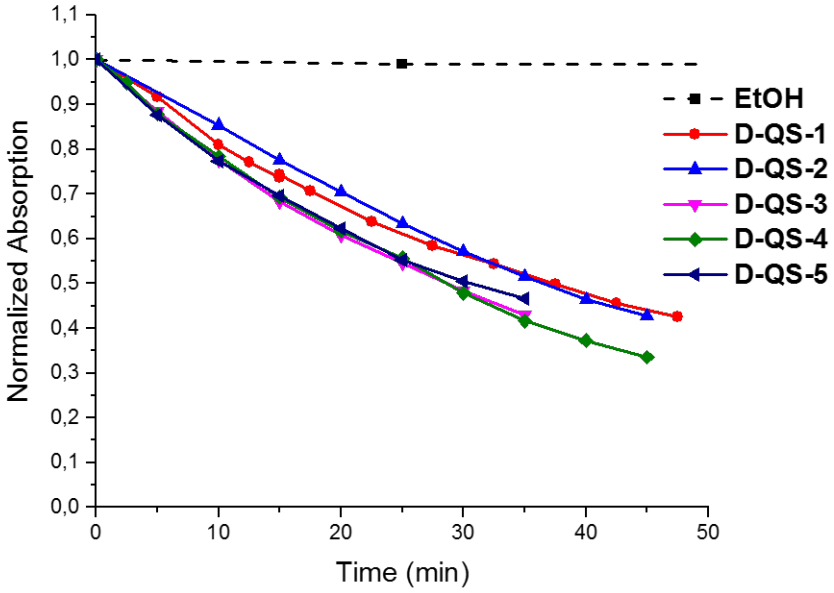

Figure 3.25: Variation of the maximum absorbance with time of DiD in EtOH and DiD-loaded Quatsomes at different [L]. Absorbance has been normalized with respect to the initial value. λ_{exc}= 660 nm, I=22 mW/cm^2

The values of PQY obtained for the different samples are comparable, meaning that there is no effect of the aggregation of the dye on the photodegradation rate of DiD-loaded Quatsomes.

Table 3.13: Photodegradation Quantum Yield (PQY) of DiD in EtOH and DiD-loaded Quatsomes at different loading of DiD

Sample	Photodegradation Quantum Yield (PQY)[a] $\times 10^{-5}$
DiD EtOH	<0.008
D-QS-1	1.3±0.4
D-QS-2	1.4±0.2
D-QS-3	1.9±0.3
D-QS-4	1.9±0.4
D-QS-5	1.8±0.4

[a] Calculated as explained in section 7.5.5. (λ_{exc}=660 nm, I=22mW/cm^2

3.1.5.2 Two-photon cross section of DiD and DiD-loaded Quatsomes

As mentioned in the Introduction, two-photon microscopy (TPM), which is based on the excitation of a fluorophore by the simultaneous absorption of two near-infrared (NIR) photons, is growing as a useful tool, especially for systems in which deep-tissue imaging is desirable.

In the current literature, there is huge amounts of papers and reviews on the design and properties of molecular probes with strong two-photons response [179, 180]. In this case, high 2PA cross-sections (σ_2) and 2PA action cross-section (σ_2*Φ) are required. σ_2 is directly affected by the molecular structure of the probe and high values of σ_2 are generally reached in molecules having a polarizable π-conjugated bridge with strong electron rich component (π-donor, D) or electron withdrawing component (π-acceptor, A) at both ends [181]. Generally, the stronger is the donor/acceptor pair, the greater is the extent of the intramolecular charge transfer (ICT), which is the driving force of the non-linearity. This leads to large transition dipoles moments and low excitation energies required and, subsequently, to high 2P cross-sections (σ_2). Furthermore, to achieve an efficient ICT process, a highly de-localized π-electron cloud, that acts as linker between the D/A ends is also required.

The strong effort of synthetic chemists aiming to design such probes is justified by the poor 2P response that commercial dyes generally have. Xu et al. measured the 2PA cross section in different solvents of dyes commonly used for biological applications, such as rhodamine B, bodipy, DiI, fluorescein [182]. They showed that all these fluorophores have indeed low 2P cross-sections, generally lower than 10^2GM (1 GM=10^{-50}cm^4).

Cyanine-like dyes have shown tuneable non linear optical response via the

modification of their molecular structures. The extended π-conjugated backbone and the presence of different substituents as end groups (both electron donor, D or acceptors, A) lead to the formation of different structural architectures such as symmetrical quadrupolar D-π-D (or D-π-A-π-D), A-π-A (or A-π-D-π-A), or asymmetrical dipolar (or push-pull) D-π-A demostrating different optical properties [183] [184, 185]. Carbocyanines like DiI, DID and DiR (Figure 3.2) are symmetrical quadrupolar dyes with a D-π-D motif.

To our knowledge, not many works exist in literature describing the non linear properties of dyes which form aggregates. Collini et al. [186] found an enhancement of the non linear response of porphirine dyes when self-assembled as J-aggregates. Some other groups have observed that a high two-photon absorption can be reached by intercalation of a dye in a matrix such as clay nano-sheets [187] or lipid nanoparticles [188]. An increase in dye concentration has been reported to be the cause of the decrease on the 2P absorption bands [189]. Drobizhev et al. [190] showed that the 2P cross section can be manipulated by changing the electrostatic environment of the chromophore being dependent on the squared difference between permanent dipole moments of the excited and ground state. Despite some carbocyanines have been tested as 2P probes even in imaging applications [148], the literature lacks so far of papers describing the effects on 2P cross section of the incorporation of cyanines, or other common fluorophores, loaded in vesicles.

Two-photon absorption cross-sections of DID in ethanol and DiD-QS in water were measured in a wide spectral range by two-photon excited fluorescence (TPEF) technique with femtosecond excitation pulses by Siarhei Kurhuzenkau in the laboratory of CREOL (University of Central Florida) under the supervision of Prof. Eric Van Stryland. The quadratic dependence of the fluorescence intensity on the pumping pulse energy was observed for each excitation wavelength (not shown here) indicating the two-photon nature of the excitation process. See Experimental Part 1.4.7 for details on 2-Photon cross section measurements. 2-P absorption spectra of DiD in EtOH, D-QS-3 and D-QS-5, are shown in Figure 3.26, along with the 1-photon absorption spectrum of DiD in EtOH.

DiD, D-QS-3 and D-QS-5 show a narrow main 2PA band centered at 800 nm, with a maximum 2P absorption wavelength (λ_{2p}) blue-shifted than twice the maximum 1P absorption wavelength (λ_{1p}), as generally exhibited by symmetrical dyes. Maximum values of around 2P-cross section of 900 GM were observed, in agreement with other results in literature on polymethine dyes with five chain units between the indolium terminal groups (720 GM) [185][191]. A weak allowed 2PA band in correspondence of the

shoulder of linear absorption spectrum (at 600 nm) is attributed to the symmetric breaking of the molecule [191].

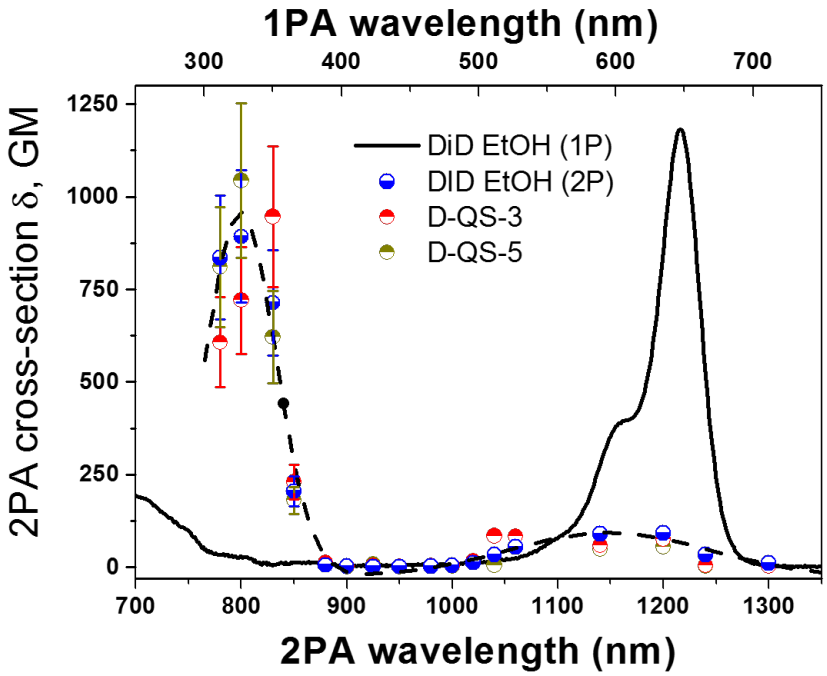

Figure 3.26: Two-photon absorption spectra of DiD, D-QS-3 and D-QS-5. Continous line: 1-photon absorption of DiD in EtOH. Colored dots: 2-photon spectra of DiD in EtOH (blue), D-QS-3 (red), D-QS-5 (green). A dashed line with the shape of 2-P spectra is shown as a guide to the eye. TPEF measuremens were performed with a Ti:sapphire laser, frequency doubled, delivering 150 fs pulses at 1kHz.

The interdigitation of DiD in QSs bi-layer does not produce any significant change on the 2P cross section compared to DiD in EtOH, meaning that the strong charge of the quaternary ammonium surfactant (CTAB) does not have any dramatic effect on the intramolecular charge transfer process of DiD. Furthermore, we found no appreciable variations on the σ_2, measured by TPEF, due to the presence of the H-aggregates. This result may be ascribed to the fact that H-aggregates are not fluorescent, as shown in Figure 3.24, so they do not produce any fluorescent signal both under 1P- and 2-P excitation. A different result may be expected in measurements of σ_2 made by other techniques, as for example with Z-scan.

3.1.5.3 Effect of fluorophore loading on colloidal and optical properties of DiI-loaded Quatsomes (I-QS)

In the Section3.1.1.2 it has been shown that DiI can be dispersed in water by using Quatsomes, obtaining bright and long-term stable samples (I-QS-1).

Likewise studied in the case of DiD-loaded Quatsomes, the effect of the loading on the colloidal and optical properties of DiI-loaded Quatsomes has also been evaluated. Three samples of DiI-loaded Quatsomes have been prepared by DELOS-SUSP, as explained in Experimental Section 7.5.2. The samples are listed in Table 3.14, along with the mean size one week and two months after the preparation, measured by DLS (see Experimental Section 1.3.1). For each sample two batches have been prepared, to check reproducibility of the results. Only minor differences have been detected in all the cases.

Morphology of the three studied samples one week after the preparation (stored at 4°C) is shown in the cryoTEM images in Figure 3.27.

Table 3.14: DiI-loaded Quatsomes obtained along with the corresponding size distributions one week and two months after the preparation.

Sample	**[L]**[a] **$\times 10^{-3}$**	**Size (one week)**[b] **nm**	**Size (two months)**[b] **nm**	**Z-potential**[b] **mV**
I-QS-1	0.6	72±43	69±52	82±18
I-QS-3	3.3	73±47	76±46	95±14
I-QS-5	7	70±45	73±48	94±12

[a] [L]=$moles_{DiI}$/($moles_{chol}$+$moles_{CTAB}$. See Experimental Section 7.5.2 for details on determination of [L]

[b] Size distribution, measured by DLS (Experimental Section 7.4.1), is shown as the mean hydrodynamic diameter ± mean PdI.

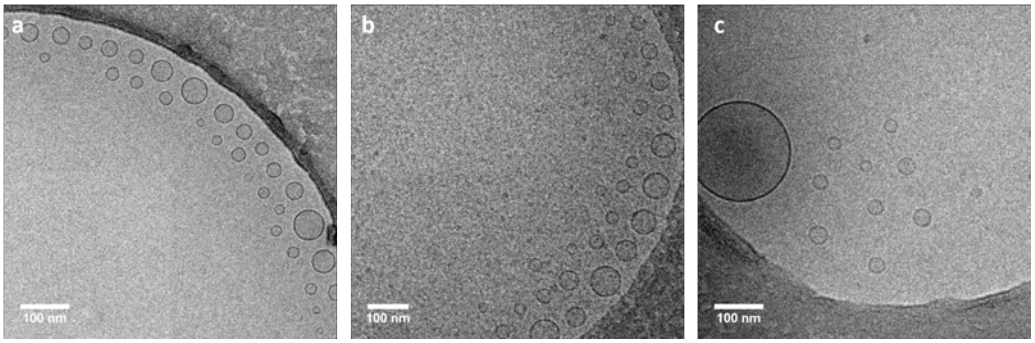

Figure 3.27: CryoTEM images of DiI-loaded QS at different loading: a) I-QS-1, b)I-QS-3, c)I-QS-5.

The anchoring of the DiI does not play any mayor effect on the average sizes of the vesicles, which remain constant over two months. The slight increase in the Z-potential, which is 16% ca higher in the samples with higher loading of the fluorophore may be due to the contribution coming from the cation present in the carbocyanine structure. Therefore, it can be safely affirmed that the inclusion of the carbocyanine in the membrane of the vesicles contributes to maintain a high stability of these

nanostructures. The cryoTEM micrographs reveal the presence of small unilamellar vesicles.

Analogously to the study conducted on DiD-loaded Quatsomes, in order to understand if the loading of DiI inside the bi-layer leads to formation of H-aggregates and dimers, the spectral properties of DiI-QS at three different loading have been studied. The normalized UV-vis absorption, excitation and emission spectra of the three samples are shown in Figure 3.28 and the photophysical properties of the samples are reported in Table 3.15.

Comparably to what observed in the case of DiD-loaded QS, the only emitting species in the samples is the monomer of DiI, even at the highest loading explored, as shown by the excitation spectra which are overlapped to the one of the probe in EtOH (Figure 3.28, b)

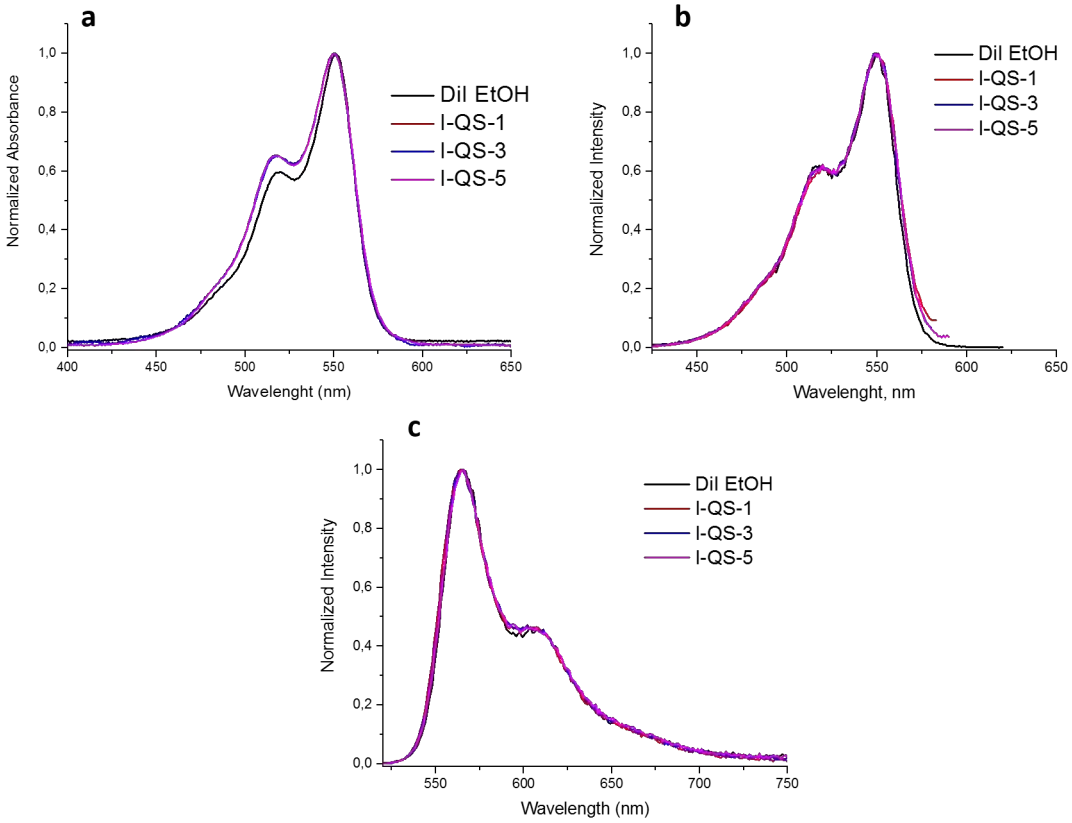

Figure 3.28: Normalized UV-vis absorption (a), excitation (b) and emission (c) spectra of DiI in EtOH and DiI-loaded QS at different loading.

Table 3.15: Photophysical properties of DiI-loaded Quatsomes at different loading.

Sample	$\lambda_{\textbf{Max abs}}$ **nm**	$\lambda_{\textbf{Max emi}}$ **nm**	$\phi^{\textbf{a}}$ %	$\epsilon^{\textbf{b}}$ $\mathbf{M}^{-1}$ cm^{-1}	**Brightness**[c] $\mathbf{M}^{-1}$ cm^{-1}
DiI EtOH	551	566	11	140,000	15,400
I-QS-1	550	565	20	115,000	23,000
I-QS-3	550	565	13	112,000	14,600
I-QS-5	550	565	10	104,000	10,400

[a] FLuorescence quantum yield ±10%. Fluorescein (0.1M NaOH) has been used as standard
[b] Molar extinction coefficients at the maximum absorption wavelength
[c] Brightness calculated as $\epsilon \times \phi$

As commented in Section3.1.1.2, the slightly higher band at 518 nm in I-QS-1, I-QS-3 and I-QS-5 absorption spectra (Figure 3.28,a) can be safely ascribed to environmental effects. Curiously, no blue shifted bands associated to the formation of H-aggregates neither dimers have been observed at higher loading, in contrast with the evidence in DiD-loaded Quatsomes absorption spectra (see Figure 3.24). This result suggests that there is a link between the length of the conjugated chain of cyanines and the tendency to form aggregates that will be discussed in the next Section. The absence, or moderate presence, of non-fluorescent aggregates is also responsible of the high fluorescence, φ, that we found in DiI-QSs samples. Surprisingly, at a low loading, the DiI is more fluorescent when inserted in the bilayer of Quatsomes as compared to the probe in EtOH. At higher loadings still high values of φ and ε have been found, with a slight decrease as effect of aggregation.

3.1.5.4 Effect of fluorophore loading on colloidal and optical properties of DiR-loaded Quatsomes (R-QS)

In line with the study performed with Quatsomes loaded with different amounts of DiI and DiD, the effect of loading on the colloidal and optical properties of DiR-loaded Quatsomes has also been evaluated.

Three samples were prepared as a proof of concept that DiR can be incorporated inside the bi-layer of the vesicles and that aggregates formation strictly depends on the length of the polymethine chain. The three samples of DiR-loaded Quatsomes have been prepared by DELOS-SUSP, as explained in Experimental Section 7.2.1. The samples are listed in Table 3.16, along with the mean size one week and two months after the preparation, measured by NTA (see Experimental Section 1.3.2). In order to check

reproducibility of the results, for each sample two batches have been prepared,. Only minor differences have been detected in all the cases. The morphology of the samples with lowest (R-QS-1) and highest loading (R-QS-5) one week after the preparation (stored at 4°C) is shown in the cryoTEM images in Figure 3.29

Table 3.16: DiR-loaded Quatsomes studied and their corresponding mean sizes one week and two months after their preparation.

Sample	**[L]**[a] **$\times 10^{-3}$**	**Size (one week)**[b] **nm**	**Size (two months)**[b] **nm**
R-QS-1	0.5	126±43	129±37
R-QS-3	2.3	118±46	122±49
R-QS-5	5	103±47	115±54

[a] [L]=moles$_{DiR}$/(moles$_{chol}$+moles$_{CTAB}$. See Experimental Section 7.5.2 for details on determination of [L]

[b] Size distribution, measured by NTA (Experimental Section 7.4.2), is shown as the mean hydrodynamic diameter ± mean PdI.

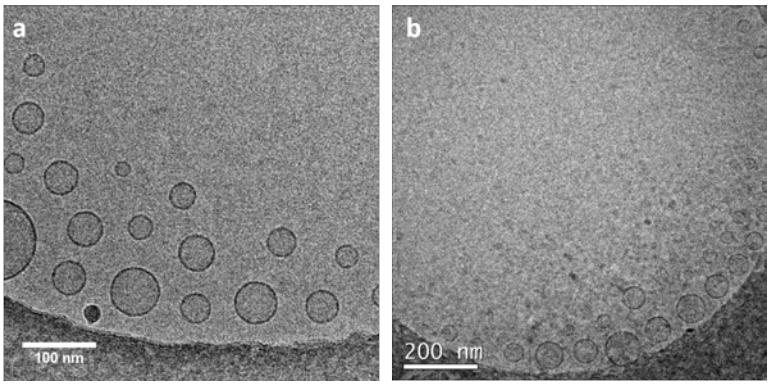

Figure 3.29: CryoTEM images of DiR-loaded QS: a) R-QS-1, b)R-QS-5.

As observed in the case of DiI- and DiD-loaded Quatsomes, the incorporation of DiR does not affect the size of the vesicles over two months, since the mean sizes are maintained over the whole observation period. Likewise their morphology is kept unvaried, as shown in the two cryoTEM micrographs.

The normalized UV-vis absorption, excitation and emission spectra of the samples, compared to DiR in EtOH, are shown in Figure 3.30 and the photophysical properties of the samples given in Table 3.17.

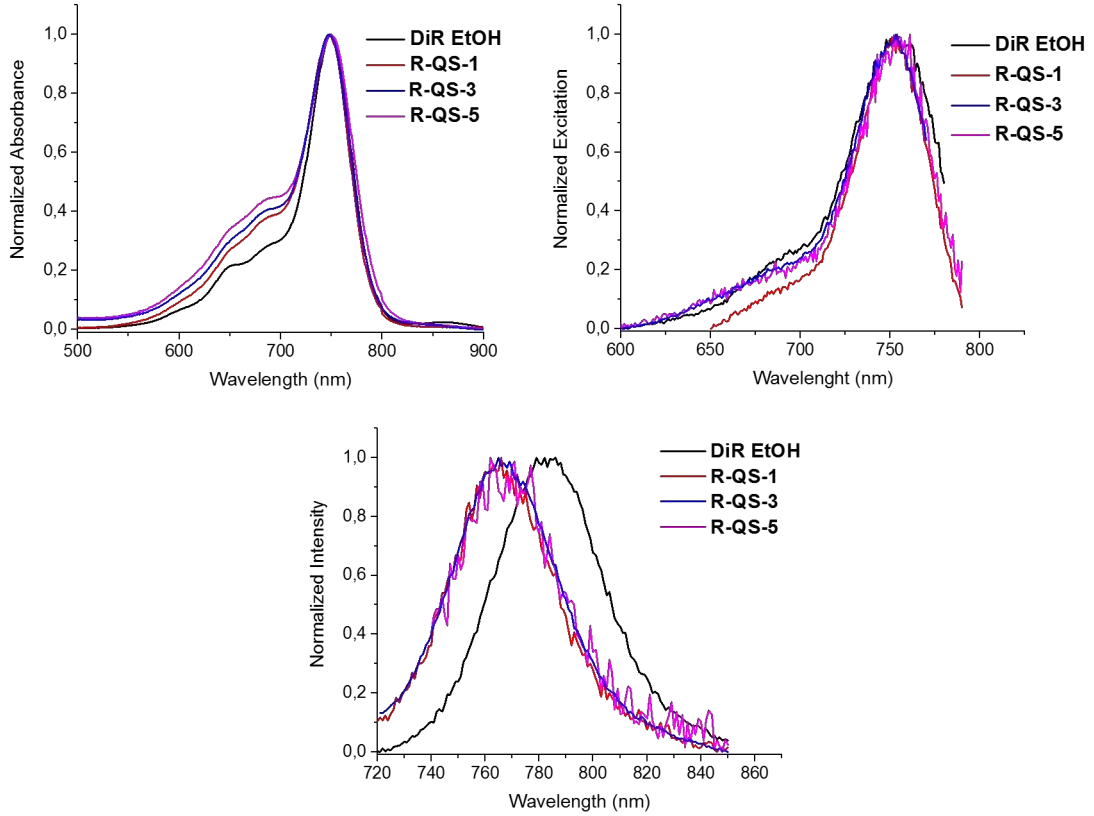

Figure 3.30: Normalized UV-vis absorption (a), excitation (b) and emission (c) spectra of DiR in EtOH and DiR-loaded QS at different loading.

Table 3.17: Photophysical properties of DiR-loaded Quatsomes at different loading

Sample	$\lambda_{\textbf{Max abs}}$ **nm**	$\lambda_{\textbf{Max emi}}$ **nm**	$\phi^{\textbf{a}}$ %	$\epsilon^{\textbf{b}}$ $\mathbf{M}^{-1}$ cm^{-1}	**Brightness**[c] $\mathbf{M}^{-1}$ cm^{-1}
DiR EtOH	749	774	10	271,000	27,100
R-QS-1	748	765	3	200,000	6,000
R-QS-3	748	765	1	170,000	1,700
R-QS-5	748	765	1	140,000	1,400

[a] FLuorescence quantum yield ±10%. Cresyl violet (MeOH) has been used as standard
[b] Molar extinction coefficients at the maximum absorption wavelength
[c] Brightness calculated as $\epsilon \times \phi$

As commented in Section3.1.1.2, a higher solvatochromism in emission is observed when the DiR is incorporated in Quatsomes membrane, as compared with DiI and DiD dyes. The excitation spectra of R-QS-1 and R-QS-3 are almost coincident with that of DiR in EtOH confirming, analogously to what observed for Quatomes loaded with DiI and

DiD, that the only emitting species in the sample is the monomer of DiR. The increased absorbance values of DiR-QSs in the region between 600 nm and 700 nm are likely due to the presence of dimers and H-aggregates of DiR. Nevertheless, the non-sharp and broad bandshape of the DiR in EtOH makes difficult to distinguish which peak is attributable to the dimers or H-aggregates of the dye.

The brightness of the DiR dramatically decreases when the fluorophore is inserted in the membrane, in comparison to the properties of the dye in EtOH. The decrease of brightness is due both to the lower extinction coefficients and quantum yield, as effect of the presence of non bright aggregates of the dye.

Kawabe et al. [192] studied the labeling of DNA with cyanines of different polymethine length (similarly to the fluorophores studied in this Thesis), finding out that the longer is the conjugated chain , the higher is the tendency to form a mix of H- and J-aggregates.

In Figure 3.31 the brightness ($\varphi x\varepsilon$) of the Quatsomes-based FONs with the carbocyanines of different polymethine chain length (n=3,5 and 7 for DiI, DiD and DiR, respectively) is plotted as function of loading.

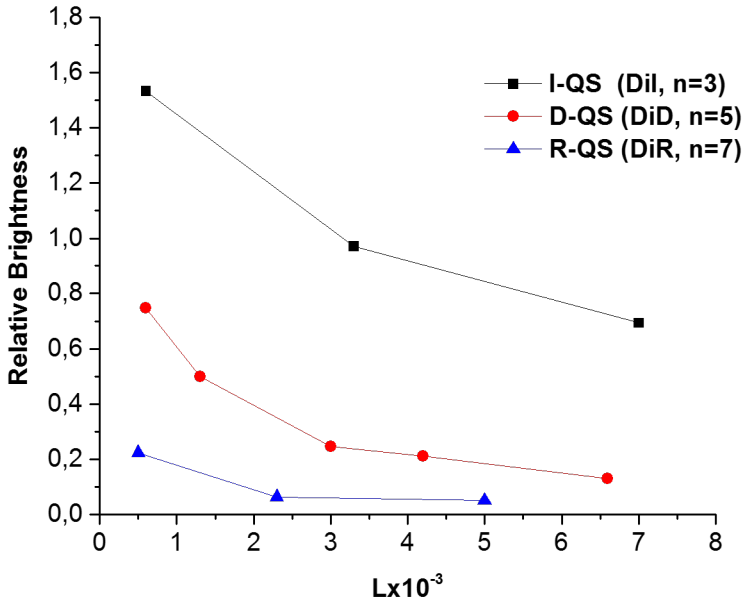

Figure 3.31: Effect of the loading on the brightness ($\varphi\varepsilon$) of the different cyanines-loaded Quatsomes. Brightness has been normalized by the brightness of each dye in EtOH.

Values of brightness have been normalized with respect to the brightness of each dye in EtOH. The results shown here agree with those of Kawabe et al. [192]. Indeed, the most abrupt decrease in brightness is obtained for the R-QS (DiR, n=7) samples: even at the lowest loading the brightness is around 20% of the value in EtOH and at the highest

loading the emission is almost totally quenched. D-QS (DiD, n=5) samples show an intermediate behavior, in which the brightness quickly decreases at the beginning and then the trend gets smoother. The case of I-QS (DiI, n=3) is the most surprising, showing an improvement of the brightness at low loading and still optimal values at the highest loading studied.

3.1.6 Summary and Perspectives

A new class of fluorescent organic nanoparticles (FONs), obtained by dispersing the hydrophobic carbocyanines (DiI, DiD and DiR) in water via the incorporation into Quatsomes (QSs) membrane, has been prepared and studied. Results show that these new FONs are highly stable, both in terms of colloidal and optical properties, over months.

- The photophysical properties of the obtained FONs are strongly dependent on the aggregation state of the fluorophore inserted in Quatsomes membrane that depends on the loading of the dye in the Quatsomes: the more non-luminescent aggregates (H-aggregates) are formed, due to an increase of dye concentration, the lower is the brightness of the cyanines-loaded Quatsomes. Moreover, it has been observed that there is a link between the length of the polymethine chain and the brightness of the corresponding Quatsomes-based FONs. Thus, Quatsomes loaded with carbocyanines with longer conjugated chains showed the more abrupt loss in brightness compared to the monomers in EtOH.

- The aggregation state of the fluorophores inside the membrane of Quatsomes is severely affected by the preparation route. Thus, the CO_2-based methodology DELOS-SUSP leads to the best compromise between distribution of the dye over the membrane of Quatsomes and morphology of the obtained vesicles.

- The optical and colloidal properties of DiD-loaded Quatsomes have been compared to those of other nanostructures of DiD in water, such as nanoparticles of DiD and CTAB micelles incorporating DiD, respectively. Results showed that both the luminescence and the colloidal stability are significantly improved when the dye is dispersed in water by mean of Quatsomes.

- Molecular Dynamics (MD) unveiled the disposition of the dye inside the membrane of the vesicles, demonstrating that the two C_{18} alkyl chains of the carbocyanines are stably interdigitated into the bi-layer. Moreover, the simulated

diffusion coefficients of the dyes within Quatsomes membrane are similar to those observed for phospholipids in liposomes, which are known to be fluid bilayers.

The results here discussed suggested that, taking advantage of the non-covalent interaction between the aliphatic chains of the dyes (the carbocyanines) and the hydrophobic compartment of Quatsomes bi-layer, it is possible to stably disperse hydrophobic dyes with long alkyl chains in water by incorporating them into Quatsomes. In order to strengthen the results obtained and withdraw a general conclusion, it is necessary to investigate whether the same strategy can be used with dyes belonging to other families, as shown in Chapter 4 and Chapter 5.

3.2 FRET-based multicolor Quatsomes

3.2.1 Introduction to multicolor nanoparticles

The possibility of simultaneously decipher different biological processes or visualize specific targets from complex living samples has driven the development of fluorescent labels for multiplex detection. In this context, multicolor materials, which can emit multiple colors under a single-wavelength excitation, are strongly interesting. Due to the poor commercial availability of probes with such characteristics, several strategies aiming to the design of multicolor fluorescent nanoparticles have been explored in the very recent years. The main advantages given by using multicolor nanoparticles for multiplexed analysis consist in the simplification of the instruments required (a microscope with a single-wavelength laser is required, for example) and the simultaneous excitation with a single wavelength laser of all the fluorophores involved in the assay [193].

Many works found in literature on the design of multicolor nanoparticles rely on a mechanism named fluorescence resonance energy transfer (FRET). FRET is a phenomenon occurring between two molecules located at a short distance. Upon excitation under illumination of one of them, the donor (D) molecule, the energy is transferred, by a non-radiative mechanism, to the other molecule, the acceptor (A), which can emit fluorescent light. It is crucial for an efficient energy transfer that the acceptor is able to absorb in the same spectral range (i.e. energy interval) as the emission of the D (resonance condition). The process occurs without emission of a photon, as a result of the long-range (<100 Å) dipole-dipole interaction between the donor and acceptor (Forster resonance energy transfer). Thus, an efficient FRET requires that both molecules are located at a distance <100 Å and have a certain reciprocal orientation, as explained later. The evidence of a FRET process is therefore the quenched emission of the D (it eventually disappears in a 100% efficient energy transfer) and the appearance of an emission band of the A fluorophore (although in some other application the acceptor is not meant to be luminescent and it works just as a quencher of D). The main parameters that rule the efficiency of a FRET process are schematized in Figure 3.32. First (Figure 3.32a), a high overlap between the emission of D and absorption of A is desirable. In addition, the efficiency of FRET depends strictly on the D quantum yield and the A molar extinction coefficients. FRET is a distance-dependent process (Figure 3.32b) and the efficiency of FRET depends on r^{-6}(in the case of Forster energy transfer), where r is the distance between D and A [158, 194]. FRET efficiency also

depends on the relative orientation between the transition dipole moments of the two molecules, as discussed afterwards.

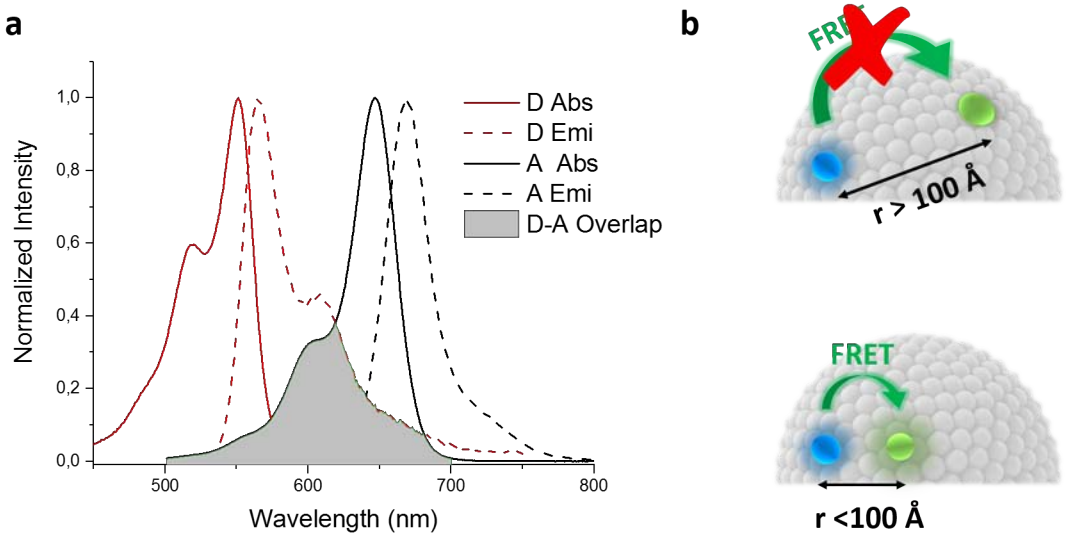

Figure 3.32: Schematization of the main parameters determining the efficiency of the FRET process within a nanoparticle. a) Extent of overlap between the emission of D and the absorption of A; b) the distance between D and A is crucial for the energy transfer, which occurs for distances r between D and A lower than 100 Å and it depends on r^{-6} (Forster energy transfer).

Concerning the design of FRET-based multicolor nanoparticles, Chen et al prepared methyl methacrylate nanoparticles incorporating naphtalimide and nitrobenzoxadiazole derivatives as FRET pair. By varying the ratios of these two dyes, the emission could be tuned obtaining a family of nanoparticles exhibiting different colors under a single excitation [195]. The authors furthermore functionalized the nanoparticles with different targeting agents managing to simultaneously detect multiple cancer cells with a single excitation wavelength. In a similar way, Xu et al. prepared FRET-based fluorescent organic nanoparticles with tuneable color, in which the acceptor and donor were used as dopant and matrix of the nanoparticle, respectively. The color of the obtained FONs showed an acceptor concentration dependent emission, as shown in Figure 3.33 [196].

Another advantage of the tuneable multicolor fluorescent nanoparticles is the possibility of designing probes with large Stokes shift, i.e. the difference between the maximum absorption and emission wavelength, a critical parameters which affects the complexity of the microscope setup and the possibility of quantification during imaging. Probes with high Stokes shift in fact guarantee, on one hand, reduced self-asborption of the emitted light, permitting quantitative analysis of the fluorescence intensity detected

and, on the other hand, adequate filters can be used to neatly separate the probe emission from unwanted background contributions, for example autofluorescence or scattering of tissues. He et al. for example, designed a FRET-based fluorescent silica nanoparticle (selecting RuBpy and methylene blue as FRET pair) with Stokes shift larger than 200 nm, which significantly improved the discrimination between fluorescent signal and background in *in vivo* mice imaging [197].

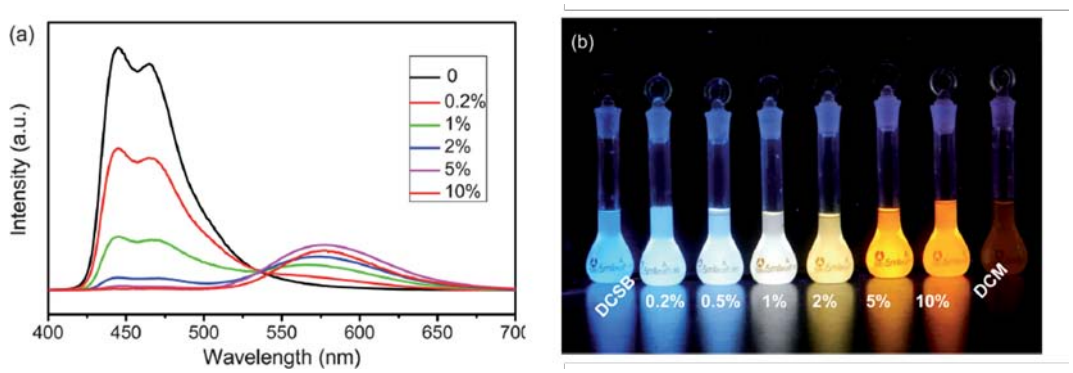

Figure 3.33: (a) Concentration dependent emission spectra of DCM-doped nanoparticles of DSCB. The emission of the obtained FONs depends on the molar ratio (from 0 to 10%) between the DCM (acceptor) and DSCB (donor). (b) Picture of the FONs suspension under the UV lamp. Adapted from [196].

Fluorophores belonging to the family of carbocyanines, previously described in Section 1.1, have been extensively investigated as dyes for FRET, thanks to their commercial availability and suitable spectral properties. The possibility of finely tuning the color emission of these molecules just by varying the length of the polymethine conjugated chain, allows to obtain dyes with different spectral characteristics and very similar physicochemical properties. Several works exist in literature about multicolor nanoparticles, both inorganic and organic, encapsulating two or more carbocyanines (DiO, DiI, DiD and DiR, with colors spanning from the green to the NIR). Wagh et al. for example studied different cases of PLGA/PEG-based nanoparticles simultaneously encapsulating some or even all the four carbocyanines [78, 198]. In this latter case, the nanoparticles under excitation at 485 nm could emit in the whole visible and up to the NIR range simply depending on the total amount and ratio of the four encapsulated carbocyanines. In another case, encapsulating DiD and DiR (in 1:1 molar ratio) for in vivo imaging applications, they obtained large Stokes shift (>100 nm) and found that higher FRET efficiency were reached for high overall fluorophore content. However, question may arise about the colloidal stability of these polymeric nanoparticles (with low Z-potential values, around -17 mV), which was monitored only for one week by the authors.

Along with the design of multicolor nanostructure, FRET has been used to monitor in real-time the effectiveness of the drug release from delivery nano-systems. To evaluate, in fact, the therapeutic benefit of drug delivery systems (DDSs), monitoring in real time the *in vivo* or in live cells release is crucial. This information can be achieved via FRET mechanism. In a multifunctional drug delivery system in which a nanoparticles carry a therapeutical payload and a pair of dyes exhibiting FRET, the integrity of the nanoparticle in its pathway towards the targeted cell/tissue can be monitored by the real-time detection of the FRET signal. However, once upon external stimuli the nanocarrier breaks down, one (or both) of the FRET-pair fluorophores will be discharged from the carrier and the FRET signal will sensibly decrease or turn off. By this mechanism, McDonald et al. assessed the cellular permeability in human colorectal carcinoma cells of nanosuspensions of DiO-DiI which, despite the poor colloidal stability of the nanoparticles (Z-potential around 10 mV), maintained their integrity, monitored by FRET mechanism, upon internalization in cells [80]. Similarly, Morton et al. monitored the *in vivo* biodistribution of polymeric micelles and their de-aggregation in mices, monitoring the FRET signal between Cy5 (donor) and Cy7 (acceptor) dyes encapsulated as model drugs [82].

Interestingly, the scientific literature lacks of studies on multicolor vesicles, including liposomal and non-liposomal formulations. For this reason, in this Section, we want to give a proof that Quatsomes can be used as structures to host FRET-pairs giving multicolor capability. The superior colloidal stability of fluorescent Quatsomes along with the fine tuning of their optical properties upon dye loading, constitute, in fact, a promising terrain for the preparation of multicolor vesicles for multiplex detection.

3.2.2 Quatsomes loaded with DiI and DiD as FRET-pair

In the Section 3.1, it was shown that hydrophobic carbocyanines (DiI, DiD and DiR) can be successfully dispersed in water by incorporating them in Quatsomes, obtaining highly stable and bright FONs. Since these dyes, as previously mentioned, have been widely used as FRET pairs, in this Section, we decided to explore the possibility of obtaining FRET-based multicolor Quatsomes by simultaneously load DiI, as donor (D), and DiD, as acceptor (A), in the membrane of the vesicles. The size scale of Quatsomes seems indeed adequate for an efficient FRET process, as indicated by the quantitative analysis of cryoTEM images which showed that most of the Quatsomes have diameters of 30-40 nm and the thickness of the membrane is around 4-5 nm [130].

By joining the normalized absorption and emission spectra of DiI- and DiD-loaded

Quatsomes studied in Section 3.1 (samples I-QS-1 and D-QS-1, respectively), it can be observed that, once incorporated in Quatsomes, the emission of DiI (I-QS-1) and the absorption of DiD (D-QS-1) are overlapped to large extent, and therefore this fluorophore pair, once incorporated in Quatsomes, is, in principle, adequate for FRET (Figure 3.34).

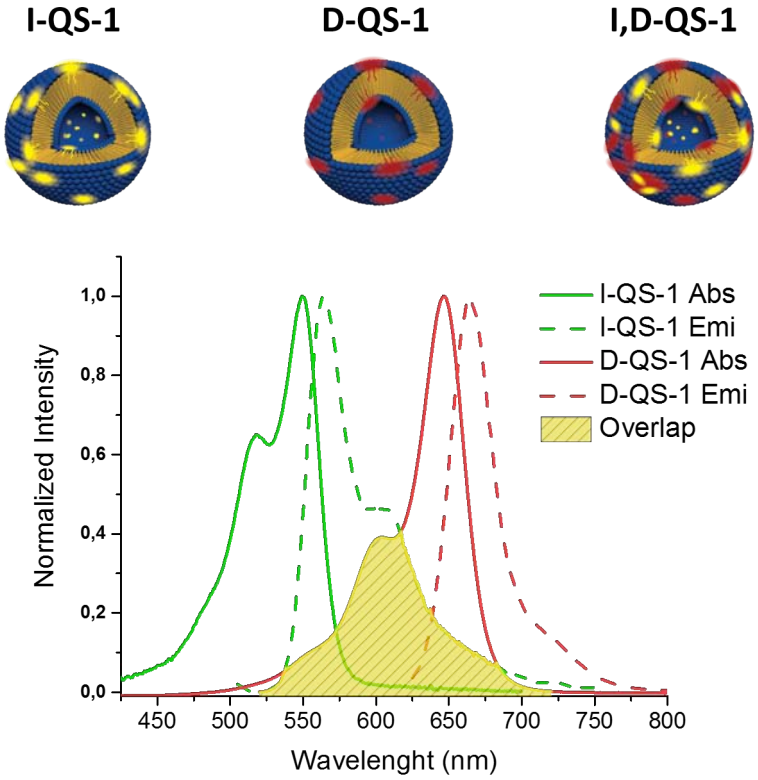

Figure 3.34: Top) Schematic representation of the samples studied in this Section. In order to evaluate the real FRET efficiency, the spectral properties of the FRET sample (I,D-QS-1) have been compared to the single-dye loaded Quatsomes (I-QS-1 and D-QS-1). Bottom) Normalized UV-vis absorption and emission spectra of I-QS-1 and D-QS-1 (the overlap extent between emission of DiI and absorption of DiD is evidenced)

An equimolar ratio between DiI and DiD was chosen in this study, because in previous works in literature it was observed that FRET efficiency close to 1 can be obtained in nanoparticles loaded with 1:1 molar ratios of cyanines pairs [78, 80].

As previously mentioned, the donor (D) and the acceptor (A), must stay within close proximity (less than $\approx$ 10 nm) in order to have a highly efficient FRET process. We speculate that the total amount of DiI and DiD loaded in Quatsomes can affect the distance between the two dyes within the membrane and have, therefore, a strong impact on the FRET efficiency. For this reason, two samples containing DiI and DiD in equimolar ratio, but with different overall fluorophore content, have been studied as

explained below. In order to make a quantitative analysis of the FRET process, the FRET samples, i.e. the ones simultaneously loaded with both DiI and DiD (named I,D-QS), have been compared with the single-dye loaded Quatsomes (I-QS and D-QS, for DiI-loaded and DiD-loaded Quatsomes, respectively).

3.2.3 Preparation and physico-chemical characterization of multi-labeled Quatsomes for FRET

The samples studied in this Chapter have been prepared by the CO_2-based method DELOS-SUSP, using the configuration shown in details in Experimental Section 7.2.1. Quatsomes simultaneously loaded with an equimolar ratio of DiI and DiD (I,D-QS samples) but different total fluorophore content have been prepared, namely I,D-QS-1 and -5. For comparison, the single-dye loaded Quatsomes samples, I-QS-1 and -5 and D-QS-1 and-5, at the same fluorophore contents were studied. All the samples studied in this Section are listed in Table 3.18.

The single-dye loaded Quatsomes were prepared as indicated in Chapter 3.1 (Section 3.1.2). For the preparation of the sample I,D-QS-1 and -5, cholesterol was dissolved in a 0.2 mM (or 2 mM, in the case of I,D-QS-5) equimolar solution of the two dyes (DiI and DiD) in EtOH. Afterwards, the solution was added to the autoclave and the standard procedure for the preparation of dye-loaded Quatsomes was followed. The samples have been purified by diafiltration (Experimental Section 7.2.2) and stored at 4°C for one week before the analysis. In order to provide an information about the amount of dye/dyes present in each sample, the loading [L] is defined as $[L]=moles_{dyes}/(moles_{chol}+moles_{CTAB})$. The amount of dyes in each sample have been evaluated by UV-vis spectroscopy while the amounts of cholesterol and surfactant used for the calculation of [L] are the nominal ones, i.e. the quantities weighted at the beginning of the DELOS-SUSP protocol. Details on the calculation of the dyes loading are provided in Section 7.5.2 of the Experimental Part. For each sample, two batches have been prepared (three in the case of I-QS-1 and D-QS-1) to check reproducibility of the results, with only minor differences detected between the batches.

The size distributions and colloidal stability of I,D-QS samples were evaluated by Nanoparticle Tracking Analysis (NTA) and results are shown in Table 3.18, where the size distributions are compared to those of single-dye loaded Quatsomes (previously studied in Chapter 3.1). As expected, no major variations were found comparing the average diameters of the single-dye loaded and multiple dyes-loaded Quatsomes. The differences between DiI-loaded Quatsomes and those in presence of DiD are ascribable

to the different techniques used in the two cases, Dynamic Light Scattering (for I-QS samples) and Nanoparticle Tracking Analysis (for D-QS and I,D-QS samples). Additionally, the samples were found stable for at least 1 month with the average size distribution which remained unchanged.

Table 3.18: Single- and multiple-dyes loaded Quatsomes studied in this Section along with their size distributions one week and one month after the preparation.

Sample	**Dye**	**[L]**[a] **$\times 10^{-3}$**	**Size (1 week)**[b] **nm**	**Size (1 months)**[b] **nm**
I-QS-1	DiI	0.6	72±43	69±52
I-QS-5	DiI	7	70±45	73±48
D-QS-1	DiD	0.6	96±40	114±33
D-QS-5	DiD	6.6	106±39	109±43
I,D-QS-1	DiI+DiD	0.75 (DiI); 0.7 (DiD)	102±51	92±36
I,D-QS-5	DiI+DiD	7 (DiI); 6.2 (DiD)	138±73	139±50

[a] [L] = $moles_{dye}/(moles_{chol}+moles_{CTAB})$.For the calculation of [L] see Experimental Section 7.5.2

[b] Size distribution is shown as the mean average hydrodynamic diameter ± mean PdI. Size distribution of I-QS samples has been measured by DLS while D-QS and I,D-QS samples were monitored by NTA (see Experimental Section 7.4.2).

The cryoTEM images, acquired one week after the preparation, of I,D-QS-1 and I,D-QS-5 (Figure 3.35) show that the simultaneous incorporation of the two different dyes in Quatsomes does not have any effect in the morphology of the vesicles

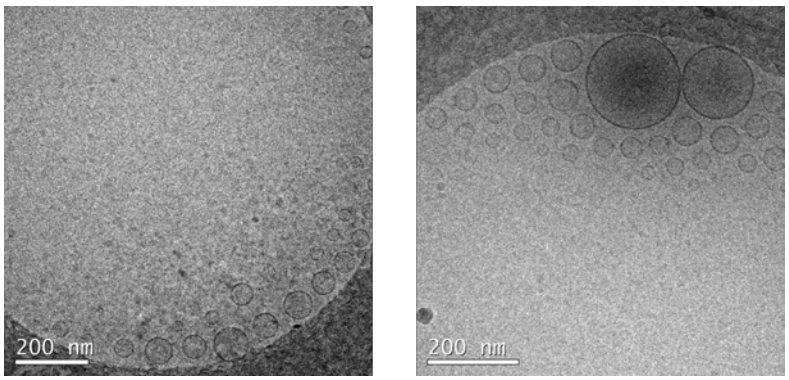

Figure 3.35: CryoTEM images of left) I,D-QS-1 and right) I,D-QS-5 one week after the preparation of the samples

3.2.4 Optical properties and FRET characterization of multiple dyes-loaded Quatsomes

The normalized UV-vis absorption and emission of I,D-QS-1 and I,D-QS-5 are shown in Figure 3.36. All the spectra have been normalized with respect to the maximum intensity of the acceptor (DID), in order to monitor the variation in relative intensity of the donor (DiI).

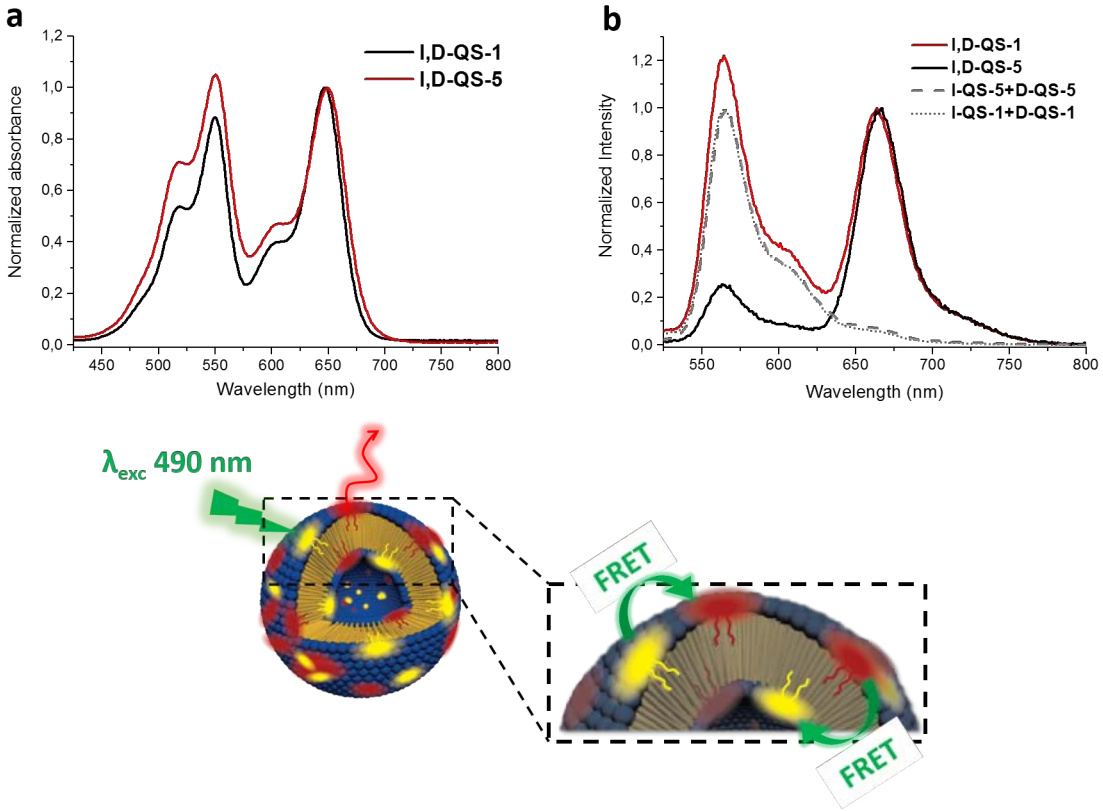

Figure 3.36: Spectral characterization of I,D-QS-1 and I,D-QS-5. UV-vis absorption (a) and emission (λ^{DiI}_{ex}=490 nm) (b) have been normalized with respect to the maximum intensity of the acceptor (DiD). The gray curves in (b) are the fluorescence spectra (acquired after one week, λ^{DiI}_{ex}=490 nm) of mixed I-QS and D-QS samples. (d) shows two hypothesized dispositions of FRET pairs in Quatsomes.

The UV-vis absorption spectra (Figure 3.36, a) show the presence of both dyes in the two formulations. Despite the almost equimolar presence of DiI and DiD in both samples, the ratio between the absorbances at 647 nm and 550 nm (wavelengths corresponding to the maximum absorption of D-QS and I-QS samples, respectively) is lower in the case I,D-QS-5 compared to I,D-QS-1. This is attributed to the higher number of aggregates of DiD (compared to number of aggregates of DiI) formed at higher loading, which have lower absorption coefficients than the monomers of DiD (as already explained in Chapter 3.1).

An excitation wavelength of 490 nm (λ^{DiI}_{ex}) was found to give a good discrimination between the two dyes, as shown in the absorption spectra of the two single-dye loaded Quatsomes (Figure 3.34). At this wavelength in fact, the absorption of DiD-loaded Quatsomes is extremely low and the samples do not fluoresce under direct light excitation (as shown in the excitation spectra of Figure 3.24). Therefore, the emission spectra of I,D-QS-1 and I,D-QS-5 (Figure 3.36, b) were collected exciting the samples at 490 nm, in order to collect only direct emission of D and emission due to FRET process from A. The presence of an intense peak at 664 nm (666 nm in the case of I,D-QS-5) unequivocally demonstrates the presence of the energy transfer between the DiI (D) and DiD (A). The difference in the fluorescence intensity of the donor shows that there is a link between the total fluorophores amount and the efficiency of the FRET process. In the emission spectrum of I,D-QS-5 sample, in fact, the contribution from the direct excitation of DiI (peak at 564 nm) is almost completely quenched, indicating a high FRET efficiency.

The energy transfer occurs between molecules which stay in close proximity within the membrane of the vesicles. Therefore, FRET can occur between D and A fluorophores disposed on the same leaflet or either on the two different leaflets (facing inward, at the inner lumen and outward, at the surrounding medium, respectively) of the bilayer of the vesicle, which is 4 nm ca. thick, as schematized in Figure 3.36, bottom.

However, to check whether the FRET behavior can have origin from the close proximity of single-dye loaded Quatsomes, I-QS-1 and D-QS-1 samples (in the other case I-QS-5 and D-QS-5 ones) were mixed together and the fluorescence spectra exciting at λ^{DiI}_{ex} (grey curves in Figure 3.36 (b), normalized with respect to the maximum emission of DiI) were acquired after one week. The small bump in the region at 664-666 nm can be associated to a very low efficient FRET signal occurring, irrelevant if compared to the samples in which DiI and DiD are simultaneously loaded in the membrane of Quatsomes. Thus, two useful information can be withdrawn. First, FRET occurring between two different single-dye loaded Quatsomes approaching to close proximity is insignificant; second, no dye inter-vesicles exchange between single-dye loaded Quatsomes occurred during one week, supporting the results already discussed in Section 3.1, demonstrating that, once the fluorophores are incorporated into the membrane of the vesicles, they do not have tendency to get out of the membrane.

Forster Theory to model FRET in Quatsomes

FRET is a physical process by which energy is transferred in a radiationless manner from an excited molecular fluorophore (D) to another fluorophore (A) by means of intermolecular long-range dipole-dipole coupling. The theory for resonance energy transfer is quite complex and several models have been developed from classical and quantum mechanical considerations. We will use a set of equation, applicable only for the Forster theory of FRET and extensively described in a review by Clegg (Ref. [199]), in order to define some characteristic parameters of the energy transfer between DiI and DiD in Quatsomes. The Forster theory is valid only in the near field distance between D and A (roughly 1-10 nm range), where interacting molecules can be approximated as point dipoles. Below this limit (Dexter zone) A and D may form complexes, while at higher distances, approximation on the electric fields of the D and A charges break down and other phenomena, such as radiative transfer become relevant [200].

The distance at which the energy transfer is 50% efficient is called the Forster distance (R_0) and it can be calculated as follow:

$$R_0 = \frac{9000(ln10)k^2\varphi_d}{128\pi^5 N_A n^4} \int F_D(\lambda)\epsilon_A(\lambda)\lambda^4 d\lambda \tag{3.1}$$

where:

k^2 = orientation factor;

φ_D= quantum yield of the donor in the absence of acceptor;

n = refractive index of the medium (water, n=1.33);

The expression within the integral (sometimes named *J*) is the overlap integral, which expresses the degree of overlap between the emission of the donor and absorption of the acceptor:

$F_D(\lambda)$ is the corrected fluorescence intensity of the donor, in the range $\lambda + \Delta\lambda$, with the total area normalized to unity;

$\varepsilon_D(\lambda)$ is the extinction coefficient of the acceptor at λ;

The term k^2 refers to the relative orientation of the transition dipole moments of D and A. It is usually approximated to 2/3, appropriate for a dynamic random averaging of the donor and acceptor and this values has been take into account in several works on FRET and it has been used as well in this Thesis.

The energy transfer efficiency E can be calculated by measuring the relative fluorescence intensity of the donor in absence (F_D) and presence (F_{DA}) of the acceptor,

given by:

$$E = 1 - \frac{F_{DA}}{F_D} = \frac{R_0^6}{R_0^6 + r^6} \tag{3.2}$$

Equation 1.2 shows that the transfer efficiency strongly depend on the distance between D and A (r): if r=0.5R_0, then the efficiency is 98.5% and if r=2R_0, the efficiency is 1.54%.

With this set of equation R_0, E and r can be calculated for the two samples I,D-QS-1 and I,D-QS-5 and the values are listed in table Table 3.19.

Table 3.19: FRET efficiency (E), Forster radius (R_0) and distance between D and A (r) of I,D-QS-1 and I,D-QS-5

Sample	**FRET efficiency (E)** %	**R_0** Å	**r** Å
I,D-QS-1	55	55.5	54
I,D-QS-5	92	60	39

In order to have a reasonable estimation of the FRET parameters calculated from the Forster model, the effect of the self-quenching of the donor (DiI) and changes in absorption spectra of the acceptor (DiD), as consequence of the loading into the vesicles must be excluded. For this reason, the values of F_D, φ_D and $\varepsilon_A$used for these calculations are those of the single-dye loaded Quatsomes at the same loading, shown in the Section 3.1.

The values listed in Table 3.19 show that, keeping the equimolar ratio between D and A, there is a strong impact of the total fluorophores content on the FRET efficiency. An almost complete energy transfer takes place in fact in the case of I,D-QS-5, while only half of the energy absorbed by DiI is transfered to DiD in the case of I,D-QS-1. The calculated distances between DiI and DiD are in the same range of the thickness of Quatsomes bilayer (around ≈ 4 nm), therefore we speculate that FRET can occur among dyes located within the same layer of the membrane or either it can be an intra-bilayer energy transfer, occurring between D and A located on the two different leaflets of the bilayer, as schematically represented in Figure 3.36, bottom.

Finally, the influence of k^2 must be taken into account. This parameter particularly depends on the rotational mobility of D and A in the timescale at which FRET occurs, i.e. during the lifetime of the donor, which is in the order of the nanoseconds. In solution,

small molecules have rotational motions of about picoseconds, much smaller than the lifetime of fluorophores. In Section 1.2.3 it has been shown that, upon insertion in Quatsomes bilayer, the carbocyanines (DiI) show diffusion movements comparable to those of a fluid membrane. It is reasonable to think therefore that rotational motion of the dyes in the membrane occur in a much faster timescale than the FRET mechanism. If this is the case, known as dynamic averaging regime, k^2can be approximated to 2/3. Moreover, depending upon the relative orientation of the transition dipole moments of D and A, k^2 is a number between 1 and 4. Since this parameter enters as the sixth root in the calculation of the distance between the two dyes, a variation of $k^2$from 1 to 4 results in an error by no more than 35% in the calculated distance, compared to the case in which k^2=2/3 has been used.

3.2.5 Summary and Perspectives

In this Section we showed a proof of concept that Quatsomes constitute a convenient platform for the nanostructuration of multiple dyes aiming to the design of FRET-based multicolor nanoparticles. Summarizing:

- The simultaneous incorporation of two carbocyanines dyes (DiI and DiD) does not influence the colloidal stability neither the morphology of the fluorescent vesicles. These two dyes constitute a suitable fluorophores FRET-pair once incorporated in Quatsomes and high FRET efficiency has been observed, when DiI and DiD are incorporated in equimolar ratio, depending on the total amount of dye incorporated.

- By checking the energy transfer between DiI and DiD, it has been showed that FRET does not occur between single-dye loaded vesicles and that intervesicular dyes exchange does not occur over one week, confirming that the dyes are stably inserted in the membrane of the vesicles and they do not have tendency to get out of the Quatsomes.

In the future, extensive studies on the possibility of including more than two dyes within the membrane, exploring the possibility of finely tuning the spectral properties of the fluorescent vesicles, are required. Furthermore, exploiting the FRET mechanism would constitute a smart strategy to monitor in real time the structure of the vesicles during the delivery of therapeutic agents, for example, providing details on the efficiency of Quatsomes as drug delivery system.

3.3 Imaging Quatsomes beyond the diffraction limit

3.3.1 Introduction to STORM microscopy

Fluorescence microscopy has gained an essential role in the study of biological events in living cells, tissues and animals thanks to its specificity and noninvasive nature. Compared to electron microscopy (EM), in which samples must be fixed, the main advantages of fluorescence microscopy are the compatibility with living biological samples through the design of minimally invasive experiments and the possibility of imaging dynamic processes. However, while EM provides near-molecular level details of a sample, the main drawback of fluorescence microscopy is the limited spatial resolution [201]. Widely used fluorescence techniques, such as confocal and wide-field microscopy, can resolve the bigger intracellular organelles but cannot resolve two interacting proteins. The resolution limit of a fluorescence microscope is due to the diffraction of light, as observed for the first time by Abbe in 1873. A point light source appears in a microscope as a blurred spot, which is defined as the point spread function (PSF) of a microscope, and if the distance between two emitters is shorter than the width of the PSF, the two emitters overlap with each other and cannot be resolved as two distinct objects [202]. The mathematical description of Abbe's theory affirms that the resolution of a microscope is limited to $\lambda/2n\sin\alpha$, in the focal plane, and $\lambda/2n\sin^2\alpha$, along the optical axis, where λ is the wavelength of the excitation light and $n\sin\alpha$ is the numerical aperture (NA) of the objective lens, *where n* is the refractive index of the medium and α is the semi-aperture-angle of the objective lens. Therefore, with very best optic setups generally the limit of lateral resolution is $\approx$ 200 nm and, in the axial direction it is $\approx$ 500 nm which exclude many biological structures and events, occurring within cells, that are too small to be resolved.

It was only at the end of the 1990s, with the boom in the early 2000s, that fundamentally new techniques revolutionized the concept of microscopy, for the first time breaking the lateral resolution diffraction limit and leading to the so-called "nanoscopy" [7]. These techniques are called "super-resolution imaging techniques", and they can be divided in two categories: a) techniques which utilize patterned excitation beam to directly reduce the size of the PSF, as in the case of the stimulated emission depletion (STED) [7]; b) techniques based on single molecules detection, relying on the principle that a single emitter can be localized with extreme accuracy if sufficient photons are collected. These last family include photoactivated localization microscopy (PALM), fluorescence photoactivation localization microscopy (FPALM) and

stochastic optical reconstruction microscopy (STORM) [203, 204, 205].

Before giving the details of the STORM process and the procedure used for the acquisition of super-resolution images, it is crucial to asses how it is possible to exactly localize emitters smaller than the limit imposed by the diffraction limit barrier. Let's imagine a situation in which a single emitter, e.g. a single fluorophore molecule, is placed under the microscope. If a sufficient number of photons is collected upon the excitation of the fluorophore, the detected light maps out the shape of the point spread function [205, 206], which is a well-known characteristic of each microscope, and it can be fitted with a Gaussian profile whose center corresponds to the location of the emitter Figure 3.37 [204].

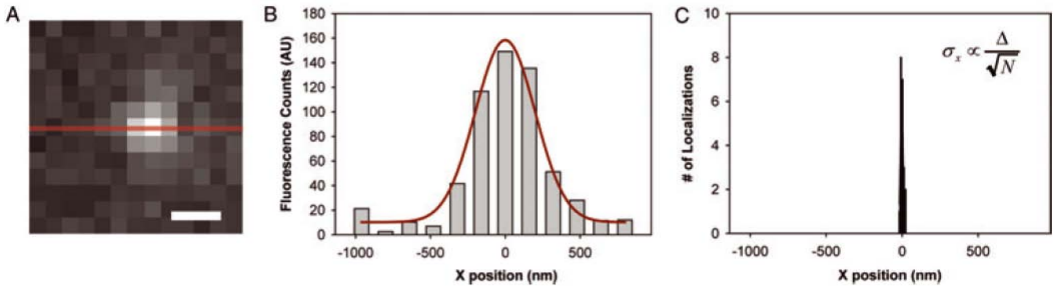

Figure 3.37: Localization of a single fluorophore. (A) Wide-field fluorescence image of a single emitting molecule embedded in a polymer thin film. (B) Photons count of each pixel (a pixel is 160 nm in width) is plotted in function of the distance from the center on the x-direction (red line of A). The data fits to a Gaussian with a high standard deviation (around 200 nm). By acquiring the same image and determining the center of the Gaussian 50 times, the position of the centre can be plotted in function of the x-axis (C), showing a drastically smaller width distribution. Adapted from Ref. [204].

The stochastic optical reconstruction microscopy (STORM) is based on the reconstruction of a fluorescence image from the highly precise localization of individual fluorophores which can be switched on and off by using light of different colors, as schematically represented in Figure 3.38A for an hypothetical hexameric densely-labeled object [207]. STORM imaging consists in following series of imaging cycles. In each step, only a sparse subset of fluorophores is switched on, in such a way that their position can be localized as explained above. Repeating this process, by stochastically turning on and localizing different fractions of the fluorophores in each cycle, it is possible to identify the positions of many fluorophores and, at the end of the process, the overall image can be reconstructed (with a resolution of ≈20 nm). In few words, STORM is based on the precise localization of single emitters and the photoswitching of individual fluorophores.

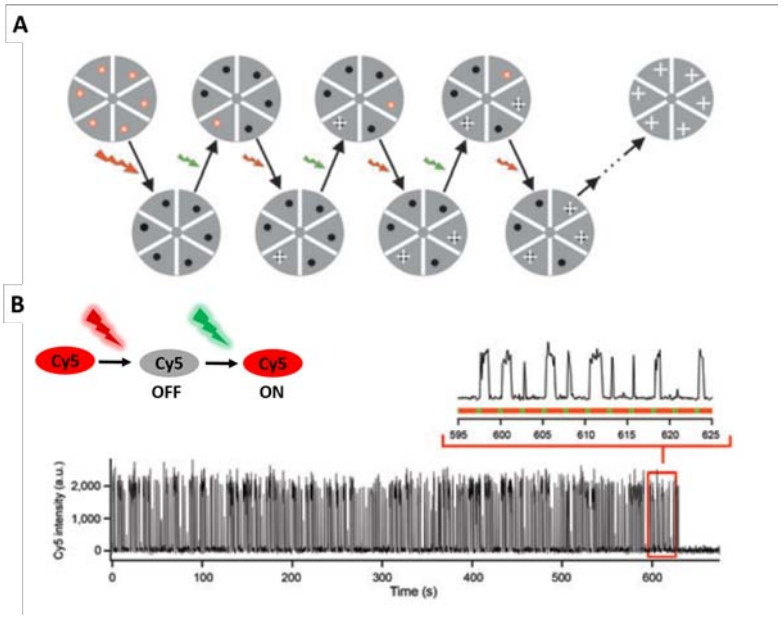

Figure 3.38: Schematic representation of a STORM imaging acquisition. (A) Sequence of cycles using an hypothetical hexameric object densely labeled with photoswitchable fluorophores which can be turned on and off using green and red laser light, respectively (B). At the beginning, all the fluorophores are switched off by the red laser. In each cycle, a green laser pulse activate the emission of only few fluorophores, which can emit until the the red laser switch them off. The photons emitted by these fluorophores in this short time interval permit their accurate localization.

STORM relies on fluorophores able to switch on and off from an excited state to a dark state. When imaging objects with a high density of fluorophores, it is important to control the concentration of the emitting single molecules to be at very low level throughout the experiments, i.e. the equilibrium between dyes which are on and those which are off must be unbalanced towards the off state. There is a wide array of photophysical and photochemical methods to achieve this control, depending on the emitting species [208]. Cyanines have been intensively studied as photoswitches for super-resolution techniques, including STORM, because the equilibrium between dark and emissive state can be tuned in several ways, including energy transfer to other dyes and the formation of a non-fluorescent product by reacting with thiols [207, 209]. The latter method it is widely diffused and it has been used for acquisition of STORM images in this Thesis and it is schematized in Figure 3.39, for the case of Cyanine 5 (Cy5), the water-soluble analogue of DiD (studied in Chapter 3.1). After illumination with red laser light, Cy5 in the excited state reacts with a thiol which “breaks” the conjugated polymethine chain forming a non emissive species. The dark-state specie has a characteristic absorption in the UV (around 310 nm) and, illumination with UV light, leads to the reversion of the molecule back to its fluorescent state [210].

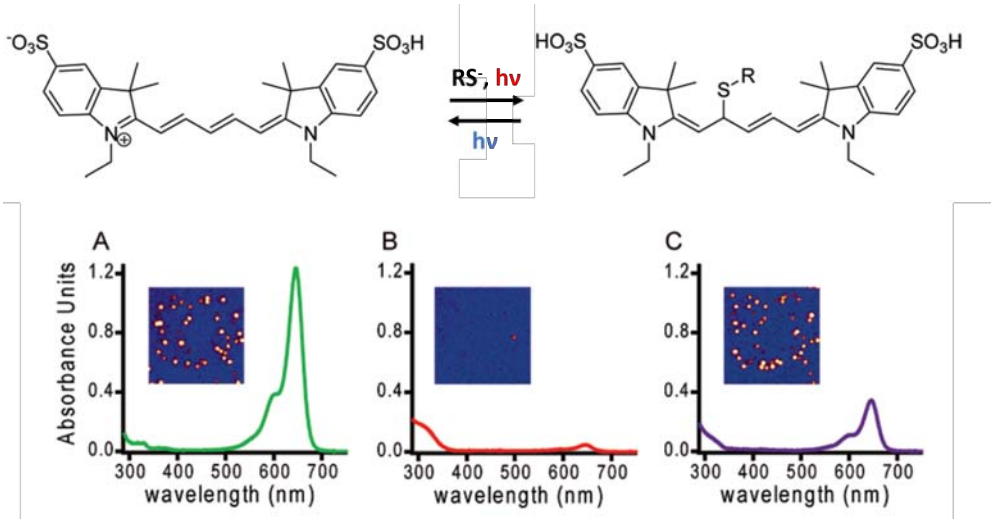

Figure 3.39: Top) Proposed photoswitching mechanism between emissive and dark state of Cy5 in presence of thiols. Bottom) Spectral analysis of the photoconversion of Cy5 in presence of thiols. (A) Absorption spectra of Cy5 with an inset which shows single fluorophores anchored to a surface. (B) After excitation with red laser, the Cy5 spectra disappear and a blue band at 310 nm appears. (C) Under UV illumination, the absorption of Cy5 at 650 nm is recovered. Adapted form Ref. [210]

Recently, STORM has been used to study the interactions between sub-difracction nanoparticles and cellular structures, allowing to acquire information on their internalization mechanism and exact localization within cells, for example. Apart of the really high resolution, analysis of STORM images provides the possibility of acquiring quantitative information at the single molecule level. For instance der Zwaag et al. recently explored the potential of STORM to obtain quantitative information on the cellular uptake and trafficking of different carriers used in nanomedicine, including silica and poly-lactic acid nanoparticles, as shown in Figure 3.40 [211]. The comparison between wide-field and STORM shows the dramatic increase in resolution. Moreover they were able to observe, for the first time with a technique different from electron microscopy, an on-going membrane engulfing of an individual nanoparticle. Image analysis allowed furthermore to get information on the nanoparticles size distribution after internalization in cells.

In other recent works, STORM has been used to acquire information on the self-assembly of supramolecular structures and the dynamics of their monomers, which are thought to have a strong impact on their performance as drug carriers. Monomer exchange pathways have been observed by STORM, for instance, in 1D supramolecular self-assembled fibers [212] or an insight on the dynamics of the of peptide amphiphiles, used as artificial components for cell signaling, showed that generally exchange of monomers and small clusters are involved [213].

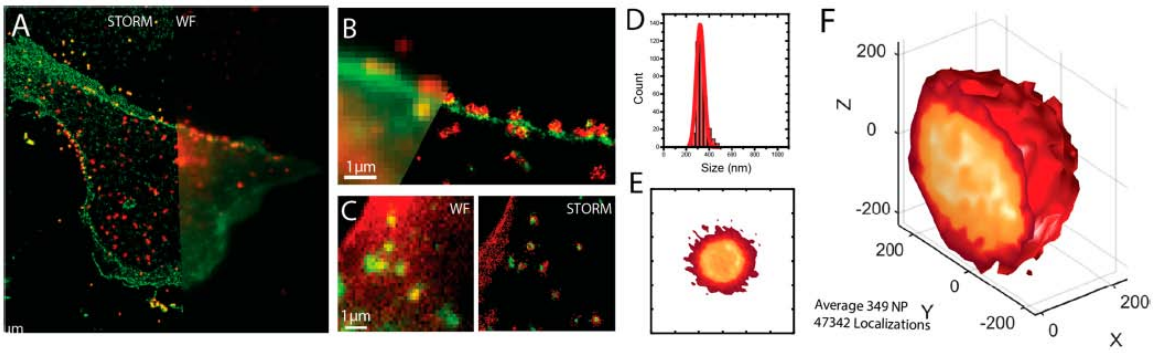

Figure 3.40: STORM imaging of ovalbumin(OVA)-coated polystyrene nanoparticles and their internalization by dendritic cells. A) Widefield (WF) and STORM comparison of dual color imaging of membrane (green) and OVA-NPs (red). B) Magnification of the membrane highlighting the exact position of the NPs close to the membrane after internalization. C) Co-localization of OVA-NPs (red) with endosomal vesicles (yellow), the overlap of yellow and red color in the STORM image suggests the localization of the OVA-NPs inside the endosomes. D) Size distribution of the internalized OVA-NPs by STORM image analysis. E), F) 2D and 3D reconstruction of the average of 350 NPs internalized in 20 different cells. From Ref. [211].

3.3.2 STORM imaging of fluorescent cyanine-loaded Quatsomes

Within this context and in collaboration with the group of Dr. Lorenzo Albertazzi at the Institute de Bioingenieria de Catalunya (IBEC), we decided to test Quatsomes, which have sizes well below the light diffraction limit, labeled with cyanines as nanoprobes for STORM imaging. Thus, a preliminary study has been carried out exploring the possibility of resolving Quatsomes structure by STORM, also after internalization in cells, and withdrawing at the same time quantitative information at the molecule level from the images analysis.

In order to explore the possibility of using STORM microscopy to resolve Quatsomes structure, some of the DiI- and DiD-loaded Quatsomes studied in Section 3.1 were tested. The samples used, I-QS-1 and D-QS-1, and their size distributions measured by Dynamic Light Scattering (I-QS-1) and Nanoparticle Tracking Analysis (D-QS-1) are listed in Table 3.20. In Figure 3.41, an insight on the morphology of I-QS-1 and D-QS-1 samples is given along with their normalized UV-vis absorption and emission spectra. The samples constitute of small unilamellar vesicles and their spectral characterization suggests that the fluorophores are mainly distributed as single fluorophores over the membrane of the vesicles and both exhibited good brightness (fluorescence quantum yield around 20% and 23% for I-QS-1 and D-QS-1 samples, respectively).

Table 3.20: Samples studied in this section and corresponding size distribution over 2 months

Sample	[L][a] $\times 10^{-3}$	Size distr.(1 week)[b] (nm)	Size distr.(2 months)[b] (nm)	Z-potential[b] (mV)
I-QS-1	0.6	72±43	69±52	82±18
D-QS-1	0.6	96±40	114±33	-

[a] [L]=moles$_{dye}$/(moles$_{chol}$+moles$_{surf}$). See Experimental Section 7.5.2 for details on determination of [L].

[b] Size distribution and Z-potential of I-QS-1 measured by DLS. Size distribution of D-QS-1 measured by NTA. Size distribution is shown as the mean average hydrodynamic diameter ± mean PdI. See Experimental Section 7.4.2 for details

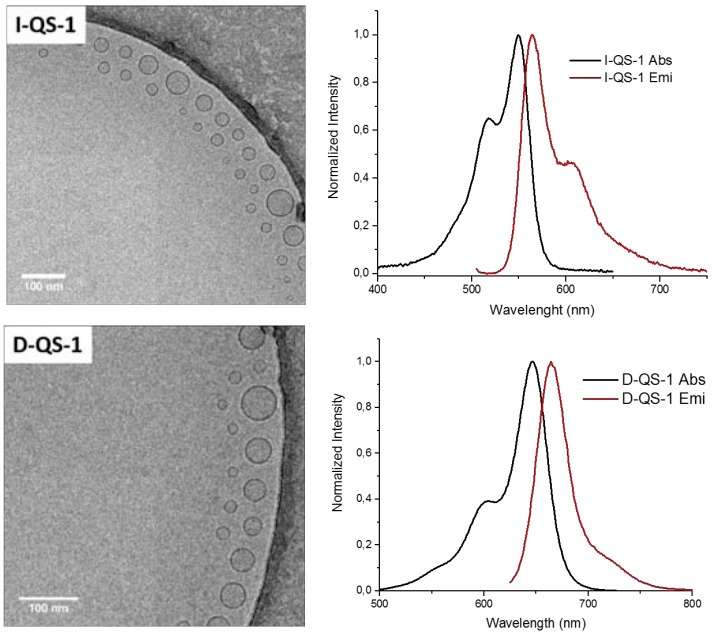

Figure 3.41: CryoTEM images and normalized UV-vis absorption and emission spectra of I-QS-1 (top) and D-QS-1 (bottom)

In Figure 3.42 (A), the steps for the acquisition of STORM images of DiI-loaded Quatsomes are schematically represented. The methodology is described in details in Section 7.8 of the Experimental Part. In few words, by simply adding a drop of the sample, I-QS-1 vesicles are immobilized by adsorption onto a glass surface of the microscope slide, likely thanks to the interaction between the strong positively charged surface of Quatsomes and negatively charged dissociated silanol groups on the surface of the glass. After 1 min of incubation, the vesicles not attached to the glass were removed by washing with MilliQ water and then with the STORM buffer. The STORM buffer contains the aminothiol (cysteamine, 100 mM), necessary for the photoswitching

of the cyanines. Afterwards, the slide was placed under the microscope for STORM images acquisition. For each image, 20,000 frames were acquired and analyzed by the Nikon NIS software, which gives as result an image with the localization (shown as white crosses in Figure 3.42B) of each fluorophore detected. To avoid overcounting, blinkings detected in consecutive frames are counted as single by the software. Finally, the images are post-processed and then analyzed, as explained in the Experimental Part, to obtain information about nanoparticles size and number of localization per vesicles.

Each cross in Figure Figure 3.42B corresponds to a fluorophore localized during the STORM acquisition, as clearly visible in the zoom in Figure 3.42C. Figure Figure 3.42D and C correspond to the same zoomed area, but in D, the 2D Gaussian intensity distribution of each localization is represented (analogously to the mechanism shown in Figure 3.37). In this way, the sum of the different intensities attributed to each localization results in highly luminous spots in correspondence of the Quatsomes and irrelevant background intensity.

The spots in which the density of localizations is higher correspond to single Quatsomes, which can be then successfully resolved by STORM. Some fluorophores are localized sparsely in the background, probably due to the high tendency of the carbocyanines to stick to the glass. However, due to the high concentration of fluorophores within the vesicles, Quatsomes can be discriminated by applying a density filter, which excludes the sparsely distributed fluorophores in the background from the high dense conglomerate.

In Figure 3.42E, the improvement in resolution obtained by STORM is shown. The two picture of the same region acquired by STORM and widefield (WF) microscopy evidence that thanks to the single localization of the fluorophores it is possible to properly resolve individual Quatsomes, while the WF gives only blurred image in which the luminescent objects are barely distinguishable.

The distribution of localizations in correspondence of the Quatsomes in Figure 3.42 seems rather uniform, meaning that there is no evidence of segregation or preferential accumulation of the fluorophores in specific zones of Quatsomes, supporting the spectroscopic results showed in the previous Sections, which evidenced a uniform distribution of isolated molecule of DiI within the membrane of I-QS-1 sample.

Apart of the capability of resolving single Quatsomes, STORM allows to achieve statistical information at the single molecule level, e.g. counting fluorophores in the image. A density-based algorithm was used to separate the background localization from the individual clusters of localizations corresponding to Quatsomes, as explained in the Experimental Part. Individual vesicles were then fitted as circles to determine

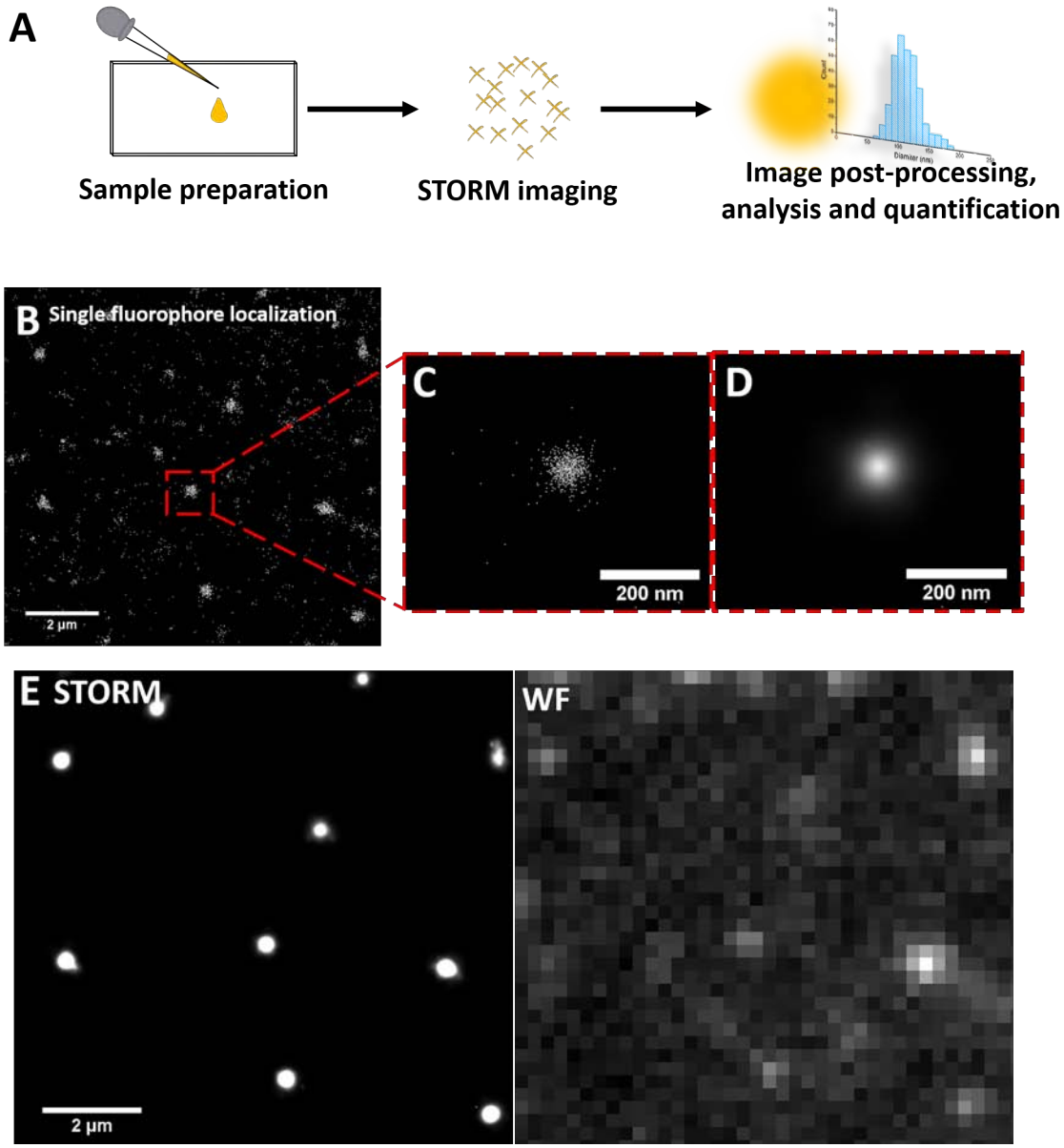

Figure 3.42: STORM imaging of DiI-labeled Quatsomes adsorbed on a glass surface. A) Schematic representation of the methodology used, comprising sample preparation, STORM imaging and data analysis. B) Single fluorophores localization, showing higher density of localized fluorophores in correspondence of Quatsomes. C, D) Zoom of a single Quatsomes, showing either the single localizations or the reconstruction attributing a 2D Gaussian fit to each localization. E) Comparison between a portion of the sample imaged by STORM (left) and widefield (right) microscopy.

information about the size and number of localizations within the fitted circles. As quality check, the circles containing too few localizations have been discarded, as they were considered not reliable for an accurate reconstruction. This procedure allows the automatic quantification of a large number of vesicles and, subsequently, quantitative information can be withdrawn. In Figure 3.43 the size distribution and the number of localization per Quatsomes obtained by STORM images analysis are shown.

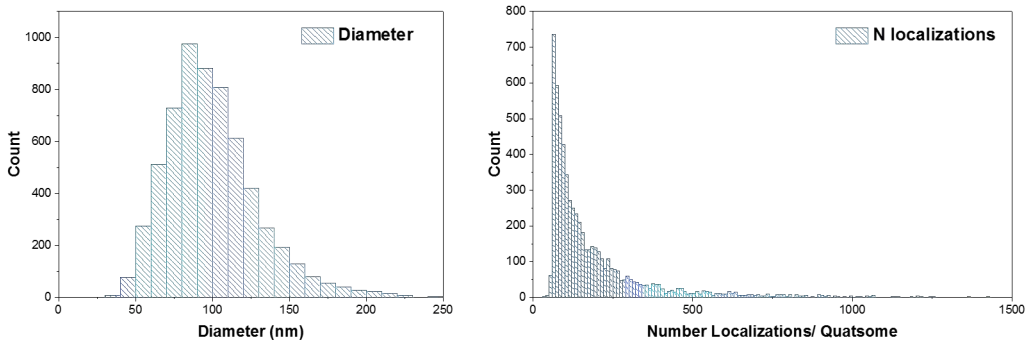

Figure 3.43: Statistic information extrapolated by the STORM images of DiI-labeled Quatsomes A) Size distribution of the resolved vesicles; B) Distribution of number of localization per single Quatsomes. 6137 vesicles analyzed in total.

The size distribution obtained by analyzing the STORM images (Figure 3.43A) reveals that the mean size of resolved Quatsomes (6137 in total) is around 99 nm, the mode is around 85 nm and very few vesicles have sizes higher than 200 nm. Comparing these values with the sizes of the vesicles detected by the CryoTEM images (I-QS-1 micrographs in Figure 3.41), Quatsomes appear a bit smaller under the electron microscope. This may be the effect of the adsorption over the glass cover, which could cause the flattening of the spherical vesicles. The histogram in Figure 3.43B shows the distribution of number of localizations per each Quatsomes, i.e. how many fluorophores have photoswitched during STORM acquisition in each circle attributed to the Quatsomes. Among the 6137 vesicles analyzed, more than 90% have less than 500 localizations and the mean of the distribution is of 193 localizations. This demonstrate the ability of such formulations to nanostructurate a high number of dyes into a small vesicles size. However, it must be remarked that the number of localizations per Quatsome may not coincide with the number of fluorophores actually incorporated within the membrane of the vesicles. During STORM imaging, in fact, it may happen that one fluorophore is photoswitched and detected more than once or that only a part of the population within each vesicles is detected and some fluorophores stay in their dark states for the entire imaging time interval. Nevertheless, even considering these number

as a very rough estimation of the number of dyes per vesicles, they agree with the theoretical number of dyes per vesicles estimated in Chapter 3.1.1. In that case, aware of the errors given by Nanoparticle Tracking Analysis in the measurement of particles concentration, it was estimated that each Quatsome (at the same dye loading used for STORM imaging) contains around 10^2 fluorophore, a number not far from what revealed by STORM images analysis.

Finally, we explored the possibility to image Quatsomes within cells by using STORM. Some super-resolution techniques, e.g. STED, have a temporal resolution which permits to acquire images of nanoparticles internalization in living cells beyond the diffraction limit. The acquisition rate is indeed in the same time-scale of dynamic processes occurring within cells. Single fluorophore-based techniques, such as STORM, require the acquisition of thousands of frames to reconstruct an image and this process takes from several seconds to minutes. Despite some works in literature report successful live cells imaging with STORM [214, 215], in order to localize the Quatsomes within HeLa cells after uptake, we first administered cyanines-loaded Quatsomes to cells (for 1.5 hours) and then cells were fixed for STORM imaging acquisition (see Experimental Section 7.8 for details).

Figure Figure 3.44 shows the Differential Interference Contrast (DIC) and STORM imaging of DiI-loaded Quatsomes (top) and DiD-loaded Quatsomes (bottom) internalized in HeLa cells.

DIC microscopy is a contrast-enhancing technique that allows the monitoring of the cells structure (cell membranes and nuclei are for example distinguishable). In the case of DiI-loaded Quatsomes, the STORM image shows that the vesicles are non-specifically distributed within the cells. It is likely that Quatsomes are internalized via an endocytosis-based mechanism and therefore they may be incorporated within endocytic vesicles spread inside the cells [211]. The sizes of the detected vesicles suggest that the Quatsomes do not suffer aggregation upon internalization, maintaining their original size.

The scenario is quite different in the case of DiD-loaded Quatsomes (Figure 3.44, bottom). In this case, the red signal is localized almost exclusively in correspondence of the cell membrane and almost no internalization occurred (except for very few red dots detected within the cell). The shape of the detected red structures seems also less round-shaped, compared to the top image (DiI-loaded Quatsomes) suggesting two possible events: a) DiD-loaded Quatsomes undergo rupture during the internalization process, which is unlikely considering that the composition and therefore the physico-chemical properties of DiI- and DiD-loaded Quatsomes are very similar or

exactly the same, being irrelevantly affected by the small differences between the two dyes; b) DiD has a better affinity to the cell membrane and an expulsion from Quatsomes bilayer and, subsequently, the staining of the cell membrane is favored. This last hypothesis could justify as well the presence of irregular red shapes within the membrane, maybe due to some clusters of the fluorophores or preferential labeling of some portions of the cells membrane.

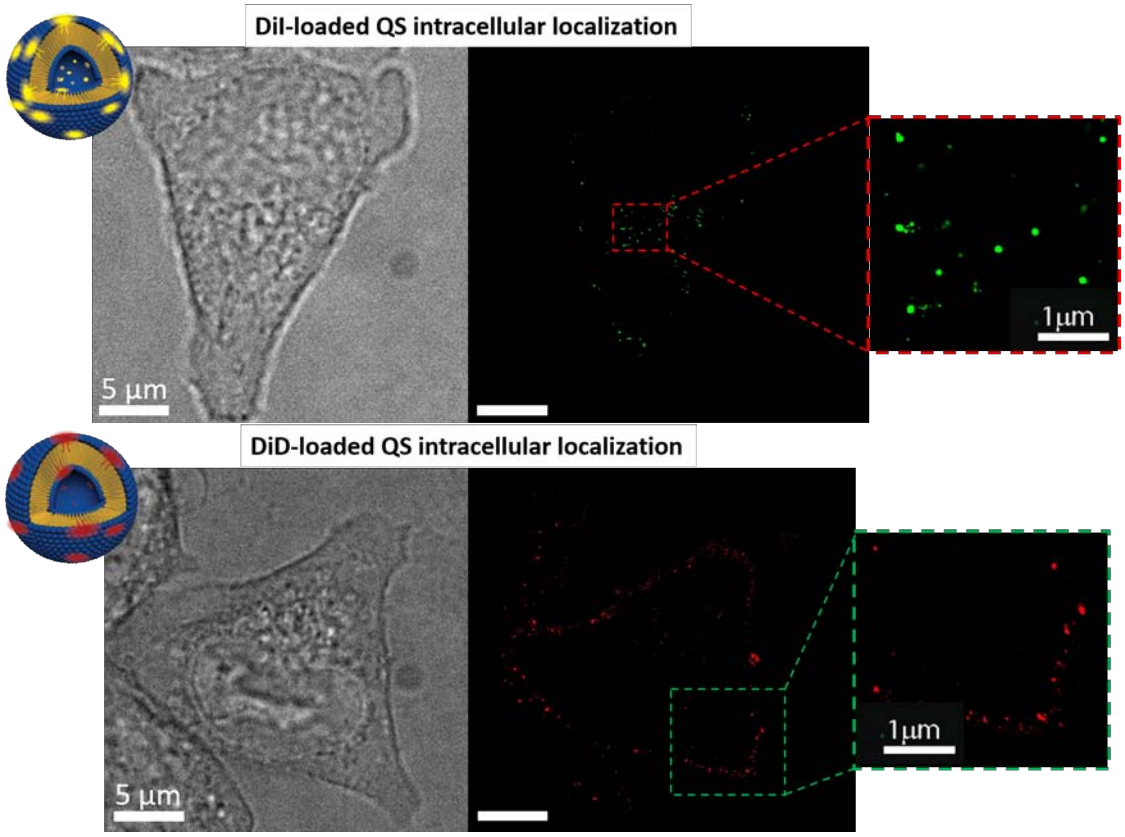

Figure 3.44: Super-resolution imaging of DiI- (top) and DiD-loaded Quatsomes (bottom) internalized in HeLa cells. After 1.5 hours exposition to Quatsomes, cells were fixed and differential interference contrast microscopy (left) and STORM images (right) were acquired.

3.3.3 Summary and Perspectives

In this Section, it has been shown that cyanine-loaded Quatsomes can be successfully resolved by STORM, a super-resolution microscopy technique which permits the detection of single fluorophores within a nanoparticles with sub-diffraction limit size. In particular we have studied and developed:

- A method using the STORM imaging technique for observing single cyanine-loaded Quatsomes, immobilized over a glass surface, which can be well resolved despite their small size.

- The analysis of the images at the molecule level that revealed quantitative information about the size of the vesicles and a rough estimation of the number of dyes localized in each vesicle.

- A preliminary study of the cells upatke of cyanine-loaded Quatsomes by STORM that showed, in the case of DiI-loaded Quatsomes, that the vesicles are internalized and individual Quatsomes are a-specifically localized within the cells. On the contrary, in the case of DiD-loaded Quatsomes, a different behavior was detected, since most of the fluorophores were localized in the cell membrane.

These preliminary results pave the way to a deep investigation about the ability of dye-loaded Quatsomes as intracellular drug delivery system and imaging nanoprobe. An extensive comprehension of the interactions of Quatsomes with cellular and sub-cellular structures, including cells membrane, proteins and subcellular organelles, is in fact a crucial factor for the successful and final development of Quatsomes and their application in nanomedicine.

4

Dispersion of Diketopyrrolepyrrole (DPP) derivatives in water

4.1 Introduction

The interest of scientists towards Diketopyrrolopyrroles (DPP) has been constant since their discovery in the 80s. However, only after the expiration of the patent [216] describing DPPs preparation in 2003, a huge number of scientific works popped up in the literature on this class of colorants [217]. DPP has a planar structure (shown in Figure 4.1) which can induce strong intermolecular interactions, i.e. hydrogen bonding and π-π stacking [218, 219]. There are several advantages that this structure offers: a) an easy and extremely diversified possible synthetic modifications; b) the core is a strong acceptor unit; c) a generally high fluorescence quantum yield; d) an exceptional thermal and photo-stability. Under patent protection they were mainly used as pigments for paint in luxury cars and colorants for polymers. Nowadays, many works exist showing their versatility in applications such as dye-sensitized and bulk heterojunction solar cells, light emitting diodes, organic field-effect transistors, multi-photons absorbing materials and fluorescence imaging [218].

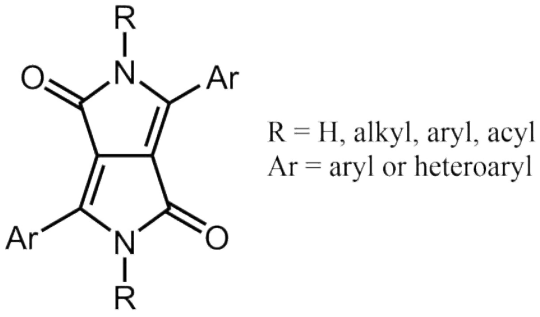

Figure 4.1: General structure of DPP molecules

The general DPP structure can be modified in different ways, obtaining derivatives exhibiting desired physical and chemical properties. Photophysics of this class of molecules can be tuned by modification of the aryl substituent in the lactame groups, for example. Grzybowski et al. [217] obtaiend a π-expanded chromophore with absorption in the near-infrared region by addition of two vinylene moieties between the nitrogen and the aryl substituent. Kaur et al. [220] recently reviewed that many DPP-based fluorescent sensors have been used for tracing biologically and environmentally important species and analytes, including anions, cations, thiols, pH and others. The DPP core can be considered an useful acceptor (A) center for the design of two-photon absorber (2PA) fluorophores showing a high two-photon cross-section, σ_{2p}. By modification with diphenylamine and triphenylamine, that act as donors (D), novel D-π-A-π-D structures with high σ_{2p} (up to 1200 GM) have been designed [221]. Dyes with π-expanded diketopyrrolopyrrole core, with a D-A-D structure, possesses a large intrinsic 2PA in the near-IR range of wavelengths, reaching maximum values of 2000 GM around 1000 nm [222].

The strong intermolecular interactions occurring in DPPs molecules are generally responsible for the low solubility and the high stability of this class of molecules. The introduction of substituents to the nitrogen atoms of DPP drastically change the physical properties of these compounds. N-substituted DPP derivatives are no longer able to form intermolecular hydrogen bonds and therefore their solubility is generally enhanced. Nevertheless the substituent of N atoms can cause a rotation out of the plane of the aryl groups and therefore have effects on the π-conjugation. Recently, some works have been addressed to the improvement of water solubility of these dyes, for example by addition of ionic groups containing a free carboxylic acid function for conjugation with amine-containing biopolymers [223]. Addition of short ethyleneglycol chains also provided a good water solubility to small DPP dyes, allowing their use in 2-P fluorescence microscopy of HeLa cells [224, 225]. However, except of the mentioned cases, only very few works exist in the literature describing feasible strategies to disperse water-insoluble DPP derivatives in aqueous media, making them useful for imaging purposes. As an alternative route to the chemical modification, several authors took advantage of the hydrophobicity of these dyes, processing them as nanoparticles, trying to limit the aggregation-caused quenching (ACQ) effect. Thus, Gao et al. [64], for example, developed a DPP molecule showing aggregated induced emission (AIE) and a good 2-P response and used it for staining of blood vessels. Some other strategies are based on DPP functionalized polymers. For example, Huang et al. [226] prepared a tiophene-DPP which was covalently linked to a biodegradable polymer chain. The

resulting nanoparticle were strongly bright thanks to the suppression of π-π stacking among the DPP chromophores.

To our knowledge, no studies have been reported in the literature on the incorporation of water-insoluble DPP derivatives in vesicles, describing the relationship between the supramolecular structure and optical properties and showing their potentiality as fluorescent probes for bioimaging.

The two DPP derivatives studied in this Thesis, DPPC8 and DPPC16, were synthesized in Prof. G. Farinola's laboratories at the Università degli Studi di Bari Aldo Moro and their structures are shown in Figure 4.2.

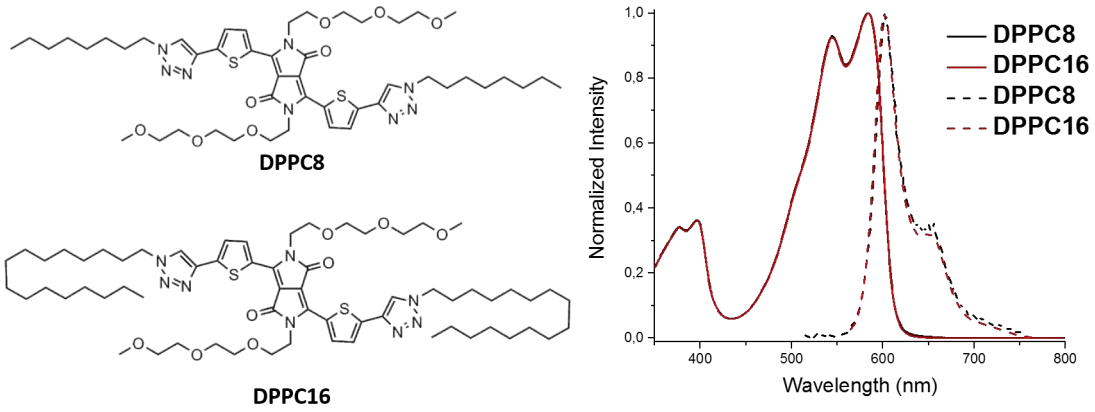

Figure 4.2: Molecular structures of DPPC8 (top) and DPPC16 (bottom) and normalized UV-vis absorption and emission spectra of the two molecules in acetone

Both molecules are thiophene-functionalized DPP (TDPP), which have attracted attention thanks to the strong intramolecular charge transfer between the electron-deficient core and the two electro-donating tiophene rings and thanks to the strong π-π stacking, which is often associated to good charge transport. Moreover, the polar triethylene glycol (TEG) chains are good stack-inducing agents for DPP-derivatives. For this reason TDPPs have been studied in organic field effect transistors [227] and to improve photovoltaic polymers efficiency [228]. Although in some previous cases, PEG chains have been used to improve water solubility [225], DPPC8 and DPPC16 are water insoluble, but the introduction of this hydrophilic moiety improves their processability in polar solvents, such as ethanol, and confers an amphiphilic character to these molecular structures. Two 1,2,3-triazole moieties, linked as terminal rings to the central TDPP core, increase the electron donating character of the DPP substituent and actively participate to the hydrogen bonding as well as π-π stacking interactions. By mean of the triazole groups it was possible to synthesize a whole family of TDPP dyes tuning their

polarity, solubility and their intermolecular interactions. Details on synthesis are reported in [229] along with some of the results that will be discussed afterwards.

DPPC8 and DPPC16 have identical conjugated structure and, consequently, similar spectral properties, as shown in the UV-vis absorption and emission spectra in Figure 4.2. The two dyes differ only in the length of the alkyl tails bounded to the triazole moieties (C_{16} and C_8 carbons in the case of DPPC16 and DPPC8, respectively).

4.2 Dispersion of DPPC8 and DPPC16 in water

We took advantage of the insolubility of DPPC8 and DPPC16 in water, exploring two different strategies, schematized in Figure 4.3, for their dispersion in aqueous environment, aiming to obtain bright and stable FONs for bioimaging applications. The first one (Figure 4.3, A) consists in the preparation of DPPC8 and DPPC16 nanoparticles (DPP-NP) by re-precipitating them in water. By this method, the strong intermolecular interactions (mainly π-π stacking between the planar fluorophores) lead to the formation of nanoparticles, without further addition of any other compound.

In the second strategy (Figure 4.3, B), we used Quatsomes as an alternative approach to bring in water these two water-insoluble dyes, dispersing them inside the membrane of the vesicles as isolated molecules, aiming to limit the aggregation-caused quenching (ACQ) that may occur due to π-π interactions between the molecules. In Chapter 3, the experimental results supported by Molecular Dynamics (MD) simulations showed that a family of non-water soluble dyes (the carbocyanines), with two C_{18} alkyl tails and a polar chromophore, could be stably incorporated in the membrane of Quatsomes, thanks to the interdigitation of the alkyl tails within the bilayer of the vesicles. The strategy presented here aims to mimic the same mechanism and it is schematically represented in the zoom of Figure 4.3B. The alkyl tails of DPPC8 and DPPC16 are meant to "anchor" the dye to the bilayer of Quatsomes, while the hydrophilic PEG chain could favor the exposition of the fluorophore to the aqueous environment.

Two classes of Quatsomes were used as DPP carriers: Quatsomes named QS, composed by the surfactant CTAB and cholesterol, and another type of Quatsomes, named (C)QS, composed by CTAB and a sterol derivative (hereinafter STER). During the course of this Thesis, it has been found that cholesterol could be entirely substituted by the sterol derivative, obtaining smaller vesicles (mean hydrodynamic diameters around 47 nm for (C)QS, a smaller value compared to the diameter of 75 nm for QS). Therefore, we found interesting to explore whether there is an impact of the composition of the vesicles on the optical properties of the DPP-loaded Quatsomes.

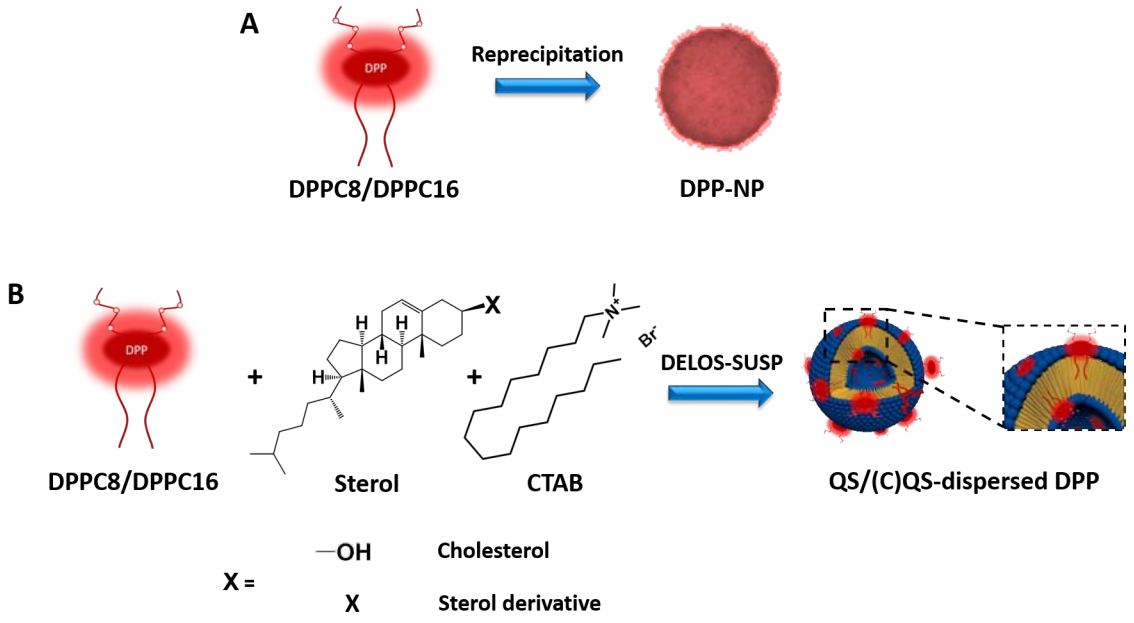

Figure 4.3: Proposed strategies for the dispersion in water of DPPs. (A) Reprecipitation for the formation of DPPs nanoparticles (DPP-NP); (B) self-assembly with a sterol and CTAB for the formation of DPP-loaded Quatsomes. Two different types of Quatsomes have been used with the latter strategy: QS, formed by CTAB and cholesterol, and a variation of Quatsomes, (C)QS, formed by CTAB and a sterol derivative.

As previously mentioned, DPPC8 and DPPC16 have identical structure, except for the length of the alkyl tails, which can severely affect the hydrophobic/hydrophilic balance of the molecule and have a strong impact on the supramolecular organization of the dyes and the optical properties of the obtained FONs. Especially concerning the insertion of the two fluorophores in the Quatsomes membranes, it must be pointed out that the aliphatic chain of DPPC16 matches that of the CTAB, while the tail of DPPC8 is half the length of the surfactant one.

In the next Section the effect of the aliphatic chain length on the supramolecular organization, colloidal and optical properties of DPPC8 and DPPC16 will be studied in detail.

4.2.1 Preparation of the DPPC8- and DPPC16-based FONs

Preparation of DPPC8-NP and DPPC16-NP DPPC8- and DPPC16-NPs were prepared with the one-step reprecipitation method, as explained in detail in the Experimental Section 7.3. Using this procedure, it is possible to obtain nanospheres of a hydrophobic compound simply by adding to water (under vigorous stirring) a small volume of a solution of the compound in an organic solvent which is miscible in large

extent with water, as for example acetone [54, 55]. In few words, 250 μL of a concentrated solution (0.4 mM) of DPPC8 (or DPPC16) were dropped over 9.75 mL of MilliQ water under vigorous stirring. A blue-violet suspension of DPPC8-NP (or DPPC16-NP) with 10 μM dye concentration is obtained.

Preparation of DPPC8-QS, DPPC16-QS and DPPC16-(C)QS DPPC8-QS, DPPC16-QS and and DPPC16-(C)QS were prepared by the CO_2-based methodology DELOS-SUSP, using the configuration shown in Experimental Section 7.2.1. In the three cases, a molar ratio 1:1 between the sterol (cholesterol or STER) and CTAB was used. Analogously to the procedure shown in the previous Chapters for the preparation of dye-loaded Quatsomes, DPPC8 (or DPPC16) was dissolved in EtOH along with the cholesterol (or STER) and then loaded into the reactor at the temperature of 45°C. Afterwards, the standard procedure for the preparation of dye-loaded Quatsomes, indicated in the Experimental Section 7.2.1, was followed. In particular, for the preparation of QS, 111 mg of cholesterol were used and, for the preparation of (C)QS, 139 mg of STER were used. However, although the phase behavior of the cholesterol/CTAB mixtures had been deeply studied in the past, during Dr. Lidia Ferrer-Tasies's Doctoral Thesis, the mixture STER/CTAB has not been studied in such a detail so far. Nevertheless, during the course of this Thesis, it has been empirically observed that STER and CTAB in 1:1 molar ratio, when processed by DELOS-SUSP, form a population of unilamellar vesicles with a mean hydrodynamic diameter of around 50 nm. For this reason, this composition was selected for studying the dispersion of DPPC16 in (C)QS.

In the case of DPPC16-loaded Quatsomes, three samples (DPPC16-QS-1, -2 and -3) with the same amounts of cholesterol and surfactant but different amounts of DPPC16 were prepared, in order to study how the fluorophore loading, [L], affects the colloidal and optical properties of the resulting FONs. As already mentioned, [L] is defined as the molar ratio between the probe and Quatsomes membrane components: $[L]=moles_{dye}/(moles_{sterol}+ moles_{CTAB})$. The amount of dye in the samples was measured by UV-vis spectroscopy, while the amounts of sterol and CTAB used for the calculations of [L] were the nominal ones, i.e. the quantities weighted at the beginning of the process (see Experimental Section 7.5.2 for details on calculation of [L]). In this way, the same concentration of vesicles in every batch is likely obtained, but each one containing a different number of fluorophores per vesicle. After their preparation, the samples were purified by diafiltration (see Experimental Section 7.2.2) and stored at 4°C for one week before analysis. For each sample, at least two batches were prepared, in order to check the reproducibility of the results and negligible differences were found in all the studied

cases.

Table 4.1: DPPC8- and DPPC16-based FONs studied in this Chapter and their corresponding composition

Sample	[L][a] $\times 10^{-3}$
DPPC8-QS-3	0.6
DPPC16-QS-1	0.2
DPPC16-QS-2	0.29
DPPC16-QS-3	0.6
DPPC16-(C)QS-3	0.63
DPPC8-NP	-
DPPC16-NP	-

a [L]=$\text{moles}_{\text{probe}}/(\text{moles}_{\text{sterol}}+\text{moles}_{\text{CTAB}}$. See Experimental Section 7.5.2 for details on determination of [L]

4.2.2 Colloidal properties of the DPPs-based FONs

Colloidal properties of DPPC8- and DPPC16-NP

The TEM images of DPPC8-NP and DPPC16-NP 1, 4 and 7 days after their preparation are shown in Figure 4.4. Uranyl acetate was used as a contrast agent for a better acquisition of the images.

One day after the preparation, DPPC8 nanoparticles, DPPC8-NPs, show a lamellar rod-like shape, 40 nm wide and 100 nm up to few μm long. The size of these rods significantly increases four days after the preparation, assuming a conformation more similar to nano-wires and the shape and size are maintained until seven days.

DPPC16-NPs have a similar morphology to the DPPC8 ones one day after the preparation, although they have a higher tendency to form clusters when adsorbed onto the TEM grid. Nevertheless the initial aspect ratio of these nanoparticles is maintained over the whole week.

The aggregation and size variation of DPPC8-NPs was followed as well by Nanoparticle Tracking Analysis (see Experimental Part 1.3.2), which allows to estimate the particles concentration, shown in Figure 4.5.

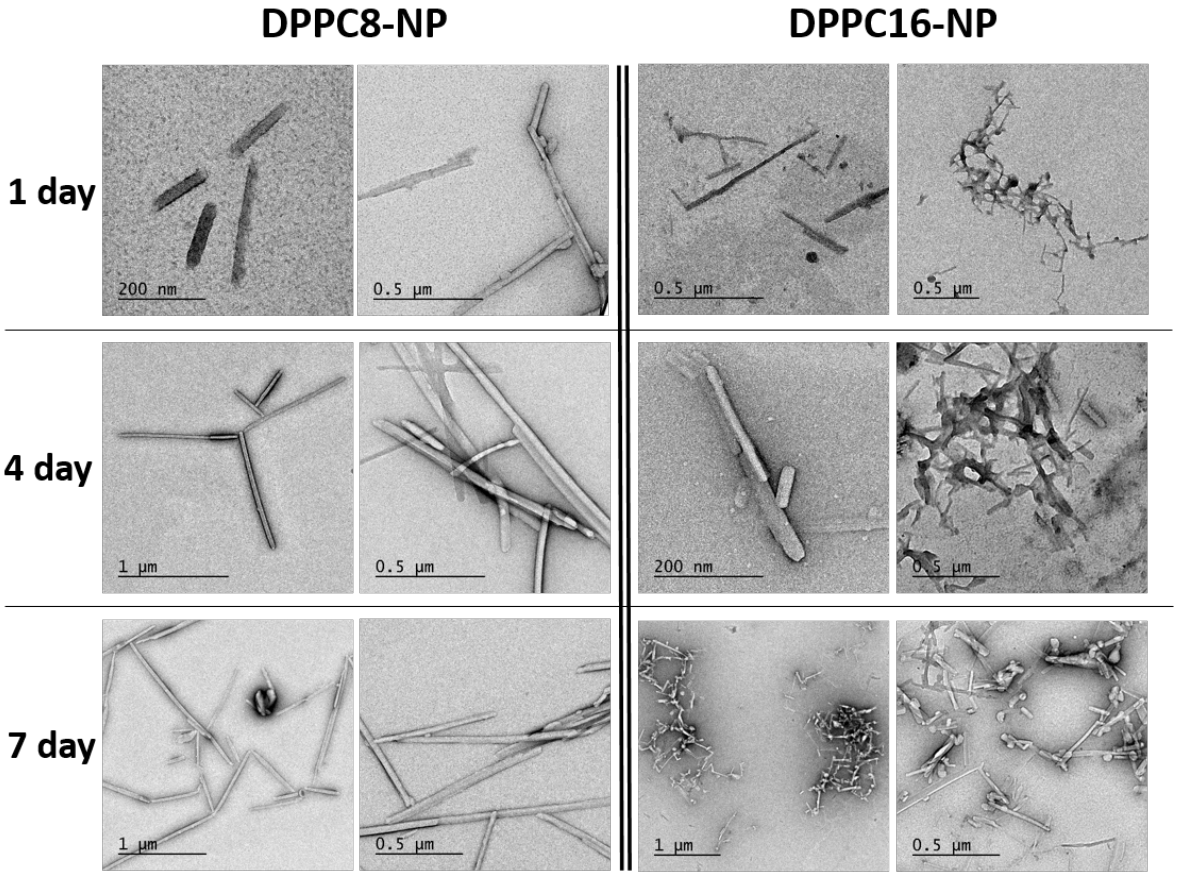

Figure 4.4: TEM images of DPPC8-NP and DPPC16-NP 1, 4 and 7 days after the preparation by reprecipiation method. Uranyl acetate was used as contrast enhancer agent. METTI PIU DESCRIZIONE

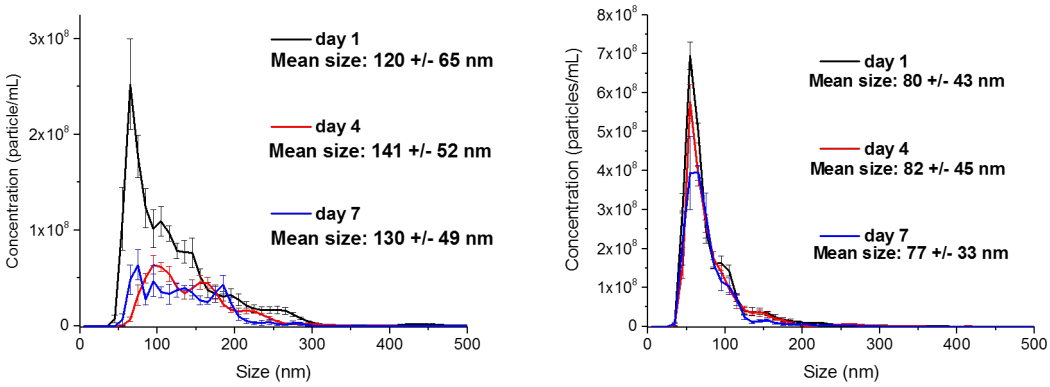

Figure 4.5: Size distribution of DPPC8-NP (let) and DPPC16-NP (right) 1, 4 and 7 days after the preparation.

NTA data support the TEM images, evidencing the dramatic change of DPP-C8 NPs size distribution profile (Figure 4.5, left) along the week after the preparation. The number of particles present in the system dramatically decreases in few days (area under the curve after four and seven days is 40% and 35%, respectively, of the initial value) and the population looks more flat over the whole size range, indicating the ongoing aggregation of the nanoparticles.

NTA size distribution of DPPC16-NP (Figure 4.5, right) shows a much slower aggregation process (82% and 73% after four and seven days, respectively, of the area under the size distribution at day one).

Notably, the mean size values provided by NTA, around 120 nm and 80 nm for DPPC8- and DPPC16-NPs at day one, respectively, do not coincide with the real sizes shown by the TEM images. This is the consequence of the principle of operation of NTA (see Section 7.4.3 of the Experimental Part), which in fact refers to the hydrodynamic diameters, i.e. the diameter of a sphere that has the same translational diffusion coefficient as the particle. So, NTA measures can fail and give misleading results when nanoparticles having different shapes than spheres are measured, as occurs in this case.

The cryoTEM images of DPPC8-NPs are shown in Figure 4.6 and will be useful for the discussion of results shown in the following Sections. The main advantage that cryoTEM offers, compared to TEM, is that images can be aquired without evaporating the solvent in which the particles are dispersed. This means that nano-objects can be imaged in their natural environment, avoiding their denaturation. Generally, in the case of cryoTEM, a higher concentration of particles is required compared to normal TEM. While in the case of DPPC16-NPs it was impossible to acquire any cryoTEM image, fortunately, few images of DPPC8-NPs could be acquired. This may be due to a better affinity between DPPC8-

NPs surface and support grid of CryoTEM and images like the ones showed below could be acquired.

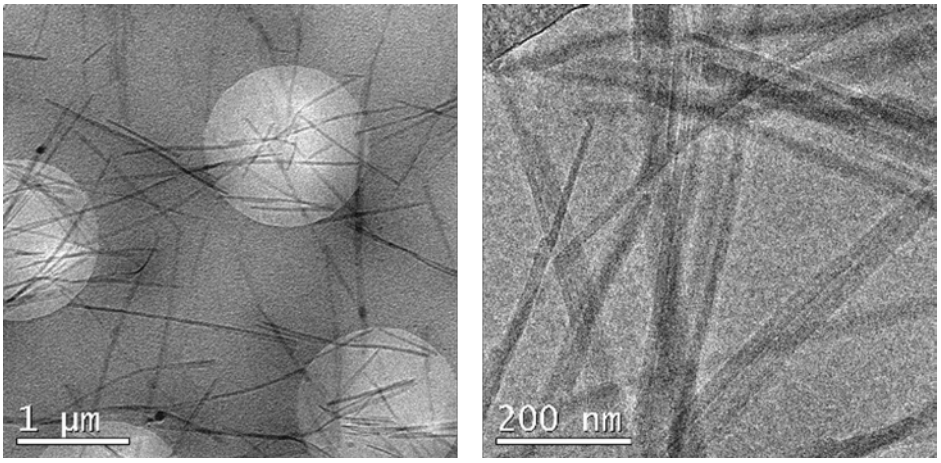

Figure 4.6: DPPC8-NPs CryoTEM micrographs acquired one week after the preparation.

Nanoparticles of DPPC8 at the cryoTEM look as same as in the TEM images, confirming the aspect ratio of these particles, with dimension of 40 nm wide and few µm long.

The tendency of tiophene-based DPPs molecules with two C_{16} alkyl chains to self-assemble on surfaces into highly orientated and elongated strips was recently shown by Wu et al. [230]. The authors of this work attributed the formation of these structures to the close packing of the conjugated backbones (with H-bonds between the C=O of the DPP unit and the hydrogen of the tiophene rings of the neighboring molecule) with the alkyl tails arranged in straight lines at the two sides of the conjugated bones. Although a similar mechanism could occur in the cases studied in this Chapter, the reason why both DPPs derivatives give nanorods when reprecipitated in water is not known and it requires further investigation.

Colloidal properties of DPPs-loaded QS and (C)-QS

In Figure 4.7, CryoTEM micrographs of the DPPC8-QS-3 (bottom) and DPPC16-QS-3 (top) one week and one month after their preparation are shown. The mean hydrodynamic diameters and size dispersions of the samples, measured by DLS, are listed in Table 4.2. Details on size distribution measurements of DPPs-loaded Quatsomes are given in the Experimental Part 1.3.1.

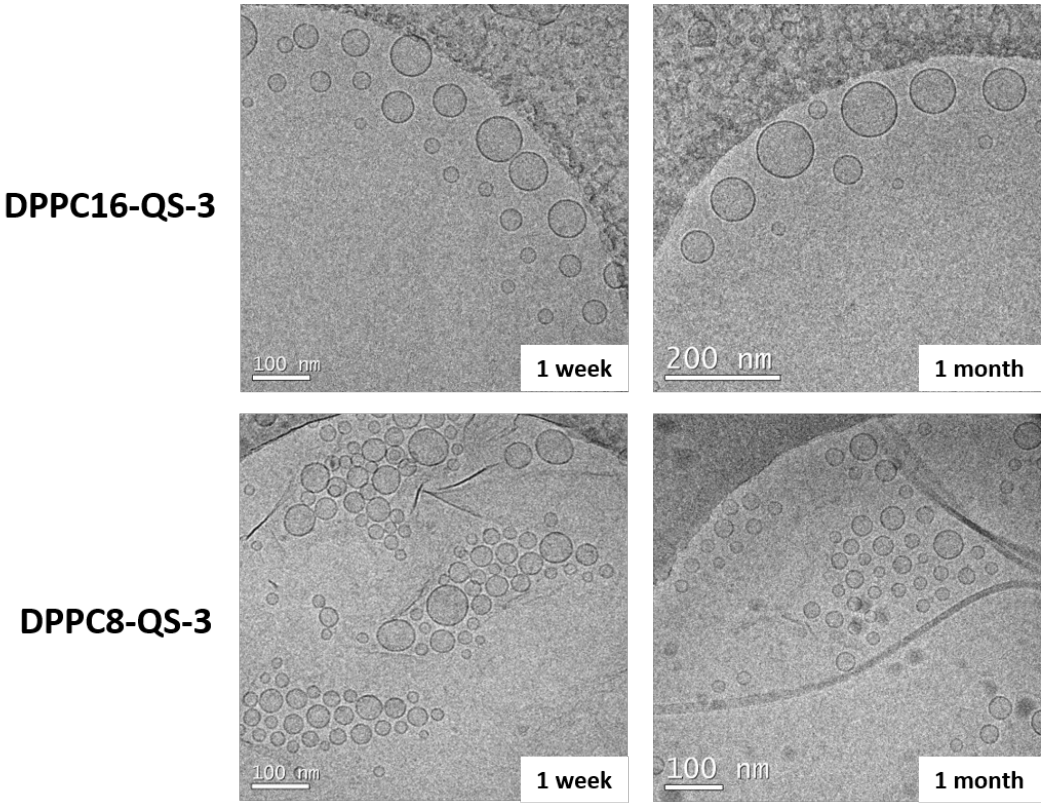

Figure 4.7: CryoTEM micrographs of QS-C16 (top) and QS-C8 (bottom) one week and one month after the preparation

DPPC16-QS-3 sample is made of vesicles with average size of less than 100 nm (measured by DLS, see Table 4.2). The sample is highly stable regarding both size and morphology, since no relevant changes were observed over time. Similar results have been obtained for the samples containing lower amounts of DPPC16, DPPC16-QS-1 and DPPC16-QS-2 (cryoTEM images not shown). On the contrary, micrographs of DPPC8-QS-3, one week after the preparation, evidence the formation of small nano-aggregates with a sheet/lamella twisted shape at the edges, along with several unilamellar nanovesicles. In few weeks, rod-like architectures appear, with one dimension of few nm and lengths up to several micrometers, showing similar aspect as the nanoparticles of DPP-C8 (DPP-C8 NPs), previously described and shown by cryoTEM images in Figure 4.6.

Since in the two cases the dyes have been dispersed in water, by using vesicles with the same composition (cholesterol and CTAB) and using the same prepation steps, likely the driving factor determining both morphology and stability of the two samples is the length of the alkyl tail of the DPPs (see Figure 4.2). Some works on the incorporation of drugs with different alkyl chain length in liposomes showed that, when prepared by thin film hydration, the highest efficiency of incorporation in liposomes is reached when the

length of the drug tail approaches that of the phospholipids constituting the liposomes [231, 232]. We speculate that a similar process occurs in the case of DPPs-loaded Quatsomes. Thus, the aliphatic chain lengths of DPPC16 (16-carbons tails) approaches that of the surfactant (CTAB, which has a 16-carbon chain too) resulting in a higher stable water dispersion of Quatsomes. On the other hand, DPPC8-QS sample is not stable over one month and the changes in observed in Figure 4.7 (bottom) can be associated either to the growth of the sheet/lamella nanoaggregates observed after one week or to the labile anchoring, due to the short alkyl chain of DPPC8 (8-carbons tails), to the QS membrane and the release of the dye to the surrounding media where a supramolecular re-organization occurs.

DPPC8-QS-3 sample can be stabilized by a small fraction of EtOH (10% in volume). Skipping the purification (diafiltration) step of DPPC8-QS-3, in fact, the sample DPPC8-QS-3(10%EtOH) can be obtained, having as same composition as DPPC8-QS-3 but a different dispersing medium (water and EtOH, instead of pure water). Notably, DPPC8 is not soluble in a mixture of EtOH (10% vol) in water. Nevertheless, CryoTEM image of DPPC8-QS-3(10%EtOH), Figure 4.8(left), showed the absence of NPs formation one month after their preparation and the appearance of small Quatsomes, suggesting that there is a strong influence of the composition of the dispersing medium on the supramolecular organization of the dye.

The vesicles obtained by dispersing DPPC16 in STER/CTAB Quatsomes, DPPC16-QS(C)-3 sample, are smaller than those obtained with cholesterol/CTAB QS (mean sizes are 55 nm and 82 nm for DPPC16-(C)QS-3 and DPPC16-QS-3, respectively) and they maintain their shape and morphology over one month (Figure 4.8, right).

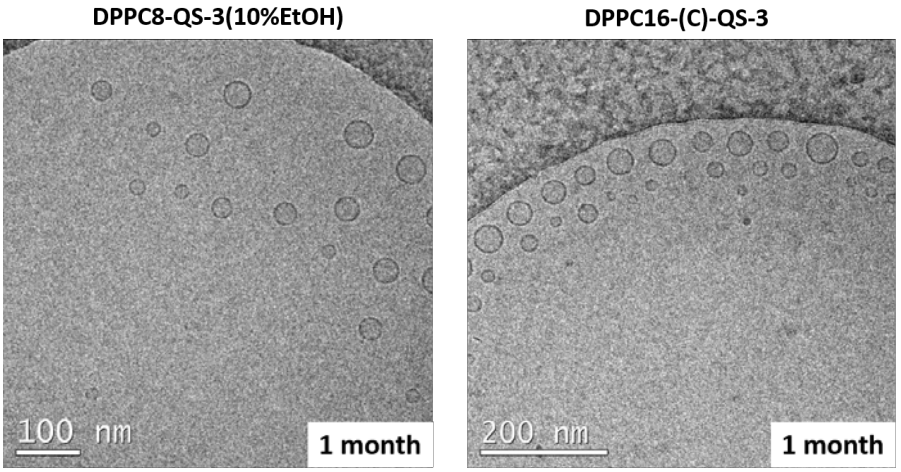

Figure 4.8: Morphology, showed by cryoTEM images, of DPPC8-QS-3(10%EtOH) and DPPC16-(C)QS-3

Table 4.2: Mean hydrodynamic diameters (one month after preparation), measured by Dynamic Light Scattering (DLS) of DPPs-loaded Quatsomes

Sample	Size (1 week)[a] (nm)	Size (1 month)[a] (nm)	Z-potential[a] (mV)
Plain QS	75±43	77±46	86±23
Plain (C)QS	47±26	44±32	72±25
DPPC16-QS-1	92±48	89±49	87±16
DPPC16-QS-2	83±42	80±38	92±21
DPPC16-QS-3	95±47	86±40	90±19
DPPC16-QS-3(10EtOH)	101±52	104±46	71±15
DPPC16-(C)QS-3	55±25	52±25	66±22

[a] Size distribution and Z-potential measured by DLS. Size distribution is shown as the mean average hydrodynamic diameter ± mean PdI. See Experimental Section 7.4.1 for details

4.2.3 Optical properties of the DPPs-based FONs

Optical properties of DPPC8- and DPPC16-NPs

The UV-vis absorption spectra of the nanoparticles of DPPC8-NPs and DPPC16-NPs were monitored over three weeks (Figure 4.9), in order to explore whether a change in the electronic transitions is associated to the change in morphology observed in Figure 4.4.

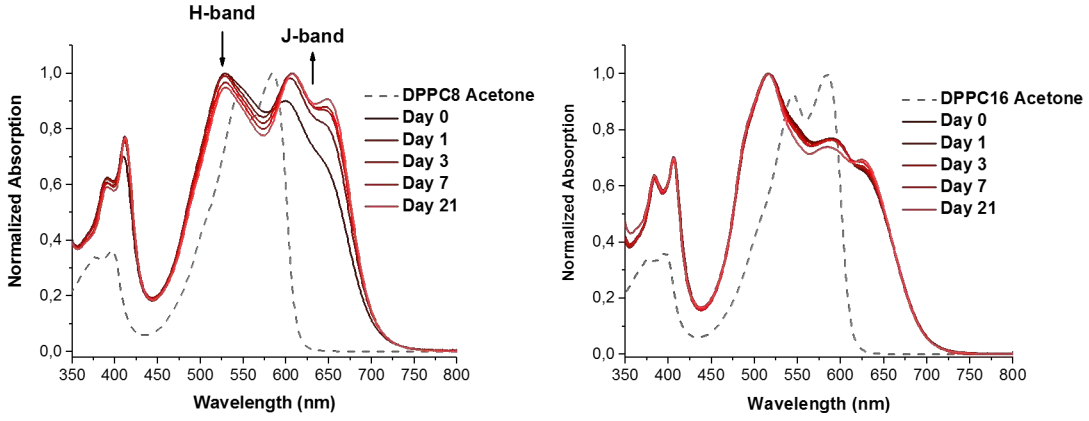

Figure 4.9: Normalized UV-vis absorption spectra of DPPC8-NP (left) and DPPC16-NP (right) monitored over three weeks.

The NPs obtained from both DPPC8 and DPPC16 showed different absorption spectra, as effect of the different length of the alkyl chains linked to the triazole moiety, which sensibly affects the intermolecular interactions and thus the spectral properties of the two suspensions. Both nanoparticles show broader absorption than the molecule in

solution, with the appearance of new peaks in both blue and red regions of the absorption bands. The spectrum of DPPC8-NPs changes over 3 weeks towards the formation of J-aggregates. Thus, whereas after their preparation the maximum absorption was at 528 nm (peak associated to H-aggregates), after 3 weeks the maximum appeared at 607 nm together with another peak at 645 nm (associated to J-aggregates), increased by 36 % in intensity, as shown in Figure 4.9 (left). The structural reorganization in the case of DPPC16-NP is much slower and less intense (Figure 4.9, right), which suggests that the long alkyl chains govern the self-assembly process.

The simultaneous presence of H- and J-aggregates, shown in Figure 4.9, is supported by fluorescence spectroscopy. In Figure 4.10 the UV-vis absorption, excitation and fluorescence spectra of DPPC8-NPs (left) and DPPC16-NPs (right) after three weeks are shown.

The appearance of both H- and J- aggregates bands in the UV-vis absorption spectra of tiophene-modified DPPs (TDPPs) has been already studied in previous works. Kirkus et al. [233] showed that for TDPPs in thin films, two optically allowed electronic transitions are expected, referring to it as Davydov splitting between H-aggregates, blue-shifted, and J-aggregates, red-shifted. The simultaneous occurrence of J- and H-type bands, is attributed to the coexistence of two polymorph structures in the solid. According to the exciton theory, this can give rise to two electronically collective allowed transitions. The relative extent of these transitions is strongly affected by the substituents of the DPP molecules, the TEG chain and the alkyl tails in the case of DPPC8 and DPPC16.

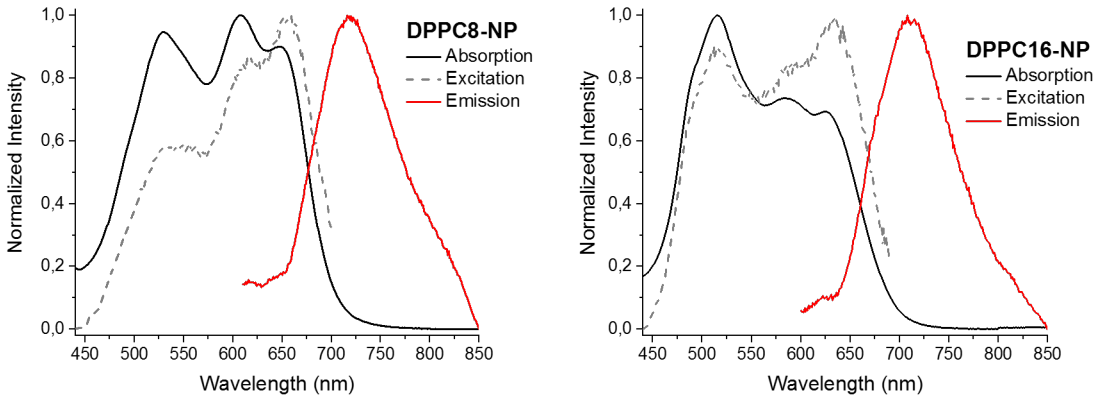

Figure 4.10: DPPC8-NPs and DPPC16-NPs normaized UV-vis absorption, excitation and emission spectra after three weeks

Both emission from the two nanoparticles are red-shifted compared to the monomer,

peaked at 720 nm and 710 nm for DPPC8-NPs and DPPC16-NPs, respectively. In both systems, the excitation spectrum is peaked in correspondence of the most red-shifted absorption band, associated to J-aggregates, in agreement with theory that predicts fluorescence emission from J-aggregates. H-aggregates are not fluorescent and therefore they should be not visible in the excitation spectra. However, a peak in correspondance of H-aggregates appears in the excitation spectra, especially in the case of DPPC16-NPs. Kirkus et al. suggest that the appearance of the H-band in the excitation spectra may be due to energy transfer between the two different polymorphs forming the nanoparticles.

Although probes showing NIR emission are desirable for fluorescence microscopy, due to the low light attenuation of the biological matter in this region, the fluorescence emission of both systems is strongly quenched (fluorescence quantum yield, φ, less than 0.1), due to the aggregation caused quenching (ACQ) effect, as shown in the Table 4.3.

Optical properties of DPP-loaded QS and (C)QS

Similarly to the case of DPPs-based nanoparticles, the variation of the of the UV-vis absorption spectra of DPPs-loaded Quatsomes over time was monitored, as shown in the normalized spectra of Figure 4.11.

In order to compare the shapes of the spectra of DPPs-loaded Quatsomes and determine the fluorescence quantum yield (φ) of these samples, scattering contribution to absorption has been removed as explained in Section 7.5.3 of the Experimental Part.

In the case of DPPC8-QS-3 (Figure 4.11a), the appearance of a new band at 660 nm is likely due to the re-organization of the fluorophores and consequent formation of new supramolecular aggregates. In the previous Section, the analogy concerning the morphological changes of DPPC8-NPs and DPPC8-QS-3 samples, both growing toward the formation of long rod-like structures, was described. Similarly, the change in the absorption spectra of DPPC8-QS-3 points to the formation of a broad peak with the appearance of the red-shifted band, likely associated to the J-aggregates, as previously shown in the case of DPPC8-NP (Figure 4.9, left). Summarizing, the dye DPPC8 showed high tendency to form elongated rod-like architectures, likely a higher stable supramolecular self-organization of the dye, in which the fluorophores are mainly arranged as J-aggregates. Oppositely, the absorption band-shape of DPPC16-QS-3 (Figure 4.11, b) did not show major change, indicating a negligible reorganization and no release of the loaded molecules towards the surrounding water. Therefore, the length of the terminal alkyl chains of the fluorophore plays a crucial role in the supramolecular organization and incorporation of the molecules into QSs. When the length of the C16

chains matches that of the surfactant, the strong interaction with the hydrophobic bi-layer of QSs, ensures the stable interdigitation of DPP molecules into the membrane. Analogously, no changes of the absorption bandshape were observed in sample containing 10% of EtOH, DPPC8-QS-3(10%EtOH) neither in the case of DPPC16-(C)QS (Figure 4.11 c and d, respectively), meaning that both strategies allow to obtain stable dispersion in water of the dye in terms of optical and colloidal properties.

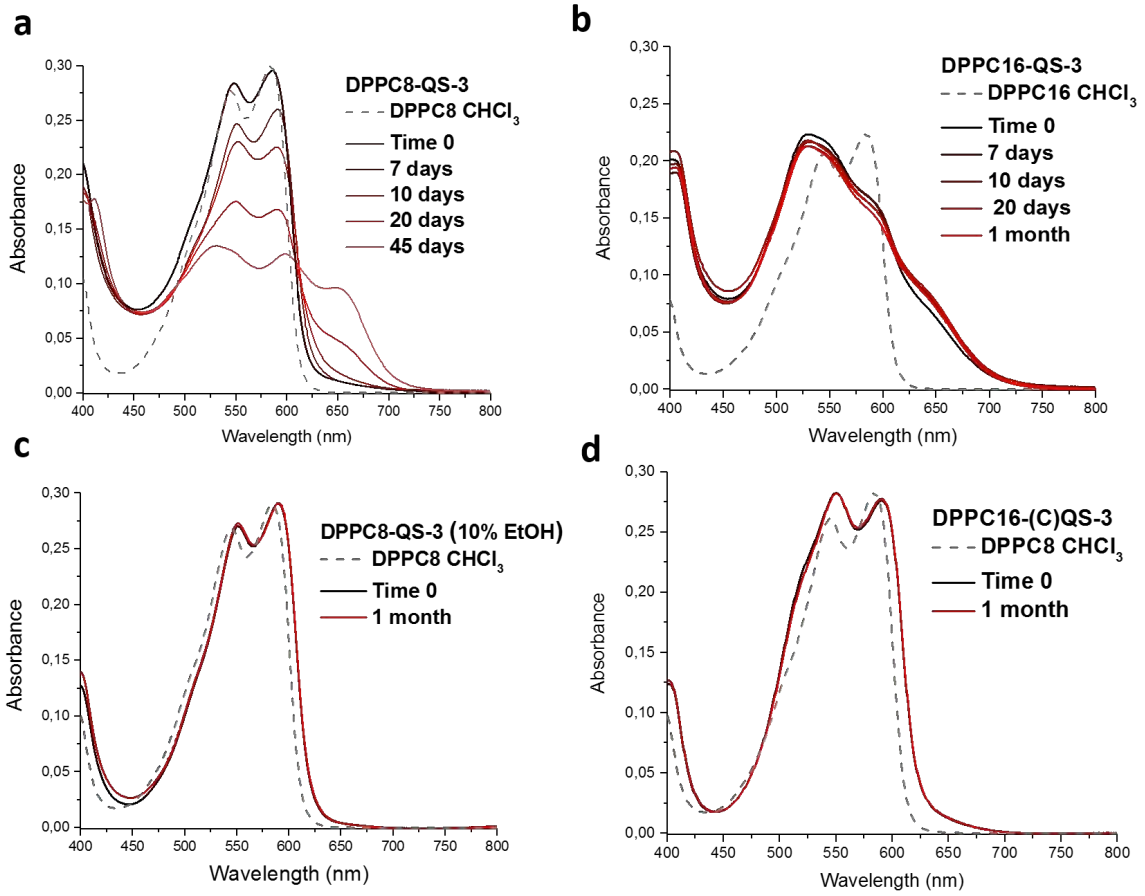

Figure 4.11: UV-vis absorption spectra of DPPs-loaded Quatsomes monitored over time: a) DPPC8-QS-3; b) DPPC16-QS-3; c) DPPC8-QS-3(10%EtOH); d) DPPC16-(C)QS-3. The absorption of DPPs in chloroform is shown in each graph for comparison.

The normalized UV-vis absorption, excitation and emission of the different DPPs-loaded Quatsomes are shown in Figure 4.12, along with the normalized UV-vis absorption spectra of DPPC16-QS samples at different loadings.

In all the studied samples, the emission is due to isolated fluorophores within the membrane of the Quatsomes and not to the aggregates formed. The excitation and emission spectra of the three DPPs-loaded Quatsomes, in fact, strongly resemble the absorption and emission spectra, respectively, of the dye dissolved in

$CHCl_3$ (Figure 4.12a), suggesting that emission is due to isolated DPP molecules incorporated into the bi-layer. This conclusion is further supported by the similarity between the shape of the excitation spectrum of DPPC16-QS-3 (Figure 4.12b) and that of the molecule in solution (Figure 4.12a), evidencing that the aggregates formed in DPPC16-QS-3 (mainly H-aggregates, appearing in the absorption spectrum at around 530 nm) are not fluorescent.

The effect of the presence of EtOH on the aggregation state of the fluorophore within the membrane of Quatsomes (10%vol) can be now comprehended looking at the Figure 4.12c. EtOH molecules likely contribute to the solvation of the DPPs backbones reducing the stacking interaction between the fluorophores and enhancing the interdigitation of the aliphatic chains within the bilayer. This hypothesis is further supported by the shape of the excitation spectrum, which resembles the absorption profile.

A similar effect, i.e. the dispersion of single fluorophores in the membrane of the vesicles, is obtained by using STER/CTAB Quatsomes, (C)QS. The absorption spectrum of DPPC16-(C)QS-3 (Figure 4.12d), is indeed more similar to that of the isolated molecules in chloroform and the aggregation (occurring in minor extent, as shown by the shoulder at 520 nm in the absorption spectrum) is less relevant than in the case of Quatsomes made by Chol/CTAB at the same loading of DPPC16 (Figure 4.12b).

The photophysical properties of the samples studied in this Chapter are resumed in Table 4.3, where the fluorescence quantum yields, φ, of the samples are listed. The estimation of the fluorescence quantum yield of the samples studied in this Thesis is based on a comparative method with a known standard, as explained in the Experimental Section 7.5.3. For the calculation of φ, the precise evaluation of the absorbance at the excitation wavelength is required, which is not trivial in the case of highly scattering samples, as the fluorescent Quatsomes. The measured absorption spectra of fluorescent quatsomes are in fact the sum of the real absorbance (due to the presence of the fluorophore) and the scattering contribution, due to the nanosize scale of the Quatsomes. In the case of DPP-loaded Quatsomes, scattering has been subtracted to the measured absorbance, in order to calculate the real absorbance of the fluorescent probes at the excitation wavelength. To do so, scattering of Quatsomes has been modeled as a Rayleigh-Tyndall type , as explained in Section 7.5.3. However, this mathematical treatment of the absorption spectra could lead to errors, difficult to quantify, in the determination of the absorbance at λ_{exc}. This consideration is particularly important for the samples DPPC16-QS-1, -2 and -3, which showed lower absorbance-to-scattering signals, in comparison with the other samples. Nevertheless,

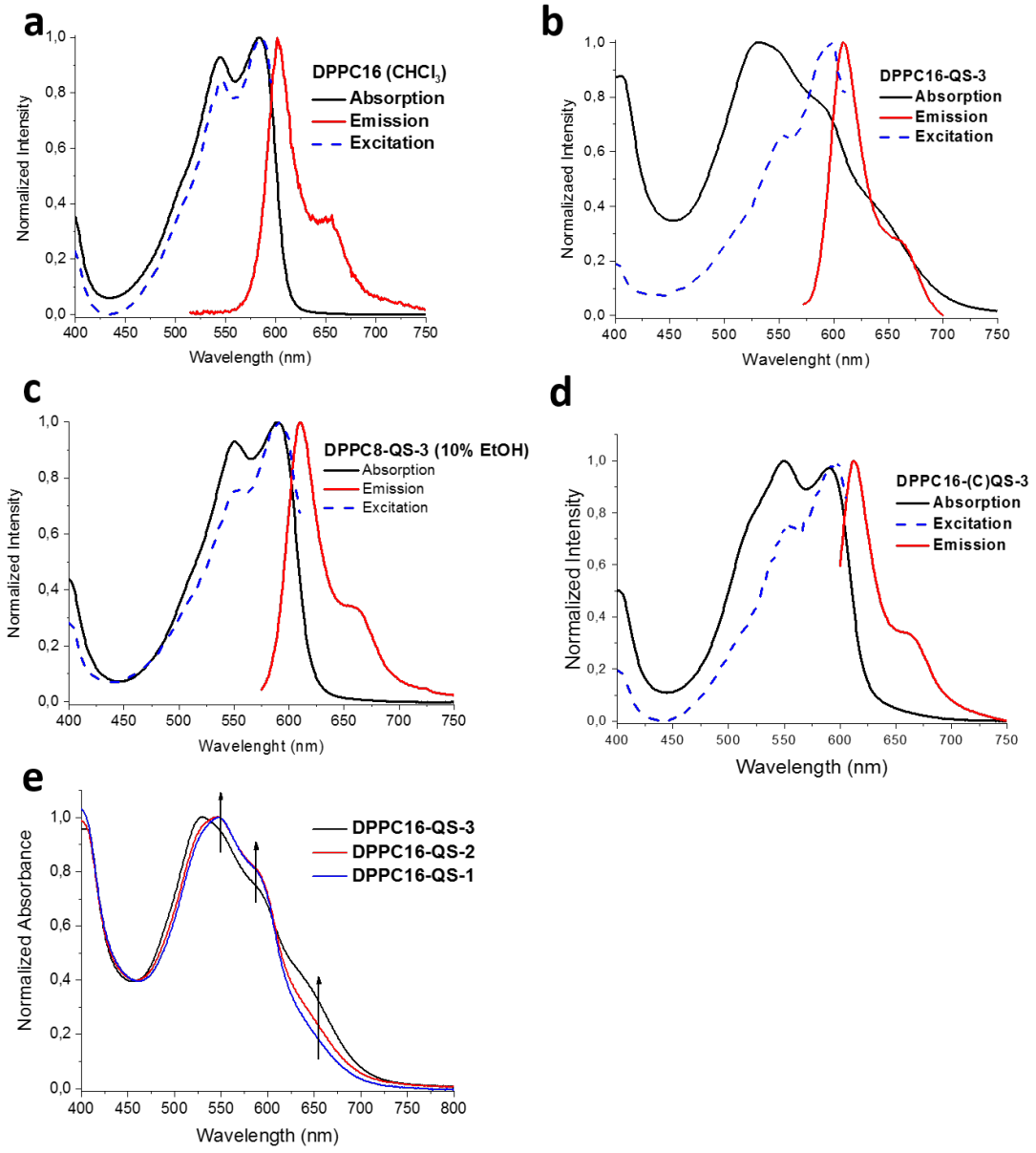

Figure 4.12: Normalized UV-vis absorption, excitation and emission spectra of DPPs-loaded Quatsomes. a) DPPC18 in $CHCl_3$; b)DPPC16-QS-3; c) DPPC8-QS-3(10%EtOH); d)DPPC16-(C)QS-3. e) comparison of the normalized UV-vis absorption spectra of DPPC16-QS samples at different loading.

to minimize the error, φ has been calculated at the wavelengths in correspondence of the maximum excitation, i.e. in the red region of the spectra (between 580 nm and 600 nm, depending on the sample) where scattering is not predominant. In conclusion, it must be stressed out that the aim of this work is to identify a trend of the samples luminescence in dependence with the aggregation state of the fluorophores and make a comparison with the dye in chloroform solution. So, the values of φ given in Table 4.3 shall be considered in terms of comparison between the different samples and not as absolute values. Due to the uncertainty in the correct estimation of the real absorbance of these samples, the molar extinction coefficient of the DPPs-loaded has not been calculated.

As previously mentioned in the analysis of the spectra in Figure 4.12, the aggregates formed by the DPPs in the membrane of Quatsomes are not fluorescent. For this reason, the fluorescence quantum yield of the samples showing an aggregation state of the dye is strongly affected by extent of aggregation (Table 4.3) and it is dependent of the excitation wavelength. For this reason, the φ values discussed below have been estimated at a λ_{exc}in correspondence of the maximum in the excitation spectra, meaning that the given φ values are the highest obtainable from these samples.

Whereas the quantum yield of the DPPs nanoparticles, DPPC16-NPs and DPPC8-NPs, is strongly quenched (φ<0.1 in both cases), the dispersion of the dyes in water by mean of Quatsomes leads to the formation of much brighter FONs. The highest value of fluorescence efficiency is obtained by dispersing DPPC16 in (C)QS (DPPC16-(C)QS-3 with φ around 40%). The comparison between DPPC16-(C)QS-3 and DPPC16-QS-3, taking into account that both sample have the same loading of fluorophore, suggests that the composition of Quatsomes bilayer determines the possibility of dispersing isolated DPPC16 molecules in the membrane of the vesicles. Although a deeper study on the interaction between STER and CTAB is necessary, aiming to assess the supramolecular configuration that these two molecules assume in the formation of small unilamellar vesicles, we speculate that the functional group of STER may act as “bulky” group, hindering the stacking of the DPPs molecules once incorporated into (C)QS vesicles and therefore favoring the dispersion of isolated fluorophores within the membrane. A similar effect has been obtained in DPPC8-QS-3(10%EtOH), with φ around 24%, but, in this case, the EtOH reduces the stacking interactions between the fluorophores.

The quenched emission of DPPC16-QS-3, whose φ is only 6%, is ascribed to the formation of no-emissive aggregates, as previously mentioned. The extent of aggregation of DPPC16 within the bilayer of Quatsomes can be modulated by the loading of the dye, as confirmed by the shape of the absorption spectra of DPPPC16-QS-1, -2 and -3,

containing different amount of DPPC16 per vesicle (Figure 4.12d). The slight changes in the absorption band shapes (decrease of the band at 660 nm and increase at 590 nm and 550 nm) and the increase of fluorescence efficiency (13% for DPPC16-QS-2 and 17% for DPPC16-QS-1 as detailed in Table 4.3), suggest that the probes are distributed in a more isolated way over the membrane of the vesicles at lower loading, as already observed in the case of Quatsomes loaded with carbocyanines (Section 3.1 of Chapter 3), another family of dyes with high ACQ tendency.

Table 4.3: Photophysical properties of DPPC8 and CPPC16 in $CHCl_3$, DPPs-NP and DPPs-loaded Quatsomes

Sample	$\lambda_{\textbf{max abs}}$ **nm**	$\lambda_{\textbf{max emi}}$ **nm**	**Fluorescence** ϕ %
DPPC8 ($CHCl_3$)	586	608	70
DPPC16 ($CHCl_3$)	586	608	70
DPPC16-NP	517	710	<0.1
DPPC8-NP	608	720	<0.1
DPPC16-QS-3(10EtOH)	590	610	24
DPPC16-QS-3	532	608	7
DPPC16-QS-2	530	608	13
DPPC16-QS-1	530	608	18
DPPC16-(C)QS-3	550	612	40

[a] FLuorescence quantum yield ±10%. Cresyl Violet (MeOH) has been used as standard. ϕ was determined exciting at the wavelength in correspondence of the maximum of the excitation spectra.

4.3 Biocompatibility and imaging of DPPC16-NPs, DPPC16-QSs and DPPC16-(C)QSs in Saos-2 cells

The study of cells viability and the imaging of DPPs-based FONs in cells were conducted by Danilo Vona, in Prof. Gianluca Farinola's laboratories, at the University of Bari, Italy.

Biocompatibility assay for DPPC16-NPs, DPPC16-QSs and DPPC16-(C)QSs was performed on Saos-2 2 cell line as adherent model cells. Saos-2 cells are model cell line used for osteoblasts adhesion tests [234] or osteosarcoma in vitro model for drug testing (anti-cancer research)[235]. In a particular case, these cells were reported for testing of specific gene targeting with cationic liposomes (phosphatidylethanolamine and 3ß-[N-(N',N'-dimethylaminoethane)-carbamoyl] cholesterol)[236].

MTT analysis was performed to measure the Saos-2 metabolic activity. Cells were

initially pre-cultured for 24h to allow adhesion, then exposed to the samples for 4h and finally re-cultured in fresh medium for 36h. All the samples were tested in triplicates. The experimental details are given in Section 7.7 of the Experimental Part.

CTAB is toxic to Saos-2 cells in the range from 0.2 mM to 2 mM [237]. For this reason, cells have been exposed to highly diluted Quatsomes samples, 7 μM and 0.7 μM of CTAB, corresponding to 1 nM and 10 nM of dye concentration, respectively. For sake of comparison, dye-free formulations were tested: CTAB surfactant, Plain QS and Plain (C)QSs, (at 7 μM and 0.7 μM, corresponding to the concentration of CTAB in DPP-loaded QS). As positive references, cells (not exposed to samples) after 10 minutes (PSCC 0) and 36 hours (PSCC*) of seeding were used. All the samples have been normalized with respect to PSCC* reference. Cells viability of the tested samples is shown in Figure 4.13.

Citotoxicity is detected in all the Quatsomes samples, in a weakly dose-dependent manner. Plain QS are more cytotoxic than CTAB, but Plain (C)QS are less cytotoxic than both CTAB and Plain QS. In general, the incorporation of the dye in QS and (C)QS has a negligible effect on cells viability. Summarizing, all the systems containing STER exhibit good relative biocompatibility (around 60%), while all those made by cholesterol and CTAB show biocompatibility lower than 60%. So, STER has an ameliorative effect on the cell viability of Quastomes.

DPPC16-NP exhibit the best biocompatibility in terms of absence of metabolic distress (in relation to PSCC*) and absence of cell death compared to initial cell density (in relation to PSCC(0))

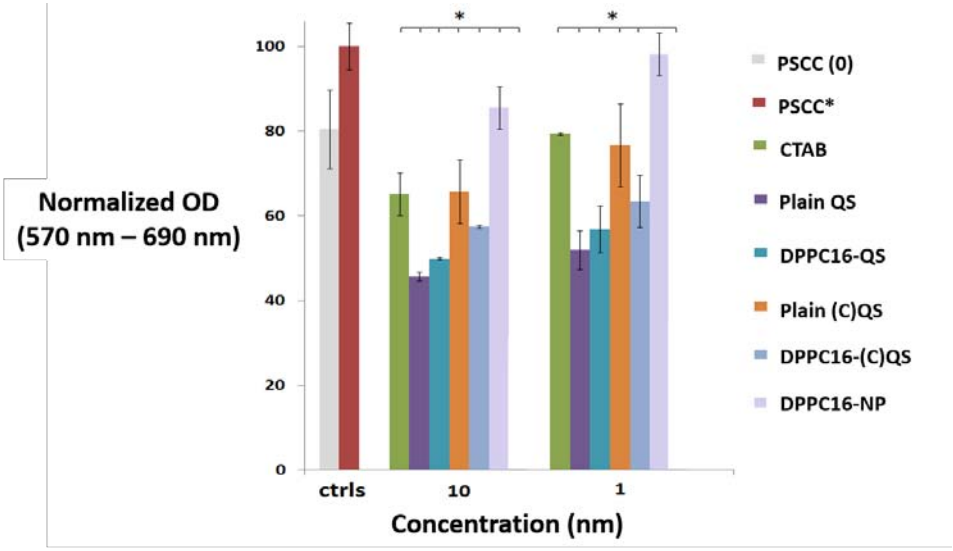

Figure 4.13: PSCC* normalized MTT values for biocompatibility assay of QS, DPPC16-QS, Plain (C)QS, DPPC16-(C)QS and DPPC16-NP. For comparison, biocompatibility of pure CTAB surfactant is reported.

Cells uptake study of DPPC8- and DPPC16-based FONs

Saos-2 cells uptake assay was performed for DPPC16-NP and the two different Quatsomes formulations (DPPC16-QS and DPPC16-(C)QS), at 10 and 1 nM concentrations (related to dye concentration) and at 1h and 4h exposition times, by using a confocal microscope. The best results were obtained after 1h of exposition to samples and the images acquired are shown in Figure 4.14 (results after 4h are not shown). DAPI and ATTO488 labels were used to verify the absence of nuclei fragmentation (DAPI channel) and cells adhesion and interaction with substrate (ATTO488 channel). The red channel is used only for DPP-based samples visualizations. Details on the cells imaging and the staining protocol are described in the Experimental Part 1.6.

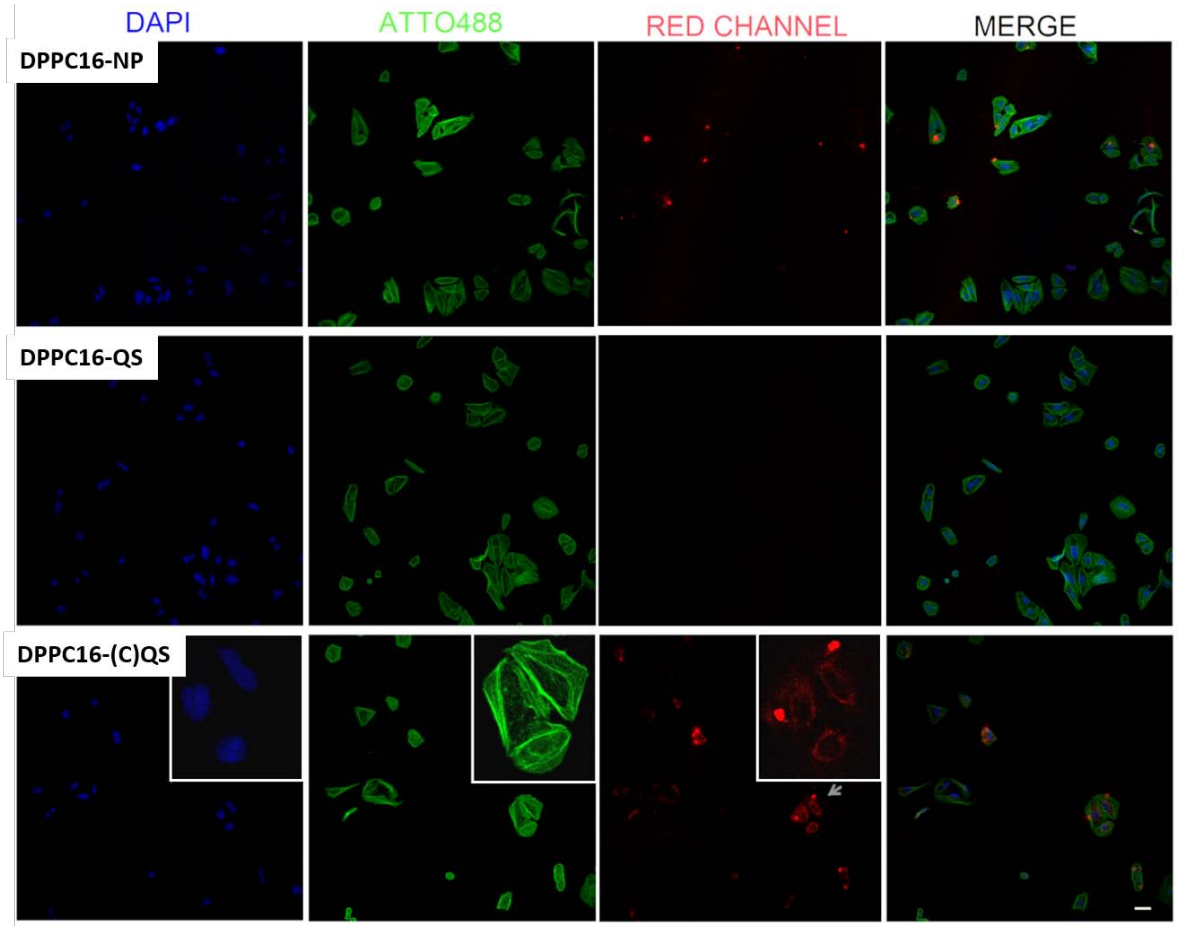

Figure 4.14: Confocal image of DAPI/ATTO488/DPP Saos-2 staining of DPPC16-NP (1 nM, top), DPPC16-QS (10 nM, middle) and DPPC16-(C)QS (10 nM, bottom) after one hour of exposition (DPPC16 concentrations are given).

In the case of DPPC16-NP, the best result was obtained at dilution to 1nM (in the case of 10 nM cells give weak/low uptake). No uptake was detected in the case of DPPC16-QSs at both concentrations (1 nM and 10 nM), while DPPC16-(C)QSs showed good uptake at

10 nM.

After 1 hour of exposition to DPPC16-NPs, actin stress fibers show good morphology and nuclei are unaltered. Strongly red emitting clusters of DPPC16-NPs were observed inside the cells, but not outside them (Figure 4.14, top). The average size of the clusters (5.1±0.9 μm), was determined via image analysis. The intracellular staining is not homogeneous, as better shown in the zoom of the confocal images and their 3D reconstruction of Figure 4.15, top. Thus, the 40% of the red clusters detected is in fact localized in the peri-nuclear region, although clusters in the cytoplasm and close to the cells membrane are as well formed. In order to better comprehend the nature of the strongly fluorescent clusters of DPPC16-NPs, *in situ* emission spectra were acquired with the microscope in the different regions of the cells where the clusters have been localized (Figure 4.15, top-right). The small shoulder in the NIR, around 710 nm, can be associated to the weak emission of the DPPC16-NPs (see Figure 4.10, right). However, the main band at 660 nm, can be ascribed to emission from isolated molecules of DPPC16, likely due to the de-aggregation of the nanoparticles, maybe as effect of the interaction with cellular proteins.

Concerning the uptake of DPPC16-QS (10 nM, 1 hour exposition time), concentric fibers in many cells appear, while DAPI channel reveals no fragmentation of the nuclei. However, there is no evidence of cells internalization (neither after 4 h and at the different concentrations tested), as shown in Figure 4.14, middle.

In the case of DPPC16-(C)QSs (Figure 4.14, bottom), actin stress fibers show generally good morphology, although some concentric stress fibers appear. After cells internalization, DPPC16-(C)QSs is non-homogeneously distributed over the cytoplasm, with a-specific formation of strongly red emitting aggregates (8.1 μm ±2.8 at 1h) especially in the peri-nuclear region and at membrane-cytoplasm interface, as supported by zoom of the confocal images and their 3D reconstruction in Figure 4.15, bottom. In few cases these aggregates have been localized as well outside the cells. Interestingly, the staining totally disappeared after 4 hours (not shown). In the case of DPPC16-(C)QSs Figure 4.15, bottom right), the spectra acquired from clusters localized close to the cells membrane and around the nuclei are similar to those acquired in water (see Figure 4.12), suggesting the integrity of DPPC16-(C)QSs after internalization in cells.

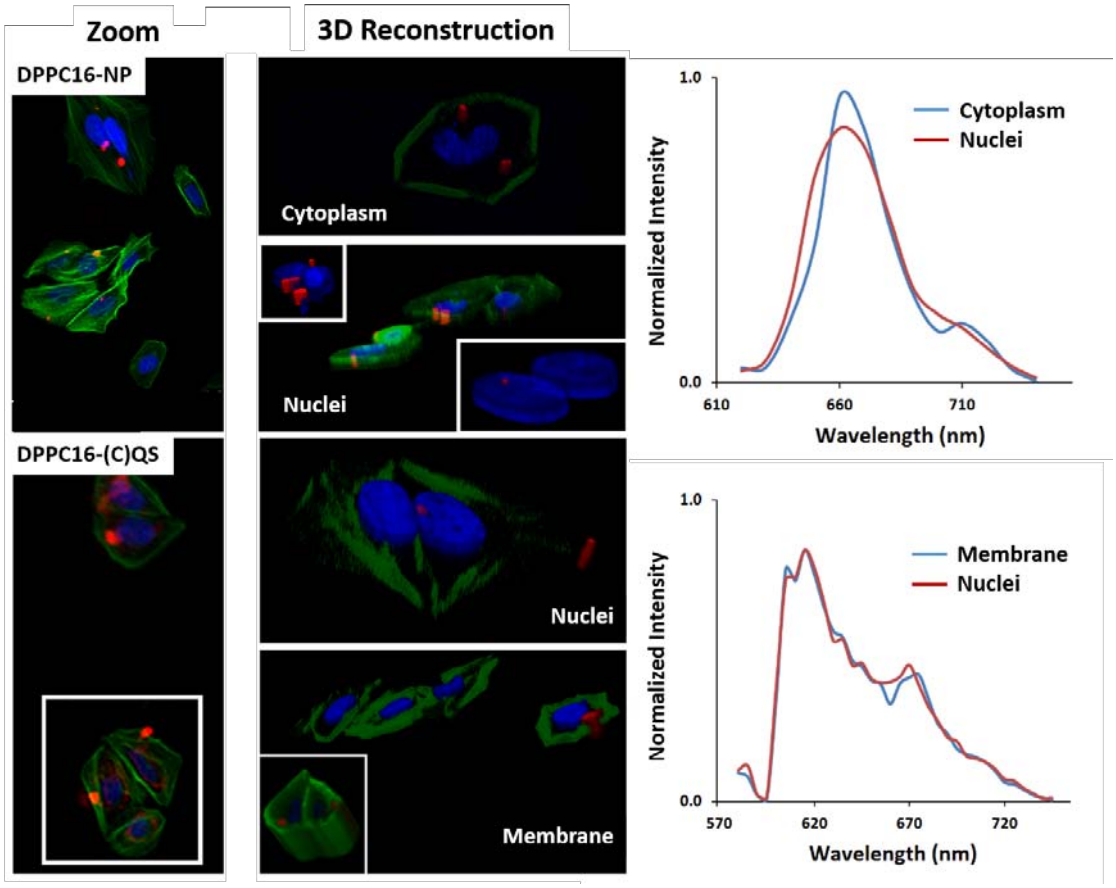

Figure 4.15: left) Confocal images and 3D reconstruction of DPPC16-NP and DPPC16-(C)QS samples at 1 hour uptake; right) emission spectra acquired by the confocal micrsocope of DPPC16-NP stained cells (top) and DPPC16-(C)QS stained cells (bottom) in different localizations.

4.4 Summary and Perspectives

In this Chapter, two diketopyrrolepyrrole derivatives, DPPC8 and DPPC16, with same conjugated structures but modified with alkyl chains of different length (C_8 and C_{16} for DPPC8 and DPPC16, respectively) have been dispersed in water preparing two types of FONs. First, the pure dyes have been precipitated in water forming DPPC8-NPs and DPPC16-NPs. Second, the dyes have been incorporated in Quatsomes, by the interdigitation of the alkyl chains within the bilayer of the vesicles. The main conclusions withdrawn from this work can be summarized as follow:

- The supramolecular organization of the dyes is driven in both cases by the length of the alkyl tails. Both DPPC16-loaded Quatsomes and DPPC16-NP are more stable in terms of colloidal and optical properties than the corresponding DPPC8-based FONs, which showed the tendency to form, after several days, long nanowires with the dye arranged forming H- and J-aggregates.

- Both DPP-NPs are weakly fluorescent (φ<0.1%) in the NIR region. When incorporated in Quatsomes, DPPC16 is much more bright, especially in the case of DPPC16-(C)QS sample (φ~40%), in which the dye was incorporated in Quatsomes made by the sterol derivative (STER) and CTAB (with mean size around 50 nm).

- The spectroscopic analysis suggested that the dyes incorporated in the membrane of Quatsomes are organized as mixtures of isolated molecules (fluorescent) and aggregates (non fluorescent). Thus, the balance between these two states of the dye and, consequently, the brightness of the obtained FONs depended on the composition of the Quatsomes, the amount of dye loaded in the vesicles and the composition of the dispersing medium.

- DPPC16-NPs and DPPC16-(C)QS were succesfully internalized by Saos-2 cells. The confocal images revealed that the probes are mainly aspecifically distributed in the cytoplasm and in the perinuclear region of the cells. The *in situ* emission spectra acquired suggest that the DPPC16-NPs likely undergo de-aggregation within the cells, while the DPPC16-(C)QSs maintain their integrity upon internalization.

The results obtained suggest that the length of the alkyl chain is a crucial parameter that rules the possibility of dispersing hydrophobic dyes in aqueous media by incorporation in Quatsomes. Bright Quatsomes-based water dispersions with high colloidal stability and good vesicle-to-vesicle homogeneity were in fact obtained in the case of DPPC16. However, further studies are required in order to comprehend how the chemical composition of the vesicles affects the colloidal and optical properties of the DPPs-loaded Quatsomes. Moreover, despite the encouraging results on cells internalization and imaging of DPPC16-(C)QSs, information on the exact localization within the cells of the FONs is still missing.

Part of the above reported results have been published in the Ref. [229]

5

LysoQSs: new pH independent lysosomal probes

5.1 Introduction

Lysosomes are membrane-bound organelles that work as digestive apparatus of most of the eukaryotic cells. These structures contain enzymes able to recycle damaged organelles and degrade nucleic acids, polysaccharides, fats and proteins[238]. They were found to take part in many processes such as phagocytosis, endocytosis and autophagy. Moreover they participate in intracellular signaling, energy metabolism, secretions and plasma membrane repair [239] [240]. Several pathologies are linked to dysfunctions of lysosomal structure and/or function including inflammation, cancer and many neurodegenerative diseases[241]. Therefore, adequate visualization of lysosomes is critical for the assessment of intracellular metabolism, cell membrane recycling and evaluation of drug and gene delivery.

As the pH of lysosomes is more acidic (pH 4.5-5) than in cytoplasm (pH 7-7.3), generally lysosomal fluorescent probes are formed by a fluorophore linked to a basic side chain (tipically an amine). Such probes are lysosome membrane-permeable in the dissociated state but impermeable after protonation at acidic pH, allowing accumulation inside the lysosomes. Some of the lysosomal fluorescent probes commercially available, such as Neutral Red, Acridine Orange and LysoSensor probes, are based on this strategy.

Despite of the variety of consolidated commercial lysosomal probes, the design of stable and specific fluorophores is still an issue. Researcher interested in dynamic aspects of lysosomal activity, often associated to variation of the internal pH, have focused their efforts in the synthesis of proper pH-sensitive probes [242]. So, acidotropic probes, as LysoSensor (Life Technologies Corp.), show a pH-dependant fluorescence increase as effect of the protonation inside the lysosomes, relieving the quenching resulting by the photoinduced electron transfer (PET) by their weakly basic side chains. In a typical PET-based probe, a fluorophore is covalently linked to an amine which, if not

protonated, quenches the fluorescent emission [158]. However, inadequate fluorescence quenching by PET can lead to high, nonspecific background signal inside the cells [243].

Fluorescent probes which accumulate inside the lysosomes, as those discussed so far, are generally used at very low concentration (around nM) in order to prevent aggregation caused quenching (ACQ) and they are easily photobleached. In this direction, Lou et al. [244] synthesized a fluorogen which contains tetraphenylethene and a coumarin moiety, showing aggregation induced emission (AIE), good photostability and good specificity to lysosomes.

However, adequate specificity of pH-dependent probes is still an issue. Once pH inside lysosomes increases, these probes may diffuse elsewhere and/or their fluorescence is quenched. Even worse, some of the existing lysosomal probes show alkalinizing effect on lysosomes after long-time incubation [243]. For example, in the case of LysoTracker probes, the manufacter suggests to incubate cells with the probes only for few minutes to avoid the increase of pH [13]. Optimized specificity can be obtained by probes which don't show pH-dependence, as in the case of Zhang et al. [245], who developed a NIR boron-dipyrromethene derivative with a high long-term specificity, due to the incorporation via endocytosis. In this sense, the design of pH-independent and photostable lysosomal probes is desired.

Despite the pros and cons of the cited small-molecule markers, the design of fluorescent probes with high and long term specificity, high photostability and which preferably don't alter the physiological conditions of lysosomes is still challenging. In this direction, specifically designed fluorescent nanoparticles constitute an adequate alternative. Hanaki et al. [246] successfully dispersed quantum dots by using sheep serum albumin (SSA), finding that these probes are long-life and highly photostable endosome/lysosome markers. However, when turning to applications, the intrinsic toxicity of QDs and the complexity of such organic/inorganic conjugates made such structures inefficient. Silica nanoparticles entrapping small organic probes [247] have also been used as efficient and photostable probe for lysosome, transported into HeLa cells through endocytosis which lead to high specificity.

Many works in literature describe the use of fluorescent organic nanoparticles (FONs) for lysosomal labeling, mostly regarding specifically tuned polymeric nanoparticles. Torchilin et al. [248], in their study of liposomes as drug carrier, showed that liposomes modified with octadecyl-rhodamine B can be accumulated in lysosomes through endocytosis.

Belfield et al. tracked lysosomes with new fluorene derivatives dispersed in water by mean of Pluronic micelles. These nanostructures are promising carriers for drug release,

thanks to the variety of actives that they can encapsulate and the high selectivity to target the lysosomes [66, 249, 250]. However, some drawbacks are related to the use of these carriers, such as long-term stability and stability upon dilution [251]. Many efforts have been dedicated by Belfield's group to the design of efficient fluorophores for 2-photon imaging, focusing as well on the development of fluorene derivatives for lysosomes tracking [66, 252]. Fluorene derivatives, like those shown in Figure 5.1, have have been largely used for one- and two-photon bioimaging. This class of fluorophores has a number of advantages as fluorescent probes: 1) the conjugated planar ring constitutes a well delocalized π-system (necessary for high 2PA probes), 2) the rigidity of the conjugated structure generally gives high fluorescence quantum yields and 3) these dyes are typically quite photostable. Another advantage is given by the easy introduction of substituents at the 9-position (R' in Figure 5.1), which helps modulating the solubility and hydrophilicity/hydrophobicity balance of the derivatives.

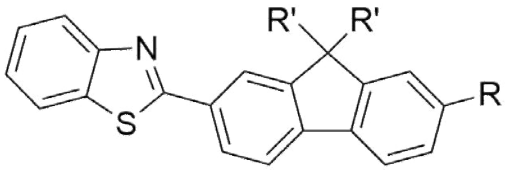

A: R=Ph_2; R'=$C_{10}H_{21}$
B: R=SCN; R'=$C_{10}H_{21}$
C: R=SCN; R'=$CH_2CH_2OCH_2CH_2OCH_3$

Figure 5.1: Structure of fluorene derivatives for bioimaging developed in Belfield's group [252]

In the previous Chapters it was showed that Quatsomes can be used as efficient scaffold for the dispersion of hydrophobic dyes in aqueous media and, in Chapter 4, it has been demonstrated that these structures can be used for the imaging of intracellular compartments without the addition of any further targeting agent, although the information about the exact localization of the Quatsomes after internalization in cells is missing yet.

A new fluorene based probe, 7-(benzo[d]thiazol-2-yl)-9,9-diethyl-N,N-dioctadecyl-9H-fluoren-2-amine (DiC18), shown in Figure 5.2, has been therefore designed and obtained by Belfield's group. This probe, non soluble in water, is a slightly modified version of an existing fluorophore with promising linear and non-linear optical properties, recently studied by Kurhuzenkau et al. [253], and therefore worthy of being studied as water-dispersed FON. The purpose of this Chapter is to explore whether DiC18 can be dispersed in aqueous media by using Quatsomes, in order to obtain bright and stable FONs preserving the optical properties

of the fluorophore. In addition to the physico-chemical and optical properties of DiC18-loaded Quatsomes, their capability for the visualization and long-term tracking of lysosomes will be examined, paving the way to the design of multifunctional systems, incorporating, for example, drugs or agents for photodynamic therapy.

DiC18 was specifically fashioned for the incorporation in Quatsomes, aiming to mimic the successful strategy that has been previously described for carbocyanines (Chapter 3) and DPPs derivatives (Chapter 4). The addition of the two C_{18} aliphatic chains to the chromophoric core of the molecule has been indeed designed with the purpose of interdigitating the two tails in the lipophilic core of the Quatsomes membrane, as it was shown in the Molecular Dynamics (MD) simulations in Chapter 3. However, DiC18 has a major difference, compared to the previously studied dyes. Thus, carbocyanines and DPPs are slightly amphiphilic, showing two lipophilic alkyl chains together with a positive charge on the molecular core and two short PEG chains, respectively, which increased the hydrophilicity of the chromophoric part of the fluorophores. On the contrary, DiC18 has no polar moieties in the structure, being therefore entirely hydrophobic.

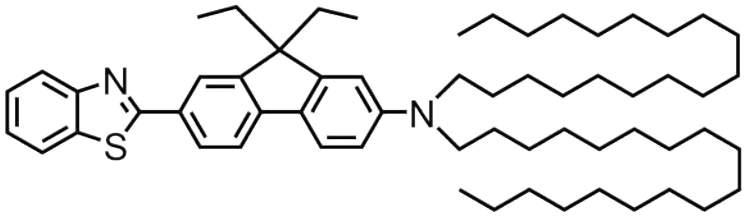

Figure 5.2: Structure of the non-water soluble and hydrophobic DiC18 fluorophore studied in this Chapter

Fluorene derivatives generally exhibit pronounced solvatochromism (especially in emission) in organic solvent [254]. Therefore, the photophyscial properties of DiC18 were firstly investigated in solvents with different polarities including dimethyl sulfoxide (DMSO), acetonitrile (ACN), toluene (TOL), dichloromethane (DCM), cyclohexane (CHX) and hexane (HEX). The optical measurements were made in Prof. Belfield's laboratories. The study of the solvatochromism of DiC18 is helpful, since it gives information on the environment surrounding of the fluorophore and its organization in nanostructures, e.g. the Quatsomes.

The synthesis of DiC18 is resumed in the Experimental Part 1.5. The linear absorption, emission spectra and photophyscial properties of DiC18 are shown in Figure 5.3 and Table 5.1.

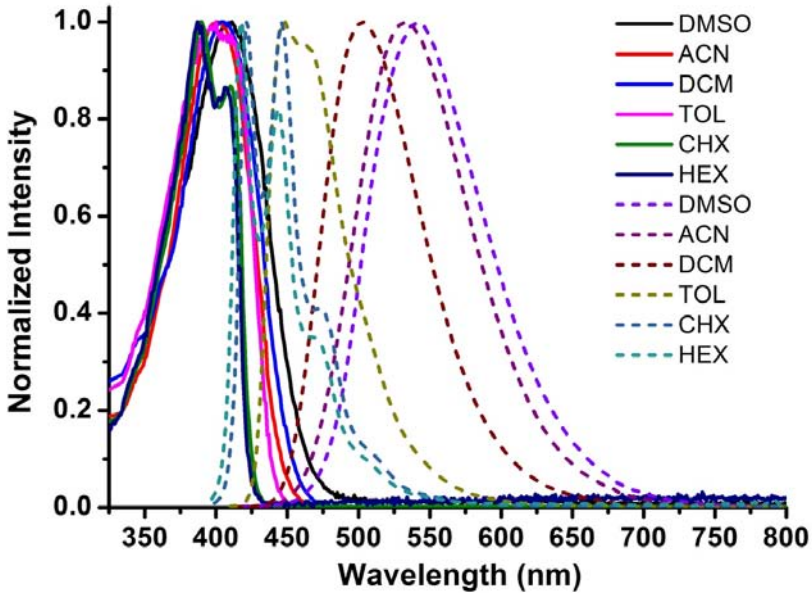

Figure 5.3: Normalized UV-vis absorption (continuous lines) and emission (dashed lines) spectra of DiC18 in solvents with different polarity

Table 5.1: Photophysical properties of DiC18 in solvents with different polarity

	P[a]	$\lambda_{\text{max abs}}$ **nm**	$\lambda_{\text{max emi}}$ **nm**	**Stoke's Shift cm** $^{-1}$	ϵ_{max} $\mathbf{M}^{-1}$ cm^{-1})	**Fluo** ϕ[b] %
HEX	0.1	387-406	418-444	1917	52	0.92
CHX	0.2	389-410	422-446	2010	52	1
TOL	2.4	400	447	2629	46	1
DCM	3.1	404	503	4872	40	1
ACN	5.8	401	532	6141	44	1
DMSO	7.2	411	541	5847	38	1

[a] Polarity index, from Solvent Guide (Burdick and Jackson Laboratories)
[b] FLuorescence quantum yield ±10%

The absorption spectra are peaked in the range from 387 to 411 nm, with only nominal variation as a function of solvent polarities. The fluorescent spectra of this asymmetrical (D-π-A) compound, resulting from excitation in the main absorption band, exhibited a bathochromic shift with strong solvent polarity dependencies. The solvatochromic behavior of DiC18 is similar to that exhibited by another fluorophore, having the same conjugated structure, studied in Ref. [253] and other fluorene derivatives that are sensitive to the environmental polarity [254]. The DiC18 compound shows an excellent fluorescent efficiency in different solvents (all close to 1) indicating that it is a promising candidate for further chemical and biological applications.

5.2 Dispersion of DiC18 in water: three different FONs

In the previous Chapters, the effect of the supramolecular organization of dyes on the optical and colloidal properties and morphology of the obtained FONs has been extensively described in relation to the carbocyanine (Chapter 3) and the DPP (Chapter 4) fluorophores. In those cases, the advantages brought by using Quatsomes as water stabilizing carriers were undoubtful. They guaranteed superior colloidal stability and better optical properties that were in most of the cases not comparable with those of other supramolecular architectures of the same dyes, such as surfactant micelles-encapsulated dye or self-assembled nanoparticles based on the π-π stacking of the dye molecules.

In a similar way, in this Chapter, three different strategies, schematized in Figure 5.4, have been pursued in order to obtain stable dispersions in water of the hydrophobic and non-water soluble DiC18. The three approaches are meant to lead to the formation of different FONs: 1) DiC18-loaded Quatsomes, 2) micelles-encapsulated DiC18 and 3) nanoparticles of DiC18. These structures will be studied with respect to the physicochemical and optical properties. The three hypothesized structures are schematically represented in Figure 5.4.

1) DiC18-loaded Quatsomes. The fluorophore has been stabilized in water by using Quatsomes, aiming to mimic the incorporation mechanism shown in the case of the carbocyanines in Chapter 3, with the interdigitation of the two aliphatic chains of the dye inside the hydrophobic bilayer of the vesicles. Two different formulations of Quatsomes were used with the purpose of dispersing DiC18 in water: a) Quatsomes made by Cholesterol and CTAB (QS) and b) Quatsomes made by Cholesterol and MKC, (M)QS. The structures of the two surfactants are shown in Figure 5.4.

CTAB (cetyltrimethylammonium bromide) and MKC (Tetradecylbenzalkonium chloride) are two quaternary ammonium surfactants, used in several pharmaceutical and cosmetics applications, Ref. [255], and they are inactive ingredient approved by the US Food and Drug Administration (www.fda.gov). Cetrimide (including CTAB) is used in cosmetics and in pharmaceutical as antimicrobial preservative. It is also used as preservative in eye-drops. Therapeutically, it is used at relatively high concentrations (0.1-1 % w/v) in aqueous solutions, creams, foams as topical antiseptic for skin, wounds and burns. It is included in nonparenteral medicines licensed in UK, included in the Canadian List of Acceptable Non-medicinal Ingredients and in the list of Existing Active Substances on the market in Europe. Benzalkonium chloride (including MKC) is used as well as antimicrobial preservative in pharmaceuticals, similarly to cetrimide. It is also

used in many other applications, such as in formulations for nasal, otic, parenteral, intra-articular, intramuscular, intraocular, topical and ophtalmic administration. It is also included in the FDA inactive ingredients database, nonparenteral medicines licensed in UK and in the Canadian List of Acceptable Non-medicinal Ingredients.

2) Micelles-encapsulated DiC18. Encapsulation in micelles is a consolidated approach for the dispersion of non-water soluble compounds, including dyes, in aqueous media [66, 174]. CTAB is a quaternary ammonium surfactant, which self-assembly into spherical micelles with a diameter of 2-3 nm at concentrations higher than the critical micellar concentration (CMC) of 1mM [177]. Therefore, the aim of this strategy is to disperse DiC18 in water by encapsulation in the hydrophobic core of CTAB micelles, the same surfactant used for the preparation of QS.

3) Nanoparticles of DiC18. Another widely employed strategy for the dispersion of non-water soluble dyes in water consists in processing them as nanoparticles (NP), driven by the strong hydrophobic interaction between the π-conjugated segments of the fluorophores [52]. Following this lead, self-assembled nanoparticles made only by DiC18 in water have been obtained.

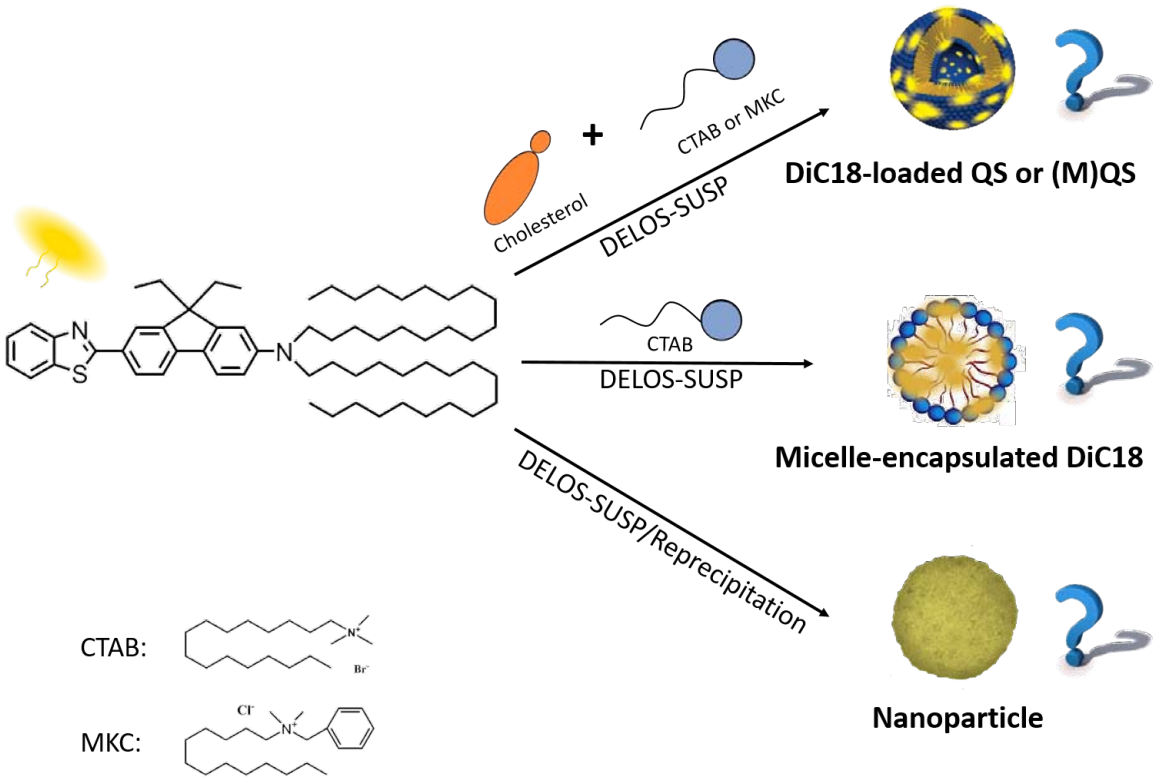

Figure 5.4: Schematic representation of the three strategies followed to disperse DiC18 in water. The hypothesized FONs obtained are schematized: top) DiC18 dispersed by using Quatsomes (DiC18-loaded QS or (M)QS); middle) DIC18-encapsulated CTAB micelles (Micelle-encapsulated DiC18); bottom) DiC18 nanoparticles (NP).

5.2.1 Preparation of the DiC18-based FONs

Preparation of DiC18-loaded QS and (M)QS DiC18-loaded QS and (M)QS were prepared by the CO_2-based methodology DELOS-SUSP, using the configuration shown in Experimental Section 7.2.1. In the first case, the Quatsomes were prepared using chol/CTAB in 1:1 molar ratio, while in the second case they were prepared using chol/MKC in 1:2 molar ratio. Analogously to the procedure shown in previous Chapters for the preparation of dye-loaded QSs, DiC18 was dissolved in EtOH along with cholesterol and loaded into the high pressure vessel at a temperature $T_w$of 308K. Afterwards, the standard procedure for the preparation of dye-loaded Quatsomes, indicated in the Experimental Section 7.2.1, has been followed. In particular, for the preparation of QS, 111 mg of cholesterol and 100 mg of CTAB were used and for the preparation of (M)QS, 111 mg of cholesterol and 202 mg of MKC (corresponding to twice moles of cholesterol) were used.

The phase behavior of the cholesterol/CTAB mixture had been deeply studied by Dr. Lidia Ferrer-Tasies in her PhD thesis [130], where she found that these two compounds in a 1:1 molar ratio form thermodynamically stable vesicles, named as Quatsomes. So far, the cholesterol/MKC mixture has not been studied in such details. However, during the course of this Thesis, it has been empirically observed that cholesterol and MKC in 1:2 molar ratio, when processed by DELOS-SUSP, form a population of unilamellar vesicles with hydrodynamic diameters of 100 nm ca. For this reason, this composition has been selected for studying the dispersion of DiC18 with (M)QS.

In both cases, three samples (DiC18-QS-1, -2, -3 and DiC18-(M)QS-1, -2, -3) with the same amounts of cholesterol and surfactant but different amount of DiC18 were prepared, in order to study how the fluorophore loading, [L], affects the colloidal and optical properties of the resultin FONs. As usual, [L] is defined as the molar ratio between the probe and quatsomes membrane component: $[L]=moles_{probe}/(moles_{chol}+moles_{surf})$. The amount of dye in the samples was measured by UV-vis spectroscopy, while the amounts of cholesterol and CTAB used for the calculations of [L] were the nominal ones, i.e. the quantities weighted at the beginning of the process (see Experimental Section 7.5.2 for details on calculation of [L]). In this way, the same concentration of vesicles in every batch is likely obtained, but each one containing a different number of fluorophores per vesicle. Samples were purified by diafiltration (see Experimental Section 7.2.2) and stored at 4°C for one week before analysis. For each sample, three batches were prepared, in order to check the reproducibility of the results and negligible differences were found in all the studied cases.

Preparation of micelles-encapsulated DiC18 In order to encapsulate DiC18 in CTAB micelles, the DELOS-SUSP configuration described in Experimental Section 7.2.1 has been used. In particular, 4.2 mL of a DiC18 solution in EtOH at different concentration were added to the high pressure vessel at T_w of 308K. Afterwards the standard DELOS-SUSP procedure has been followed. The CO_2-expanded solution of DiC18 was depressurized over 35 mL of Milli-Q water, in which 100 mg of CTAB were previously dissolved.

Three samples (DiC18-MIC-1, -2, -3), with the same amounts of CTAB but different amounts of DiC18 were prepared, in such a way that the molar ratios DiC18/CTAB were the same as those used for the preparation of QS-dispersed DiC18. For the determination of [L] and molar ratios DiC18/CTAB (listed in Table 5.2), the amount of DiC18 was measured by UV-vis spectroscopy while the amount of surfactant was the nominal one, i.e. the one weighted for the preparation of the samples.

Table 5.2: DiC18-based FONs studied in this Chapter and their corresponding composition

Sample	[L][a] $\times 10^{-3}$	DiC18/Surf[b] $\times 10^{-3}$
DiC18-QS-1	0.9	1.7
DiC18-QS-2	7	14
DiC18-QS-3	13	26
DiC18-(M)QS-1	0.5	0.8
DiC18-(M)QS-2	4.8	7.4
DiC18-(M)QS-3	9.7	14.7
DiC18-MIC-1	1.8	1.8
DiC18-MIC-2	13.3	13.3
DiC18-MIC-3	24.7	24.7
DiC18-NP	-	-

[a] [L]=$moles_{DiC18}/(moles_{chol}+moles_{surf}$. See Experimental Section 7.5.2 for details on determination of [L]

[b] Molar ratio: $moles_{DiC18}/moles_{CTAB\ or\ MKC}$

Preparation of DiC18 nanoparticles In this case, the nanoparticles of DiC18 (DiC18-NP) were prepared by reprecipitation. In fact, due to the larger volumes of DiC18 solution required for the preparation by DELOS-SUSP (4.2 mL for DELOS-SUSP and 0.1 mL for reprecipitation), the reprecipitation method was preferred, due to the low amount of dye available for the experiments. Just for comparison, only one batch of DiC18 Nanoparticles was also prepared by DELOS-SUSP and negligible differences were

found in comparison to the same sample prepared by reprecipitation.

5.2.2 Colloidal properties of the DiC18-based FONs

Colloidal properties of QS-dispersed and (M)QS-dispersed DiC18 The morphology of DiC18-QS-1, DiC18-QS-2 and DiC18-QS-3 samples one week after their preparation are shown in Figure 5.5. A cryoTEM image of DiC18-QS-3 one month after the preparation is also shown in the same picture.

The cryoTEM micrographs show that these samples are rather heterogeneous. Along with Quatsomes (small unilamellar vesicles appearing in the pictures), which are the most common objects observed, the presence of small vesicles with a "patch" has been detected. The patches (indicated with a orange arrow in Figure 5.5) appear darker in the cryoTEM images, due the higher contrast to electrons. These new architectures, named Patchy-Quatsomes, have never been found in previously studied Quatsomes [130, 134], except in one case, reported by Dr. Lidia Ferrer-Tasies in her PhD Thesis, in which Quatsomes were used to disperse in water hydrophobic silicon nanocrystals (SiNCs) capped with aliphatic chains. For this reason, the presence of Patchy-Quatsomes is attributed to the supramolecular organization of the DiC18, although it is hard to speculate on the exact composition of these structures, i.e. to establish if the patches are made only of DiC18 or a combination of DiC18 and surfactant/cholesterol molecules. In all cases only one patch per vesicle has been detected, probably due to the low loading of dye in the samples. Moreover, the presence of single molecules of DiC18 interdigitated in the bi-layer of the vesicles (in a similar manner to what observed with the carbocyanines in Chaper 3) cannot be excluded.

In the case of SiNC, capped with C_{12} aliphatic ligands, the entanglement between the Quatsomes and the inorganic nanocrystals (occurring under sonication of pre-formed Quatsomes with SiNCs) was attributed to the integration of clusters of SiNCs in the hydrophobic region of the vesicles, through the interdigitation of the aliphatic ligands into the leaflets of the bilayer. Nevertheless, the analogy with Patchy-Quatsomes is not straightforward. In this case, the supramolecular structures are fully organic and they originate from the simultaneous self-assembly of DiC18, cholesterol and CTAB, and not from the the addition of the probe to the preformed Quatsomes, as in the case of the SiNCs. However, both the systems are characterized by the presence of the alkyl chains, i.e. in the case of SiNCs, aliphatic ligands (C_{12}) were covering the nanocrystals, while in the case of DiC18-based patches, the dye has two C_{18}alkyl tails which, depending on the self-organization of the dye, may play a decisive role in the formation of these curious

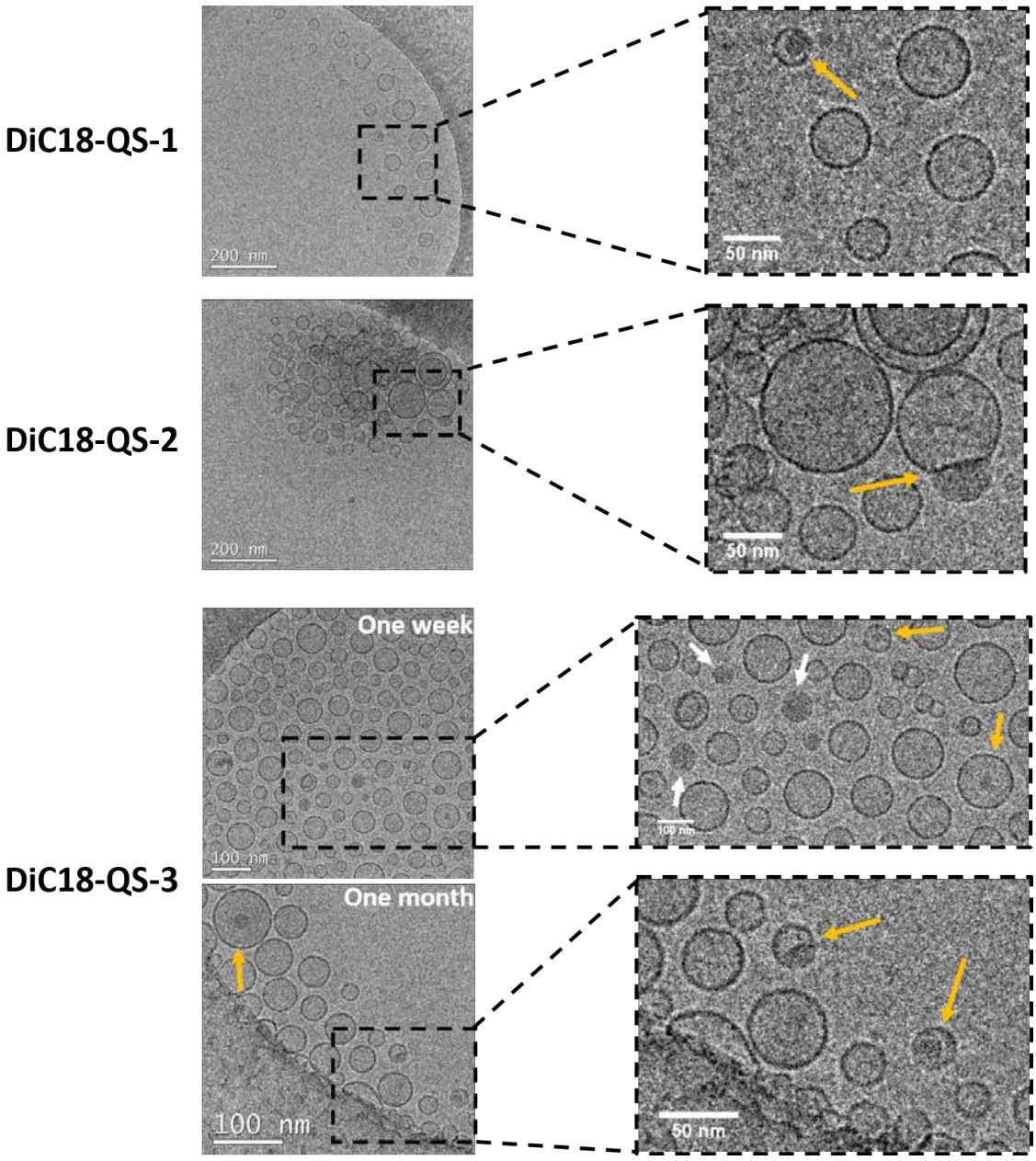

Figure 5.5: CryoTEM images of DiC18-QS-1 (top), DiC18-QS-2 (middle) and DiC18-QS-3 (bottom) one week after their preparation. Images of DiC18-QS-3 one month after the preparation are shown as well. Patchy-Quatsomes are indicated with the orange arrows; white arrows indicate other non vesicular structures attributed to DiC18 supramolecular organization.

architectures. The supramolecular arrangement of nanoparticles decorated with apliphatic chains on the surface ("hairy" nanoparticles), in fact, can be driven by the weak hydrophobic interactions among the entangled chains, which can even lead to the formation of complex multi-nanoparticles structures with tailored shape, as shown by Lee et al. [256] in the case of "hairy" gold nanoparticles covered with mixtures of hydrophobic/hyrophilic C_{12} ligands. Therefore, just for a mere speculation, a mechanism describing the interaction between the patches and Quatsomes bilayer, as the one depicted in Figure 5.6, can be hypothesized. We imagine in fact that, during the DELOS-SUSP process, patches principally formed by dye molecules exposing the alkyl tails outwards (Figure 5.6A), towards the surrounding medium, are formed. At the same time, these patches can be internalized within the bilayer of the forming Quatsomes, resulting in architectures in which the patches are covered by a cholesterol/CTAB monolayer with the hairy tails inserted between the synthons. Thus, the weak hydrophobic interaction between the alkyl chains of the dyes on the surface of the patches and the tails of CTAB, likely drives the formation of the patches within Quatsomes.

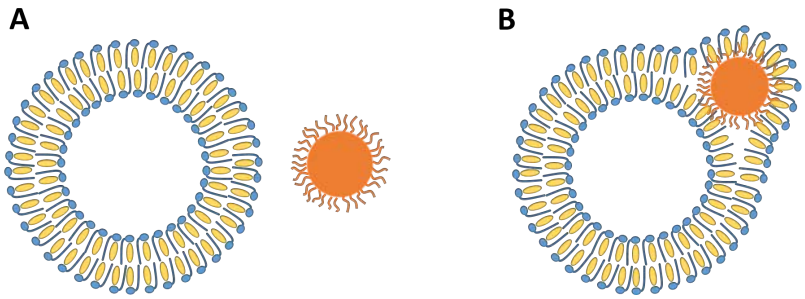

Figure 5.6: Proposed mechanism for the formation of Patchy-Quatsomes. A) Section of the Quatsomes (cholesterol is yellow and CTAB is blue), as suggested by the MD simulations, and hypothesized section of a patch (orange) in which the aliphatic tails of the dyes are facing outwards. B) Hypothesized mechanism of interaction between the patch and the bilayer, resulting in a cholesterol/CTAB monolayer covering the patch.

Along with Quatsomes and Patchy-Quatsomes, some other spare non-vesicular structures was also detected, indicated by the white arrows in Figure 5.5, bottom-right. These structures, never detected in the case of plain Quatsomes made by Cholesterol and CTAB, are ascribed as well to supramolecular assemblies of DiC18, alone or in combination with cholesterol and CTAB, that are completely isolated and not bound to the vesicles, in contrast with the patches observed in Patchy-Quatsomes. Furthermore, it is important to remark, that these considerations rely on the cryoTEM micrographs, which do not give a statistical information on the samples, being based only on the

observation of a few single particles. Deeper study on these kind of systems are therefore necessary to reveal their composition and nature. By exploiting techniques which allow to measure average properties of the bulk samples, such as SWAXS (small- and wide-angle X-ray scattering), one could enlighten the supramolecular organization of these nanoparticles.

Interestingly, the structure observed one week after the preparation are maintained over one month, meaning that the morphology of these samples does not change over this period of time.

DiC18-(M)QS samples showed the same morphology of DiC18-QS ones, as indicated in Figure 5.7, with three representative images of DiC18-(M)QS at the three different loadings.

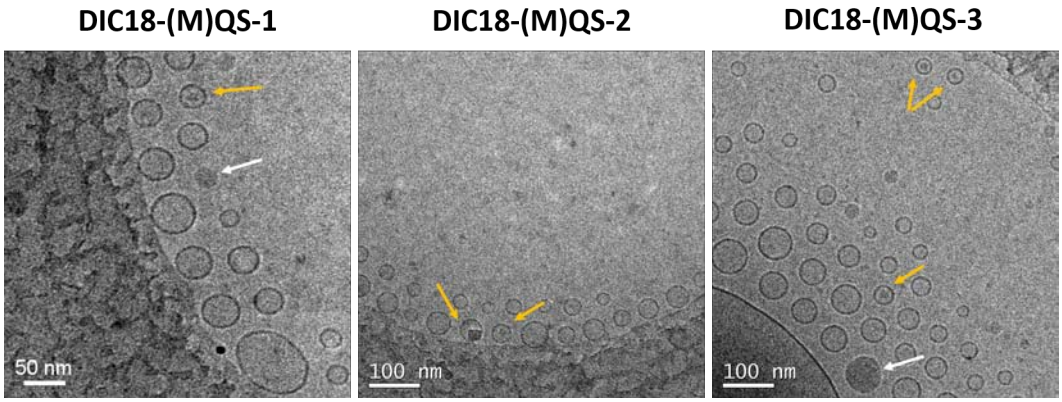

Figure 5.7: CryoTEM images of DiC18-(M)QS-1, -2 and -3 samples one week after their preparation. In these images, the same structures observed for DiC18-QS samples (Figure 5.5) are detected. Patchy-Quatsomes are indicated with the orange arrows; white arrows indicate other non vesicular structures attributed to DiC18 supramolecular organization.

The size distribution (Figure 5.8), mean hydrodynamic diameters and colloidal stability of DiC18-QS and DiC18-(M)QS samples were evaluated by Dynamic Light Scattering (DLS) and results are listed in Table 5.3. The DLS is equipped with a 632 nm laser, at which DiC18 is transparent (see Experimental Section 7.4.1 for details on DLS). Quatsomes made by Cholesterol/MKC are a bit bigger than those made by Cholesterol/CTAB (around 101 nm and 68 nm, respectively) and with a slight dependence on DiC18 loading, since their sizes decrease upon addition of DiC18. In the case of DiC18-QS, the average size is independent of the DiC18 loading. The values of Z-potentials, conferred by the positive charge of the quaternary ammonium surfactants, are high in all the cases and similar to the values obtained for plain Quatsomes. Notably, the average sizes are maintained over the examination period evidencing, along with the high Z-potential values, the strong colloidal stability of these samples.

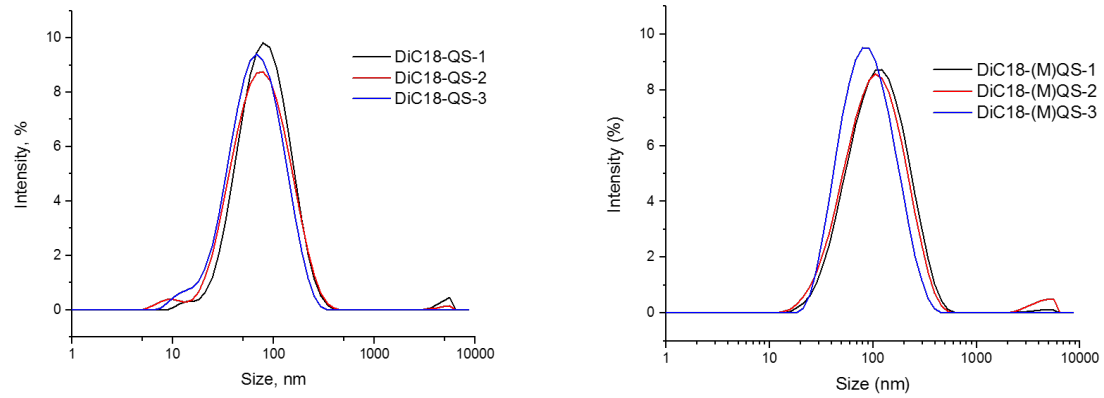

Figure 5.8: Size distribution of DiC18-QS and DiC18-(M)QS samples measured by DLS one week after their preparation

Table 5.3: Size distribution and Z-potential of DiC18-QS and DiC18-(M)QS one week and two months after their preparation, measured by DLS

Sample	Size(1 week)[a] (nm)	Size(2 months)[a] (nm)	Z-potential[a] (mV)
Plain QS	68±31	67±34	82±24
DiC18-QS-1	70±38	73±35	86±20
DiC18-QS-2	58±30	55±28	78±27
DiC18-QS-3	60±32	60±30	75±18
Plain (M)QS	101±48	108±50	84±17
DiC18-(M)QS-1	93±48	103±52	86±17
DiC18-(M)QS-2	87±49	94±50	94±18
DiC18-(M)QS-3	75±37	81±41	85±18

[a] Size distribution and Z-potential measured by DLS. Size distribution is shown as the mean average hydrodynamic diameter ± mean PdI. See Experimental Section 7.4.1 for details

Colloidal properties of micelles-encapsulated DiC18 In order to have an insight of the morphology of the micelles-encapsulated DiC18, cryoTEM images at the different ratios between DiC18 and CTAB were acquired and the representative images (two for each sample) are shown in Figure 5.9.

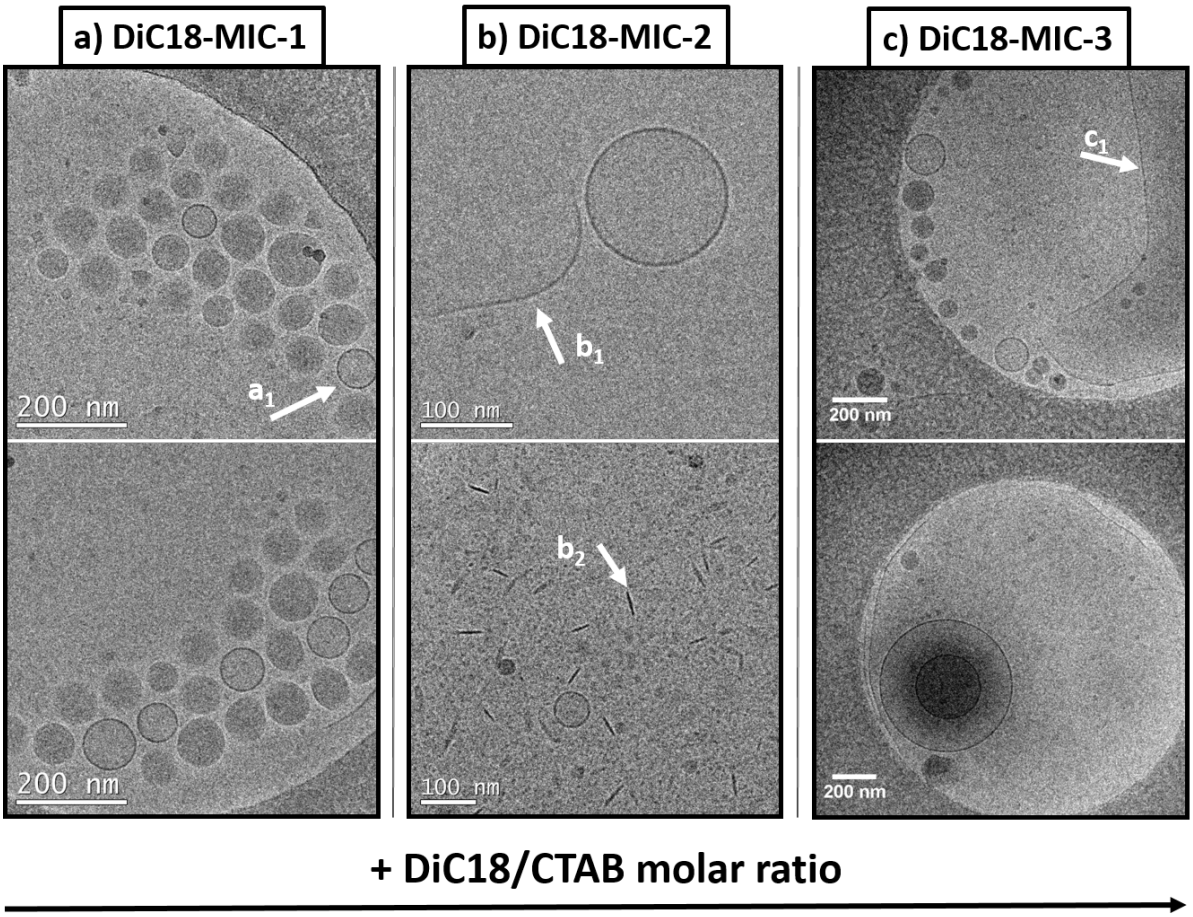

Figure 5.9: CryoTEM images of DiC18-MIC samples at different molar ratios between DiC18 and CTAB: a) DiC18-MIC-1 (molar ratio DiC18/CTAB: $1.8x10^{-3}$); b) DiC18-MIC-2 (molar ratio DiC18/CTAB: $13.3x10^{-3}$); c) DiC18-MIC-3 (molar ratio DiC18/CTAB: $24.7x10^{-3}$). In each column, top and bottom images refer to the same sample.

These images show that the nature of the formed colloidal phase strictly depends on the molar ratio between the two components. Although the morphology of these samples is rather complex, useful information on the phase behavior of CTAB and DiC18 mixture can be withdrawn. Thus, at the lowest DiC18/CTAB ratio (Figure 5.9, left), a high number of entirely filled round-shaped nanoparticles is detected. Such structures, similar to some of those observed in the case of DiC18-QS samples (white arrows in Figure 5.5), can be ascribed to supramolecular assemblies of DiC18 and CTAB. It can be safely excluded that these structures are made only by CTAB, taking into account that at this concentration (7 mM ca.) CTAB forms micelles, with sizes of 2-3 nm, which can not be detected by electron microscopy. Along with these structures, very few small unilamellar vesicles (a_1 Figure 5.9, left) have been detected as well. At higher DiC18/CTAB ratio (CTAB-MIC-2) new structures appears, as worm-like micelles (b_1 in Figure 5.9, b) and several disk-like micelles (b_2 in Figure 5.9, b). At the highest ratio explored some bigger vesicle appeared,

along with some sheet-like membrane with twisted edges (c_1 in Figure 5.9, c).

Some of the architectures appearing in Figure 5.9 (disk- and worm-like micelles for example) can be linked to those showed in the phase study of cholesterol/CTAB mixtures at different ratios between the two compounds [134]. In that case, exploring a large range of compositions, it was found that a single phase composed by small unilamellar vesicles, the Quatsomes, could be formed at cholesterol/CTAB molar ratio equal to 1. Unfortunately, the phase study of the DiC18/CTAB binary mixture in a wider range of composition has not been realized, due to the large amount of DiC18 that such kind of study would require and the limited quantity available of DiC18 in our laboratories.

Due to the complexity of this system and the poor information withdrawn from the cryoTEM images on the self-organization of these two molecules, only the colloidal properties have been analyzed and the samples have been discarded for the study of the optical properties.

Colloidal properties of DiC18 nanoparticles The size distributions of DiC18 NPs, measured by DLS, on the same day of the preparation and after 10 days are shown in Figure 5.10.

Average size of the nanoparticles increases from 101 nm up to 184 nm, during the 10 days following the preparation. The colloidal instability of this system is highlighted as well by the Z-potential (around -1 mV), testifying that without any further stabilizing agent, these nanoparticles are not stable in water.

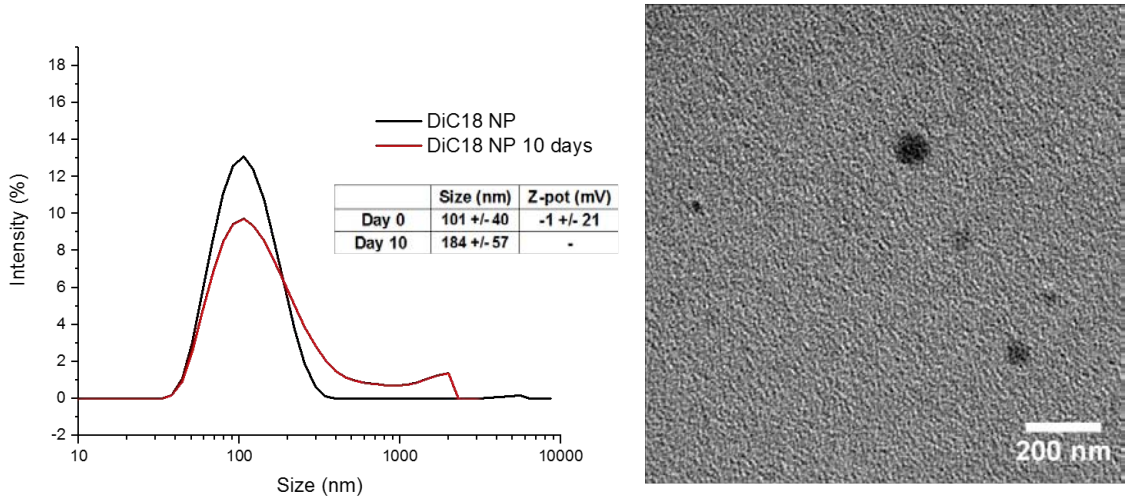

Figure 5.10: Left) Size distribution of DiC18 NP measured by DLS. Right) TEM image of DiC18 NP acquired on the same day of the preparation. Uranyl acetate was used as contrast agent.

Morphology of DiC18 NPs is shown in the TEM images acquired using uranyl acetate

as contrast agent (Figure 5.10), acquired on the same day of the preparation. DiC18 NPs are round-shaped objects, with diameter of around 100 nm or less, in accordance to the average size measured by DLS.

5.2.3 Optical properties of the DiC18-based FONs

As previously mentioned, a critical analysis of the optical properties of DiC18-MIC samples has been skipped, at the moment, due to the poor information that has been extracted so far on the structural organization and complex heterogeneity of the architectures discussed in the previous Section. Therefore, the study of the photophysical properties will be focused only on Quatsomes-dispersed DiC18 (DiC18-QS and DiC18-(M)QS samples) and DiC18 nanoparticles (DiC18-NP).

A picture of three vials containing DiC18 in THF, DiC18 NP and DiC18-QS-2 (all the samples diluted to the same concentration of fluorophore, 2 μM) under UV lamp (λ_{exc}= 388 nm) is shown in Figure 5.11. Even at first glance, it can be observed that the dye in THF is brighter than DiC18-QS-2 which is brighter than DiC18 NP. It looks as well that DiC18-QS-2 has a bit more blue-ish color than DiC18 NP. This picture well represents the spectroscopic properties of the different samples, described below.

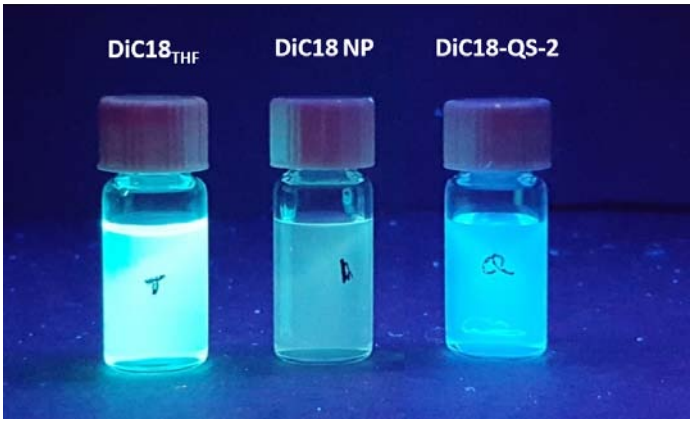

Figure 5.11: Photograph of three vials containing DiC18 in THF, and suspensions of DiC18 NPs and DiC18-QS-2 in water (from left to right) under illumination with a UV lamp (388 nm).

The normalized absorbance, excitation and emission spectra of DiC18-QS-1, -2 and -3 (compared to DiC18 in THF) and DiC18 NPs are showed in Figure 5.12 a-d, while the photophysical properties are summarized in Table 5.4. The photophysical properties of DiC18-(M)QS samples are also included in Table 5.4, but the spectra are omitted, since they exactly overlap to those of DiC18-QSs.

9,10-Diphenylanthracene (9,10 DPA) in cyclohexane has been used as standard for the

determination of the fluorescence quantum yield (φ). See the Experimental Section 7.5.3 for details on the determination of the optical properties.

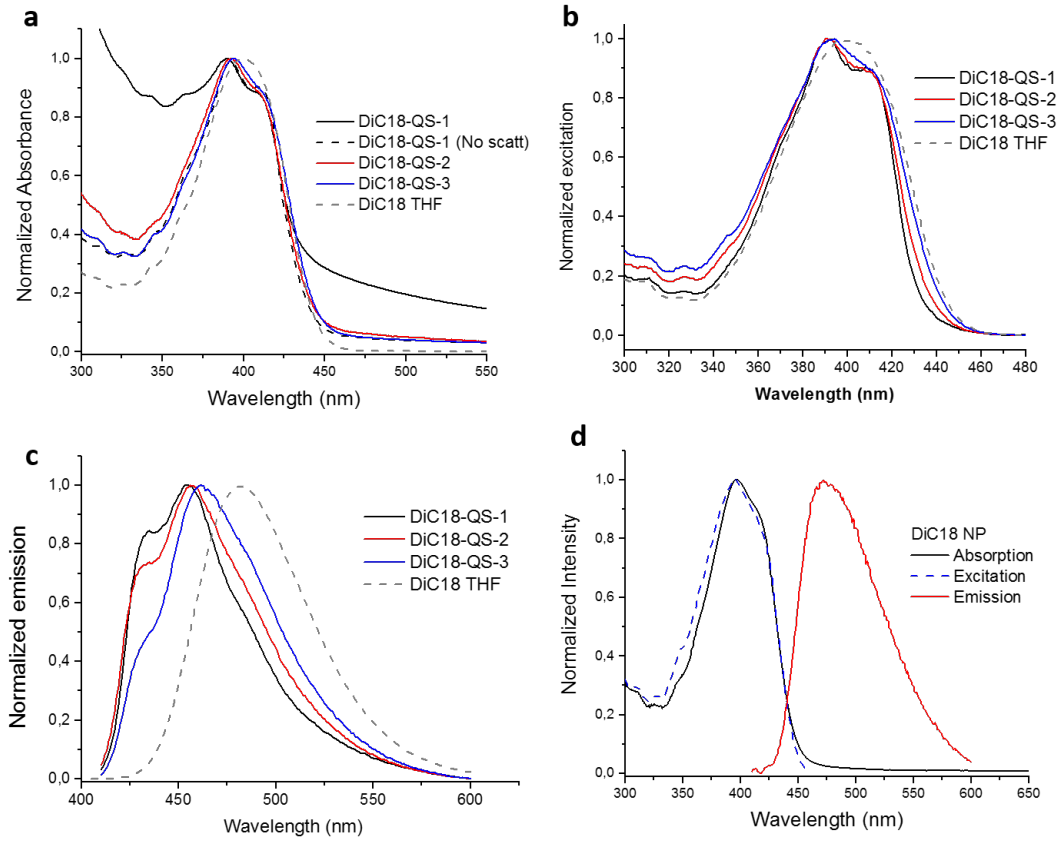

Figure 5.12: Normalied absorption (a), excitation (b) and emission (c) of DiC18-QS-1, -2 and -3 in water and DiC18 in THF. Normalized absorption, excitation and emission of a water suspension of DiC18 NPs (d).

As a consequence of their nanometric size distributions, Quatsomes scatter light in the UV-vis range. Especially at low DiC18 loadings (DiC18-QS-1 in Figure 5.12,a), in which the absorption to scattering ratio is low, the absorption spectrum may be misinterpreted. For this reason, and in order to have a good estimation of the quantum yield of the system, scattering contribution has been subtracted from the absorption spectrum, as explained in the Experimental Part 1.4. The absorption spectra of the other two samples (DiC18-QS-2 and -3) are shown as originally acquired, without any mathematical treatment, although a small tail in the blue edge of the UV-vis absorption spectrum of DiC18-QS-2 due to scattering is still present.

Table 5.4: Photophysical properties of a solution of DiC18 in THF and of suspensions of DiC18-QS, DiC18-(M)QS and DiC18 NP samples

	$\lambda_{\text{max abs}}$ **nm**	$\lambda_{\text{max emi}}$ **nm**	**Stoke's Shift** **cm** $^{-1}$	$\epsilon^{\mathbf{a}}$ (**M**$^{-1}$ cm^{-1})	$\phi^{\mathbf{b}}$ %
DiC18 (THF)	400	482	4,250	44,000	85
DiC18-QS-1	392	452	3,390	39,000	46
DiC18-QS-2	394	455	3,400	40,000	37
DiC18-QS-3	394	461	3,690	36,000	21
DiC18-(M)QS-1	394	453	3,300	40,000	40
DiC18-(M)QS-2	395	459	3,530	38,000	33
DiC18-(M)QS-3	395	468	3,950	38,000	25
DiC18 NPs	395	472	4,130	37,000	10

[a] Molar extinction coefficient at the maximum absorption wavelength
[b] Fluorescence quantum yield ±10%. 9,10-Diphenylanthracene (9,10 DPA) in cyclohexane has been used as standard

The slight positive solvatochromism in absorption (from 391 nm to 394 nm from DiC18-QS-1 to DiC18-QS-3) and emission (from 452 nm to 461 nm from DiC18-QS-1 to DiC18-QS-3) increasing the DiC18 loading in Quatsomes suggests a slight change in the polarity around the fluorophores, paralelling the bathochromic shift of the DiC18 in solvents with higher polarity (Figure 5.3). Along with the red-shift of the main emission peak, increasing the polarity of the solvent (Figure 5.3) a shoulder in the blue edge of the emission spectra decreases and the shape of the spectra become broader, similar to what is observed in Figure 5.12c at higher loading of DiC18. On the other hand, normalized excitation spectra of DiC18-QS-1, -2, -3 and DiC 18 in THF are well overlapped to the absorption spectra. Emission of DiC18 NP is slightly red-shifted (peaked at 472 nm) compared to DiC18-QS samples, but the fluorescence quantum yield of Quatsomes-dispersed DiC18 samples are really high (0.46, 0.37 and 0.21 respectively for DiC18-QS-1, -2 and -3) and in the best case almost five times higher than that DiC18 NP (around 10%).

In conclusion, despite the slightly red-shifted emission displayed by DiC18 NPs, which is desired in view of possible application as bio-imaging probes, Quatsomes-based FONs are much brighter, irrespective of the surfactant used. These results are in line with those shown by Andrade et al. [66], in which an extremely bright fluorene derivative (φ in hexane 95% ca.) was dispersed in water by using Pluronic micelles and successfully used for lysosomal tracking. In that case, after micelles encapsulation, the φ of the dye was around 35%, a loss of the same magnitude of the

values shown in this Thesis.

The long-term stability upon storage (at 5°C) of DiC18-QS and DiC18-(M)QS at different loadings was monitored also by UV-vis spectroscopy. Absorption spectra of the monitored samples one week and two months after their preparation are shown in Figure 5.13

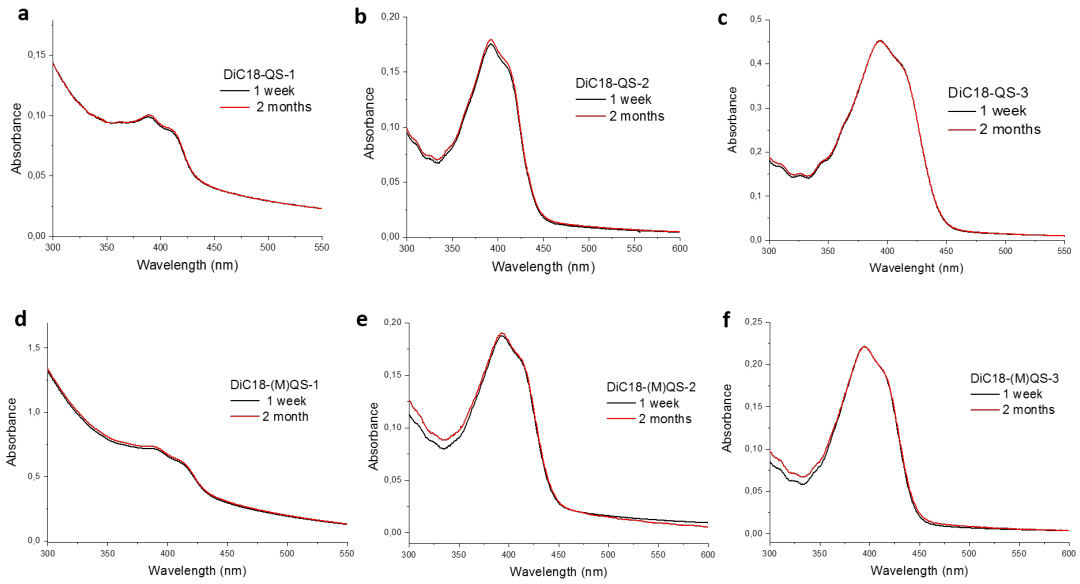

Figure 5.13: Stability (monitored by UV-vis absorption) under storage conditions (4°C) of water suspension of DiC18-QS-1, -2 and -3 (a, b and c, respectively) and DiC18-(M)QS-1, -2 and -3 (d, e and f, respectively)

The UV-vis absorption spectra of the six samples are maintaining the same shapes and intensity over the two months in which the samples have been analyzed, showing that no re-organization of the fluorophore neither any release to the surrounding media is occurring under the exhamination period for both, DiC18-QS and DiC18-(M)QS systems.

As already mentioned, the main function of lysosomes in cells is to work as a digestive system by using an array of enzymes that are capable of breaking down all types of biological macromolecules. It is essential for a probe used for lysosomal imaging to be stable in acidic environment because all of the lysosomal enzymes are acidic hydrolases, which are active at the acidic pH of ca. 5 that is maintained within lysosomes. The pH stability of DiC18-QS-3 and DiC18-(M)QS-3 (not shown) was checked by measuring the steady-state absorption and emission spectra in a series of PBS buffers with different pH. DiC18-QS-3 was diluted by using the PBS buffer at the different pH, in order to reach absorbances < 0.1 and then the emission intensity was checked. The measurements were made by Xinglei Liu at the New Jersey Institute of Technology (NJIT).

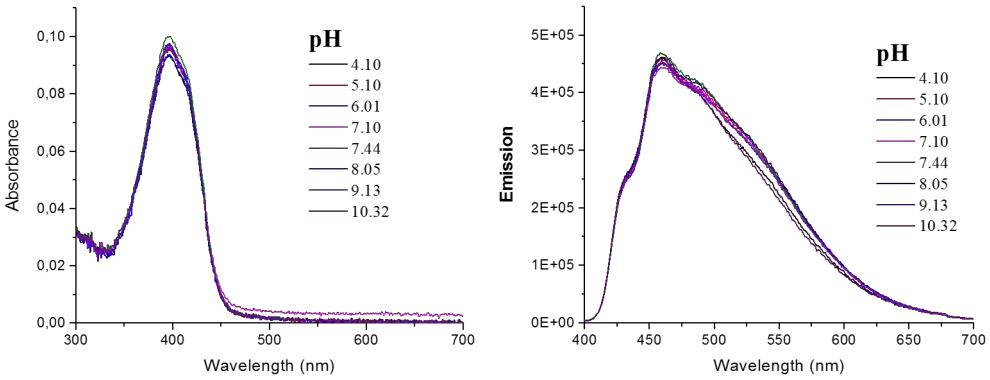

Figure 5.14: Absorption (left) and emission (right) of DiC18-QS-3 at different pH, from 4.10 to 10.32., adjusted with PBS.

The emission spectra in PBS is slightly broader (a tail in emission reaches 700 nm) than that in MilliQ water (emission was in the range between 400 nm and 600 nm).

As showing in Figure 5.14, only small fluctuations were observed on absorption and emission spectra, indicating the good stability of DiC18-QS-3 over the pH range of 4.10 to 10.32. So, contrary to most of the common lysosomal probes, Quatsomes-dispersed DiC18 fluorescence intensity is independent of the pH, which is a desirable property in the cases of exact intracellular localization of lysosomes irrespective of pH variations, usually associated to alterations of their activity [245].

5.3 Cell viability and imaging of DiC18-based FONs

All the measurements described in this Section have been performed by Xinglei Liu, in Prof. Kevin Belfield's laboratories at the New Jersey Institute of Technology. In order to demonstrate the potential utility of the fluorophore DiC18 and the Quatsomes loaded with DiC18, the viability in HeLa cells was studied, via the MTS assay, as previously done in other cases [257].

MTS assay consists of a slightly modified version of the more common MTT assay (previously described in Chapter 4). The only difference is that, upon addition to living cells, MTS reagent is reduced to a formazan dye which is soluble in cell culture medium, avoiding then a further step of solubilization of the unsoluble formazan produced by cells during the MTT assay [258]. In few words, the MTS is a one-step MTT assay. MTS assay was performed to check cells metabolic activity of HeLa cells which were incubated for 22 hours in presence of the samples. See Experimental Section 7.7 for all the details on cell viability measurements. To test the cytotoxicity, DiC18 has been initially dissolved in DMSO, then diluted with cell growth medium (DMEM) and finally added to cells. To test the cytotoxicity of Quatsomes-based samples, the samples were initially diluted with DMEM and then added to the cells culture. The values of cells viability are plotted against the nominal concentration of surfactant, i.e. the concentration of surfactant used for the preparation of the Quatsomes-based samples, since these compounds have some degree of toxicity. The obtained results from cell viability tests are shown in Figure 5.15.

Figure 5.15 (a) shows the viability data for HeLa cells after 24 h incubation with several concentrations of the DiC18 probe where a low cytotoxicity was observed up to the concentration of 40 μM. Citotoxicity of DiC18-QS and DiC18-(M)QS are shown in Figure 5.15 (b) and (c). CTAB and MKC are quaternary ammonium surfactants and their cytotoxicity to different human cells has been previously studied [237][259]. Furthermore, the cytotoxicity of the surfactant CTAB to Saos-2 cells is discussed in Chapter 4. The cytotoxicity of Plain QS (Chol/CTAB) and Plain MKC-QS (Chol/MKC) are also shown in Figure 5.15 as well, to determine whether the DiC18 has any effect on the viability of the Quatsomes.

The results indicate that the effect of DiC18 loading is negligible, and the cytotoxicity is mainly ruled by the concentration of surfactant (CTAB or MKC). Good viability was obtained for DiC18-QS at the concentration of 0.022 mM (CTAB concentration) and for DiC18-(M)QS at 0.04 mM (MKC concentration), showing that the MKC, compared to CTAB, has an ameliorative effect in term of toxicity to HeLa cells. This beneficial extent could be attributed, in some extent, to the shielding of the positive charge due to the

phenyl group in the cationic head of the surfactant.

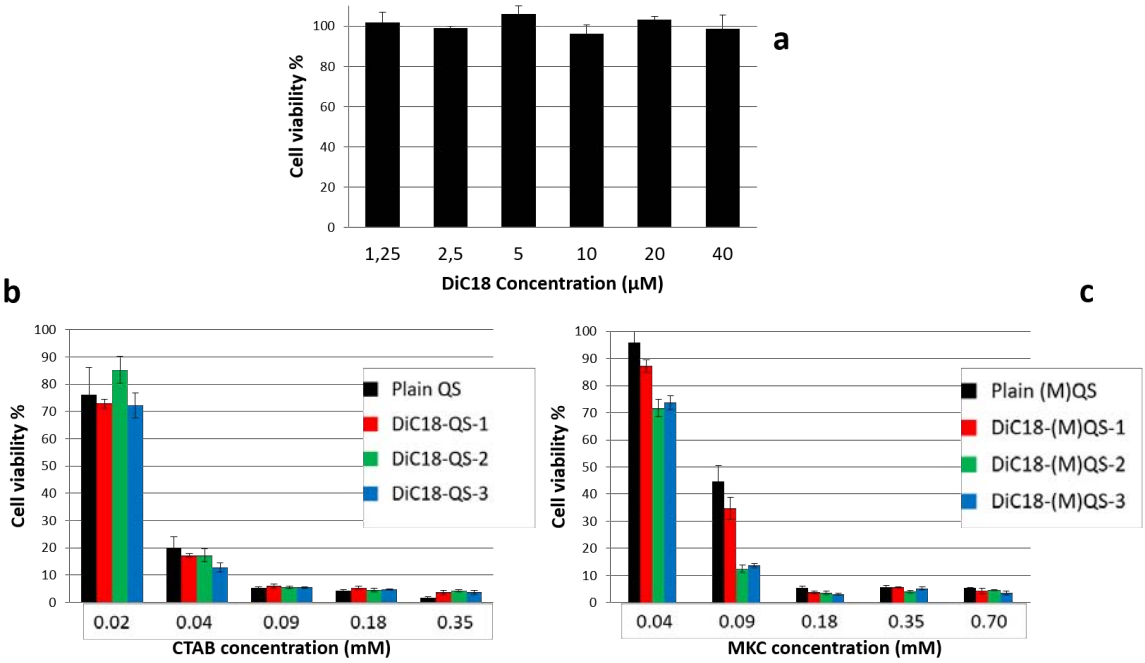

Figure 5.15: Cell viability assay (MTS) of HeLa cells incubated with (a) DiC18; (b) Plain QS (Chol/CTAB) and DiC18-QS-1, -2, -3 and (c) Plain (M)QS and DiC18-(M)QS-1, -2, -3.

5.3.1 Cell imaging and colocalization study of Quatsomes-dispersed DiC18

In order to prove that the systems studied so far can be used as probes for intracellular imaging, epithelial colorectal carcinoma cells, HCT 116, were incubated in presence of DiC18, DiC18-QS-3 and DiC18-QS-3 and then fluorecence microscopy images were acquired. HCT 116 cells have been employed in previous works as model cells for intracellular imaging with fluorene derivatives [252].

In the case of DiC18 staining, a 2 mM solution of DiC18 in DMSO was prepared, then diluted up to 20 µM with the the cells growth medium (DMEM, 1% vol DMSO) and incubated with cells for 2 hours. DMSO has low toxicity on living tissues and cells (generally at concentrations lower than 2% vol) and this method is generally applied for cells and tissue imaging with non-water soluble fluorophores [260]. Moreover, DMSO is a cells membrane permeation enhancer and this method has been applied successfully with other fluorene derivatives [261] and with many commercial labels, including those for lysosomal tracking, such as LysoTracker and LysoSensor Probes (additional information is given in ThermoFisher webpage).

Analogously, aqueous suspensions of DiC18-QS-3 and DiC18-(M)QS-3 were diluted by DMEM growth medium to a nominal concentration of surfactant of 0.02 mM and 0.04 mM (referred to the concentration of surfactant in the samples), respectively, and then incubated for 2 hours with cells. Details on cells staining are given in the Experimental Section 7.7.

Differencial Interference Contrast (DIC) image (left) and confocal fluorescence image (right) of the cells treated with compound DiC18 for two hours is shown inFigure 5.16.

DIC microscopy is a contrast-enhancing technique by which images of transparent specimens can be acquired (here the cells structure is monitored). Upon excitation at 377 nm (close to the maximum excitation wavelength, Figure 5.12) , no fluorescence (Figure 5.16, right) is detected. It is possible that the fluorophore DiC 18, initially dissolved in DMSO, forms aggregates when diluted with the growth medium (the DMEM) before addition to cells and thus these aggregates are not efficiently internalized by cells. Therefore, the conventional protocol based on the dissolution of a fluorophore in DMSO can not be applied in the case of DiC18.

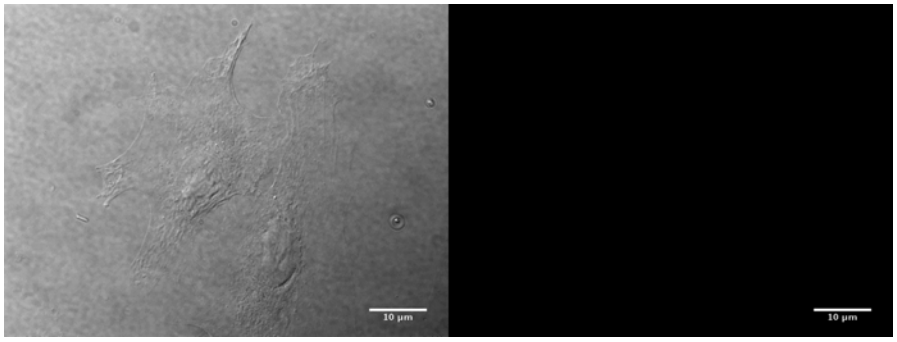

Figure 5.16: Fluorescence images of HCT-116 cells incubated with DiC 18 (20 µM, 2h). left, Differencial Interference Contrast (DIC) microscopy; (b) fluorescence images (Excitation: 377 nm).

On the other hand, HCT 116 cells incubated with DiC18-QS-3 and DiC18-(M)QS-3 provide bright images, as shown in Figure 5.17, probing that dispersing DiC18 in Quatsomes is a feasible strategy to provide good fluorescence signals in cell cultures and to introduce non-water soluble probes into cells for *in vitro* or *in vivo* applications.

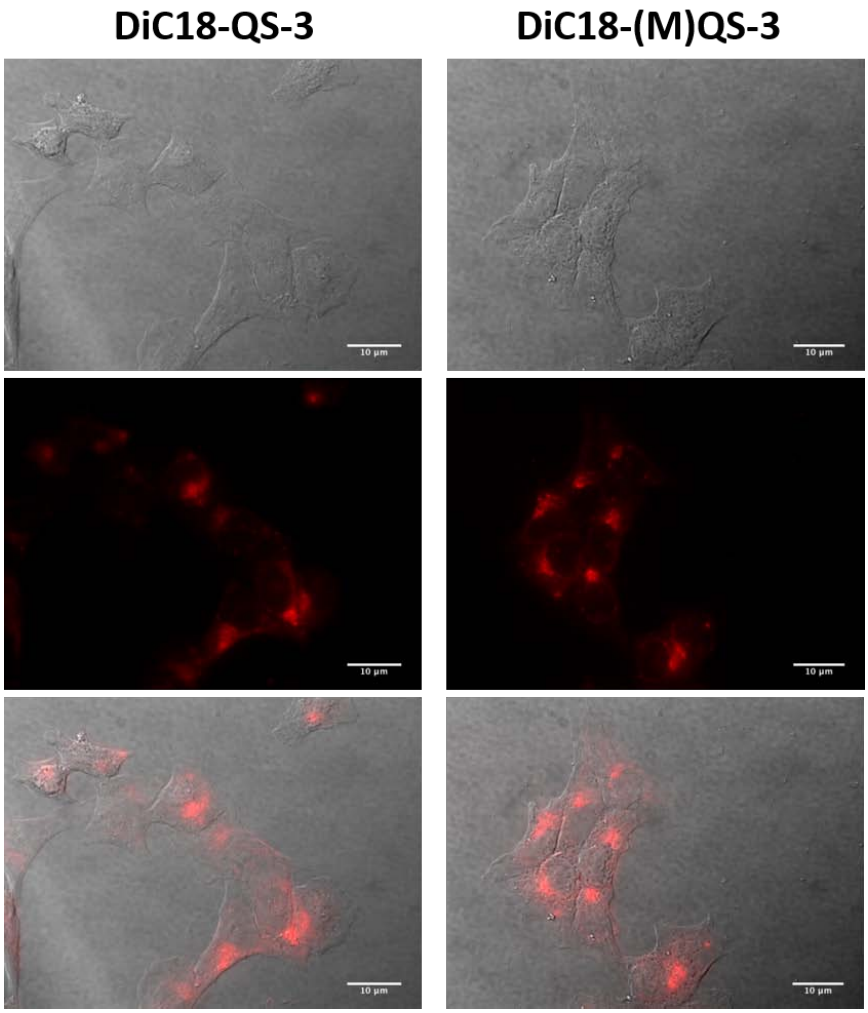

Figure 5.17: Fluorescence images of HCT 116 cells incubated with DiC18-QS-3 (0.02 mM, 2h) and DiC18-(M)QS-3 (0.02 mM, 2h). Top, DIC microscopy image; middle, fluorescence images; bottom, merged images. 60x, oil immersion objective (Excitation: 377 nm).

Images in Figure 5.17 show a bright and spread fluorescent signal, proofing that DiC18-QS and DiC18-(M)QS are successfully incorporated inside the HCT116 cells. However no information about the exact intra-cellular localization of the two FONs can be acquired by these images. Therefore, in order to obtain more information about the exact distribution in the intra-cellular compartments of DiC18-QS and DiC18-(M)QS, a colocalization study was performed by using a lysosomal marker, LysoTracker Red (LT Red), and a mitochondrial marker, MytoTracker Red (MT Red) in combination with the DiC18-based Quatsomes. Fluorescence colocalization analysis is used to determine whether two molecules are associated with the same structure [262], e.g. a particular protein with an endosome or, as in the case of FONs, a nanoparticle in a cellular structure.

In order to visualize the cellular distribution of DiC18-QS and DiC18-(M)QS, the

colocalization study was conducted in two cells lines, HCT 116 and COS 7, commonly employed for internalization studies [263][239]. Fluorescence microscopy images, collected for HCT116 cells co-stained with the two commercial markers (L Red and MT Red) and DiC18-QS-3 (or DiC18-(M)QS-3) are shown in Figure 5.18.

Green channel is related to the fluorescent signal of DiC18-QS (or DiC18-(M)QS) while the red one is related to the LysoTracker Red (LT Red) or the MitoTracker Red (MT Red). The merged images are the result of the overlap between the red and the green channel. Looking at Figure 5.18, it can be observed that, in both the cases, DiC18-QS-3 and DiC18-(M)QS-3, the image merged between the green and LT Red channels appears mostly yellow. This means that the DiC18-QS, as DiC18-(M)QS, are localized in the same regions of the cells, i.e. within the lysosomes, and this specificity is non dependent of the surfactant used (MKC or CTAB) and occurs irrespective of the cell line used. Similar results were obtained for HCT116 and Cos7 cell lines, suggesting a broad and general utility of these new probes. On the other hand, the fluorescent regions in the channels of MT Red and DiC18-QS (or DiC18-(M)QS) are well separated, suggesting that the labeled Quatsomes are not localized inside mitochondria.

Another relevant property of lysosomal probes is the ability to provide long-term imaging [263]. For this reason, cells were incubated with LT Red and DiC18-QS-3 (or DiC18-(M)QS-3) for 2 hours treatment, as previously done with the co-localization experiment. But in this case, after rinsing with PBS, cells were further incubated with fresh DMEM medium until reaching 4, 6 and 8 hours incubation, in order to check any possible migration of the labeled Quatsomes to other cells compartment and/or any degradation of the probes over the observation time ((Figure 5.19)). After 8 hours of treatment a bright signal is still detected and DiC18-QS-3 maintain the same location with LT Red, the lysosomal marker, as shown by the merged images.

In conclusion, the cells images and the co-localization study demonstrate that by using Quatsomes loaded with DiC18 it is possible to target and stably track lysosomes along time with a really high selectivity. For this reason, we decided to name these new lysosomal probes as LysoQS and Lyso(M)QS, for chol/CTAB and chol/MKC Quatsomes, respectively. These results also suggest that LysoQS and Lyso(M)QS are promising candidates for the long-term lysosomal tracking applications, involving the monitoring of lysosome distribution and activity.

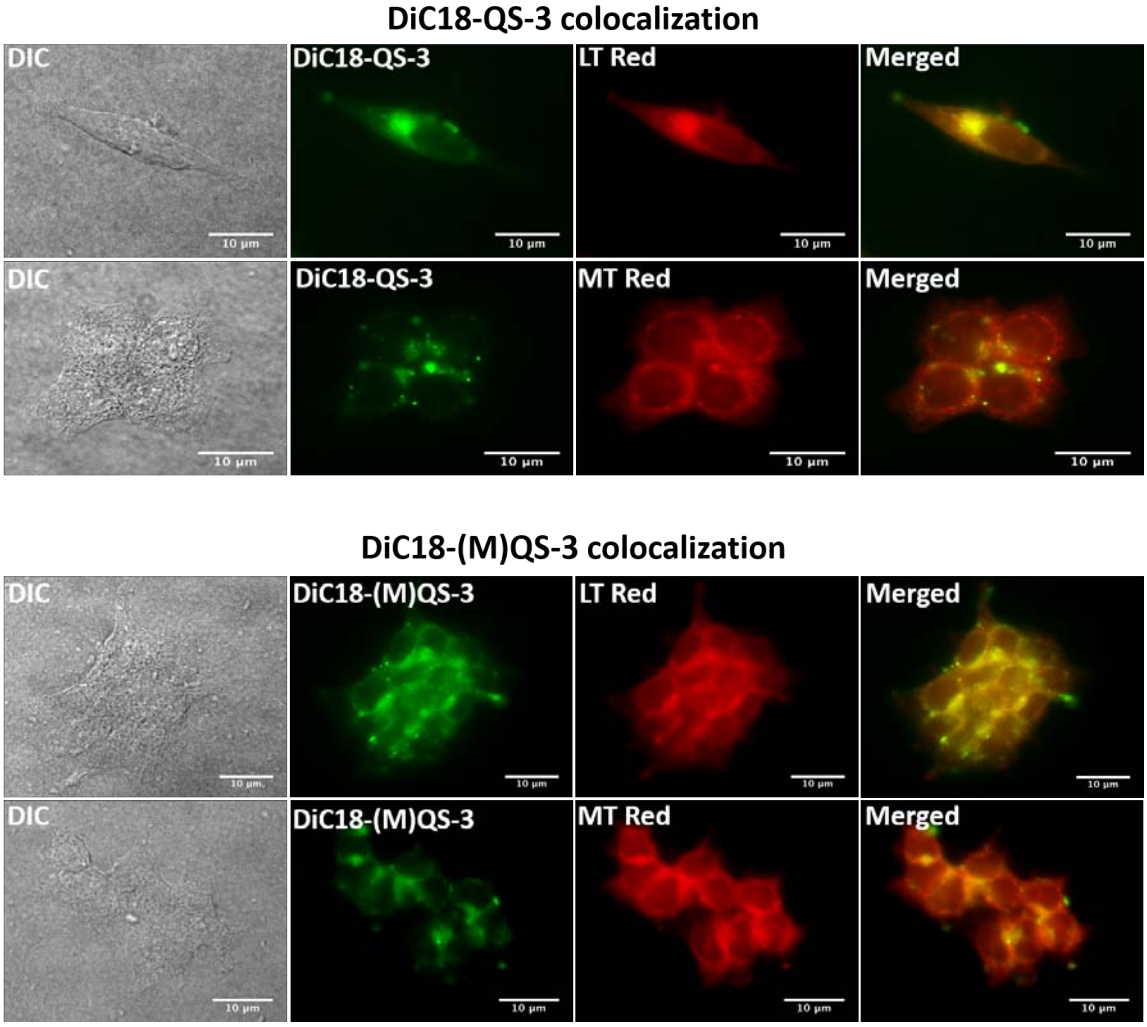

Figure 5.18: Colocalization images of HCT 116 cells incubated with DiC18-QS-3 at 0.02 mM (top) and DiC18-(M)QS-3 at 0.04 mM (bottom), incubated for 2h. From left to right: DIC images; DiC18-QS or DiC18-(M)QS green channel; Lysotracker Red (75 nM, 2h) or Mitotracker Red (400nM, 45 min) red channel; merged images of green and red channel. 60x, oil immersion objective.

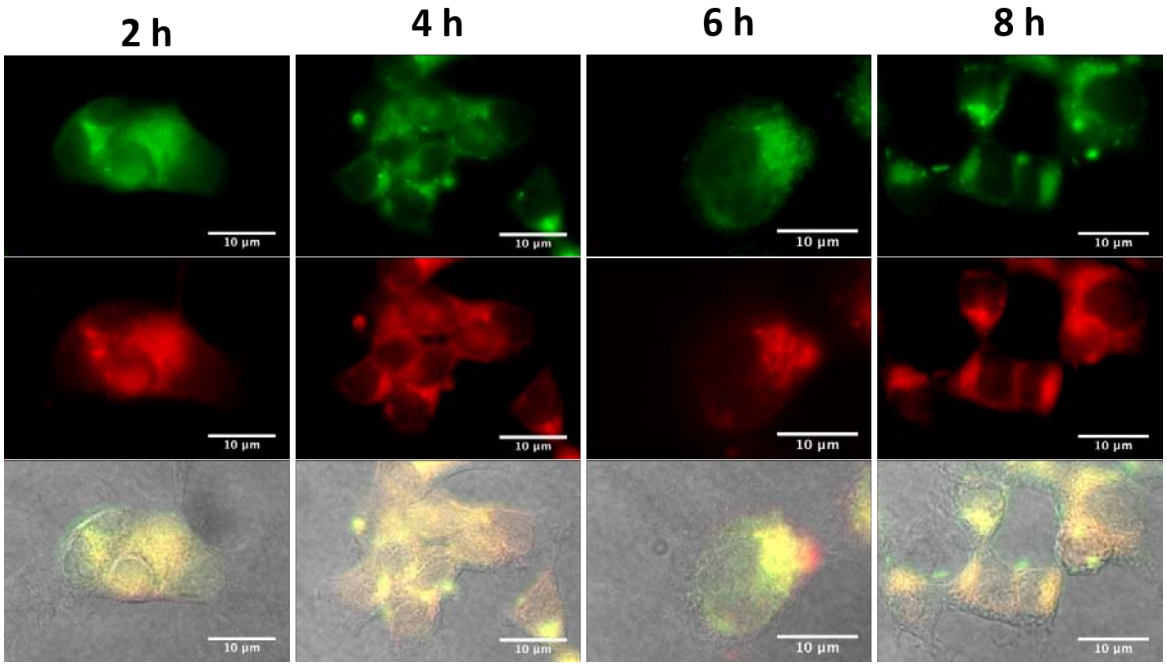

Figure 5.19: Long-term lysosome tracking images of HCT 116 cells incubated with DiC18-QS-3 (0.044 mM, 2h), and Lysotracker Red (75 nM, 2h). Fluorescence images of (A) DiC18-QS-3; (B) Lysotracker Red; and (C) merged images; 60x, oil immersion objective

5.4 Summary and Perspectives

- New lysosome-specific fluorescent nanoparticles have been obtained by using Quatsomes to stably disperse in aqueous media a non-water soluble fluorene derivative (DiC18). This new fluorescent probe, named LysoQS, in the case of Quatsomes made by cholesterol/CTAB, or Lyso(M)QS, in the case of Quastomes made by cholesterol/MKC, constitutes of a mixture of different nano-objects: Quatsomes, Patchy-Quatsomes and other spherical architectures ascribable to other supramolecular organizations of the dye.

- Despite the morphological heterogeneity, LysoQS and Lyso(M)QS are strongly stable, both in terms of colloidal and spectral properties, over two months. The study of the photophysical properties of these new probes indicates that these structures are highly bright, with the fluorescence efficiency that reaches almost 50%, depending on the load of fluorophore. Moreover, no effect of the pH has been noticed on the optical properties of LysoQS, indicating that these probes can be used for the tracking of the lysosomes independently of their activity.

- Biological tests suggested that these innovative FONs can be used, without being

cytotoxic, up to concentrations high enough for acquiring excellent images. Fluorescence microscopy images, showed that LysoQS and Lyso(M)QS are two strongly specific lysosomal probes: co-localization study with LT Red, indicated a high localization of LysoQS inside the lysosomes and not in other intracellular compartments, such as the mitochondria. Furthermore, during long-term imaging (up to 8 hours) no migration to other cellular areas has been observed.

In conclusion, LysoQS and MKC-LysoQS are two specific lysosomal probes, fulfilling many of the requirements necessary for an efficient lysosomes tracking, including high stability and specificity, possibility of long term imaging and pH non-sensitiveness. These properties make these fluorescent nanoparticles good candidates for the development of more complex systems with the inclusion, for example, of actives for lysosomal-addressed drug delivery and photodynamic therapy.

6

Conclusions

The following conclusions have been withdrawn from the work accomplished in this PhD Thesis on the preparation of self-assembled fluorescent nanovesicles and their use as fluorescent probes for bioimaging:

- A new class of fluorescent organic nanoparticles (FONs) can be obtained by self-assembly of organic fluorophores with sterols and quaternary ammonium surfactants. These small unilamellar vesicles, named Quatsomes, incorporating organic fluorophores showed excellent colloidal stability and structural homogeneity along with superior optical properties, in comparison with the fluorophore in solution.

- Fluorescent Quatsomes can be obtained using fluorophores with different physicochemical and optical properties. Thus, anionic water-soluble dyes (i.e. fluorescein) can be nanostructured over Quatsomes surface, taking advantage of the electrostatic interaction among the dye and the membrane of the Quatsome. On the other hand, lipophilic and non water-soluble dyes modified with long alkyl chains (C_{16}-C_{18}) can be incorporated within the membrane of Quatsomes, exploiting the hydrophobic interaction between the alkyl tails and the lipophilic compartment of Quatsomes bilayer. By the latter strategy, highly stable and bright fluorescent nanovesicles are obtained, as shown in the case of several families of dyes including cyanine, diketopyrrolopyrrole (DPPs) and fluorene derivatives.

- Fluorescent Quatsomes showed enhanced optical properties, e.g. brightness, and higher colloidal stability in comparison with other nanostructures in water of the same fluorophores. Moreover, it has been demonstrated that when these FONs were prepared by the DELOS-SUSP method, a compressed CO2-based process, a homogenous membrane composition and supramolecular arrangement are guaranteed, leading to higher optical performances.

- The study of DPP-based and fluorene-based Quatsomes suggested that the length

of the alkyl chains linked to the fluorophore (case of DPP) and its hydrophilic-hydrophobic balance (case of fluorene) play a crucial role in supramolecular interaction of the dye with the quatsome membrane and the corresponding optical properties of the FONs.

- It was probed that multicolor nanovesicles, based on a highly efficient fluorescence resonance energy transfer (FRET) mechanisms between different carbocyanines simultaneously loaded into Quatsomes membrane, can be obtained.

- Cells imaging with fluorescent Quatsomes, revealed the effectiveness of these fluorescent probes under the microscope for in vitro applications. It has been demonstrated that fluorene-based Quatsomes (LysoQS) constitute a strongly specific lysosomal probe. Furthermore, cyanines-loaded Quatsomes were used as probes for super-resolution microscopy technique (STORM) which allowed visualizing and resolving single Quatsomes structures upon internalization in cells.

Based on these conclusions, this Thesis demonstrates that fluorescent Quatsomes, thanks to the combination of superior colloidal, structural and optical qualities, have a strong potential as new fluorescent nanoprobes for bioimaging, theranostics and, generally, nanomedicine applications.

7

Experimental Part

7.1 Materials and methods

5-Cholesten-3β-ol (Chol, purity 95%) was purchased from Panreac (Barcelona, Spain). Hexadecyltrimethylammonium bromide (CTAB, BioUltra for molecular biology ≥99.0%) was purchased from Sigma-Aldrich. Myristalkonium Chloride (MKC, Pharma quality) was purchased from FeF Chemicals (Denmark). Fluorescein sodium salt (FL, 98.5-100.5% of purity) was obtained from Fluka. 1,1'-dioctadecyl-3,3,3',3'-tetramethyl-indocarbocyanine perchlorate (DiI), 1,1'-dioctadecyl-3,3,3',3'-tetramethyl-indodicarbocyanine perchlorate (DiD), 1,1'-Dioctadecyl-3,3,3',3'-Tetramethylindotricarbocyanine Iodide (DiR) were purchased from Life Technologies (Carlsbad, USA). Milli-Q water was used for all the samples preparation (Millipore Ibérica, Madrid, Spain). Ethanol (Teknochroma, Sant Cugat del Vallès, Spain) was purchased with high purity. Carbon dioxide (99,9% purity) was purchased by Carburos Metálicos S.A. (Barcelona, Spain). Sodium hydroxide (NaOH, ≥98.0%) was obtained from Panreac. All the chemicals were used without further purification.

7.2 Preparation of dye-loaded Quatsomes

7.2.1 Preparation by the DELOS-SUSP method

7.2.1.1 Description of the equipment

The equipment used for the preparation of Quatsomes by DELOS-SUSP is shown in Fig Figure 7.1. It is composed by of a 11.8 mL reactor (RX) in which the temperature is controlled by a external jacket; a thermostated syringe pump (model 260D, ISCO Inc., Lincoln, US) (P) to introduce CO_2 inside RX through valve V-4; a depressurization valve (V-7), from which the expanded liquid solution is depressurized into the aqueous phase

placed in a collector (C) located after V-7. A gas filter (FG) (6 μm pores size) is located before V-7. N_2 can be introduced through V-6 directly from a pressurized reservoir. A one-way valve is located after V-6 to prevent contamination of CO_2 in the N_2 line. V-2, V-3 and V-5 are dividing the CO_2 and N_2 pipelines with other equipment. There is also a pressure indicator (PI) and other one-way valve before the reactor.

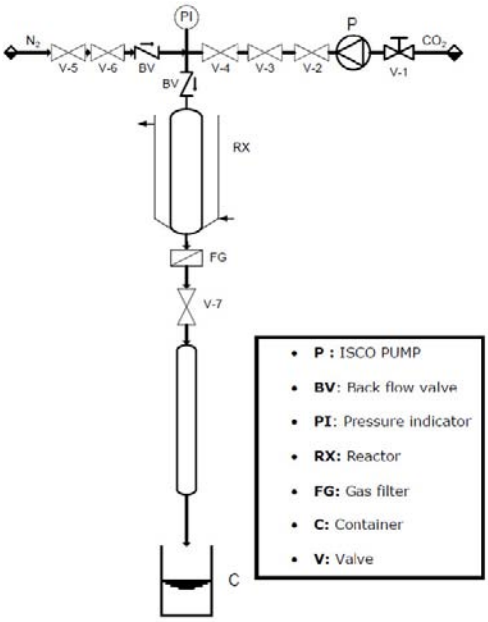

Figure 7.1: Scheme of the DELOS-SUSP set-up. Adapted from ref [130]

7.2.1.2 Experimental procedure

The preparation of dye-loaded Quatsomes by DELOS-SUSP was performed as following. A EtOH solution (4.2 mL) of all the non-water soluble components is introduced into the reactor at working temperature T_w (T_w=308 K). After 20 minutes of equilibration the vessel was pressurized with CO_2 (entering through V-4) at the working pressure $P_w$of 10MPa in order to have an expanded liquid ethanol solution with a molar fraction X_{CO_2}= 0.6. Afterwards, the expanded ethanol solution is maintained at working conditions for one hour, in order to homogenize the system, keeping V-4 opened in order to prevent any pressure decrease due to possible minor leaks of CO_2. The CO_2-expanded solution is then depressurized from P_w to atmospheric pressure through the valve V-7 over 35 mL of aqueous solution where the surfactant has been previously dissolved. A current of N_2 at P_w is used as embolus to push down the expanded solution maintaining constant the pressure in the reactor during depressurization. The aim of the gas filer is to prevent any unsolved compound present in the CO_2-expanded solution to reach the aqueous solution of surfactant. Quatsomes made by different types of sterols and surfactants

have been studied during this Thesis. QS, made by Cholesterol and CTAB; (M)QS made by Cholesterol and MKC (Chapter 5); (C)QS, made by a sterol derivative (STER) and CTAB (Chapter 4). The different Quatsomes families are resumed in Table 7.1, along with their composition and quantities of sterols and surfactants required for the preparation by DELOS-SUSP.

Table 7.1: Types of Quatsomes prepared in this Thesis along with their composition and quantities used for their preparation by DELOS-SUSP

Quatsomes name	Composition	Molar ratio	Sterol mg	Surfactant mg
QS	Cholesterol/CTAB	1:1	111	100
(M)QS	Cholesterol/MKC	1:2	111	202
(C)QS	STER/CTAB	1:1	139	100

7.2.1.3 Solubility of cholesterol in CO_2-expanded EtOH

The solubility behavior of the compounds introduced into the reactor in the CO_2-expanded organic solvent is one of the main parameters that rules the formation of cholesterol-rich vesicles by DELOS-SUSP. It is necessary indeed that these compounds are soluble in the CO_2-organic solvent mixture at the working conditions (T_w, P_w, X_{CO_2}). Figure 7.2 shows the solubility of cholesterol in CO_2-expanded ethanol at different X_{CO_2} at a fixed T_w and P_w. At the molar fraction used for the preparation of Quatsomes by DELOS-SUSP (X_{CO_2}= 0.6), the CO_2 acts as co-solvent, which means that at the working conditions a single phase is obtained inside the reactor and cholesterol is completely dissolved in the CO_2-EtOH mixture.

The solubility of the hydrophobic fluorophores in CO_2-EtOH mixture has not been studied, due to the high prices and the large amounts that would be required in order to make such experiments. However, all the dyes used in this work were soluble in EtOH at T_w and atmospheric pressure at the required concentrations in order to have the desired amount of dye loaded into Quatsomes. Nevertheless, in all the cases tested, no residual solid has been found in the gas filter, meaning that at the concentrations tested, all the dyes were soluble in the CO_2-expanded ethanol solution.

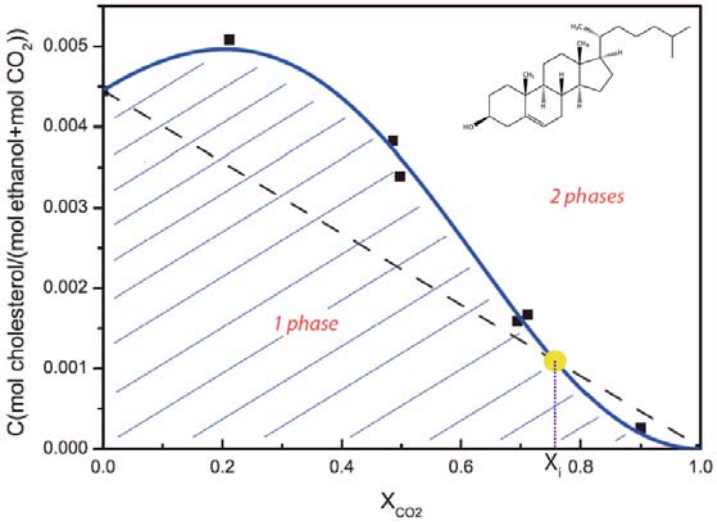

Figure 7.2: Solubility curve (solid blue line) of cholesterol in ethanol/CO_2 mixture at 10MPa and 308 K. The dashed line is the ideal solubility behavior of the three components system. X_i (X_i=0.76) is the intersection point between ideal and real solubility curves. Adapted from Ref. [91]

7.2.2 Samples purification by diafiltration

Diafiltration (Spectrum Laboratories, Inc.) refers to a tangential flow filtration for the removal of permeable molecules (impurities, salts, solvents etc.) from a solution or, like in this case, a colloidal suspension. It is a faster method than dyalisis and it is based on similar principles. For these reasons, it has been used in all cases showed along the Thesis for the purification of dye-loaded Quatsomes. By selecting an appropriate membrane it can be used as well to exchange buffers, modify concentrations, adding salts and other processes. In our case, diafiltration is used to remove EtOH, which is present in 10% vol. after preparation of Quatsomes by DELOS-SUSP, as well as CTAB molecules which are not forming Quatsomes and other possible water soluble impurities present in the samples. The selection of an appropriate membrane, which is placed into a column, is critical for a succesful separation. In our case mPES MicroKros filter column (100 kDa MWCO) have been used. The setup for diafiltration, KrosFlo Research IIi TFF System (SpectrumLabs, USA), is schematized in Figure 7.3.

A rotating pump circulates the sample from the process reservoir through the column and back to the original vessel at a fixed flow rate. The pressure difference between inside/outside of the membrane is the driving force for the separation of low molecular weight compounds that can pass through the pores of the membrane. For every drop of permeate a drop of fresh buffer is added to the process reservoir. Diafiltration was run until 7 times the volume of the sample was collected in the permeate reservoir.

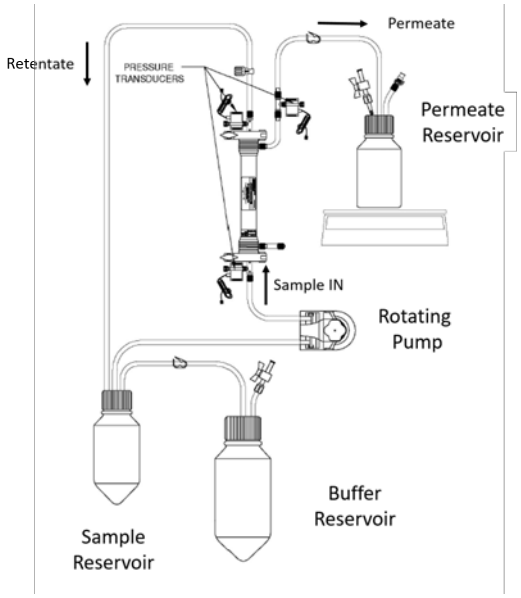

Figure 7.3: Scheme of the diafiltration setup used in this Thesis for the purification of dye-loaded Quatsomes. Acquired from SpectrumLabs webpage.

7.3 Preparation of dye nanoparticles by the reprecipitation method

In this Thesis, the method firstly proposed by Kasai et al. [264] for the preparation of repricitated fluorescent nanoparticles was followed [57, 265]. The reprecipitation method (sometimes called simply precipitation or solvent displacement method) has been chosen in the cases of DiD (Chapter 3), DPPs (Chapter 4) and DiC18 (Chapter 5) for the preparation of dye nanoparticles to compare to the dye-loaded Quatsomes. It is a simple, economic ad highly reproducible route for the preparation of nanospheres. The reprecipitation method required bot a solvent and non-solvent phases of the compound to be precipitated. The solvent phase consists of an organic solution of the dye, while the non-solvent phase consist of a solvent in which the dye is not soluble (in some works reported in literature surfactants and/or other stabilizing agents are eventually added). In order to have the formation of the particles, the organic solvent used must be totally miscible in water. Thus, for the particle preparation, the organic solution of the fluorophore is added in one shot to the aqueous solution under vigorous stirring. The mechanism of submicron particles formation involves the diffusion of the organic solvent into the aqueous phase, creating a local supersaturation and spontaneous nucleation forming small particles which finally grow as submicron particles. The properties of the obtained nanoparticles may be affected by several parameters,

including the concentration of the dye, organic/aqueous phase ratio, injection rate and method of addition, stirring velocity and time, temperature [54, 55].

The dyes reprecipitated nanoparticles prepared in this Thesis are listed in Table 7.2 along with their preparation details. In all cases, nanoparticles with a final concentration of 10 μM (dye concentration in water) were prepared. Small volumes of organic solution of the dyes, previously filtered using Teflon filter with 220 nm pores size, were added to large volumes of water (organic/aqueous phase ratios <2.5% vol) at room temperature, under vigorous stirring for 30 minutes.

Table 7.2: Fluorescent reprecipitated nanoparticles studied and corresponding preparation details

Sample	**Dye**	**Organic solvent**	**Dye conc.** [a] **mM**	**O/W ratio** [b] **vol. %**
D-NP	DiD	EtOH	1	1
DPPC8-NP DPPC16-NP	DPPC8 DPPC16	Acetone	0.4	2.5
DiC18-NP	DiC18	EtOH	1	1

[a] Dye concentration in the organic solvent
[b] Organic solvent/water volume ratio

7.4 Colloidal characterization of dye-loaded Quatsomes

7.4.1 Dynamic light scattering (DLS)

Particle size distributions and zeta potential (Z-potential) were measured using a dynamic light scattering analyzer combined with non-invasive backscatter technology (NIBS) (Malvern Zetasizer Nanoseries, Malvern Instruments, U.K.). Measurements were run without any further modification or dilution of the samples (volume of the used cell is around 1 mL).

The DLS used in this Thesis is equipped with a 4mW He-Ne laser (λ=633 nm) and with a thermostated chamber. The detector angle is fixed at 173° in order to collect mostly backscatter signal which is preferable in case of small particles. Size distributions have been reported in terms of scattering intensity, meaning that these values provide information about the percentage of light scattered by particles of each size in a sample. These values are reliable because they are the raw data collected by the detector of the DLS without further processing, which are usually based on assumptions on sample geometry, for example.

DLS measures the time-dependent fluctuations of light scattered by particles under Brownian motion (resulting from collisions with solvent molecules) which is directly related to the size of the particles. By analyzing the fluctuations of light scattered, the diffusion coefficient of the particles is calculated and then, by mean of the Stokes-Einstein equation, their hydrodynamic diameter can be extracted. The hydrodynamic diameter corresponds to the diameter of a sphere that has the same translational diffusion coefficient as the particle. As a consequence, the values obtained by DLS are related to particles with their hydration shell, depending therefore not only on the real particle size but as well on medium composition, surface structure etc.

The size distributions reported in this work are expressed as $Size_{mean} \pm PdI_{mean}$, where PdI is the standard deviation (expressed in nanometers) of a Gaussian curve that fits the size distribution of the nanoparticles. Size and PdI are averaged over three consecutive measurements on the same volume of samples. Differences between the Size and PdI values calculated from each measurement are negligible (standard deviation over the three measurements < 5%), thanks to the robustness of the technique, and therefore the error over the three measurements is omitted. More information on Size and PdI calculations are given in the ISO standards 13321:1996 E and ISO 22412:2008.

Colloidal stability of the systems presented in this work has been monitored by checking periodically the mean size and size distribution and by measuring the Z-potential. The Z-potential is an electrokinetic property of colloids. It is defined as the electric potential at the slipping plane (located in the double layer distribution of charges) relative to a point away from the interface of the particle. Colloids showing high values, both positive or negative, of Z-potential (generally higher in absolute value than 30 mV) are considered stable, while colloids showing low Z-potential tend to aggregate with time and eventually flocculate [266]. Z-potential is calculated as a mean value over three measurements on the same volume of sample.

The DLS equipped with a 633 nm laser was used for all the samples which do not absorb neither emit if irradiated at this wavelength. In fact, especially for dyes with strong extinction coefficients at 633 nm and high fluorescence efficiency (like the case of DiD), measurements from DLS can be severely affected by both absorbed and emitted light and eventually lead to misleading interpretation of results [157]. In these cases, Nanoparticle Tracking Analysis (Section 1.4.2), equipped with a 488 nm laser, was used as a technique to monitor the size distribution of the fluorescent Quatsomes.

The only exception was represented by DPPC16-QS-1, -2 and -3 (shown in Chapter 4), where the DLS (633 nm laser) was employed. These samples indeed showed a relevant

absorbance at 633 nm (Abs_{633nm}= 0.4*Abs_{MAX}). Nevertheless, while these samples are not fluorescent when excited at 633 nm, they are bright if excited at 488 nm (laser equipped in Nanoparticle Tracking Analysis device). In order to exclude errors due to the detection of fluorescent light and for comparison with the other DPPs-loaded Quatsomes, DLS has been used for the determination of the size distribution of such samples.

In the case of DPPs reprecipitated nanoparticles (DPP-C8 NPs and DPP-C16 NPs), strong absorption was detected at both 488 nm and 630 nm, but fluorescence signal is so low (efficiency <0.1) that has no effect on the measurements. In this case, the error on average size and size distribution is given by the shape (not spherical) of the particles. Nevertheless, information from NTA has been used to obtain information about the evolution of nanoparticles concentration as effect of the aggregation.

7.4.2 Nanoparticle Tracking Analysis (NTA)

Size distribution of dye-loaded Quatsomes showing high absorption in the red region of the visible spectra has been measured by Nanoparticle Tracking Analysis, using a Nanosight NS300 (Malvern Instruments, U.K.) equipped with a sCMOS camera and a 488 nm laser, schematically shown in Figure 7.4.

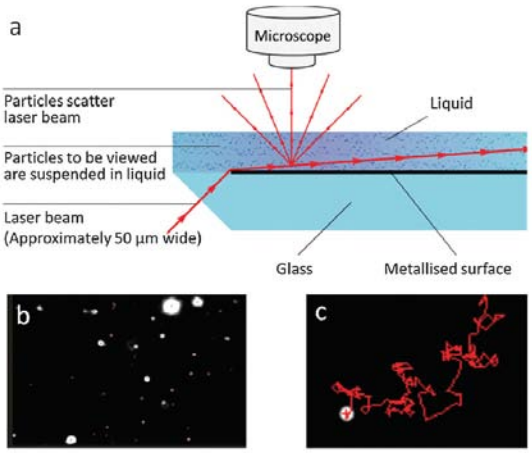

Figure 7.4: Illustration of NTA method. (a) Scheme of Nanosight configuration. (b) a typical frame captured by Nanosight. (c) Typical tracking of a nanoparticle motion by NTA software. Adapted from ref [267]

Unlikely the DLS, which is an ensemble method giving information of the bulk size distribution of a sample, the NTA is a single particle tracking method, which can therefore track and count particles in a liquid. Although the physics behind NTA and DLS is similar (light scattering of nanoparticles moving under Brownian motion), the NTA principle of operation is quite different. The laser beam is indeed focused through the nanoparticle

suspension and the scattered light is collected by a optical microscope, equipped with a 20X objective lens, onto which the sCMOS camera is mounted. A video of particles moving under Brownian motion in a field of view of 100μm x 80μm x 10μm is then recorded and analyzed by the NTA software (Figure 7.4 b and c). With this technique all dye-Quatsomes systems absorbing in the red region of the visible spectra have been analyzed. Samples have been diluted (1/10000) with Milli-Q water in order to reach the optimum number of particles/frame (from 50 to 90), as suggested by the instrument manual.

The theory of Rayleigh light scattering is well established and the intensity of scattered light strictly depends on the refractive index n of the particles (Bohren and Huffman, 1983; Kerker, 1969). The higher is n, the higher is the intensity of light scattered. Therefore, for materials with high refractive index (e.g. metals or semiconductors), it is possible to accurately determine size down to 10-15 nm by using NTA, while for very weakly scattering materials, such as organic nanoparticles, the minimum size of nanoparticles detectable is around 40-45 nm [267, 268]. In this context, problems arise when measuring size distribution of nanovesicles, like Quatsomes. The size distribution of Quatsomes and dye-loaded Quatsomes is generally narrow and average hydrodynamic diameters are around 70-80 nm (by DLS). The size distribution extracted by a quantitative analysis of cryoTEM images (see [130]) shows that most of the Quatsomes have diameters between 30 and 40 nm which are real and not hydrodynamic particle diameters.

The effect of the detection limit of NTA in the determination of average sizes and size distribution of Quatsomes is shown in Figure 7.5, where the size distributions of a sample of plain Quatsomes measured by DLS and then by NTA are reported.

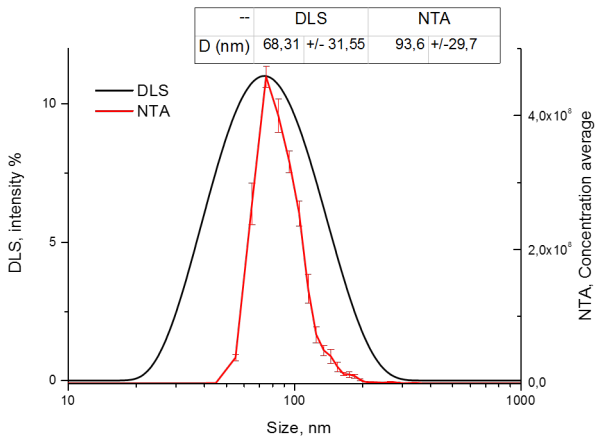

Figure 7.5: Comparison between the size distributions of the same sample of plain Quatsomes obtained by DLS (black curve) and Nanosight (red curve)

Despite some other works showed a pretty good agreement between size distribution by DLS and NTA, for example in the case of polystyrene beads [269], in the case of Quatsomes, all the nanoparticles with size below 50 nm are not detected by NTA. For this reason the mean diameter of the particles, reported in the Figure 7.5, measured by NTA is 30% ca. higher than that measured by DLS (94 nm and 68 nm by NTA and DLS respectively). For the same reason, a big extent of uncertainty is expected in the concentration of nanoparticle reported by NTA. The number of Quatsomes tracked by NTA oscillates between 10^{12} to 10^{13} particles/mL, but this value is surely an underestimation of the real particles concentration.

7.4.3 Cryogenic transmission electron microscopy (cryo-TEM) and transmission electron microscopy (TEM)

The morphology of the nanoparticles presented in this Thesis has been studied using cryogenic transmission electron microscopy (cryo-TEM). The images were acquired with the helps of the technitian at the Servei de Microscòpia of the Univeritat Autònoma de Barcelona. The images were obtained with a JEOL JEM-2011 microscopy (JEOL LTD, Tokio, Japan) operating at 120 kV. For cryoTEM images, the preparation of the frozen samples was performed in a vitrification system with controlled environment (CEVS) Leica, model EM-CPC (Leica Microsystems, Germany). A few μl drop of sample was placed in a copper grid coated with a perforated carbon film (QUANTIFOIL carbon thin film). Excess solution was removed by blotting with filter paper. Right after this the grid was plunged into a liquid ethane held at a temperature just above its freezing point (94 K). The vitrified sample was then transferred to the microscope for analysis. To prevent sample perturbation and the formation of crystals, the specimens were kept cool (77 K) during the transfer and the viewing procedure.

For TEM images, samples were prepared by placing few drops of a solution of the nanoparticles on a copper grid coated with a perforated polymer film and dried for 1 minute before placing the sample holder into the microscope.

7.5 Optical characterization of dye-loaded Quatsomes

7.5.1 UV-vis spectroscopy

Absorbance spectra were acquired on a Varian Cary 500 UV-vis-NIR spectrophotometer (Agilent Technologies) or a Lambda 650 (Perkin Elmer) spectrophotometer. Spectra were

acquired by placing samples in a quartz cell with 1cm path length.

7.5.2 Determination of dye loading [L] and yield of incorporation (YI) in Quatsomes

All the fluorophores and corresponding molar extinction coefficients at the maximum absorption wavelength (ε) in proper solvents are listed in Table 7.3. A solution of known concentration of the fluorophore was prepared and the absorbance of five dilutions was measured. ε was calculated applying the Lambeert-Beer law, as the slope of the straight line fitting the five points on a absorbance vs concentration plot.

Table 7.3: Fluorophores used in this Thesis and their corresponding molar extinction coefficients at the maximum absorption wavelength (ε)

Fluorophore	$\epsilon_{\mathbf{EtOH}}$[a] $\mathbf{M}^{-1}$ cm^{-1}
DiI	140,000
DiD	246,000
DiR	271,000
Fluorescein	77,000[b]
DPPC16	45,000
DPPC8	45,000
DiC18	44,000[c]

[a] Molar extinction coefficient at maximum absorption wavelength
[c] in water at pH=9
[c] in THF

In order to estimate the loading [L], the concentration of fluorophore in each prepared sample was first calculated. To do so, a a known volume of organic solvent (the same in which the ε of the dye was calculated) was added to the samples with volume ratios solvent/QS_{sample} of at least 20:1. The addition of the organic solvent provoked the rupture of the vesicles (checked by DLS or NTA) and the dissolution of the membrane components, including the fluorophore, in the solvent. In order to calculate the concentration of the dye, the absorbance of the obtained solution was divided by the ε of the dye. For each fluorophore, it has been first checked that the presence of cholesterol and surfactants does not have any effect on absorption bandshapes and intensities. The loading [L] was then calculated as follow: $[L] = \frac{moles_{fluorophore}}{moles_{surfactant}+moles_{cholesterol}}$. The amount of surfactant and cholesterol used for the determination of [L] are the nominal ones, i.e.

the amounts that were weighted for the preparation of the solution in the DELOS-SUSP protocol. The concentrations of the dyes in each sample prepared by DELOS-SUSP along with the resulting dye loadings are listed in Table 7.4.

Knowing the amount of fluorophore loaded into the vesicles allowed to calculate the extinction coefficient at the maximum absorption wavelength, ε, of dye-loaded QSs. For each sample, at least three dilutions with Milli-Q water to a known dye concentration were prepared. Then the absorbance of these dilutions was measured (Absorbance always was kept below 0.5). The slope of the plot absorbance vs concentration is the ε of dye-loaded Quatsome samples. When necessary, the scattering contribution was subtracted as explained in Section 7.5.4.

The yield of fluorophore incorporation (YI) in the preparation of dye-loaded Quatsomes by DELOS-SUSP has been calculated by dividing the concentration of the dye in Quatsomes by the nominal concentration of the fluorophore, i.e. the amount of dye placed in the reactor divided by the final volume of the sample. YI is always lower than 100% because the fluorophore can be partially retained inside the reactor.

In all cases tested, the concentration of fluorophore did not decrease as effect of diafiltration, which is in fact a process meant to wash out the ethanol and rest of low molecular weight water-soluble compounds. The values of YI for each sample prepared by DELOS-SUSP are listed in Table 7.4.

Table 7.4: Samples studied in this Thesis along with the fluorophore final concentration, yields of incorporation (YI) and loading ([L]).

Fluorophore	**Sample**	**Conc.**[a] μ**M**	**YI**[b] %	**[L]**[c] $\times$ **10**$^{-3}$
DiD	D-QS-1	8	80	0.57
	D-QS-2	18	90	1.3
	D-QS-3	42	84	3
	D-QS-4	60	79	4.2
	D-QS-5	92	92	6.6
DiI	I-QS-1	8.5	87	0.6
	I-QS-3	46	92	3.3
	I-QS-5	100	100	7
DiR	R-QS-1	7	72	0.5
	R-QS-3	32	66	2.3
	R-QS-5	70	70	5
DiI+DiD	I,D-QS-1	10(I), 10(D)	100	0.75(I), 0.7 (D)
	I,D-QS-5	100(I), 87(D)	≈90-100	7(I), 6.2 (D)
DPPC16	DPPC16-QS-1	3	93	0.2
	DPPC16-QS-2	4	80	0.29
	DPPC16-QS-3	9	85	0.6
	DPPC16-(C)QS-3	9	92	0.63
DPPC8	DPPC8-QS-3	8.5	85	0.6
DiC18	DiC18-QS-1	10	100	0.7
	DiC18-QS-2	98	98	7
	DiC18-QS-3	180	92	13
	DiC18-(M)QS-1	10	100	0.5
	DiC18-(M)QS-2	102	100	4.8
	DiC18-(M)QS-3	202	98	9.7

[a] Fluorophore concentration in the sample after the preparation by DELOS-SUSP and diafiltration

[b] Yield of fluorophore incorporation calculated as the measured fluorophore concentration divided by the nominal one.

[c] Fluorophore loading: [L]=moles$_{\text{fluorophore}}$/(moles$_{\text{sterol}}$+moles$_{\text{surfactant}}$.

7.5.3 Fluorescence spectroscopy

Fluorescence spectra were collected with a Varian Cary Eclipse (Agilent Technologies) or a Fluoromax-3 (Horiba Jobin Yvon) fluorescence spetrophotometers. For fluorescence and excitation spectra, samples with maximum absorbance < 0.2 have been used.

7.5.4 Determination of fluorescence quantum yield (φ) and light scattering correction

Fluorescence quantum yields φ were determined by a comparative method, by using standards of known φ excitable at wavelengths close to those of the samples, as suggested in Ref [158].

Optical densities of the samples are kept below 0.2 to avoid inner filter effects, or the optical densities of sample and reference (r) are matched at the excitation wavelenght. Slit widths have been set at 2.5 nm (or smaller) in excitation and emission.

The following equation has been used to calculate the φ of the samples

$$\varphi = \varphi_r \frac{I}{I_r} \frac{OD_r}{OD} \frac{n^2}{n_r^2} \tag{7.1}$$

where I, OD and n are the integrated fluorescence emission, the optical density at the excitation wavelength and the refractive index of the sample, while I_r, OD_r and n_r are the integrated fluorescence emission, the optical density at the excitation wavelength and the refractive index of the reference used.

By using the protocol provided by Horiba [270], the quantum yield values are given with a ±10% error. In Table 7.5 the standards associated to each fluorophore used in this work are listed.

The samples showing formation of non-fluorescent aggregates, as in the case of Quatsomes loaded carbocyanines or DPPs, φ depends on the excitation wavelength. In order to exclude misleading results and in order to properly compare the samples studied, the maximum φ has been determined, i.e. the φ calculated exciting at the wavelength in correspondence of the maximum of the excitation spectra.

Table 7.5: Fluorophores and corresponding references used for the calculation of φ

Fluorophore	Reference
DiI	Fluorescein (0.1M NaOH)
DiD	Cresyl Violet (MeOH)
DiR	Cresyl Violet (MeOH)
Fluorescein	Fluorescein (0.1M NaOH)
DPPC16	Cresyl Violet (MeOH)
DPPC8	Cresyl Violet (MeOH)
DiC18	9,10 DPA (cyclohexane)

Quatsomes are nanovesicles with diameters of less than 100 nm. Nanoparticles of such small sizes scatter light in the UV-visible region and determination of fluorescence quantum yield of scattering samples is not trivial [271]. For samples showing low absorbance/scattering ratio (generally samples with low loading of dye or sample loaded with dyes with low extinction coefficient) it was necessary to remove contribution from scattering in order to evaluate the real absorbance, necessary for the calculation of the φ. In principle, scattering contribution to the measured absorbance can be avoided during the acquisition of the spectra simply by placing a reference cuvette with a solution that scatters light exactly as the measured sample does. Nevertheless, in our case, it was impossible to follow this strategy, due to the different scattering signal given by each Quatsomes batch prepared by the DELOS-SUSP method.

In the mathematical model used, the measured absorbance ($A_{measured,\lambda}$) can be partitioned into light that is actually absorbed ($A_{corrected,\lambda}$) and the apparent absorption that is due to light scattering at a given wavelength ($A_{LS,\lambda}$) in such a way that:

$$A_{corrected,\lambda} = A_{measured,\lambda} - A_{LS,\lambda}$$

In the case of fluorescein- and cyanines-loaded Quatsomes (Chapter 2 and 3, respectively), a mathematical model for scattering removal has been used as suggested in Ref [272]. The apparent absorption of plain QS (without any fluorophore) can be modeled (in a short wavelength region) in accordance with the Rayleigh approximation of light scattering from particles much smaller than the wavelength of the incident light as follow:

$$A_{LS,\lambda} = c_1 \lambda^{-4} + c_2$$

Where c_1 and c_2 are two coefficients for wavelength-dependent light scattering and baseline offset, respectively. Usually, it can be assumed that these two values are constant,

in a short wavelength range, for example at the edges of the main absorption peak of the dye. Thus, if it is known that the measured absorbance at two wavelengths at the edges of the main absorption peak is only due to scattered light, then c_1 and c_2 can be exactly determined. An example is shown in the case of I-QS-1 sample in Figure 7.6a, where c_1 and c_2 have been calculated at 650 nm and 400 nm.

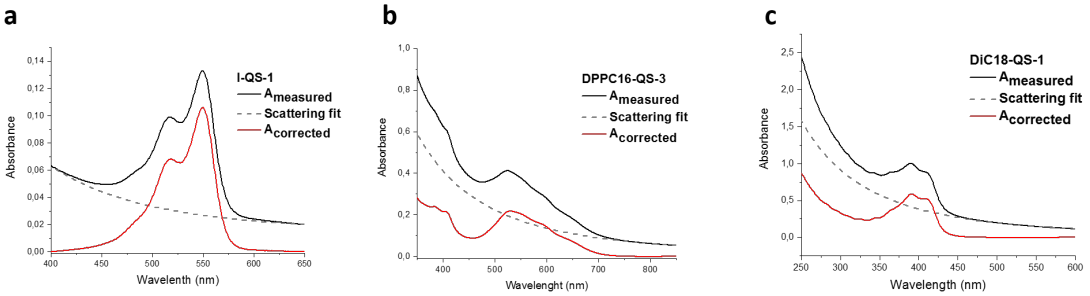

Figure 7.6: Correction of UV-vis absorption spectrum for the scattering contribution in three different cases, discussed along the Thesis. a) I-QS-1 (Chapter 3); b) DPPC16-QS-3 (Chapter 4); c) DiC18-QS-1 (Chapter 4).

A different method for the scattering subtraction was used in the case of DPPs-loaded Quatsomes (Chapter 4) and in the case of DiC18-QS-1 (Chapter 5). Due to the peculiar absorption bandshapes of these dyes , it was not possible to find two wavelengths with known absorbance at the edges of the main absorption peak for the determination of c_1 and c_2. Therefore $A_{LS,\lambda}$was determined accounting for the Rayleigh/Tyndall-type scattering as $A_{LS,\lambda}=a\lambda^n$, where a and n were determined by the least squares fitting of the measured absorption spectrum at wavelengths larger than those where absorption was observed, as shown in Figure 7.6b and c [273, 274].

Although, this method is efficient for the scattering subtraction in a broad region of the NIR-visible spectrum, some residual scattering contribution is still visible in the blue-UV edge of the spectrum. In the case of the DPPs-based FONs, this residual contribution is irrelevant in the estimation of φ, which is in fact calculated at the $\lambda_{Max\ Exc}$, in the range 580-600 nm for all the DPPs-based FONs.

In the case of DiC18-QS samples (Chapter 5), scattering was removed only in the sample with lowest fluorophore loading (DiC18-QS-1). In order to verify that the method used is valid, the condition of Abs_{333nm} = 0.35*Abs_{MAX}, verified for LysoQS-2 and LysoQS-3 (shown as acquired, without any mathematical treatment) and therefore independent of the DiC18 loading, was verified in the corrected absorption spectrum of DiC18-QS-1, meaning that the method used is valid for scattering subtraction in this case.

7.5.5 Determination of the quantum yield of photoreaction (PQY) of DiD (EtOH) and DiD-loaded Quatsomes

Photobleaching is a process by which a molecule undergo photoinduced chemical decomposition upon absorption of light and its a crucial parameter that determines the applicability of dyes in imaging and other applications involving laser-induced fluorescence [166][275].

In this Thesis the quantum yields of photoreaction were measured using either the absorption or fluorescence methods propoesd by Belfield and Bondar [142, 143].

Photobleaching of a dye can be quantified by the quantum yield of photoreaction (PQY), defined as $PQY = N/Q$, where N and Q are the number of molecules that undergo photodegradation and number of absorbed photons, respectively. N can be determined by measuring the evolution with time of absorption (highly concentrated samples) or fluorescence, depending on the method selected.

The determination of PQY was based on the following assumptions:

a) the entire volume of sample placed in a cuvette is irradiated simultaneously, i.e. the effect of diffusion processes on the photochemical kinetics are negligible;

b) In the case of the fluorescence method, the optical density at the absorption maximum before irradiation $OD_0(\lambda_{max})$ was below 0.1, i.e. the irradiation intensity, I_0, can be assumed constant in the entire cuvette

c) the optical density and fluorescence of the products of photoreaction is negligible.

Under these conditions, the PQY can be simply expressed as a function of the variation of absorbance or fluorescence with time. A thorough mathematical description of the method used is given in [143].

The output of a Kr^+ laser (at 476.2 nm) and a diode laser (660 nm) was used for excitation of Fluorescein and DID samples respectively.

7.5.6 Determination of two-photon absorption cross section of DiD (EtOH) and DiD-loaded Quatsomes

Two-photon absorption cross-sections of dyes in solution and dye-loaded Quatsomes were measured by a two-photon excited fluorescence (TPEF) technique with femtosecond excitation pulses. The output of optical parametric amplifier HE-TOPAS-Prime (Light Conversion), pumped by Coherent Legend Elite Duo HE+ was frequency doubled in 1mm BBO crystal resulting in 1kHz, ~150 fs (FWHM) pulse train that was used for sample excitation. Fluorescence signal was measured with PTI

QuantaMaster spectrofluorimeter and the quadratic dependence of the fluorescence intensity on the pumping pulse energy was observed for each excitation wavelengths indicating the two-photon nature of the excitation process.

The values of 2PA cross section σ_{2P} were determined as follows [276][66]:

$$\sigma_{2P}^{S} = \sigma_{2P}^{R} \frac{\langle F(t)\rangle_S C_R \Phi_R \varphi_R \langle P(t)\rangle_R^2}{\langle F(t)\rangle_R C_S \Phi_S \varphi_S \langle P(t)\rangle_S^2} \tag{7.2}$$

where <F(t)> and <P(t)> are the time-averaged fluorescence measured and laser source excitation power, respectively. C is the molecular concentration and Φ is a geometric factor depending on the excitation geometry. The subscript S and R refer to the sample and reference compound.

7.6 Synthesis of the fluorene derivative DiC18

The 7-(benzo[d]thiazol-2-yl)-9,9-diethyl-N,N-dioctadecyl-9H-fluoren-2-amine (DiC18) has been synthesized in the laboratories of Prof. Kevin Belfield (NJIT, USA).

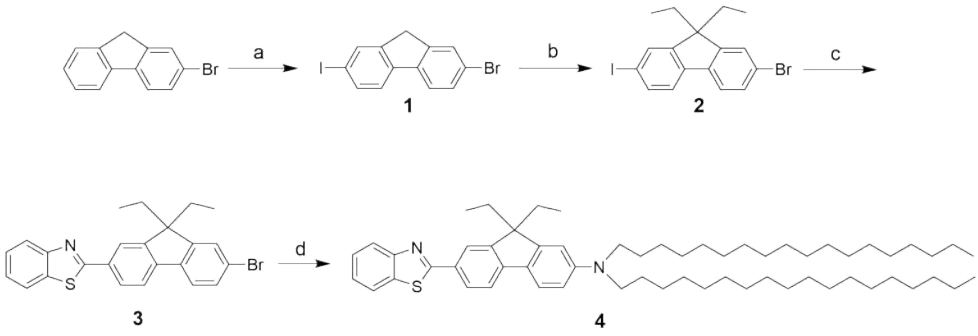

Figure 7.7: Synthetic route of desired compounds. Reagents and conditions: (a) I_2, KIO_3, HOAc, H_2SO_4, H_2O, 100 °C, 2 h, 80%; (b) bromoethane, KI, KOH, DMSO, room temperature, 12 h, 73%; (c) 2-(tri-n-butylstannanyl)benzothiazole, $Pd(PPh_3)_4$, toluene, reflux, 8 h, 43%; (d) dioctadecylamine, $Pd(OAc)_2$, $(t\text{-}Bu)_3P$, t-BuONa, toluene, reflux, 16 h, 84%.

Synthesis of 2-(7-bromo-9, 9-diethyl-9H-fluoren-2-yl)benzo[d]thiazole (3) To a solution of 2 (0.85 g, 2.0 mmol) and 2-(tri-n-butylstannanyl)benzothiazole (0.84 g, 2.0 mmol) in 10 mL anhydrous toluene was added Pd(PPh3)4 (0.23 g, 0.2 mmol) under N2 atmosphere. The reaction mixture was heated to reflux for 8 h under N2. After cooling to room temperature, the solvent was removed under reduced pressure. The crude mixture was purified by flash column chromatography using ethyl acetate/hexane (1/10), giving

the desired compound 3 as a white powder (0.37 g, 43%). 341H NMR (400 MHz, CDCl3): δ (ppm) 8.13 – 8.09 (m, 2H), 8.04 (d, J = 7.9 Hz, 1H), 7.92 (d, J = 7.9 Hz, 1H), 7.77 (d, J = 7.9 Hz, 1H), 7.62 (d, J = 8.4 Hz, 1H), 7.50 (s, 3H), 7.40 (t, J = 7.5 Hz, 1H), 2.20 – 2.03 (m, 4H), 0.35 (t, J = 7.3 Hz, 6H). 13C NMR (101 MHz, CDCl3): δ (ppm) 168.54, 154.53, 153.13, 150.73, 143.61, 139.80, 135.29, 133.12, 130.53, 129.17, 127.80, 127.51, 126.67, 126.51, 125.31, 123.35, 122.32, 121.96, 121.72, 120.33, 57.03, 32.80, 8.65. HRMS (ESI, m/z): calcd for C24H20BrNS ([M+H]+) 434.0573; found 434.0587.

Synthesis of 7-(benzo[d]thiazol-2-yl)-9,9-diethyl-N,N-dioctadecyl-9H-fluoren-2-amine (4), DiC 18 A mixture of compound 3 (0.13 g, 0.3 mmol), dioctadecylamine (0.31 g, 0.6 mmol), Pd(OAc)2 (0.020 g, 0.03 mmol), (t-Bu)3P (0.012 g, 0.06 mmol), and t-BuONa (0.058 g, 0.6 mmol) in 5 mL anhydrous toluene was heated to reflux under N2 atmosphere for 16 h. Toluene was removed in vacuo after the reaction mixture was cooled to room temperature. The residue was dissolved into 10 mL CH2Cl2 and washed with brine (10 mL × 2). The organic layer was dried over MgSO4, and concentrated under reduced pressure. The crude product was purified by flash column chromatography using ethyl acetate/pentane (1/200) as the eluent to give 4 (DiC 18) as yellow oil (0.22 g, 84%). 351H NMR (400 MHz, CDCl3): δ (ppm) 8.13 – 8.06 (m, 2H), 7.99 – 7.90 (m, 2H), 7.62 – 7.58 (m, 1H), 7.53 – 7.49 (m, 2H), 7.37 – 7.42 (m, 1H), 6.66 (d, J = 8.4 Hz, 1H), 6.60 (s, 1H), 3.45 – 3.27 (m, 4H), 2.20 – 1.99 (m, 4H), 1.65 (s, 4H), 1.29 (s, 60H), 0.93 – 0.89 (m, 6H), 0.42 (t, J = 7.2 Hz, 6H). 13C NMR (101 MHz, CDCl3): δ (ppm) 169.47, 154.69, 152.78, 150.01, 149.29, 146.03, 135.18, 131.08, 130.20, 129.18, 127.81, 127.44, 126.46, 126.26, 125.34, 124.82, 123.53, 123.02, 121.59, 121.32, 118.24, 111.43, 106.59, 56.30, 51.66, 44.07, 33.15, 32.10, 29.87, 29.72, 29.51, 29.37, 27.56, 27.43, 22.83, 22.34, 14.19, 8.77. HRMS (DART, m/z): calcd for C60H94N2S ([M+H]+) 875.7210; found 875.7239.

7.7 Description of the methods used for biological assays and cells imaging

7.7.1 Cell viability and imaging of DPPs-based nanostructures

These measurements were conducted by Danilo Vona in Prof. Gianluca Farinola's laboratories at the University of Bari, Italy.

Samples and cells preparation DPPC16-QS, DPPC16-(C)QS and DPPC16-NP samples were diluted with fresh cells medium (McCoy´s 5A Modified Medium, 3 mL) up to concentrations of 10 nM and 1 nM (referred to fluorophore concentration), corresponding to 7 μM and 0.7 μM of CTAB, respectively. Dye-free formulations (CTAB, Plain QS, Plain (C)QS) were diluted to the same concentrations (7 μM and 0.7 μM, referred to CTAB) in order to test the effect of the dye on biocompatibility.

Human osteosarcoma (Saos-2) cell line was used for cell viability and imaging. Cells were routinely grown in McCoy´s 5A (Modified) medium supplemented with 15% heat-inactivated fetal bovine serum (FBS), 50 IU/mL penicillin, 50 IU/mL streptomycin, and 200 mM glutamine and maintained at 37°C in a saturated humid atmosphere of 95% air and 5% CO2 in 75 cm2 flasks (Barloworld Scientific, UK).

For adhesion pre-experiment, cells were detached with a trypsin/EDTA solution (1 mL, Sigma) and resuspended in the cell growth medium. Each well was seeded with 1 mL of medium (at a concentration of $2*10^4$ cells/mL). Cells were cultured for 24 hours to allow adhesion, before addition of the samples. After the adhesion, samples and controls, prepared as described before, were added to cells. At the same time, three positive controls (cells not exposed to samples, PSCC) were prepared with fresh medium. Cells were exposed to samples for 4 hours, and finally fresh medium was used to let cells (both exposed to samples and controls) grow for 36 hours before MTT assay.

Cells viability To measure the metabolic activity of the Saos2, MTT analysis was performed according to the manufacturer instruction (SIGMA). Briefly, the enzyme substrate, 3-(4,5-dimethylthiazol-2-yl)-2,5-diphenyl tetrazolium bromide (MTT reagent), at 5 mg/mL in PBS, was added to the cells after the 36 hours required for cells growth (*see above*). Cells were incubated for about 2 h (37°C and 95% CO_2) until the substrate was converted to violet water insoluble formazan crystals, accumulated into the cytoplasm of viable cells and then dissolved using 1 mL of lysis buffer (500 ml Isopropanol, 55 ml Triton X100, 4.58 ml HCl). The absorbance (at 570 nm) of formazan was then measured at 570 nm and cell viability calculated. As references, MTT for cells not exposed to samples after 10 minutes (PSCC) and after 36 hours (PSCC*) was measured too. All samples were analyzed in triplicate.

Cells imaging To monitor the internalization of DPPC16-QS, DPPC16-(C)QS and DPPC16-NP, cells were incubated with samples for 1 hour and 4 hours and then fixed with 4% formaldehyde/PBS, for 20 min, permeabilized with PBS containing 0.1% Triton X-100 and incubated with Alexa Fluor 488 phalloidin (green fluorescent probe, Molecular

Probes) for 20–30 min. After rinsing, the Vectashield mountant plus DAPI (Vector Laboratories, UK) was added for the observation of cell nuclei (blue fluorescent probe) with a confocal microscopy.

A confocal laser scanning microscope Leica SP8 X with up-right configuration, was used. 3D and λ scan images were performed using a UV/Diode laser with 405-600 nm range of excitation wavelength and a HC PL APO CS2 63x/1.40 Oil objective. Emission spectra were recorded in the 570-738 nm spectral range.

7.7.2 Cell viability and imaging of DiC18-loaded Quatsomes (LysoQS and MKC-LysoQS)

These measurements were conducted by Xinglei Liu in Prof. Kevin Belfield's laboratories at the New Jersey Institute of Technology (NJIT).

Cell viability Cell viability of DiC18 and DiC18-loaded Quatsomes was measured by the MTS assay.

HCT 116 cells were initially pre-cultured in the growth medium (DMEM supplemented with 10% fetal bovine serum and 1% penicillin and streptomycin) at 37 °C in atmosphere with 5% CO_2, until a concentration of at least 6×10^3 cells per well was reached in each well.

Cells were then incubated with different samples at different concentrations (see Figure XXX in the main test) for 22 hours. Afterwards 20 μL of CellTiter 96 Aqueous One solution reagent (the MTS compound), which is reduced to the colored formazan product by the living cells, was added into each well followed by further incubation for 2 h at 37 °C. The respective absorbance values were read on a Tecan Infinite® M200 PRO plate reader spectrometer at 490 nm to determine the relative amount of formazan produced and calculate the correspondant cell viability.

Cell imaging HCT-116 cells were placed onto poly-D-lysine coated coverslips placed into 24-well glass plates (5×10^4 cells per well) and pre-incubated for 48 hours before incubating with the probes.

A 2 mM stock solution of DiC18 in DMSO was prepared. The solution was diluted to 5 μM, 10 μM, 15 μM, 20 μM with the growth medium, DMEM, and incubated with HCT-116 cells for 2 h. After incubation, the cells were rinsed two times with PBS buffer. Cells were then fixed with 3.7% formaldehyde solution in PBS buffer for 10 minutes. After that, cells were washed again (two times) with PBS. To reduce the auto-fluorescence, a solution of

NaBH4 (1mg/mL) in PBS buffer was used to treat the fixed cells for 10 minutes and after rinsing again (two times with PBS and deionized water), cells were mounted on microscope slides using an anti-fade mounting media (Prolong Gold).

The same procedure was followed for staining with LysoQS-1, -2 and -3 and MKC-LysoQS-1, -2 and -3. LysoQS were diluted with DMEM cell medium up to a concentration of 0.022 mM (referred to CTAB concentration) and MKC-LysoQS to 0.02 mM (referred to MKC concentration).

Fluorescence microscopy images were recorded on an inverted microscope (Olympus IX70) equipped with a QImaging cooled CCD and a 100 W mercury lamp. In order to improve the fluorescence background-to-image ratios, fluorescence images were obtained using a customized filter cube.

For the colocalization study, Lysotracker Red DND-99 (LT Red) was purchased as 1 mM stock solution in anhydrous DMSO, while MitoTracker Red FM (MT Red, solid) was dissolved in anhidrous DMSO to get a 1 mM stock solution. For co-staining the cells, LysoQS (or MKC-LysoQS) and LT Red (or MT Red) were diluted with DMEM cell medium up to 0.022 mM, in the case of LysoQS (or 0.2 mM for MKC-LysoQS) and 75 nM, in the case of LT Red and then incubated with cells for 2 hours. For the co-staining experiments with MT Red (diluted with DMEM up to 400 nM), initially the cells were incubated with LysoQS (or MKC-LysoQS) for 2 hours, following the incubation with MT Red for additional 45 minutes. Then cells were rinsed as previously explained and mounted on microscope slide for imaging. The Pearson's correlation coefficient for QS-CTAB III and QS-MKC III was calculated by Fiji, an image processing software.

For the long-term images, the same procedure explained for the co-staining of LysoQS (or MKC-LysoQS) with LT Red was applied, using the same concentrations. Cells were initially incubated with LysoQS (or MKC-LysoQS) and LT Red for 2 hours and then washed with PBS buffer before incubating again with DMEM cell medium for additional 2, 4 or 6 hours. After this additional incubation, cells were rinsed as previously mentioned and mounted on microscope slides for imaging.

7.8 Description of the STORM sample preparation and imaging

The acquisition of the STORM images was performed by Natalia Feiner in Dr. L. Albertazzi's laboratories at the Institute for Bioengineering of Catalonia (IBEC).

In order to acquire the STORM images, in vitro cyanin-loaded QS were immobilized by adsorption onto the surface of a flow chamber assembled from a glass slide and a coverslip (24mm x 24 mm, thickness 0.15 mm) separated by double-sided tape. After being incubated for 10-15 minutes unbound Quatsomes were removed by washing the chamber twice with MilliQ water and then twice with the STORM buffer. Then, TetraSpeck™ Microspheres (0.1 µm, Life Technology) were added and immobilized by adsorption onto the surface to correct the drift during acquisition. Finally, non-adsorbed TetraSpeck™ Microspheres were removed by washing the chamber twice with STORM buffer. The STORM buffer contains PBS, an oxygen scavenging system (0.5 mg/mL glucose oxidase, 40 µg/mL catalase), 5% (w/v) glucose and 100 mM cysteamine. In cells experiments, after fixation, the same STORM buffer was added directly to the wells.

STORM images were acquired using a Nikon N-STORM system configured for total internal reflection fluorescence (TIRF) imaging. DiI-QS were imaged by means of a 561nm laser (80 mW) and TetraSpeck™ Microspheres were imaged by means of a 488nm (80 mW) (only in the case of in vitro QS). No activation UV light was employed, since the spontaneous switching of the fluorophores from the dark to the excited state was adequate for images acquisition. Fluorescence was collected by means of a Nikon 100x, 1.49 NA oil immersion objective and passed through a quad-band pass dichroic filter (97335 Nikon). Images were acquired onto a 256x256 pixel region (pixel size 0.16µm) of a Hamamatsu ORCA- Flash 4.0 camera at 10 ms integration time. 20,000 frames were acquired for each image. STORM images were analyzed with the STORM module of the NIS element Nikon software.

During STORM-imaging, the Nikon software generates a list of localizations by Gaussian fitting of blinking dyes in the acquired movie of conventional microscopic images. A density-based algorithm was applied to identify individual Quatsomes and separate them from the background, following the same procedure shown in the Supplementary Information of [211]. In this algorithm, localizations which have at least x neighboring localization within y nanometers are clustered together with these neighbors. Iteratively, neighboring points for these newly added neighbors are also detected, until no points are added anymore and a cluster is completely identified. In this way, background localizations due to detector noise, background fluorescence or other causes were eliminated and the individual clusters saved separately. The clusters obtained are then fitted as circles to determine the exact localization and size of each NP. Circles which contained too few localizations for an accurate analysis were discarded.

Annexes

AI: Short description of the characteristics of fluorescent probes

The phenomena occurring between the absorption and emission of light by a molecule are described by the Jablonski diagram, so called after Prof. Alexander Jablonski, one of the fathers of the modern fluorescence spectroscopy. A simplified version of the diagram is shown in Figure 7.8, where all the transitions necessary to describe the results of this Thesis are depicted [158].

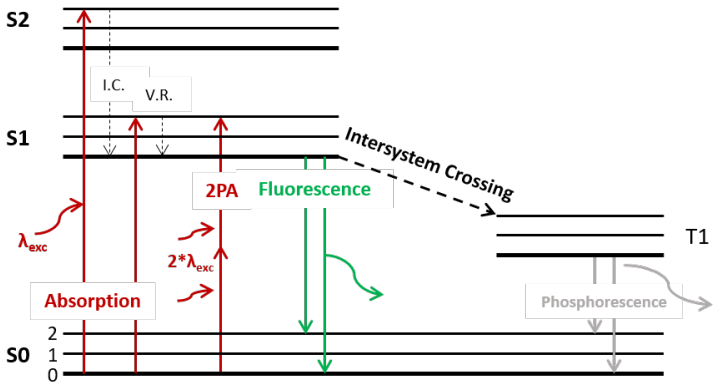

Figure 7.8: Simplified version of Jablonski diagram showing all the transitions of interest for understanding the results of this Thesis.

Light absorption is a transition occurring in a too short time (around 10^{-15} s) for the displacement of the nuclei, for this reason it is depicted as a vertical transition (Franck-Condon principle). Following light absorption, several processes may occur. If the fluorophore is excited from the singlet electronic ground state (S_0) to higher energy vibrational levels of the singlet excited states (S_1 and S_2), it relaxes rapidly to the lowest vibrational state of S_1, by mean of two possible processes called internal conversion (I.C.), mainly due to interactions with solvent, and vibrational relaxation (V.R.). As the timescales of I.C and V.R. (10^{-12}s) are much smaller than those of fluorescence (10^{-8}s), generally they are completed prior to emission.

Decay from the excited state can occur via emission of photons (fluorescence) or either molecules can undergo spin conversion to the triplet state T_1 (intersystem crossing), which will be useful to understand some photodegradation mechanisms described in Chapter 3. Emission from T_1 is called phosphorescence, but the description

of systems showing phosphorescence is beyond the objective of this Thesis.

Absorption spectrum When molecules are exposed to light having an energy which matches the electronic transition between the different singlet states ($S_0$to S_1, $S_0$to S_2etc.), light is absorbed with promotion of electrons to the excited state. A spectrophotometer can record the wavelength at which the transition occurs along with the intensity of light absorbed. The resulting spectrum, the absorption spectrum, is a graph of absorbance plot versus wavelength.

Molar extinction coefficient (ε) By knowing the absorbance of a specie of known concentration at a given wavelength, it is possible to calculate the molar extinction coefficient (ε), by applying the Beer-Lambert law: $A = \varepsilon c l$, where A is the absorbance, c is the concentration of the fluorophore and l is the length of the light path through the sample. ε is a measure of how strongly a molecule attenuates light at a given wavelength.

Emission spectrum When a fluorophore releases energy from the excited states via emission of photons, the molecule can drop to several vibrational levels of the ground state and therefore the emitted photons will have different energies, i.e. different wavelengths/frequencies. In a typical fluorescence measurement the excitation wavelength is fixed and the detection wavelength is varied. The detected intensity of emitted light is then plotted versus the wavelength to build up the emission spectrum of the fluorophore.

Excitation spectrum In order to collect the excitation spectrum, the light emitted by the fluorophore is collected at a fixed wavelength while the excitation wavelength is scanned all over its absorption spectrum. If a fluorophore is dissolved in an organic solution, for example a cyanine in EtOH (see Chapter 3), the excitation spectrum and the absorption spectrum are superimposeble, which means that the highest emission intensity is given exciting the fluorophore at its maximum absorption wavelength. On the other hand, if other fluorescent species or aggregates are also present, or other more complex factors are affecting the measurements, the excitation and absorption spectra differ.

Stokes shift The Jablonski diagram shows that energy of the emission is less than that of absorption, which means that fluorescence occurs at lower energies (or higher wavelengths) than absorption. The difference (in wavelength or frequency units)

between the position of the maximum absorption and emission is called Stokes shift. This parameter is really important when moving to applications in fluorescence microscopy. In fact the greater the Stokes shift, the easier is to separate the excitation light from emission light.

Fluorescence quantum yield (φ) and brightness The fluorescence quantum yield (φ) is the ratio of number of photons emitted to the number of photons absorbed. The easiest way to calculate the φ of a dye is to refer to standard samples of known φ values (see Experimental Part 1.4). As evidenced in the Jablonski diagram, the fluorescence emission always occurs from the lowest vibrational state of the excited state. For this reason, the φ of a fluorophore is independent of the excitation wavelength.

The brightness is the product of the molar absorption coefficient at the excitation wavelength (ε) and the fluorescence quantum yield (φ). It is used as a measure of the intensity of the fluorescence signal obtainable upon excitation at a specific wavelength or wavelength region. A bright fluorescent probe has a high capacity to absorb light (high ε) and it is able to efficiently convert the energy absorbed in fluorescent signal (high φ).

Two photon absorption cross section (σ_{2p}) The excitation from the ground to the excited state can occur through the simultaneous absorption of two photons (2PA process) with, more or less, half energy (i.e. double wavelength) of those that would have promoted one-photon excitation. As result, it is possible to use red and infrared light (in the biological transparency window) to excite a fluorophore by 2-photon excitation. The two photon absorption cross section (σ_{2p}) describes the probability of the simultaneous absorption of two photons and transition of the fluorophore to an excited state that differs energetically from the ground state by the energy of the two photons.

A2: Molecular Dynamics (MD) simulations

Methodology

All the MD simulations were performed using NAMD2 2.9 software[277]on a Lenovo computer cluster (108 Compute Nodes and 24 cores CPU) at the Jawaharlal Nehru Centre for Advanced Scientific Research (JNCASR), India. The equations of motions were solved with a time step of 2fs. Electrostatic interactions were computed using the particle mesh Ewald summation method (PME) with the standard settings in NAMD (1 Å spatial resolution and every update was enforced in 2 time steps). In all the simulations, the temperature was maintained at a constant (298 K) value using the Langevin thermostat with a relaxation constant of 1 ps-1. The pressure was adjusted to 1 atm employing the Nosé-Hoover-Langevin piston, as implemented in NAMD2, with an oscillation period of 100 fs and a decay time of 50 fs.

In all the simulated systems, the same sequence was followed for the build-up as well as for the equilibrations. First, an initial configuration of the dye was built employing the VMD and the Gaussian View program[278]. The energy of the initial configuration was minimized for 100 steps following the combined conjugate gradient and the line search procedure implemented in NAMD 2.9. Then, the dye was introduced in the simulation box, n dimensions x, y, z Å, where the MD simulations were carried out. In every simulation case, the parameters and protocols were fixed as required. To perform the simulations, the total charge of the system should be fixed to zero. Thus, the total system charge has to be balanced by adding ions (according to each system). As a continuation of it, the energy of the resulting system was minimized again. After energy minimization, a short NPT run was performed (i.e. the volume constraint was not imposed) in order to make sure that the simulation box that includes all the molecules added to the previous system are able to interact within the volume of the simulation box. Finally, a long simulation run was performed for each system under the conditions (normal pressure) described before, in order to ensure that the statistics are reliable. All the final simulations were performed considering zero superficial tension along z direction. This is consistent to mimic the experimental conditions of interest.

The results presented in this Thesis correspond to averages over the production part of the MD trajectories, obtained after discarding the initial equilibration/relaxation period. All the snapshots and the monitoring of the simulation (evolution of energy, simulation box, temperature, pressure, etc.) were performed using the VMD program.

The atomic density profiles in the bilayer simulations were obtained by using a

VMD-plug-in called Density Profile Tool [279], a software package that computes the one-dimensional density profiles of molecular systems. The profiles were averaged over the XY coordinates and over the production (equilibrium) part of the trajectory. Moreover, to see the interaction between some atoms of interest, we have computed the radial distribution functions, g(r), by using a g(r) GUI plug-in. We also have used the Hydrogen Bonds plug-in, in order to count the number of hydrogen bonds formed throughout the trajectory. The search was restricted to a single selection in the whole frame range of the simulation. Finally, we are interested in finding the diffusion coefficient of the molecules inside the bilayer. To obtain diffusion coefficient a home-made script was used, which runs in VMD to read the NAMD trajectories.

MD simulations describing the membrane of cholesterol/CTAB Quatsomes including interactions between cholesterol and CTAB, atomic density profiles along the bilayers and free energy calculations can be found in ref [130, 134], where methods and details used for such simulations are discussed as well.

Protocol for modeling and build-up of the initial configurations and equilibration of DiI-QS

In order to simulate DiI inside Quatsomes, it was first necessary to obtain the force fields of this dye. As no information on DiI could be found in any repository, the strategy consisted in modifying a similar molecule, whose atomic coordinates and the parameters set, needed to calculate the potential energy, are available on the web. The required parameters of DiI were obtained, in a complementary manner, by two sources. The chromophoric part of DiI (same as Cy3 dye) has been previously modeled in [280]. Moreover, the DiI has been modeled by Gaussian View software. So, the parameters for the two C_{18} alkyl chains were obtained from the CGneFF using the optimized structure.

As mentioned in Chapter 1, pag XXX, two simulations (namely S5 and S6) have been carried out in order to compare two types of DII-QSs preparation methods and then study the diffusion of the DII while inside the QSs. In the first simulation (S5) the DiI molecule isinitially outside the membrane. For that, the molecule is added on the top of the simulation box and then it is solvated. In the second one (S6) the DII molecule is inserte it QSs membrane and this is considered as the starting point of the simulation. In this case, no salvation was required.

Initial geometry of the DiI model compounds were generated from the topology information present in the force field. This initial geometry was subjected to a 100 ps minimization. The minimized geometries of the DII on the QS system were then

immersed in a pre-equilibrated cubic water box of size 45Åx40Åx146Å. For all of the subsequent minimizations and MD simulations, periodic boundary conditions were employed. Next, the systems were subjected to a 100 ps minimization again. This was followed by a 1 ns simulation in the NPT ensemble at 1 atm and 298 K. Finally, both the simulation runs were carried out for NPT and superficial tension equal to 0 in the ensemble.

Protocol for modeling and build-up of the initial configurations and equilibration of Fl-QS

$Fl^{2-}$was modeled by using CGenFF parameters and validating them with QM and MM calculations.

As mentioned in Chapter XX, four simulations (S1, S2, S3 and S4) of Fl-QS were run. Each simulation refers to a different experiment, in particular a different ratio between Fl and CTAB, as shown in Table XX of Chapter XX. In all the simulations, Fl^{2-} has been added on the top of the simulation box in such a way that at the starting point the Fl^{2-} molecules is far away from the QS surface. This is in order to avoid conditioning of their trajectory during the simulation. Water molecules are added using VMD plug-in in order to solvate only the added Fl molecules and to obtain the experimental density of the solvent. As a consequence, the cubic box size will be increasing in z direction only. Once the system is solvated, Na^{+}ions were added to the system in order to balance the total charge of the system. Periodic boundary conditions are applied for all the molecular simulations in all directions and are based on a cubic box of 43.5x36.1x144.5 Å3. X and Y lengths were considered to be fixed for all the simulations, while Z length was slightly changed in each simulation, depending on the solvated system volume required. To end up with an equilibration run of 100 ps in time steps of 2 fs will be required to let both parts merge while equilibrating and it will be followed by carrying out a NPT run of 1 ns for every simulation performed. After energy equilibration and NPT ensemble simulation, MD simulations will be performed by using the NAMD2 program at fixed T, p and zero surface tension. Simulation times were 110 ns, 120 ns, 110 ns and 90 ns for S1, S2, S3 and S4, respectively.

Bibliography

[1] Vasilis Ntziachristos. Going deeper than microscopy: the optical imaging frontier in biology. *Nature methods*, 7(8):603–614, 2010.

[2] Ivana Martinić, Svetlana V. Eliseeva, and Stéphane Petoud. Near-Infrared Emitting Probes for Biological Imaging: Organic Fluorophores, Quantum Dots, Fluorescent Proteins, Lanthanide(III) Complexes and Nanomaterials. *Journal of Luminescence*, (Iii), 2016.

[3] F Helmchen and W Winfried Denk. Deep tissue two-photon microscopy. *Nature Methods*, 2(12):932–940, 2005.

[4] Demirhan Kobat, Nicholas G Horton, and Chris Xu. In vivo two-photon microscopy to 1.6-mm depth in mouse cortex. *Journal of Biomedical Optics*, 16(10):106014, 2011.

[5] Ciceron O. Yanez, Alma R. Morales, Xiling Yue, Takeo Urakami, Masanobu Komatsu, Tero A H Järvinen, and Kevin D. Belfield. Deep Vascular Imaging in Wounds by Two-Photon Fluorescence Microscopy. *PLoS ONE*, 8(7):4–9, 2013.

[6] Bonnie O. Leung and Keng C. Chou. Review of super - Resolution fluorescence microscopy for biology. *Applied Spectroscopy*, 65(9):967–980, 2011.

[7] Stefan W Hell. Toward fluorescence nanoscopy. *Nature biotechnology*, 21(11):1347–55, 2003.

[8] Ben N G Giepmans, Stephen R Adams, Mark H Ellisman, and Roger Y Tsien. The Fluorescent Toolbox for Assessing Protein Location and Function. *Science*, 312(5771):217 LP – 224, apr 2006.

[9] Akihiro Kusumi, Taka A Tsunoyama, Kohichiro M Hirosawa, Rinshi S Kasai, and Takahiro K Fujiwara. Tracking single molecules at work in living cells. *Nat Chem Biol*, 10(7):524–532, jul 2014.

[10] Ute Resch-Genger, Markus Grabolle, Sara Cavaliere-Jaricot, Roland Nitschke, and Thomas Nann. Quantum dots versus organic dyes as fluorescent labels. *Nature Methods*, 5(9):763–775, 2008.

[11] Eva Hemmer, Antonio Benayas, François Légaré, and Fiorenzo Vetrone. Exploiting the Biological Windows: Current Perspectives on Fluorescent Bioprobes Emitting above 1000 nm. *Nanoscale Horiz.*, 1(3), 2016.

[12] Namhun Kim, Jongho Lee, Hyuncheol An, Changhyun Pang, Sung Min Cho, and Heeyeop Chae. Color temperature control of quantum dot white light emitting diodes by grafting organic fluorescent molecules. *J. Mater. Chem. C*, 2(46):9800–9804, 2014.

[13] The United States Life Technology Corp. *The Molecular Probes Handbook*. 2005.

[14] Alexander L. Antaris, Hao Chen, Kai Cheng, Yao Sun, Guosong Hong, Chunrong Qu, Shuo Diao, Zixin Deng, Xianming Hu, Bo Zhang, Xiaodong Zhang, Omar K. Yaghi, Zita R. Alamparambil, Xuechuan Hong, Zhen Cheng, and Hongjie Dai. A small-molecule dye for NIR-II imaging. *Nature Materials*, 15(2):235–242, 2015.

[15] Juliette Mérian, Julien Gravier, Fabrice Navarro, and Isabelle Texier. Fluorescent nanoprobes dedicated to in vivo imaging: From preclinical validations to clinical translation. *Molecules*, 17(5):5564–5591, 2012.

[16] Hak Soo Choi, Khaled Nasr, Sergey Alyabyev, Dina Feith, Jeong Heon Lee, Soon Hee Kim, Yoshitomo Ashitate, Hoon Hyun, Gabor Patonay, Lucjan Strekowski, Maged Henary, and John V Frangioni. Synthesis and In Vivo Fate of Zwitterionic Near-Infrared Fluorophores. *Angewandte Chemie International Edition*, 50(28):6258–6263, 2011.

[17] Zongren Zhang and Samuel Achilefu. Synthesis and Evaluation of Polyhydroxylated Near-Infrared Carbocyanine Molecular Probes. *Organic Letters*, 6(12):2067–2070, 2004.

[18] Robert M Hoffman. The multiple uses of fluorescent proteins to visualize cancer in vivo. *Nat Rev Cancer*, 5(10):796–806, oct 2005.

[19] G. Ulrich Nienhaus and Jörg Wiedenmann. Structure, dynamics and optical properties of fluorescent proteins: Perspectives for marker development. *ChemPhysChem*, 10(9-10):1369–1379, 2009.

[20] Nathan C Shaner, Michael Z Lin, Michael R McKeown, Paul a Steinbach, Kristin L Hazelwood, Michael W Davidson, and Roger Y Tsien. Improving the photostability of bright monomeric orange and red fluorescent proteins. *Nature methods*, 5(6):545–551, 2008.

[21] Paula J Cranfill, Brittney R Sell, Michelle A Baird, John R Allen, Zeno Lavagnino, H Martijn de Gruiter, Gert-Jan Kremers, Michael W Davidson, Alessandro Ustione, and David W Piston. Quantitative assessment of fluorescent proteins. *Nature Methods*, 13(7):557–562, 2016.

[22] Jon S Donner, Sebastian A Thompson, César Alonso-Ortega, Jordi Morales, Laura G Rico, Susana I C O Santos, and Romain Quidant. Imaging of Plasmonic Heating in a Living Organism. *ACS Nano*, 7(10):8666–8672, oct 2013.

[23] Stefan Behme. Fundamentals of Quality Assurance. In *Manufacturing of Pharmaceutical Proteins*, pages 167–182. Wiley-VCH Verlag GmbH and Co. KGaA, 2009.

[24] Marco P Monopoli, Christoffer Aberg, Anna Salvati, and Kenneth A Dawson. Biomolecular coronas provide the biological identity of nanosized materials. *Nat Nano*, 7(12):779–786, dec 2012.

[25] Andre E Nel, Lutz Madler, Darrell Velegol, Tian Xia, Eric M V Hoek, Ponisseril Somasundaran, Fred Klaessig, Vince Castranova, and Mike Thompson. Understanding biophysicochemical interactions at the nano-bio interface. *Nat Mater*, 8(7):543–557, jul 2009.

[26] Quyen T Nguyen and Roger Y Tsien. Fluorescence-guided surgery with live molecular navigation [mdash] a new cutting edge. *Nat Rev Cancer*, 13(9):653–662, sep 2013.

[27] Daniel Jaque, Cyrille Richard, Bruno Viana, Kohei Soga, Xiaogang Liu, and Jose García Solé. Nanoparticles for optical bio-imaging. *Advances in Optics*, 8(1):In press, 2016.

[28] B Devika Chithrani, Arezou A Ghazani, and Warren C W Chan. Determining the Size and Shape Dependence of Gold Nanoparticle Uptake into Mammalian Cells. *Nano Letters*, 6(4):662–668, apr 2006.

[29] E K Lim and B H Chung. Preparation of pyrenyl-based multifunctional nanocomposites for biomedical applications. *Nat Protoc*, 11(2):236–251, 2016.

[30] Eun-Kyung Lim, Taekhoon Kim, Soonmyung Paik, Seungjoo Haam, Yong-Min Huh, and Kwangyeol Lee. Nanomaterials for Theranostics: Recent Advances and Future Challenges. *Chemical Reviews*, 115(1):327–394, jan 2015.

[31] Draft Agreed, Draft Rev, Rapporteurs Release, Drafting Group, Nanomedicines End, Workings Parties Discussion, Q W P Draft Rev, Pkwp Draft Rev, Guideline Consistency, and Group Adoption. Reflection paper on the data requirements for intravenous liposomal products developed with reference to an innovator liposomal product. 44(February):1–13, 2013.

[32] Mengjun Chen and Meizhen Yin. Design and development of fluorescent nanostructures for bioimaging. *Progress in Polymer Science*, 39(2):365–395, 2014.

[33] Ken-Tye Yong, Wing-Cheung Law, Rui Hu, Ling Ye, Liwei Liu, Mark T Swihart, and Paras N Prasad. Nanotoxicity assessment of quantum dots: from cellular to primate studies. *Chem. Soc. Rev.*, 42(3):1236–1250, 2013.

[34] Jung Kwon Oh. Surface modification of colloidal CdX-based quantum dots for biomedical applications. *J. Mater. Chem.*, 20(39):8433–8445, 2010.

[35] Thomas J Deerinck. NIH Public Access. *Imaging*, 36(1):112–116, 2009.

[36] H S Choi, W Liu, P Misra, E Tanaka, J P Zimmer, B Itty Ipe, M G Bawendi, and J V Frangioni. Renal clearance of quantum dots. *Nature biotechnology*, 25(10):1165–1170, 2007.

[37] Jisung Kim, Mia J Biondi, Jordan J Feld, and Warren C W Chan. Clinical Validation of Quantum Dot Barcode Diagnostic Technology. *ACS Nano*, 10(4):4742–4753, apr 2016.

[38] Wen-Han Zhang, Xiao-Xiao Hu, and Xiao-Bing Zhang. Dye-Doped Fluorescent Silica Nanoparticles for Live Cell and In Vivo Bioimaging. *Nanomaterials*, 6(5):81, 2016.

[39] Riccardo Marega, Eko Adi Prasetyanto, Carine Michiels, Luisa De Cola, and Davide Bonifazi. Fast Targeting and Cancer Cell Uptake of Luminescent Antibody-Nanozeolite Bioconjugates. *Small*, 12(39):5431–5441, 2016.

[40] Susanta Kumar Bhunia, Arindam Saha, Amit Ranjan Maity, Sekhar C Ray, and Nikhil R Jana. Carbon nanoparticle-based fluorescent bioimaging probes. *Scientific reports*, 3:1473, 2013.

[41] O Mongin, T R Krishna, M H Werts, A M Caminade, J P Majoral, and M Blanchard-Desce. A modular approach to two-photon absorbing organic nanodots: brilliant

dendrimers as an alternative to semiconductor quantum dots? *Chem Commun (Camb)*, (8):915–917, 2006.

[42] Anne Marie Caminade, Aurélien Hameau, and Jean Pierre Majorai. Multicharged and/or water-soluble fluorescent dendrimers: Properties and uses. *Chemistry - A European Journal*, 15(37):9270–9285, 2009.

[43] Liliang Chu, Shaowei Wang, Kanghui Li, Wang Xi, Xinyuan Zhao, and Jun Qian. Biocompatible near-infrared fluorescent nanoparticles for macro and microscopic in vivo functional bioimaging. *Biomedical Optics Express*, 5(11):4076–4088, nov 2014.

[44] Peng Liu, Shuang Li, Yaocheng Jin, Linghui Qian, Nengyue Gao, Shao Q Yao, Fei Huang, Qing-Hua Xu, and Yong Cao. Red-Emitting DPSB-Based Conjugated Polymer Nanoparticles with High Two-Photon Brightness for Cell Membrane Imaging. *ACS Applied Materials and Interfaces*, 7(12):6754–6763, 2015.

[45] E. Ramanjaneya Reddy, Swapna Yellanki, Raghavendra Medishetty, Lahiri Konada, Neeraja P. Alamuru, Devyani Haldar, Kishore Parsa, Pushkar Kulkarni, and Marina Rajadurai. Red Fluorescent Organic Nanoparticle Bio-Probes: A Novel Photostable Cytoplasmic Stain for Long Term In Vitro and In Vivo Visualization. *ChemNanoMat*, pages n/a–n/a, 2015.

[46] Hendrik Deschout, Francesca Cella Zanacchi, Michael Mlodzianoski, Alberto Diaspro, Joerg Bewersdorf, Samuel T Hess, and Kevin Braeckmans. Precisely and accurately localizing single emitters in fluorescence microscopy. *Nature methods*, 11(3):253–66, 2014.

[47] Andreas Reisch and Andrey S. Klymchenko. Fluorescent Polymer Nanoparticles Based on Dyes: Seeking Brighter Tools for Bioimaging. *Small*, 12(15):1968–1992, 2016.

[48] Valentin Magidson and Alexey Khodjakov. Chapter 23 - Circumventing Photodamage in Live-Cell Microscopy. In Greenfield Sluder Biology and David E Wolf B T Methods in Cell, editors, *Digital Microscopy*, volume Volume 114, pages 545–560. Academic Press, 2013.

[49] Victoria B Rodriguez, Scott M Henry, Allan S Hoffman, Patrick S Stayton, Xingde Li, and Suzie H Pun. Encapsulation and stabilization of indocyanine green within

poly(styrene-alt-maleic anhydride) block-poly(styrene) micelles for near-infrared imaging. *Journal of Biomedical Optics*, 13(1):14010–14025, 2008.

[50] Vishal Saxena, Mostafa Sadoqi, and Jun Shao. Enhanced photo-stability, thermal-stability and aqueous-stability of indocyanine green in polymeric nanoparticulate systems. *Journal of Photochemistry and Photobiology B: Biology*, 74(1):29–38, mar 2004.

[51] Kateryna Trofymchuk, Andreas Reisch, Ievgen Shulov, Yves Mely, and Andrey S Klymchenko. Tuning the color and photostability of perylene diimides inside polymer nanoparticles: towards biodegradable substitutes of quantum dots. *Nanoscale*, 6(21):12934–12942, 2014.

[52] Adrien Kaeser and Albertus P H J Schenning. Fluorescent nanoparticles based on self-assembled ??-conjugated systems. *Advanced Materials*, 22(28):2985–2997, 2010.

[53] Freek J M Hoeben, Pascal Jonkheijm, E. W. Meijer, and Albertus P H J Schenning. About supramolecular assemblies of pi-conjugated systems. *Chemical Reviews*, 105(4):1491–1546, 2005.

[54] C. E. Mora-Huertas, H. Fessi, and A. Elaissari. Influence of process and formulation parameters on the formation of submicron particles by solvent displacement and emulsification-diffusion methods: Critical comparison. *Advances in Colloid and Interface Science*, 163(2):90–122, 2011.

[55] Stéphanie Lacour. *Emerging questions for emerging technologies: Is there a law for the nano?* 2013.

[56] Ju Mei, Nelson L C Leung, Ryan T K Kwok, Jacky W Y Lam, and Ben Zhong Tang. Aggregation-Induced Emission: Together We Shine, United We Soar! *Chemical Reviews*, 115(21):11718–11940, 2015.

[57] Kassem Amro, Jonathan Daniel, Guillaume Clermont, Talia Bsaibess, Mathieu Pucheault, Emilie Genin, Michel Vaultier, and Mireille Blanchard-Desce. A new route towards fluorescent organic nanoparticles with red-shifted emission and increased colloidal stability. *Tetrahedron*, 70(10):1903–1909, 2014.

[58] Emilie Genin, Zhenghong Gao, Juan A. Varela, Jonathan Daniel, Talia Bsaibess, Isabelle Gosse, Laurent Groc, Laurent Cognet, and Mireille Blanchard-Desce.

"Hyper-Bright" Near-Infrared Emitting Fluorescent Organic Nanoparticles for Single Particle Tracking. *Advanced Materials*, 26(14):2258–2261, 2014.

[59] Jingdong Luo, Zhiliang Xie, Jacky W. Y. Lam, Lin Cheng, Ben Zhong Tang, Haiying Chen, Chengfeng Qiu, Hoi Sing Kwok, Xiaowei Zhan, Yunqi Liu, and Daoben Zhu. Aggregation-induced emission of 1-methyl-1,2,3,4,5-pentaphenylsilole. *Chemical Communications*, 381(18):1740–1741, 2001.

[60] Ju Mei, Yuning Hong, Jacky W Y Lam, Anjun Qin, Youhong Tang, and Ben Zhong Tang. Aggregation-induced emission: The whole is more brilliant than the parts. *Advanced Materials*, 26(31):5429–5479, 2014.

[61] Xin Zhang, Zhijian Chen, and Frank Würthner. Morphology control of fluorescent nanoaggregates by co-self-assembly of wedge- and dumbbell-shaped amphophilic perylene bisimides. *Journal of the American Chemical Society*, 129(16):4886–4887, 2007.

[62] Qiuli Zhao and Jing Zhi Sun. Red and near infrared emission materials with AIE characteristics. *Journal of Materials Chemistry C*, 4(45):10588–10609, 2016.

[63] Tao Jiang, Dongyu Li, Yandi Hang, Yuting Gao, Hequn Zhang, Xinyuan Zhao, Xin Li, Bo Li, Jun Qian, and Jianli Hua. Tetraphenylethene end-capped diketopyrrolopyrrole fluorogens with AIE and large two-photon absorption cross-sections features and application in bioimaging. *Dyes and Pigments*, 133:201–213, 2016.

[64] Yuting Gao, Guangxue Feng, Tao Jiang, Chiching Goh, Laiguan Ng, Bin Liu, Bo Li, Lin Yang, Jianli Hua, and He Tian. Biocompatible Nanoparticles Based on Diketo-Pyrrolo-Pyrrole (DPP) with Aggregation-Induced Red/NIR Emission for In Vivo Two-Photon Fluorescence Imaging. *Advanced Functional Materials*, 25(19):2857–2866, 2015.

[65] Hewei Luo, Songjie Chen, Zitong Liu, Chuang Zhang, Zhengxu Cai, Xin Chen, Guanxin Zhang, Yongsheng Zhao, Silvio Decurtins, Shi-Xia Liu, and Deqing Zhang. A Cruciform Electron Donor-Acceptor Semiconductor with Solid-State Red Emission: 1D/2D Optical Waveguides and Highly Sensitive/Selective Detection of H2S Gas. *Advanced Functional Materials*, 24(27):4250–4258, 2014.

[66] Carolina D. Andrade, Ciceron O. Yanez, Maher A. Qaddoura, Xuhua Wang, Curtesa L. Arnett, Sabrina A. Coombs, Jin Yu, Rania Bassiouni, Mykhailo V. Bondar,

and Kevin D. Belfield. Two-photon fluorescence lysosomal bioimaging with a micelle-encapsulated fluorescent probe. *Journal of Fluorescence*, 21(3):1223–1230, 2011.

[67] Casey A Dougherty, Joseph C Furgal, Mallory A van Dongen, Theodore Goodson, Mark M Banaszak Holl, Janet Manono, and Stassi DiMaggio. Isolation and Characterization of Precise Dye/Dendrimer Ratios. *Chemistry (Weinheim an der Bergstrasse, Germany)*, 20(16):4638–4645, apr 2014.

[68] Tristan Barrett, Gregory Ravizzini, Peter L Choyke, and Hisataka Kobayashi. Dendrimers Application Related to Bioimaging. *IEEE engineering in medicine and biology magazine : the quarterly magazine of the Engineering in Medicine and Biology Society*, 28(1):12–22, 2009.

[69] Benjamin Gruber and Burkhard König. Self-Assembled Vesicles with Functionalized Membranes. *Chemistry - A European Journal*, 19(2):438–448, 2013.

[70] Isabelle Texier, Mathieu Goutayer, Anabela Da Silva, Laurent Guyon, Nadia Djaker, Véronique Josserand, Emmanuelle Neumann, Jéro Bibette, and Françoise Vinet. Cyanine-loaded lipid nanoparticles for improved in vivo fluorescence imaging. *Journal of biomedical optics*, 14(5):054005, 2015.

[71] Fabienne Danhier, Eduardo Ansorena, Joana M Silva, Régis Coco, Aude Le Breton, and Véronique Préat. PLGA-based nanoparticles: An overview of biomedical applications. *Journal of Controlled Release*, 161(2):505–522, jul 2012.

[72] Daniela Gontero, Mathieu Lessard-Viger, Danny Brouard, A. Guillermo Bracamonte, Denis Boudreau, and Alicia V. Veglia. Smart multifunctional nanoparticles design as sensors and drug delivery systems based on supramolecular chemistry. *Microchemical Journal*, 130:316–328, 2017.

[73] Ragini Jenkins, Mary K Burdette, and Stephen H Foulger. Mini-review: fluorescence imaging in cancer cells using dye-doped nanoparticles. *RSC Adv.*, 6(70):65459–65474, 2016.

[74] Hao Liu and Daocheng Wu. In vivo Near-infrared Fluorescence Tumor Imaging Using DiR-loaded Nanocarriers. *Current Drug Delivery*, 13(Ivm):40–48, 2016.

[75] Qingxin Mu, Hui Wang, and Miqin Zhang. Nanoparticles for imaging and treatment of metastatic breast cancer. *Expert Opinion on Drug Delivery*, 14(1):123–136, jan 2017.

[76] Anne Katrin Kirchherr, Andreas Briel, and Karsten Mäder. Stabilization of indocyanine green by encapsulation within micellar systems. *Molecular Pharmaceutics*, 6(2):480–491, 2009.

[77] Liraz Larush and Shlomo Magdassi. Formation of near-infrared fluorescent nanoparticles for medical imaging. *Nanomedicine*, 6(2):233–240, feb 2011.

[78] Anil Wagh, Steven Y Qian, and Benedict Law. Development of biocompatible polymeric nanoparticles for in vivo NIR and FRET imaging. *Bioconjugate chemistry*, 23(5):981–92, 2012.

[79] Hongtao Chen, Sungwon Kim, Li Li, Shuyi Wang, Kinam Park, and Ji-Xin Cheng. Release of hydrophobic molecules from polymer micelles into cell membranes revealed by Forster resonance energy transfer imaging. *Proceedings of the National Academy of Sciences of the United States of America*, 105(18):6596–6601, 2008.

[80] Tom O. McDonald, Philip Martin, Joseph P. Patterson, Darren Smith, Marco Giardiello, Marco Marcello, Violaine See, Rachel K. O'Reilly, Andrew Owen, and Steve Rannard. Multicomponent organic nanoparticles for fluorescence studies in biological systems. *Advanced Functional Materials*, 22(12):2469–2478, 2012.

[81] Zhimin Tao, Guosong Hong, Chihiro Shinji, Changxin Chen, Shuo Diao, Alexander L Antaris, Bo Zhang, Yingping Zou, and Hongjie Dai. Biological Imaging Using Nanoparticles of Small Organic Molecules with Fluorescence Emission at Wavelengths Longer than 1000 nanometers. *Angewandte Chemie International Edition*, 52(49):13002–13006, 2013.

[82] Stephen W Morton, Xiaoyong Zhao, Mohiuddin A Quadir, and Paula T Hammond. FRET-enabled biological characterization of polymeric micelles. *Biomaterials*, 35(11):3489–3496, apr 2014.

[83] Thomas Delmas, Anne-Claude Couffin, Pierre Alain Bayle, François de Crécy, Emmanuelle Neumann, Françoise Vinet, Michel Bardet, Jérôme Bibette, and Isabelle Texier. Preparation and characterization of highly stable lipid nanoparticles with amorphous core of tuneable viscosity. *Journal of Colloid and Interface Science*, 360(2):471–481, aug 2011.

[84] Thomas Delmas, Hélène Piraux, Anne-Claude Couffin, Isabelle Texier, Françoise Vinet, Philippe Poulin, Michael E Cates, and Jérôme Bibette. How To Prepare and Stabilize Very Small Nanoemulsions. *Langmuir*, 27(5):1683–1692, mar 2011.

[85] Wolkmar Weissig Torchilin, V. *Liposomes-A practical approach-2nd edition*. 2003.

[86] Pierandrea Ninham, Barry W.; Lo Nostro. Molecular Forces and Self Assembly. *Cambridge University Press*, 2010.

[87] Yogeshkumar Malam, Marilena Loizidou, and Alexander M Seifalian. Liposomes and nanoparticles: nanosized vehicles for drug delivery in cancer. *Trends in Pharmacological Sciences*, 30(11):592–599, jan 2017.

[88] Rupa R. Sawant and Vladimir P. Torchilin. Liposomes as smart pharmaceutical nanocarriers. *Soft Matter*, 6(17):4026, 2010.

[89] G. M. Whitesides. Self-Assembly at All Scales. *Science*, 295(5564):2418–2421, 2002.

[90] Vincenzo Guida. Thermodynamics and kinetics of vesicles formation processes. *Advances in Colloid and Interface Science*, 161(1-2):77–88, dec 2010.

[91] Elisa Elizondo Sáez de Vicuña. New molecule based nanostructured drug carriers prepared using compressed fluids. page 258, 2010.

[92] T Musacchio and VP Torchilin. Recent developments in lipid-based pharmaceutical nanocarriers. *Front Biosci*, pages 1388–1412, 2011.

[93] Pranali P. Deshpande, Swati Biswas, and Vladimir P Torchilin. Current trends in the use of liposomes for tumor targeting. *Nanomedicine*, 8(9):1509–28, 2013.

[94] Dimitrios Papakostas, Fiorenza Rancan, Wolfram Sterry, Ulrike Blume-Peytavi, and Annika Vogt. Nanoparticles in dermatology. *Archives of Dermatological Research*, 303(8):533, 2011.

[95] Milad Fathi, M R Mozafari, and M Mohebbi. Nanoencapsulation of food ingredients using lipid based delivery systems. *Trends in Food Science and Technology*, 23(1):13–27, 2012.

[96] Zhong-Kai Cui, Anne Bouisse, Nicolas Cottenye, and Michel Lafleur. Formation of pH-Sensitive Cationic Liposomes from a Binary Mixture of Monoalkylated Primary Amine and Cholesterol. *Langmuir*, 28(38):13668–13674, sep 2012.

[97] Lisa Sercombe, Tejaswi Veerati, Fatemeh Moheimani, Sherry Y. Wu, Anil K. Sood, and Susan Hua. Advances and challenges of liposome assisted drug delivery. *Frontiers in Pharmacology*, 6(DEC):1–13, 2015.

[98] Elisa Elizondo, Evelyn Moreno, Ingrid Cabrera, Alba Córdoba, Santiago Sala, Jaume Veciana, and Nora Ventosa. *Liposomes and other vesicular systems: Structural characteristics, methods of preparation, and use in nanomedicine*, volume 104. 2011.

[99] N Grimaldi, F Andrade, N Segovia, L Ferrer-Tasies, S Sala, J Veciana, and N Ventosa. Lipid-based nanovesicles for nanomedicine. *Chemical Society Reviews*, 45:6520–6545, 2016.

[100] M Dubois and T Zemb. Phase behavior and scattering of double-chain surfactants in diluted aqueous solutions. *Langmuir*, 7(7):1352–1360, jul 1991.

[101] Francesca Caboi and Maura Monduzzi. Didodecyldimethylammonium Bromide Vesicles and Lamellar Liquid Crystals. A Multinuclear NMR and Optical Microscopy Study. *Langmuir*, 12(15):3548–3556, jan 1996.

[102] Anne S Ulrich. Biophysical Aspects of Using Liposomes as Delivery Vehicles. *Bioscience Reports*, 22(2):129–150, 2002.

[103] Christopher Kirby, Jacqui Clarke, and Gregory Gregoriadis. Effect of the cholesterol content of small unilamellar liposomes on their stability in vivo and in vitro. *Biochemical Journal*, 186(2):591–598, feb 1980.

[104] Gregory Gregoriadis and Christine Davis. Stability of liposomes invivo and invitro is promoted by their cholesterol content and the presence of blood cells. *Biochemical and Biophysical Research Communications*, 89(4):1287–1293, aug 1979.

[105] R.C.C. New. *Preparation of liposomes*. 1990.

[106] Dr. a. K. Bhandari J.S. Dua, Prof. A. C. Rana. Review Article LIPOSOME : METHODS OF PREPARATION AND APPLICATIONS. *International Journal of Pharmaceutical Studies and Research*, 3:7, 2012.

[107] F Szoka, F Olson, T Heath, W Vail, E Mayhew, and D Papahadjopoulos. Preparation of unilamellar liposomes of intermediate size (0.1-0.2 mumol) by a combination of reverse phase evaporation and extrusion through polycarbonate membranes. *Biochimica et biophysica acta*, 601(3):559–571, 1980.

[108] Dixon J Woodbury, Eric S Richardson, Aaron W Grigg, Rodney D Welling, and Brian H Knudson. Reducing Liposome Size with Ultrasound: Bimodal Size Distributions. *Journal of Liposome Research*, 16(1):57–80, jan 2006.

[109] M J Hope, M B Bally, G Webb, and P R Cullis. Production of large unilamellar vesicles by a rapid extrusion procedure. Characterization of size distribution, trapped volume and ability to maintain a membrane potential. *Biochimica et Biophysica Acta (BBA) - Biomembranes*, 812(1):55–65, 1985.

[110] N Berger, A Sachse, J Bender, R Schubert, and M Brandl. Filter extrusion of liposomes using different devices: comparison of liposome size, encapsulation efficiency, and process characteristics. *International Journal of Pharmaceutics*, jul 2001.

[111] Abeer A W Elzainy, Xiaochen Gu, F Estelle R Simons, and Keith J Simons. Hydroxyzine- and Cetirizine-Loaded Liposomes: Effect of Duration of Thin Film Hydration, Freeze-Thawing, and Changing Buffer pH on Encapsulation and Stability. *Drug Development and Industrial Pharmacy*, 31(3):281–291, jan 2005.

[112] Louise A Meure, Neil R Foster, and Fariba Dehghani. Conventional and Dense Gas Techniques for the Production of Liposomes: A Review. *AAPS PharmSciTech*, 9(3):798, 2008.

[113] Michael A W Eaton. Improving the translation in Europe of nanomedicines (a.k.a. drug delivery) from academia to industry. *Journal of Controlled Release*, 164(3):370–371, dec 2012.

[114] James Jennings, Mariana Beija, Alexandre P Richez, Samuel D Cooper, Paul E Mignot, Kristofer J Thurecht, Kevin S Jack, and Steven M Howdle. One-Pot Synthesis of Block Copolymers in Supercritical Carbon Dioxide: A Simple Versatile Route to Nanostructured Microparticles. *Journal of the American Chemical Society*, 134(10):4772–4781, mar 2012.

[115] Irene Pasquali and Ruggero Bettini. Are pharmaceutics really going supercritical? *International Journal of Pharmaceutics*, 364(2):176–187, dec 2008.

[116] E Reverchon and R Adami. Nanomaterials and supercritical fluids. *The Journal of Supercritical Fluids*, 37(1):1–22, feb 2006.

[117] Elisa Elizondo, Jaume Veciana, and Nora Ventosa. Nanostructuring molecular materials as particles and vesicles for drug delivery, using compressed and supercritical fluids. *Nanomedicine*, 7(9):1391–1408, 2012.

[118] François Cansell and Cyril Aymonier. Design of functional nanostructured materials using supercritical fluids. *The Journal of Supercritical Fluids*, 47(3):508–516, jan 2009.

[119] Santiago Sala, Elisa Elizondo, Evelyn Moreno, Teresa Calvet, Miguel Angel Cuevas-Diarte, Nora Ventosa, and Jaume Veciana. Kinetically driven crystallization of a pure polymorphic phase of stearic acid from CO2-expanded solutions. *Crystal Growth and Design*, 10(3):1226–1232, 2010.

[120] Santiago Sala, Alba Co, Evelyn Moreno-calvo, Elisa Elizondo, Maria Munto, Paula Elena Rojas, Maria a Larrayoz, Nora Ventosa, and Jaume Veciana. Crystallization of Microparticulate Pure Polymorphs of Active Pharmaceutical Ingredients Using CO 2 -Expanded Solvents Crystal Growth of Organic Materials (CGOM9). *Growth (Lakeland)*, 2012.

[121] Nora Ventosa, Santiago Sala, Jaume Veciana, Joaquim Torres, and Joan Llibre. Depressurization of an Expanded Liquid Organic Solution (DELOS): A New Procedure for Obtaining Submicron- Or Micron-Sized Crystalline Particles. *Crystal Growth and Design*, 1(4):299–303, 2001.

[122] N Ventosa, S Sala, and J Veciana. DELOS process: a crystallization technique using compressed fluids: 1. Comparison to the GAS crystallization method. *The Journal of Supercritical Fluids*, 26(1):33–45, may 2003.

[123] Mary Cano-Sarabia, Nora Ventosa, Santiago Sala, Cristina Patiño, Rocío Arranz, and Jaume Veciana. Preparation of uniform rich cholesterol unilamellar nanovesicles using CO2-expanded solvents. *Langmuir*, 24(6):2433–2437, 2008.

[124] Ingrid Cabrera, Elisa Elizondo, Olga Esteban, José Luis Corchero, Marta Melgarejo, Daniel Pulido, Alba Córdoba, Evelyn Moreno, Ugutz Unzueta, Esther Vazquez, Ibane Abasolo, Simó Schwartz, Antonio Villaverde, Fernando Albericio, Miriam Royo, Maria F. García-Parajo, Nora Ventosa, and Jaume Veciana. Multifunctional nanovesicle-bioactive conjugates prepared by a one-step scalable method using CO2-expanded solvents. *Nano Letters*, 13(8):3766–3774, 2013.

[125] Ingrid Cabrera, Ibane Abasolo, José L Corchero, Elisa Elizondo, Pilar Rivera Gil, Evelyn Moreno, Jordi Faraudo, Santi Sala, Dolores Bueno, Elisabet González-Mira, Merche Rivas, Marta Melgarejo, Daniel Pulido, Fernando Albericio, Miriam Royo, Antonio Villaverde, Maria F García-Parajo, Simó Schwartz, Nora Ventosa, and Jaume Veciana. α-Galactosidase-A Loaded-Nanoliposomes with Enhanced Enzymatic Activity and Intracellular Penetration. *Advanced Healthcare Materials*, 5(7):829–840, 2016.

[126] M H J Santana, R L Ventosa, D E Martinez, A J A Berlanga, P I Cabrera, and M J Veciana. Vesicles which include epidermal growth factor and compositions that contain same, 2014.

[127] Eduardo F. Marques. Size and stability of catanionic vesicles: effects of formation path, sonication, and aging. *Langmuir*, 16(11):4798–4807, 2000.

[128] Eric W. Kaler, Kathleen L. Herrington, A. Kamalakara Murthy, and Joseph A. N. Zasadzinski. Phase behavior and structures of mixtures of anionic and cationic surfactants. *Journal of Physical Chemistry*, 96:6698–6707, 1992.

[129] Hiroyuki Fukuda, Koji Kawata, Hideshi Okuda, and Steven L Regen. Bilayer-forming ion pair amphiphiles from single-chain surfactants. *J. Am. Chem. Soc.*, 112(4):1635–7, 1990.

[130] Lidia Ferrer-Tasies. Cholesterol and Compressed CO2: a Smart Molecular Building Block and Advantageous Solvent to Prepare Stable Self-assembled Colloidal Nanostructures. page 293, 2016.

[131] Elisa Elizondo, Jannik Larsen, Nikos S. Hatzakis, Ingrid Cabrera, Thomas Bjørnholm, Jaume Veciana, Dimitrios Stamou, and Nora Ventosa. Influence of the preparation route on the supramolecular organization of lipids in a vesicular system. *Journal of the American Chemical Society*, 134(4):1918–1921, 2012.

[132] H T Jung, B Coldren, J A Zasadzinski, D J Iampietro, and E W Kaler. The origins of stability of spontaneous vesicles. *Proceedings of the National Academy of Sciences of the United States of America*, 98(4):1353–1357, feb 2001.

[133] Suzana Šegota and D. urd ica Težak. Spontaneous formation of vesicles, 2006.

[134] Lidia Ferrer-Tasies, Evelyn Moreno-Calvo, Mary Cano-Sarabia, Marcel Aguilella-Arzo, Angelina Angelova, Sylviane Lesieur, Susagna Ricart, Jordi Faraudo, Nora

Ventosa, and Jaume Veciana. Quatsomes: Vesicles formed by self-assembly of sterols and quaternary ammonium surfactants. *Langmuir*, 29(22):6519–6528, 2013.

[135] Nadia Barbero, Ermanno Barni, Claudia Barolo, Pierluigi Quagliotto, Guido Viscardi, Lucia Napione, Simona Pavan, and Federico Bussolino. A study of the interaction between fluorescein sodium salt and bovine serum albumin by steady-state fluorescence. *Dyes and Pigments*, 80(3):307–313, 2009.

[136] Xin Wang, Meng Luo Ji, Ji Wang, and Zhi Chang Qi. Trace acquirement technology of real-time systems based on WCET analysis. *Ruan Jian Xue Bao/Journal of Software*, 17(5):1232–1240, 2006.

[137] Aimin Song, J Zhang, M Zhang, T Shen, and J Tang. Spectral properties and structure of ?uorescein and its alkyl derivatives in micelles. *Colloids and Surfaces A: Physicochem.Eng.Aspects*, 167:253–262, 2000.

[138] Ebru Bozkurt, TuÇ§ba Bayraktutan, Murat Acar, and Mahmut Toprak. Spectroscopic studies on the interaction of fluorescein and safranine T in PC liposomes. *Spectrochimica Acta - Part A: Molecular and Biomolecular Spectroscopy*, 101:31–35, 2013.

[139] Robert Sjöback, Jan Nygren, and Mikael Kubista. Absorption and fluorescence properties of fluorescein. *Spectrochimica Acta Part A: Molecular and Biomolecular Spectroscopy*, 51(6):L7 – L21, 1995.

[140] Soma Biswas, Subhash Ch. Bhattacharya, Pratik K. Sen, and Satya P. Moulik. Absorption and emission spectroscopic studies of fluorescein dye in alkanol, micellar and microemulsion media. *Journal of Photochemistry and Photobiology A: Chemistry*, 123(1-3):121–128, 1999.

[141] Loling Song, R. P M Van Gijlswijk, I. Ted Young, and Hans J. Tanke. Influence of fluorochrome labeling density on the photobleaching kinetics of fluorescein in microscopy. *Cytometry*, 27(3):213–223, 1997.

[142] Kevin D Belfield, Mykhailo V Bondar, Olga V Przhonska, and Katherine J Schafer. Photochemical properties of (7-benzothiazol-2-yl-9,9-didecylfluoren-2-yl)diphenylamine under one- and two-photon excitation. *Journal of Photochemistry and Photobiology A: Chemistry*, 162(2-3):569–574, 2004.

[143] Kevin D. Belfield, Mykhailo V. Bondar, Yong Liu, and Olga V. Przhonska. Photophysical and photochemical properties of 5,7-di-methoxycoumarin under one- and two-photon excitation. *Journal of Physical Organic Chemistry*, 16(1):69–78, 2003.

[144] M. Talhavini and T.D.Z. Atvars. Photostability of xanthene molecules trapped in poly(vinyl alcohol) (PVA) matrices. *Journal of Photochemistry and Photobiology A: Chemistry*, 120(2):141–149, 1999.

[145] H B Kostenbauder. Photochemical Macromolecules Reactions in Presence of Surfactants. 94:83–94, 1971.

[146] Amaresh Mishra, Rajani K. Behera, Pradipta K. Behera, Bijaya K. Mishra, and Gopa B. Behera. Cyanines during the 1990s: a review. *Chemical Reviews*, 100(6):1973–2011, 2000.

[147] Yves H Meyer, Moana Pittman, and Pascal Plaza. Transient absorption of symmetrical carbocyanines. *Journal of Photochemistry and Photobiology A: Chemistry*, 114(1):1–21, 1998.

[148] Edward S. Ruthazer and Hollis T. Cline. Multiphoton Imaging of Neurons in Living Tissue: Acquisition and Analysis of Time-Lapse Morphological Data. *Real-Time Imaging*, 8(3):175–188, 2002.

[149] M G Honig and R I Hume. Fluorescent carbocyanine dyes allow living neurons of identified origin to be studied in long-term cultures. *The Journal of Cell Biology*, 103(1):171–187, jul 1986.

[150] Frank Würthner, Theo E. Kaiser, and Chantu R. Saha-Möller. J-aggregates: From serendipitous discovery to supramolecular engineering of functional dye materials. *Angewandte Chemie - International Edition*, 50(15):3376–3410, 2011.

[151] A. Eisfeld and J. S. Briggs. The J- and H-bands of organic dye aggregates. *Chemical Physics*, 324(2-3):376–384, 2006.

[152] W West, W West, and Sandra Pearce. The Dimeric State of Cyanine Dyes. 566(1956):1894–1903, 1964.

[153] Suresh Gadde, Elizabeth K. Batchelor, and Angel E. Kaifer. Controlling the formation of cyanine dye H- and J-aggregates with cucurbituril hosts in the

presence of anionic polyelectrolytes. *Chemistry - A European Journal*, 15:6025–6031, 2009.

[154] AK Chibisov, VI Prokhorenko, and H Görner. Effects of surfactants on the aggregation behaviour of thiacarbocyanine dyes. *Chemical Physics*, 250(1):47–60, 1999.

[155] Junfeng Xiang, Ciping Chen, Zhongwei Chen, Wenpeng Yan, Xicheng Ai, Yang Liu, and Guangzhi Xu. Photoinduced Electron Transfer from the Excited J-Aggregate State of a Thiacarbocyanine Dye to TiO2 Colloids. *Journal of Colloid and Interface Science*, 254(1):195–199, 2002.

[156] Collera Garcia-Jimenez, Khramov, Sanchez Obregon. Formation of J-aggreates of cyanine dyes in bilayer lipid vesicles. *Chemical Physics Letters*, 331(1):42–46, 2000.

[157] D. Geissler, C. Gollwitzer, A. Sikora, C. Minelli, M. Krumrey, and U. Resch-Genger. Effect of fluorescent staining on size measurements of polymeric nanoparticles using DLS and SAXS. *Anal. Methods*, 7(23):9785–9790, 2015.

[158] Joseph R. Lakowicz. *Principles of fluorescence spectroscopy*. 2006.

[159] Yuhui Lin, Ralph Weissleder, and Ching-hsuan Tung. Novel Near-Infrared Cyanine Fluorochromes : Synthesis , Properties , and Bioconjugation. pages 605–610, 2002.

[160] Peter J Sims, Alan S Waggoner, Chao-Huei Wang, and Joseph F Hoffman. Mechanism by which cyanine dyes measure membrane potential in red blood cells and phosphatidylcholine vesicles. *Biochemistry*, 13(16):3315–3330, 1974.

[161] Na Zhao, Jacky W Y Lam, Herman H Y Sung, Hui Min Su, Ian D. Williams, Kam Sing Wong, and Ben Zhong Tang. Effect of the counterion on light emission: A displacement strategy to change the emission behaviour from aggregation-caused quenching to aggregation-induced emission and to construct sensitive fluorescent sensors for Hg2+ detection. *Chemistry - A European Journal*, 20(1):133–138, 2014.

[162] Ratnakar B. Mujumdar, Lauren a Ernst, Swati R Mujumdar, Christopher J Lewis, and Alan S Waggoner. Cyanine dye labeling reagents: sulfoindocyanine succinimidyl esters. *Bioconjugate Chemistry*, 4(2):105–11, 1993.

[163] Kathrin Klehs, Christoph Spahn, Ulrike Endesfelder, Steven F. Lee, Alexandre Fürstenberg, and Mike Heilemann. Increasing the brightness of cyanine

fluorophores for single-molecule and superresolution imaging. *ChemPhysChem*, 15(4):637–641, 2014.

[164] S. Lepaja, H. Strub, and D.-J. Lougnot. Photophysical Study of a Series of Cyanines. *Z. Naturforsch*, 38 a:56–60, 1983.

[165] Alexander S. Tatikolov and Sílvia M B Costa. Effects of normal and reverse micellar environment on the spectral properties, isomerization and aggregation of a hydrophilic cyanine dye. *Chemical Physics Letters*, 346(3-4):233–240, 2001.

[166] C Eggeling and R Rigler. Photostability of Fluorescent Dyes for Single-Molecule Spectroscopy :. 1999.

[167] Songjie Yang, He Tian, Heming Xiao, Xinghong Shang, Xuedong Gong, Side Yao, and Kongchang Chen. Photodegradation of cyanine and merocyanine dyes. *Dyes and Pigments*, 49(2):93–101, 2001.

[168] Hari S. Muddana, Samudra Sengupta, Ayusman Sen, and Peter J. Butler. Enhanced brightness and photostability of cyanine dyes by supramolecular containment. *arXiv.org*, page 20, 2014.

[169] S A Soper, H L Nutter, R A Keller, L M Davis, and E B Shera. The Photophysical Constants of Several Fluorescent Dyes Pertaining to Ultrasensitive Fluorescence Spectroscopy. *Photochemistry and Photobiology*, 57(6):972–977, 1993.

[170] Jeffrey T Buboltz and Gerald W Feigenson. A novel strategy for the preparation of liposomes: rapid solvent exchange. *Biochimica et Biophysica Acta (BBA) - Biomembranes*, 1417(2):232–245, mar 1999.

[171] A D Bangham and R W Horne. Negative staining of phospholipids and their structural modification by surface-active agents as observed in the electron microscope. *Journal of Molecular Biology*, 8(5):660–IN10, 1964.

[172] Abolfazl Akbarzadeh, Rogaie Rezaei-Sadabady, Soodabeh Davaran, Sang Woo Joo, Nosratollah Zarghami, Younes Hanifehpour, Mohammad Samiei, Mohammad Kouhi, and Kazem Nejati-Koshki. Liposome: classification, preparation, and applications. *Nanoscale Research Letters*, 8(1):102, feb 2013.

[173] Christian D Lorenz, Jordi Faraudo, and Alex Travesset. Hydrogen Bonding and Binding of Polybasic Residues with Negatively Charged Mixed Lipid Monolayers. *Langmuir*, 24(5):1654–1658, mar 2008.

[174] Rayna Bryaskova, Nikolai I Georgiev, Stefan M Dimov, Rumiana Tzoneva, Christophe Detrembleur, Abdullah M Asiri, Khalid A Alamry, and Vladimir B Bojinov. Novel nanosized water soluble fluorescent micelles with embedded perylene diimide fluorophores for potential biomedical applications: Cell permeability, localization and cytotoxicity. *Materials Science and Engineering: C*, 51:7–15, jun 2015.

[175] G. B. Behera, P. K. Behera, and B. K. Mishra. Cyanine Dyes: Self Aggregation and Behaviour in Surfactants A Review. *Journal of Surface Science and Technology*, 23(1/2):1, 2007.

[176] Vijay Patel, Nilesh Dharaiya, Debes Ray, Vinod K Aswal, and Pratap Bahadur. pH controlled size/shape in CTAB micelles with solubilized polar additives: A viscometry, scattering and spectral evaluation. *Colloids and Surfaces A: Physicochemical and Engineering Aspects*, 455:67–75, aug 2014.

[177] Per Ekwall, Leo Mandell, and Peter Solyom. The aqueous cetyl trimethylammonium bromide solutions. *Journal of Colloid and Interface Science*, 35(4):519–528, 1971.

[178] Martin Pisárčik, Ferdinand Devínsky, and Matúš Pupák. Determination of micelle aggregation numbers of alkyltrimethylammonium bromide and sodium dodecyl sulfate surfactants using time-resolved fluorescence quenching. *Open Chemistry*, 13(1):922–931, 2015.

[179] Milosz Pawlicki, Hazel A. Collins, Robert G. Denning, and Harry L. Anderson. Two-photon absorption and the design of two-photon dyes. *Angewandte Chemie - International Edition*, 48(18):3244–3266, 2009.

[180] Hwan Myung Kim and Bong Rae Cho. Small-Molecule Two-Photon Probes for Bioimaging Applications. *Chemical Reviews*, 115(11):5014–5055, 2015.

[181] Lei Guo and Man Shing Wong. Multiphoton excited fluorescent materials for frequency upconversion emission and fluorescent probes. *Advanced Materials*, 26(31):5400–5428, 2014.

[182] Chris Xu, R M Williams, Warren Zipfel, and Watt W Webb. Multiphoton excitation cross sections of molecular fluorophores. *Bioimaging*, 4:198–207, 1996.

[183] Honghua Hu, Dmitry A. Fishman, Andrey O. Gerasov, Olga V. Przhonska, Scott Webster, Lazaro A. Padilha, Davorin Peceli, Mykola Shandura, Yuriy P. Kovtun, Alexey D. Kachkovski, Iffat H. Nayyar, Art??m E. Masunov, Paul Tongwa, Tatiana V. Timofeeva, David J. Hagan, and Eric W. Van Stryland. Two-photon absorption spectrum of a single crystal cyanine-like dye. *Journal of Physical Chemistry Letters*, 3(9):1222–1228, 2012.

[184] Lazaro a. Padilha, Scott Webster, Olga V. Przhonska, Honghua Hu, Davorin Peceli, Jonathan L. Rosch, Mikhail V. Bondar, Andriy O. Gerasov, Yuriy P. Kovtun, Mykola P. Shandura, Alexey D. Kachkovski, David J. Hagan, and Eric W. Van Stryland. Nonlinear absorption in a series of Donor-pi-Acceptor cyanines with different conjugation lengths. *Journal of Materials Chemistry*, 19(40):7503, 2009.

[185] Jie Fu, Lazaro a. Padilha, David J. Hagan, Eric W. Van Stryland, Olga V. Przhonska, Mikhail V. Bondar, Yuriy L. Slominsky, and Alexei D. Kachkovski. Molecular structure two-photon absorption property relations in polymethine dyes. *Journal of the Optical Society of America B*, 24(1):56, 2007.

[186] Elisabetta Collini, Camilla Ferrante, Renato Bozio, Andrea Lodi, and Glauco Ponterini. Large third-order nonlinear optical response of porphyrin J-aggregates oriented in self-assembled thin films. *Journal of Materials Chemistry*, 16(16):1573, 2006.

[187] Kenji Kamada, Yoshihiko Tanamura, Kosei Ueno, Koji Ohta, and Hiroaki Misawa. Enhanced two-photon absorption of chromophores confined in two-dimensional nanospace. *Journal of Physical Chemistry C*, 111(30):11193–11198, 2007.

[188] Junlong Geng, Kai Li, Dan Ding, Xinhai Zhang, Wei Qin, Jianzhao Liu, Ben Zhong Tang, and Bin Liu. Lipid-PEG-folate encapsulated nanoparticles with aggregation induced emission characteristics: Cellular uptake mechanism and two-photon fluorescence imaging. *Small*, 8(23):3655–3663, 2012.

[189] Aliasghar Ajami, Peter Gruber, Maximilian Tromayer, Wolfgang Husinsky, Jürgen Stampfl, Robert Liska, and Aleksandr Ovsianikov. Evidence of concentration dependence of the two-photon absorption cross section: Determining the true cross section value. *Optical Materials*, 47:524–529, 2015.

[190] Mikhail Drobizhev, Nikolay S Makarov, Shane E Tillo, Thomas E Hughes, and Aleksander Rebane. Two-photon absorption properties of fluorescent proteins. 8(5):393–399, 2011.

[191] Richard S. Lepkowicz, Olga V. Przhonska, Joel M. Hales, Jie Fu, David J. Hagan, Eric W. Van Stryland, Mikhail V. Bondar, Yuriy L. Slominsky, and Alexei D. Kachkovski. Nature of the electronic transitions in thiacarbocyanines with a long polymethine chain. *Chemical Physics*, 305(1-3):259–270, 2004.

[192] Yutaka Kawabe and Sho Kato. Spectroscopic study of cyanine dyes interacting with the biopolymer, DNA. *Dyes and Pigments*, 95(3):614–618, 2012.

[193] Xiaolan Chen, M. Carmen Estévez, Zhi Zhu, Yu Fen Huang, Yan Chen, Lin Wang, and Weihong Tan. Using aptamer-conjugated fluorescence resonance energy transfer nanoparticles for multiplexed cancer cell monitoring. *Analytical Chemistry*, 81(16):7009–7014, 2009.

[194] Bernard Valeur. *Molecular Fluorescence*, volume 8. 2001.

[195] Jian Chen, Fuhua Huang, Hong Wang, Ya Li, Shengli Liu, and Pinggui Yi. One-pot preparation of multicolor polymeric nanoparticles with high brightness by single wavelength excitation. *Journal of Applied Polymer Science*, 132(8):1–9, 2015.

[196] Zhenzhen Xu, Qing Liao, Xingrui Shi, Hui Li, Haoli Zhang, and Hongbing Fu. Full-color tunable organic nanoparticles with FRET-assisted enhanced two-photon excited fluorescence for bio-imaging. *Journal of Materials Chemistry B*, 1(44):6035–6041, 2013.

[197] Xiaoxiao He, Yushuang Wang, Kemin Wang, Mian Chen, and Suye Chen. Fluorescence resonance energy transfer mediated large stokes shifting near-infrared fluorescent silica nanoparticles for in vivo small-animal imaging. *Analytical Chemistry*, 84(21):9056–9064, 2012.

[198] Anil Wagh, Faidat Jyoti, Sanku Mallik, Steven Qian, Estelle Leclerc, and Benedict Law. Polymeric nanoparticles with sequential and multiple FRET cascade mechanisms for multicolor and multiplexed imaging. *Small*, 9(12):2129–2139, 2013.

[199] R. M. Clegg. Fluorescence resonance energy transfer. *Current Opinion in Biotechnology*, 6(1):103–110, 1995.

[200] Igor Medintz and Niko Hildebrandt. *FRET - Forster Resonance Energy Transfer*. WILEY-VCH Verlag, 2014.

[201] Marta Fernandez-Suarez and Alice Y Ting. Fluorescent probes for super-resolution imaging in living cells. *Nat Rev Mol Cell Biol*, 9(12):929–943, 2008.

[202] Kelly Rae Chi. Super-resolution microscopy: breaking the limits. *Nature Methods*, 6(1):15–18, 2009.

[203] Ricardo Henriques, Caron Griffiths, E. Hesper Rego, and Musa M. Mhlanga. PALM and STORM: Unlocking live-cell super-resolution. *Biopolymers*, 95(5):322–331, 2011.

[204] W. E. Moerner. Microscopy beyond the diffraction limit using actively controlled single molecules. *Journal of Microscopy*, 246(3):213–220, 2012.

[205] Michael A. Thompson, Julie S. Biteen, Samuel J. Lord, Nicholas R. Conley, and W. E. Moerner. *Molecules and Methods for Super-Resolution Imaging*, volume 475. Elsevier Inc., 1 edition, 2010.

[206] Jeff Gelles, Bruce J Schnapp, and Michael P Sheetz. Tracking kinesin-driven movements with nanometre-scale precision. *Nature*, 331(6155):450–453, feb 1988.

[207] Michael J Rust, Mark Bates, and Xiaowei W Zhuang. Sub-diffraction-limit imaging by stochastic optical reconstruction microscopy (STORM). *Nat Methods*, 3(10):793–795, 2006.

[208] Tyler J. Chozinski, Lauren A. Gagnon, and Joshua C. Vaughan. Twinkle, twinkle little star: Photoswitchable fluorophores for super-resolution imaging. *FEBS Letters*, 588(19):3603–3612, 2014.

[209] Taekjip Ha and Philip Tinnefeld. Photophysics of Fluorescence Probes for Single Molecule Biophysics and Super-Resolution Imaging. *Annu Rev Phys Chem*, 63(2):595–617, 2012.

[210] Graham T. Dempsey, Mark Bates, Walter E. Kowtoniuk, David R. Liu, Roger Y. Tsien, and Xiaowei Zhuang. Photoswitching mechanism of cyanine dyes. *Journal of the American Chemical Society*, 131(51):18192–18193, 2009.

[211] Daan Van Der Zwaag, Nane Vanparijs, Sjors Wijnands, Riet De Rycke, Bruno G. De Geest, and Lorenzo Albertazzi. Super Resolution Imaging of Nanoparticles Cellular Uptake and Trafficking. *ACS Applied Materials and Interfaces*, 8(10):6391–6399, 2016.

[212] Lorenzo Albertazzi, Remco W Van Der Hofstad, and E W Meijer. Probing Exchange Pathways in Super-Resolution Microscopy. *Science (New York, N.Y.)*, 491(6183):10–15, 2014.

[213] Ricardo M P da Silva, Daan van der Zwaag, Lorenzo Albertazzi, Sungsoo S Lee, E W Meijer, and Samuel I Stupp. Super-resolution microscopy reveals structural diversity in molecular exchange among peptide amphiphile nanofibres. *Nature communications*, XXX(XXX):XXX, 2016.

[214] Susan Cox. Super-resolution imaging in live cells. *Developmental Biology*, 401(1):175–181, 2015.

[215] S A Jones, S H Shim, J He, and X W Zhuang. Fast, three-dimensional super-resolution imaging of live cells. *Nature Methods*, 8(6):499–U96, 2011.

[216] A D Iqbal and L D Cassar. Process for colouring highly molecular organic material and polycyclic pigments, 1985.

[217] Marek Grzybowski, Eliza Glodkowska-Mrowka, Tomasz Stoklosa, and Daniel T Gryko. Bright, Color-Tunable Fluorescent Dyes Based on π-Expanded Diketopyrrolopyrroles. *Organic Letters*, 14(11):2670–2673, jun 2012.

[218] Marek Grzybowski and Daniel T. Gryko. Diketopyrrolopyrroles: Synthesis, reactivity, and optical properties. *Advanced Optical Materials*, 3(3):280–320, 2015.

[219] Matinder Kaur and Dong Hoon Choi. Diketopyrrolopyrrole: brilliant red pigment dye-based fluorescent probes and their applications. *Chemical Society Reviews*, 44(1):58–77, 2015.

[220] Matinder Kaur and Dong Hoon Choi. Diketopyrrolopyrrole: brilliant red pigment dye-based fluorescent probes and their applications. *Chemical Society reviews*, 44(1):58–77, 2015.

[221] Er Qian Guo, Pei Hua Ren, Yan Li Zhang, Hai Chang Zhang, and Wen Jun Yang. Diphenylamine end-capped 1,4-diketo-3,6-diphenylpyrrolo[3,4-c]pyrrole (DPP) derivatives with large two-photon absorption cross-sections and strong two-photon excitation red fluorescence. *Chemical communications (Cambridge, England)*, (39):5859–61, 2009.

[222] Marek Grzybowski, Vincent Hugues, Mireille Blanchard-Desce, and Daniel T Gryko. Two-Photon-Induced Fluorescence in New pi-Expanded Diketopyrrolopyrroles. *Chemistry A European Journal A European Journal*, 20(39):12493–12501, 2014.

[223] Elodie Heyer, Pauline Lory, Jérôme Leprince, Mathieu Moreau, Anthony Romieu, Massimo Guardigli, Aldo Roda, and Raymond Ziessel. Highly Fluorescent and Water-Soluble Diketopyrrolopyrrole Dyes for Bioconjugation. *Angewandte Chemie International Edition*, 54(10):2995–2999, 2015.

[224] Hussein Ftouni, Frédéric Bolze, Hugues de Rocquigny, and Jean-François Nicoud. Functionalized Two-Photon Absorbing Diketopyrrolopyrrole-Based Fluorophores for Living Cells Fluorescent Microscopy. *Bioconjugate Chemistry*, 24(6):942–950, jun 2013.

[225] Hussein Ftouni, Frédéric Bolze, and Jean François Nicoud. Water-soluble diketopyrrolopyrrole derivatives for two-photon excited fluorescence microscopy. *Dyes and Pigments*, 97(1):77–83, 2013.

[226] Shuo Huang, Shiying Liu, Kai Wang, Cangjie Yang, Yimin Luo, Yingdan Zhang, Bin Cao, Yuejun Kang, and Mingfeng Wang. Highly fluorescent and bioresorbable polymeric nanoparticles with enhanced photostability for cell imaging. *Nanoscale*, 7(3):889–895, 2015.

[227] Catherine Kanimozhi, Nir Yaacobi-Gross, Kang Wei Chou, Aram Amassian, Thomas D Anthopoulos, and Satish Patil. Diketopyrrolopyrrole-Diketopyrrolopyrrole-based conjugate copolymer for high mobility organic field effect transistors. *Journal of the American Chemical Society*, 134(40):16532–16535, oct 2012.

[228] Wei-Hsuan Chang, Jing Gao, Letian Dou, Chun-Chao Chen, Yongsheng Liu, and Yang Yang. Side-Chain Tunability via Triple Component Random Copolymerization for Better Photovoltaic Polymers. *Advanced Energy Materials*, 4(4):1300864—-n/a, 2014.

[229] Angela Punzi, Eliana Maiorano, Francesca Nicoletta, Davide Blasi, Antonio Ardizzone, Nora Ventosa, Imma Ratera, Jaume Veciana, and Gianluca Maria Farinola. 1,2,3-Triazole-Diketopyrrolopyrrole Derivatives with Tunable Solubility and Intermolecular Interactions. *European Journal of Organic Chemistry*, 2016(15):2617–2627, 2016.

[230] Yican Wu, Jinxing Li, Bao Zha, Xinrui Miao, Lei Ying, and Wenli Deng. Intermolecular H···OâC bonds induced 2D self-assembly of thiophene based diketopyrrolopyrrole derivative. *Surface and Interface Analysis*, (January), 2017.

[231] Ming T. Liang, Nigel M. Davies, and Istvan Toth. Encapsulation of lipopeptides within liposomes: Effect of number of lipid chains, chain length and method of liposome preparation. *International Journal of Pharmaceutics*, 301(1-2):247–254, 2005.

[232] Maria Laura Immordino, Paola Brusa, Flavio Rocco, Silvia Arpicco, Maurizio Ceruti, and Luigi Cattel. Preparation, characterization, cytotoxicity and pharmacokinetics of liposomes containing lipophilic gemcitabine prodrugs. *Journal of Controlled Release*, 100(3):331–346, 2004.

[233] Mindaugas Kirkus, Linjun Wang, Sébastien Mothy, David Beljonne, Jérôme Cornil, René A J Janssen, and Stefan C J Meskers. Optical properties of oligothiophene substituted diketopyrrolopyrrole derivatives in the solid phase: Joint J- and H-type aggregation. *Journal of Physical Chemistry A*, 116(30):7927–7936, 2012.

[234] E. M. Czekanska, M. J. Stoddart, R. G. Richards, and J. S. Hayes. In search of an osteoblast cell model for in vitro research. *European Cells and Materials*, 24:1–17, 2012.

[235] Hecheng Ma, Chaoliang He, Yilong Cheng, Zhiming Yang, Junting Zang, Jianguo Liu, and Xuesi Chen. Localized Co-delivery of Doxorubicin, Cisplatin, and Methotrexate by Thermosensitive Hydrogels for Enhanced Osteosarcoma Treatment. *ACS Applied Materials and Interfaces*, 7(49):27040–27048, dec 2015.

[236] M. Hirao, K., Sugita, T., Kubo, T., Igarashi, K., Tanimoto, K., Murakami, T. ... Ochi. Targeted gene delivery to human osteosarcoma cells with magnetic cationic liposomes under a magnetic field. *International Journal of Oncology*, 22:1065–1071, 2003.

[237] Marie Kalbácová, Martina Verdánová, Filip Mravec, Tereza Halasová, and Miloslav Pekar. Effect of CTAB and CTAB in the presence of hyaluronan on selected human cell types. *Colloids and Surfaces A: Physicochemical and Engineering Aspects*, 460:204–208, oct 2014.

[238] Xin Chen, Yue Bi, Tianyang Wang, Pengfei Li, Xin Yan, Shanshan Hou, Catherine E. Bammert, Jingfang Ju, K. Michael Gibson, William J. Pavan, and Lanrong Bi.

Lysosomal Targeting with Stable and Sensitive Fluorescent Probes (Superior LysoProbes): Applications for Lysosome Labeling and Tracking during Apoptosis. *Scientific Reports*, 5:9004, 2015.

[239] CooperGM. *The cell: A molecular approach- 2nd edition*. Sinauer Associates, 2010.

[240] Carmine Settembre, Alessandro Fraldi, Diego L Medina, and Andrea Ballabio. Signals from the lysosome: a control centre for cellular clearance and energy metabolism. *Nat Rev Mol Cell Biol*, 14(5):283–296, may 2013.

[241] Fengkai Fan, Si Nie, Dongmei Yang, Meijie Luo, Hua Shi, and Yu Hui Zhang. Labeling lysosomes and tracking lysosome-dependent apoptosis with a cell-permeable activity-based probe. *Bioconjugate Chemistry*, 23(6):1309–1317, 2012.

[242] Yongkang Yue, Fang-Jun Huo, Songyi Lee, Caixia Yin, and Juyoung Yoon. A review: the trend of progress about pH probes in cell application in recent years. *The Analyst*, 2016.

[243] Hao Zhu, Jiangli Fan, Qunli Xu, Honglin Li, Jingyun Wang, Pan Gao, and Xiaojun Peng. Imaging of lysosomal pH changes with a fluorescent sensor containing a novel lysosome-locating group. *Chemical communications (Cambridge, England)*, 48(96):11766–8, 2012.

[244] Xiaoding Lou, Mengshi Zhang, Zujin Zhao, Xuehong Min, Abdul Hakeem, Fujian Huang, Pengcheng Gao, Fan Xia, and Ben Zhong Tang. A photostable AIE fluorogen for lysosome-targetable imaging of living cells. *J. Mater. Chem. B*, 4(32):5412–5417, 2016.

[245] Xinfu Zhang, Chao Wang, Zhuo Han, and Yi Xiao. A Photostable Near-Infrared Fluorescent Tracker with pH- Independent Speci fi city to Lysosomes for Long Time and Multicolor Imaging. pages 1–8, 2014.

[246] Ken Ichi Hanaki, Asami Momo, Taisuke Oku, Atsushi Komoto, Shinya Maenosono, Yukio Yamaguchi, and Kenji Yamamoto. Semiconductor quantum dot/albumin complex is a long-life and highly photostable endosome marker. *Biochemical and Biophysical Research Communications*, 302(3):496–501, 2003.

[247] Hui Shi, Xiaoxiao He, Yuan Yuan, Kemin Wang, and Dan Liu. Nanoparticle-based biocompatible and long-life marker for lysosome labeling and tracking. *Analytical Chemistry*, 82(6):2213–2220, 2010.

[248] Alexander Koshkaryev, Ritesh Thekkedath, Cinzia Pagano, Igor Meerovich, and Vladimir P Torchilin. Targeting of lysosomes by liposomes modified with octadecyl-rhodamine B. *Journal of drug targeting*, 19(8):606–614, 2011.

[249] Natalya Rapoport, Alexander Marin, Yi Luo, Glenn D Prestwich, and Md. Muniruzzaman. Intracellular Uptake and Trafficking of Pluronic Micelles in Drug Sensitive and MDR Cells: Effect on the Intracellular Drug Localization. *Journal of Pharmaceutical Sciences*, 91(1):157–170, jan 2002.

[250] Rajib Basak and Ranjini Bandyopadhyay. Encapsulation of Hydrophobic Drugs in Pluronic F127 Micelles: Effects of Drug Hydrophobicity, Solution Temperature, and pH. *Langmuir*, 29(13):4350–4356, apr 2013.

[251] Qihe Gao, Qing Liang, Fei Yu, Jian Xu, Qihua Zhao, and Baiwang Sun. Synthesis and characterization of novel amphiphilic copolymer stearic acid-coupled F127 nanoparticles for nano-technology based drug delivery system. *Colloids and Surfaces B: Biointerfaces*, 88(2):741–748, dec 2011.

[252] Sheng Yao, Hyo Yang Ahn, Xuhua Wang, Jie Fu, Eric W. Van Stryland, David J. Hagan, and Kevin D. Belfield. Donor-acceptor-donor fluorene derivatives for two-photon fluorescence lysosomal imaging. *Journal of Organic Chemistry*, 75(12):3965–3974, 2010.

[253] S A Kurhuzenkau, A W Woodward, S Yao, K D Belfield, Y O Shaydyuk, C Sissa, M V Bondar, and A Painelli. Ultrafast spectroscopy, superluminescence and theoretical modeling of a two-photon absorbing fluorene derivative. *Phys. Chem. Chem. Phys. Phys. Chem. Chem. Phys*, 18(18):12839–12846, 2016.

[254] Kevin D Belfield, Alma R Morales, Bong-Soo Kang, Joel M Hales, David J Hagan, Eric W Van Stryland, Victor M Chapela, and Judith Percino. Synthesis, Characterization, and Optical Properties of New Two-Photon-Absorbing Fluorene Derivatives. *Chemistry of Materials*, 16(23):4634–4641, nov 2004.

[255] M. Queen R. Rowe, P. Sheskey. *Handbook of Pharmaceutical Excipients - 6th edition*. Pharmaceutical Press, 2009.

[256] Hee Young Lee, Sun Hae Ra Shin, Aaron M. Drews, Aaron M. Chirsan, Sean A. Lewis, and Kyle J M Bishop. Self-assembly of nanoparticle amphiphiles with adaptive surface chemistry. *ACS Nano*, 8(10):9979–9987, 2014.

[257] Kevin D Belfield, Mykhailo V Bondar, Alma R Morales, Xiling Yue, Gheorghe Luchita, Olga V Przhonska, and Olexy D Kachkovsky. Two-Photon Absorption and Time-Resolved Stimulated Emission Depletion Spectroscopy of a New Fluorenyl Derivative. *ChemPhysChem*, 13(15):3481–3491, oct 2012.

[258] Terry L Riss, Richard A Moravec, Andrew L Niles, and Lisa Minor. Cell Viability Assays.

[259] N Vlachy, D Touraud, J Heilmann, and W Kunz. Determining the cytotoxicity of catanionic surfactant mixtures on HeLa cells. *Colloids and Surfaces B: Biointerfaces*, 70(2):278–280, may 2009.

[260] Stephen W. Paddock. *Confocal Microscopy*, volume 122. 1998.

[261] Jiang Ouyang, Qiguang Zang, Wansong Chen, Liqiang Wang, Shuo Li, Ren Yu Liu, Yuanyuan Deng, Zhao Qian Liu, Juan Li, Liu Deng, and You Nian Liu. Bright and photostable fluorescent probe with aggregation-induced emission characteristics for specific lysosome imaging and tracking. *Talanta*, 159:255–261, 2016.

[262] Kenneth W Dunn, Malgorzata M Kamocka, and John H McDonald. A practical guide to evaluating colocalization in biological microscopy. *American Journal of Physiology - Cell Physiology*, 300(4):C723–C742, apr 2011.

[263] Xuhua Wang, Dao M Nguyen, Ciceron O Yanez, Luis Rodriguez, Hyo-Yang Ahn, Mykhailo V Bondar, and Kevin D Belfield. High-Fidelity Hydrophilic Probe for Two-Photon Fluorescence Lysosomal Imaging. *Journal of the American Chemical Society*, 132(35):12237–12239, sep 2010.

[264] Hitoshi Kasai, Hari Singh Nalwa, Hidetoshi Oikawa, Shuji Okada, Hiro Matsuda, Nobutsugu Minami, Atsushi Karuta, Katsumichi Ono, and Akio Mukoh. A Novel Preparation Method of Organic Microcrystals.pdf. *Jpn. J. Appl. Phys.*, 31:L1132 – L1134, 1992.

[265] Elisa Campioli, C??dric Rouxel, Marco Campanini, Lucia Nasi, Mireille Blanchard-Desce, and Francesca Terenziani. Enforcing luminescence at organic nanointerfaces: Luminescence spatial confinement and amplification in molecular-based core-shell nanoparticles. *Small*, 9(11):1982–1988, 2013.

[266] Patrick Saulnier, Brigitte Pech, Jacques-emile Proust, and Jean-pierre Benoit. Physico-chemical stability of colloidal lipid particles. 24:4283–4300, 2003.

[267] Jing Shang and Xiaohu Gao. Chem Soc Rev Nanoparticle counting : towards accurate. *Chemical Society Reviews*, 43:7267–7278, 2014.

[268] Bob Carr and Matthew Wright. Nanoparticle Tracking Analysis Nanoparticle Tracking Analysis. 44(0), 2012.

[269] Vasco Filipe, Andrea Hawe, and Wim Jiskoot. Critical Evaluation of Nanoparticle Tracking Analysis (NTA) by NanoSight for the Measurement of Nanoparticles and Protein Aggregates. 27(5):796–810, 2010.

[270] Horiba. A Guide to Recording Fluorescence Quantum Yields - Horiba Protocol. Technical report, www.jyhoriba.co.uk.

[271] Christian Würth, Markus Grabolle, Jutta Pauli, Monika Spieles, and Ute Resch-genger. Relative and absolute determination of fluorescence quantum yields of transparent samples. *Nature protocols*, 8(8):1535–50, 2013.

[272] J. Zachary Porterfield Zlotnick and Adam. A Simple and General Method for Determining the Protein and Nucleic Acid Content of Viruses by UV Absorbance. 407(2):281–288, 2011.

[273] Gent Winder. Correction of Light-Scattering Errors in Spectrophotometric Protein Determinations.

[274] H A Scheraga. Effect of Light Scattering on Ultraviolet Difference Spectral. 82(6):4790–4792.

[275] Alberto Diaspro, Giuseppe Chirico, Cesare Usai, Paola Ramoino, and Jurek Dobrucki. Photobleaching. In *Handbook of Biological Confocal Microscopy*, pages 690–702. 2006.

[276] Marius A Albota, Chris Xu, and Watt W Webb. Two-photon fluorescence excitation cross sections of biomolecular probes from 690 to 960 nm. pages 1–5, 1998.

[277] James C Phillips, Rosemary Braun, Wei Wang, James Gumbart, Emad Tajkhorshid, Elizabeth Villa, Christophe Chipot, Robert D Skeel, Laxmikant Kalé, and Klaus Schulten. Scalable molecular dynamics with NAMD. *Journal of Computational Chemistry*, 26(16):1781–1802, 2005.

[278] W Humphrey, A Dalke, and K Schulten. VMD: visual molecular dynamics. *Journal of molecular graphics*, 14(1):27–28,33–38, feb 1996.

[279] Toni Giorgino. Computing 1-D atomic densities in macromolecular simulations: The density profile tool for VMD. *Computer Physics Communications*, 185(1):317–322, 2014.

[280] Justin Matthew Spiriti. Applications of Adaptive Umbrella Sampling in Biomolecular Simulation. *PhD dissertation, Arizona University*, 1(August), 2015.

Patents and Publications

- N. Ventosa, J. Veciana, A. Ardizzone, A. Painelli, S. Kurhuzenkau, C. Sissa, "Stable fluorescent nanovesicles, method for obtaining them and uses thereof", EU Patent Application submitted.

- A. Punzi, E. Maiorano, F. Nicoletta, D. Blasi, A. Ardizzone, N. Ventosa, I. Ratera, J. Veciana, G. M. Farinola, "1,2,3-Triazole–Diketopyrrolopyrrole Derivatives with Tunable Solubility and Intermolecular Interactions", Eur. J. Org. Chem. 2016, 2617–2627

Papers in preparation

- "Nanostructuring Lipophilic Dyes in Water Using Stable Vesicles – Quatsomes – as Scaffolds and their use as Probes for Bioimaging"

- "LysoQS: a new lysosomal probe based on fluorene derivative Quatsomes-based water dispersion"

- "Water dispersion of diketopyrrolopyrroles derivatives by mean of Quatsomes"